

MINI
SYMPOSIUM
VERFAHRENSTECHNIK
2025

Book of Abstracts

ISBN 978-3-200-10576-8



9 783200 105768

**19. Mini Symposium Verfahrenstechnik &
10. Partikelforum**

1. – 2. Juli 2025 | MCI | Innsbruck

Book of Abstracts

IMPRINT

1st Edition, July 2025
Copyright © MCI Internationale Hochschule GmbH
Editors: Prof. Dr.-Ing. Martin Pillei, Barbara Koller
Cover: Barbara Koller
www.mci.edu

DISCLAIMER

The abstracts are the sole responsibility of the respective authors who submitted them.
Content subject to errors and omissions.

Preface Rector

MENTORING THE MOTIVATED!

With 3,600 students, 1,000 full and part-time faculty, 300 partner universities, 18,000 alumni, and countless satisfied employers around the world the MCI has achieved an internationally acknowledged position as MCI | THE ENTREPRENEURIAL SCHOOL® which is complemented by numerous reputed awards, respected accreditations and excellent rankings.

With the help of its owners, sponsors and partners, MCI drives the positioning of Innsbruck and Austria as center for academic dialogue and international communication.

Research at MCI generates knowledge and delivers solutions for our partners. Our research activities do not only add value for our students and team, but they support industry and society with new or improved products, processes, market opportunities and a higher level of competitiveness.

We are happy to host the 19th Mini Symposium Chemical and Process Engineering this year. It is a great opportunity to once again bring together expertise from all over Austria and other countries in order to exchange ideas and push ahead with innovation and research. Let's look forward to inspiring presentations, stimulating discussions and a new impetus for our work!



Prof. Dr. Andreas Altmann

Rector and Executive Director
MCI

Preface Research, Development & Technology Transfer

The 19. Mini Symposium on Chemical & Process Engineering is a forum where PhD candidates from Austrian universities are invited to present their research and engage in cross-institutional networking.

This year, MCI has the pleasure of hosting this event for the second time in Western Austria. In line with its motto, *Bridging University and Business*, MCI – together with its Technology and Life Sciences Departments – continues to conduct both fundamental and applied research in close cooperation with industry and academia. The collaboration among Tyrolean universities forms a strong and dynamic network for interdisciplinary scientific work and provides a solid foundation for a forward-looking research landscape. This Symposium once again offers an outstanding opportunity to strengthen ties between Austrian universities and researchers in Chemical Process Engineering and Particle Technology.

The abstracts compiled in this volume cover a broad spectrum of topics in chemical, pharmaceutical, energy and process engineering. They present innovative data, methodologies, and scientific results. To ensure the high quality of all contributions, a peer-review process was conducted by experts, who generously contributed their time and expertise in the field of Chemical Process Engineering.

On behalf of MCI, I wish you a stimulating symposium filled with engaging talks and enriching discussions in the unique and welcoming atmosphere of Innsbruck, right in the heart of the Alps.



Prof. Dr.-Ing. Martin Pillei

Head of Research & Development
Head of Department & Studies
Industrial Engineering & Mgmt.

Program | July 1st

From 12:00	Registration	Foyer
13:00	Welcome Prof. Dr. Andreas Altmann, Rector MCI Prof. Dr.-Ing. Martin Pillei, Head of Department Research & Development	024
13:30	Keynotes „KI-Energiemanagement in der Praxis“ Dr. Benjamin Mörzinger (nista), DI Harald Tschenett (TRM) „From Green Carbon to Gold: A Rare Case of Modern Alchemy“ Dr. rer.nat. Robert Salchner, Syncraft	024 027
14:00	Presentations Session Energy & Process Engineering Session Renewables	024 027
15:00	Coffee Break	Foyer
15:20	Presentations & Rapid Oral Sessions Session Energy & Process Engineering Session Renewables	024 027
16:20	Break	Foyer
16:30	Poster Session Lab Tour	Foyer
18:00	Time to commute and arrive at dinner location	
19:00	Dinner at Restaurant Villa Blanka www.villablanka.com	

Program | July 2nd

08:30	Welcome & Coffee	Foyer
09:00	Keynote “P2X Jenbach – best practice in renewable Hydrogen production“ Dr. Andreas Burger (TiNext)	024
09:30	Presentations & Rapid Oral Sessions Session Hydrogen and its Applications	024
10:30	Coffee Break	Foyer
10:45	Presentations & Rapid Oral Sessions Session Circular Economy & Recycling Session Environmental	024 027
12:40	Lunch Closing Handover Marini Best Presentation Award Best Poster Award	Foyer
14:30	Excursion to Glockengießerei Grassmayr www.grassmayr.at	Foyer
17:00	Get together & Good bye	City

Content | Day 1

Energy & Process Engineering | Presentations

Manuel Berger	MCI	CFD development and testing of a self-priming vane pump for a flow rate of 2 m ³ /h at 300 rpm	19
Luca Nohel	MCI	Development of a single-channel model of electrically heated monoliths for dry reforming of methane	23
Doris Ostner-Kaineder	JKU Linz FH OÖ Wels	Multi-material textile waste as biomass feedstock: using fused filament fabrication to investigate optimal stirrer geometries in non-Newtonian media	27
Safdar Abbas	TU Wien	Evaluating pretreatment process impacts in a multi-product wheat straw biorefinery using prospective life cycle assessment	33
Simon Schneiderbauer	JKU Linz	A continuous particle model for the simulation of direct reduction of iron ore in fluidized beds	39

Energy & Process Engineering | Posters

Enatri Enan	JKU Linz	Bubble-particle interactions: A study on film drainage and particle cutting	42
Daniel Rattinger	MCI	Photocatalyst Development for Water Reclamation: From TiO ₂ to Boron Nitride-Based Composites	43
Lucia Colleselli	MCI	Biosynthesis of silver nanoparticles using <i>Penicillium ochrochloron</i> and <i>Saccharomyces cerevisiae</i> extracts	44
Lucia Colleselli	MCI	Biosynthese von Silber- & Goldnanopartikeln basierend auf terrestrischen Mikroalgen	45

Renewables | Presentations

Michael Kresta	MCI	A novel two stage bubbling fluidized bed gasification process - Practical Insights from gasification of mixed waste wood fractions	49
Theresa Brunauer	BOKU	Evaluation of an electrically heated bubbling fluidized bed gasification reactor	53
Sheekofeh Saberi	MU Leoben K1-MET GmbH	Computational analysis of carbon-neutral biofuels pyrolysis and combustion	57
Thomas Rasl	BOKU	Simulation of a novel steam gasification process with in-situ char separation via an overflow pipe to generate negative emission syngas from biomass	61
Antonia Biebighäuser	BOKU	Techno-economic assessment of CO ₂ capture technologies in SNG upgrading from biomass steam gasification	65

Renewables | Posters

Marija Jeremic	MU Leoben	Project "Reallabor Holzgas" – Biomass Syngas Methanation from a 10 kW Prototype to the planned 5 MW Pilot Plant	70
Stavroula Zervopoulou	TU Wien	A Multi-Component Learning Curve Framework for Estimating SAF Production Costs Using Solar-Assisted Fast Pyrolysis	71
Enzo Komatz	MU Leoben	Sustainable Aviation Fuels (SAF)	72

Content | Day 2

Hydrogen and Its Applications | Presentations

Abdolreza Aghajanpour	MU Leoben	Direct-Fired Furnace for Steel Strip Reheating: High-Fidelity CFD Analysis of Pure H ₂ versus Austrian Pipeline Natural Gas Firing	75
Severin Sendlhofer	MU Leoben	Methanation of Biogenic CO ₂ vs. Fossil CO ₂ from Industrial Point Sources: A Techno-Economic and Feedstock Comparison	79

Hydrogen and Its Applications | Posters

Selina Haller	MCI	BIOcubed: Biosynthesis of Green Hydrogen Using a Newly Discovered Microorganism	85
Elias Vigl	MU Leoben	Hydrogen Storage in Magnesium-Based Metal Powders: Influence of Production and Activation Methods	86
Joel Edjokola	TU Graz	Platinum-cobalt ORR Catalyst Degradation in LT-PEFCs: Effects of Anode-Cathode Humidity Gradients	87
Lucas Schuchter	MCI	Lifecycle Greenhouse Gas Emissions and Energy Efficiency of Fuel Cell Electric Trucks in Alpine Applications	88

Circular Economy & Recycling | Presentations

Ulrich Hirn	TU Graz	Producing Packaging Paper from Post-Consumer Textile Waste	93
Emerson Barros de Souza	K1-MET GmbH	Numerical development of thermal pre-treatment for Li-ion battery recycling	97
Anton Rudolph	HS Kempten	QualiCheese – Haltbarkeitsoptimierung von Schnittkäse in ökologisch nachhaltigen Verpackungen	101
Johanna Müller	MCI	Shelf Life Optimization of Cheese Considering Ecologically Sustainable Packaging	105
Anna Lipp	TU Wien	Recovery of polyolefins from mixed waste in Tyrol: Status, qualities and critical parameters for recycling	109

Circular Economy & Recycling | Posters

Julia Mühl	TU Wien	Glass recovery from fluidized bed bottom ashes from municipal solid waste incineration	114
Lydia Challandes	MCI	Aufwertung von Bierhefe-Abfällen zur Biosynthese von Silbernanopartikel	115

Environmental | Presentations

David Gurtner	MCI	Activated Carbon from Gasified Waste Wood: Potential and Challenges	119
Judith Schobel	MCI	Adsorptive Removal of PFAS Using a Fluorinated Ion Exchange Polymer	123
Simon Moll	MU Leoben	On the formation of a galvanic element in blast furnaces and its use for process diagnostics	127
Sarah Reiter	MU Leoben	Carbonation behavior of Ca-rich steel slags: Influence of process parameters and mineralogical composition	131
Nina Schlemmer	K1-MET GmbH	Mechanistical approach for the electrical conductivity calculation of oxidic melts with focus on steelmaking slags	135

Environmental | Posters

Maximilian Käfer	TU Graz	Towards Robust Fuel Cell Systems: Mitigating the Risks of Over-Humidification	141
Igor Schweiggel	MCI	Calibration of a Concrete Pump for Automated Shotcrete Application in Tunneling	142
Alexander Trischack	TU Wien	Decolourisation of Starch Hydrolysates Using Activated Carbon and Ultrafiltration	143
Jana Marx	MCI	Upscaling of the Removal of Pharmaceuticals from Wastewater with Multi-channel Mixed-matrix membranes into pilot scale	144
Christian Margreiter	MCI	Desorption of Micropollutants from Bio-based Gasification Chars in Wastewater Treatment	145

d'arbo
Seit 1879



Wir danken unseren Sponsoren

MEMZEP



Energy & Process Engineering Presentations

Day 1

CFD development and testing of a self-priming vane pump for a flow rate of 2 m³/h at 300 rpm

M. Berger^{1,*}, L. Zingerle², T. Senfter², C. Mayerl², M. Pillei²

1: Dept. of Medical Technologies, MCI Innsbruck, Austria

2: Dept. of Industrial Engineering & Management, MCI Innsbruck, Austria

* Corresponding author: manuel.berger@mci.edu

Keywords: Vane pump, self-priming, 2m³/h, 300 rpm

Research field: Computational and experimental fluid dynamics

Abstract

Vane pumps are used for industrial fluid handling due to the efficient transfer and priming abilities. The development and optimization are key areas in engineering research for enhancing operational reliability and performance. Integrating computational fluid dynamics techniques provides detailed insights into fluid behavior, i.e. velocity profiles. This article focuses on transient analysis and experimental comparison of flow rates for a newly designed self-priming vane pump. Simulations using Ansys Fluent and experiments with a 3D printed pump were conducted at 300 rpm. In Ansys Design Modeler and Meshing the preprocessing for Fluent is done. Afterwards, a transient, density-based solver with the $k-\omega$ -SST RANS turbulence model with a time step size of 0.0001388 seconds is chosen to simulate one rotation of the pump. Fluent settings incorporated dynamic mesh motion for rotating volumes, utilizing user-defined functions (UDFs) out of the Ansys tutorial "FLUENT-MDM-tut-06vane-pump.pdf". A setup consisting of a frequency converter, an asynchronous motor and the ultra-sonic flow measurement device Panametrics TransPort PT900 is used to measure the inlet flow rate of the pump experimentally. Comparison of CFD simulation result (2.7 m³/h) and experimental measurement result (1.749 m³/h) shows a difference in the flow rate, which can be explained with the leakiness of the vanes in the experiment that is not taken into account in the CFD simulation. The pretty-old UDF code designed for Fluent 13 can be still compiled with the very new Fluent 2023R2 and allow further investigations with leakiness.

Introduction

Self-priming vane pumps [1] play a crucial role in various industrial applications, offering efficient fluid transfer and priming capabilities without external assistance. The development and optimization of these pumps have become a focal point in engineering research, aiming to improve operational reliability and performance in diverse applications. The integration of CFD [2] techniques in pump design and analysis can support and give detailed insights into fluid flow behavior, i.e. velocity distributions. Researchers have extensively explored the application of CFD in pump studies, as highlighted in works such as [3], showcasing the versatility and accuracy of CFD simulations in predicting pump performance under varying conditions. This paper focuses on the transient CFD analysis and experiments to compare the inlet flow rate of the self-priming rotary vane pump at 300 rpm.

Preprocessing of the CFD simulation

Geometrical design parameters are chosen as shown in Fig. 1, which seems form basic knowledge to design a pump permissible. Simulations are performed in Ansys 2023 R2 with the software packages Design Modeler, Meshing and Fluent. The overall presented approach is based on the Ansys tutorial "Vane Pump Modeling in ANSYS FLUENT.pdf" with the corresponding c-files vane.c, gerotor_vance_smoothing.c, tait.c and the input.txt file. This

tutorial is adapted to the design needs of the new self-priming vane pump to simulate the complex mesh motion. Initially the pump is designed in Autodesk Inventor 2022 software. In Fig. 1, the inlet and outlet pump diameters that are not shown are 9.7 mm. Initially, the pump geometry is imported into Ansys Design Modeler and split up into the four rotors and the fixed inlet and outlet geometries. With the "Form new part" command the four rotor bodies are combined to fluid-pump part and the inlet and outlet fixed bodies are combined to fluid-pipes part. The now generated 2 parts and 6 bodies are not connected, since there is the need for two mesh interfaces I_{in} and I_{out} . Later on in the meshing process no connection of the mesh points, interfaces and interpolation between the different meshes are performed. Due to the rotating mesh, connected mesh knots are not allowed. Subsequently, in the meshing process with Ansys Meshing a CFD mesh with linear elements, is generated. The default sizing function "capture curvature" is used, "capture proximity" is not activated. The rotor width is set with an edge sizing parametrized with 15 divisions, in radial direction 30 divisions and in z-direction 50 divisions. In z-direction the rotor is 0.057 m. No boundary layers are introduced due to complex mesh rotation process and the knowledge that the fluid flow velocity in the rotor is similar to the rotational speed. Finally, the inlet and outlet fixed bodies are meshed with a body sizing of 1 mm and the default inflation method with 5 layers. The final mesh consists of 299730 nodes and 639518 elements based on tetrahedrons with 4 knots, hexahedrons with 8 knots and for the boundary layer cells wedges with 6 knots. The maximum skewness is 0.79 (< 0.9) and the aspect ratio is 39.77 (< 1000) so that the mesh should be numerically stable within the CFD solution process. Fig. 1 shows a slice through the main axis. The Ansys meshfile in format .mshdb is converted to a Fluent mesh file .msh.

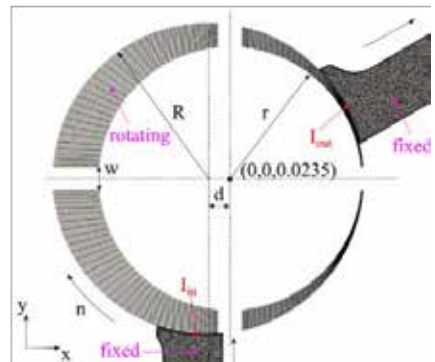


Fig. 1: Slice through the generated CFD mesh of the vane pump. Radius of the rotor $r = 0.0425$ m, Radius of the pump housing $R = 0.05$ m, offset $d = 0.007$ m, vane width $w = 0.008$ m and the pump rotational speed $n = 300$ rpm in clockwise direction. Since there are two fixed bodies and four rotating bodies, there are two mesh interfaces I_{in} and I_{out} . Inlet and outlet pump diameter which is not shown in figure is 0.097 m.

CFD simulation

The .msh file is opened in Fluent 2023 R2. Since the volumes are changing during rotation, the transient density based solver is chosen. The rotational speed is set to $n = 300$ rpm. The default $k-\omega$ -SST RANS turbulence model is chosen to deal with insufficient spatial and temporal resolution to model turbulence with artificial viscosity. For the investigation water with a density $\rho=998.2$ kg/m³ and a dynamic viscosity $\eta=0.001003$ Pas is chosen. Both boundary conditions, pump inlet and outlet, are set to ambient pressure with a turbulent intensity $TI=5\%$ and a hydraulic diameter $d_{hyd} = 0.0097$ m. Interfaces are automatically detected in Fluent to interpolate data between the fixed and rotating meshes. Compiled user defined functions (UDFs) are used for rotation. The input.txt file serves the parameters for vane.c, gerotor_vane_smoothing.c and tait.c, which is shown in Tab. 1. At the left column are the parameter names, at the right column are the parameter values. The file definition is found in the header of vane.c.

Tab. 1. Parameter names and values for the input.txt file

Parameter names	Parameter values
If outer shape is circle --> 0	0
If inner shape is circle --> 0	0
Number of vanes	4
Single core flag --> 0	0
Core IDs	7
Number of gaps	0
Gap id	Default -1
Inner profile will rote --> 1, else 0	-1 (clockwise direction)
RPM, inner circle radius, vane width, and gap size	-300.0 42.5e-3 8.0e-3 0.0e-3
outer radius and offset	50.0e-3 7e-3
initial vane angle	0
Equally spaced vanes --> 0	0

The UDF files are compiled with the newly build-in compiler with the libudf library name and the three c-files. The overall mesh motion is controlled by the UDFs. For the dynamic mesh motion setting, the diffusion based smoothing method and the In-Cylinder option is used to set the rotational speed 300 rpm. The crank period is set to 360° and crank angle step size is set to 0.01. One rotation, 360°, is simulated with an angle resolution of 0.25°. With these parameters the temporal resolution is automatically calculated to 0.0001388 s. 1440 time steps or a final simulation time of 0.2 s is achieved. Furthermore, dynamic mesh zone events are applied on the volumes of the vanes with vane_pump_core::libudf and the surfaces of the vanes with walls::libudf with type "user-defined".

The following Tab. 2 shows the methods for the numerical solution process. The initialization is performed with standard initialization with 0 for all physical quantities and the variables of the turbulence model (Gauge Pressure = 0 Pa, X Velocity = 0 m/s, Y Velocity = 0 m/s, Z Velocity = 0 m/s, Turbulent Kinetic Energy = 0 m²/s², Specific Dissipation Rate = 0 1/s). For the solution process the scaled residual threshold for continuity, x-velocity, y-velocity, z-velocity, k and ω is set to 1e-6. A maximum of 150 iterations/time step were performed. Physical monitors to evaluate the temporal volume flow rate and mass flow rate at the inlet and the outlet boundary condition, are defined.

Tab. 2. Parameters of the solution process

Parameter names	Parameter values
Formulation	SIMPLE
Flux Type	Roe-FDS
Spatial Discretization: Gradient	Least Squares Cell Based
Spatial Discretization: Flow	Second Order Upwind
Spatial Discretization: Turbulent Kinetic Energy	Second Order Upwind

Spatial Discretization
Specific Dissipation Rate
Transient Formulation

Second Order Upwind
Second Order Implicit

Experimental setup

Fig. 2 shows the experimental setup. The 3D printed rotary vane pump is powered by the asynchronous motor ABB M2AA 071B-4. The frequency converter ABB ACS355-01E-02A4-2 sets the desired rotational speed. With the data acquisition box from national instruments DAQ NI USB-6003, LabView and a inductive sensor that counts the revolution, the desired speed of 300 rpm is set. The flow rate is measured at the inlet pipe of the pump with the measurement device PT900. Experiments are performed with water at room temperature, taken and passed back to a reservoir from a tank with 90 liters.

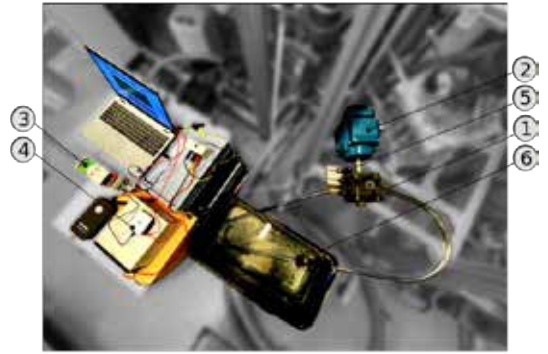
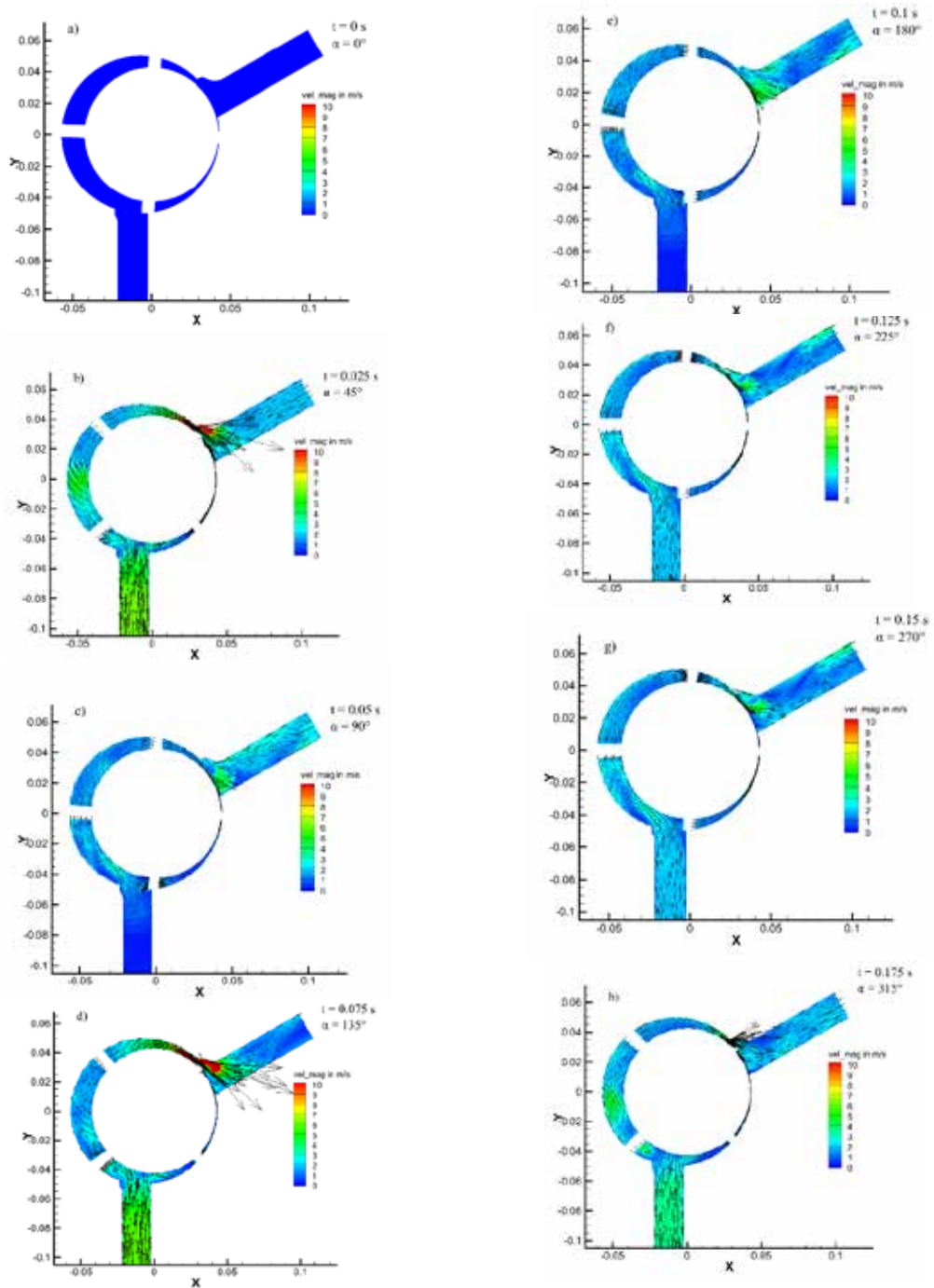


Fig. 2: Experimental setups shows the rotary vane pump (1) with an asynchronous motor (2) that is driven by a frequency converter (3) and a data acquisition box (4) with multiple analog and inputs and outputs to detect the rotational speed (5) as well as the set of the desired rotational speed and the ultra-sonic flow measurement device (6).

Results

Fig. 3 shows the velocity magnitude $vel_mag = \sqrt{v_x^2 + v_y^2 + v_z^2}$ as scalar field and the vel_mag scaled vectors at the selected x-y plane at the center of the inlet/outlet diameter. In a) the initialized field at $t = 0$ s, $\alpha = 0^\circ$ is shown. From b) to i) results in steps of 0.025 s or 45° are shown. In b), d) there is the highest velocity because of the smallest cross-section related to continuity equation. Due to pump configuration it happens that there is a reverse flow situation at the inlet, see e), and a reverse flow situation at the outlet, see c), e) and i). This effect can be also seen at the volume flow evaluation in Fig. 3. For sure, the volume flow rate is changing temporally as a function of time. The temporal averaged CFD fluid flow at the inlet of this one revolution of the pump is 2.7 m³/h. The experiment shows a flow of 1.74 m³/h. This smaller flow rate can be explained, that the vanes are not 100 percent sealed.

In the following Fig. 4 the CFD simulation result of the inlet flow rate is shown. This is evaluated by the surface integral of the velocity vector field on the inlet surface. Results show repeating oscillatory changes due to suction and ejection moments of the 360° rotation, due to the vanes passing by at the inlet and the outlet cross-section.



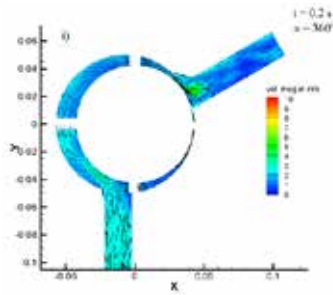


Fig. 3: 2D slices out of a 3D CFD simulation result of the rotary vane pump at 0°, 90°, 135°, 180°, 225°, 270°, 315° and 360° at the time of 0 s, 0.025 s, 0.05 s, 0.075 s, 0.1 s, 0.125 s, 0.15 s, 0.175 s and 0.2 s. The pump rotational speed is 300 rpm. The color shows the velocity magnitude in m/s, the corresponding vectors the direction of the flow.

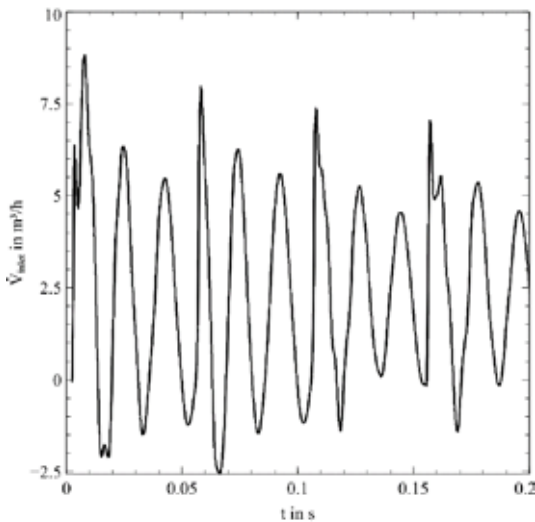


Fig. 4: CFD simulation result of the vane pump inlet volume flow rate \dot{V}_{inlet} at 300 rpm. One can see the oscillatory pump motion at the flow rate. The time t in seconds of 0.2 corresponds to one rotation 360° of the pump.

Discussion

Within this study, the files of the tutorial FLUENT-MDM-tut-06vane-pump.pdf for Fluent 13 with the used files input.txt, vane.c, gerotor_vane_smoothing.c and tait.c are adapted to simulate the fluid flow a new developed self-priming rotary-vane pump for flow rates of 2 m³/h at a rotational speed of 300 rpm. With the new Fluent version 2023 R2 it is still possible to compile the files with the new built-in compiler not using the Microsoft Visual studio ones, as it was necessary in previous versions. First, incompressible simulations were tried to solve, but those did not converge. The reason is that within the vanes the volume is changing as a function of time and rotation. Since in the simulation the fluid has no gap, and conservation of mass must hold, the density must change. The disadvantage of this approach is a much smaller needed time step size within the simulation, to achieve convergence. The tutorial also allows gaps within the vanes, but due to much more complexity, this

approach was so far not followed. Though, this could be performed in a future analysis. Furthermore, in the vanes, due to complex mesh motion, no boundary layers are added. Since the fluid has similar speed that the vanes, viscosity and the boundary layer influences the flow hardly. Therefore, this simplification is acceptable. All simulations are performed with second order accuracy, in this preliminary study, there was no need for a mesh convergence study. From experiences in the field of computational fluid dynamics, a global parameter like the investigated inlet volume flow rate is not that sensitive to the spatial resolution. With 2.7 m³/h the simulation shows a higher flow rate than the experiment with 1.7 m³/h. Even though, when the simulation is not correct with the experiments, it can be used to optimize the pump and reduce experimental afford.

References

- [1] Y. Inaguma and A. Hibi, "Vane Pump Theory for Mechanical Efficiency," *Proc. Inst. Mech. Eng. Part C J. Mech. Eng. Sci.*, vol. 219, no. 11, pp. 1269–1278, Nov. 2005.
- [2] J. H. Ferziger and M. Peric, *Computational methods for fluid dynamics*. Springer Science & Business Media, 2012.
- [3] N. K. SUZUKI KAZUNARI, NAKAMURA YOSHINARI, YAKABE SHINJI, WATANABE HIROHITO, "Characteristics Prediction of Vane Pump by CFD Analysis," *KYB Tech. Rev.*, pp. 8–15, 2016.

Development of a single-channel model of electrically heated monoliths for dry reforming of methane

L. Nohel^{1,*}, L. Bertolini¹, E. Caliskan², P. Pichler¹, V. Schallhart¹, M. Wilhelm¹, L. Möltner¹, E. Klemm²

1: Department of Process & Energy Engineering, MCI The Entrepreneurial School, Austria

2: Institute of Technical Chemistry, University of Stuttgart, Germany

* Correspondent author: luca.nohel@mci.edu

Keywords: catalysis, electrification, methane reforming, modelling

Abstract

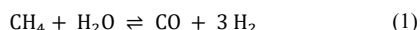


The chemical industry is a major emission source of greenhouse gases, where 67 % of these emissions originate from combustion of fuels. Steam methane reforming (SMR) is among the largest endothermic processes in industry and a major production route for syngas globally. Syngas, a mixture of H₂ and CO, serves as base chemical for various processes. Conducted in large catalytic reformers with heat supplied from natural gas burners, syngas production accounts for approximately 3 % of global carbon dioxide emissions. eQATOR, a Horizon Europe research project aims to change the status quo of fired heating towards electric heating. This is done by using electrically conductive monolithic catalyst supports, which are heated resistively. Precise temperature control, achievable with resistive heating, opens the possibility of conducting dry reforming of methane (DRM), where CO₂ and CH₄ react to syngas. This makes it possible to utilize biogas as educt-gas.

In this work, a 2D single-channel model of an electrically heated monolith for DRM is developed using Matlab. The system is considered at 850 °C, atmospheric pressure and the volume flow of feed-gas at these conditions is 30 m³ h⁻¹. The reaction kinetics are determined via experiments with the Ni/CeZrO₂ catalyst and the reaction conducted at these conditions. The model is used to describe a whole cascade of monoliths, all of which are individually heatable. After ten monoliths, the conversion of CH₄ reaches 86 %. The model shows that the consideration of radial mass transport to and from the walls of the monolith channel is important to not overestimate the conversion of CH₄.

Introduction

The fight to minimize the negative impacts of climate change by reducing greenhouse gas emissions is one of the greatest challenges humanity faces today. The chemical industry is a major source of greenhouse gases. 67 % of the emissions of chemical industry come from the combustion of fuels for heat generation.^[1] Especially endothermic processes, carried out at high temperatures, come with large heat demands, often covered by fossil fuel combustion. Syngas, a mixture of CO and H₂, is an important base chemical for many processes in the chemical industry. Among production routes from coal and petroleum, natural gas is used as a precursor.^[2,3] Syngas production is estimated to account for 3 % of global CO₂ emissions.^[4] The reaction to produce syngas from natural gas is the steam methane reforming (SRM) reaction:



This reaction is strongly endothermic ($\Delta H^\circ = 206 \text{ kJ mol}^{-1}$) and is typically carried out in large, packed bed catalytic reactors, equipped with natural gas burners at the walls. Wismann et al. describe the large temperature gradients forming in such a reactor, originating from the strongly endothermic reaction coupled with the design of the reactor.^[5] This leads to a decrease in efficiency of the overall process. Another possible route to syngas from CH₄ is dry reforming of methane (DRM):

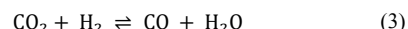
This reaction is also strongly endothermic ($\Delta H^\circ = 247 \text{ kJ mol}^{-1}$) but is up to now not established in industry. This is due to various side reactions occurring during DRM that can cause solid carbon formation on the catalyst, leading to deactivation.^[6] To avoid these undesired side reactions, precise temperature control is needed, which is a major challenge with the current fired heated reactor layout.

The eQATOR research project, funded by Horizon Europe, aims to develop electrically heated reactors for CH₄ reforming. One technology is the direct, resistive heating of electrically conductive monolithic reactors. As shown in the PhD thesis of Wismann, a drastic size reduction of the reactors and precise temperature control is made possible with electric heating.^[4] This opens the path to using DRM with biogas, already containing about 40 % of CO₂ and 60 % CH₄.^[6]

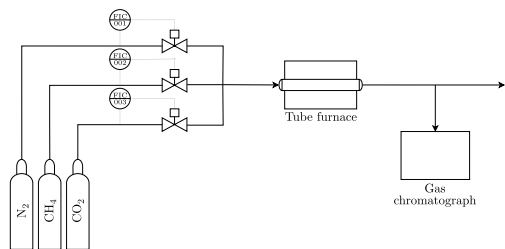
Methodology

This work comprises two major parts, experiments to determine the reaction kinetics and the development of a numeric model of a monolithic reactor.

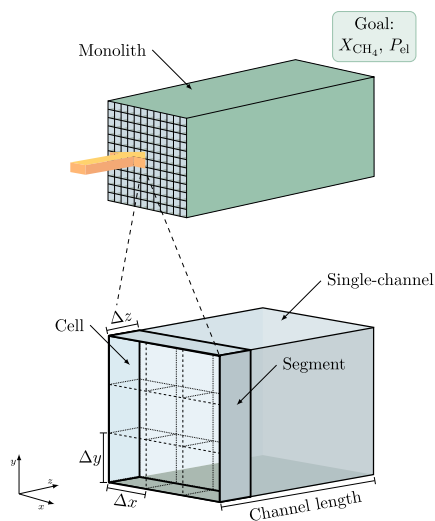
Kinetics experiments: In the system at hand, two chemical reactions are considered, the before-shown DRM reaction, and the reverse water-gas shift (RWGS) reaction:



The RWGS reaction is considered an important side reaction when looking at DRM, lowering the H₂/CO ratio of the product to < 1. To determine the reaction kinetics, laboratory experiments are conducted. Literature kinetics proposed by Nguyen et al. are used as a starting point and are then adjusted to describe the measurements.^[7] A schematic representation of the experimental setup can be seen in Figure 1. The used Ni/CeZrO₂ catalyst is placed in a tube furnace (Nabertherm RHS 50/250) and heated to 850 °C under inert N₂ atmosphere. A mixture of CO₂, CH₄ and N₂ is fed to the reactor. After passing the catalyst, the product gas composition is measured via a gas chromatograph (Agilent Technologies 7890B). With a developed 1D model of the laboratory reactor in Matlab, a Levenberg-Marquardt optimization routine is implemented to optimize the literature kinetics to describe the conducted experiments.

Figure 1: Experimental setup for kinetic experiments^[8]

2D single-channel model: Models of monoliths come in different levels of complexity, including washcoat layer, single-channel, multi-channel, and whole reactor models. As a compromise between accuracy and computational demand, single-channel models are most extensively applied in practice.^[9] A single-channel model assumes every channel to show similar behavior and a homogeneous distribution of catalyst as well as educt. This assumption allows one channel to describe a whole monolith. The scheme of the model is shown in Figure 2, where a single channel of a monolith is resolved through a numerical mesh consisting of “cells” in x and y direction and “segments” in z direction. As indicated in the figure, the goal is to determine the conversion of CH_4 and the needed electrical heating power.

Figure 2: Scheme of 2D single-channel model for DRM^[8]

In the modeling of a monolith, different assumptions are frequently made. The flow is assumed to be only one-directional, in this case in z direction. Further, the flow regime is fully developed laminar and treated as incompressible.^[9] Table 1 shows the initial conditions for the developed model.

Table 1: Initial conditions and geometric parameters for the modelling

Initial conditions of for the model	
Monolith temperature	850 °C
Gas temperature	850 °C
Pressure	101325 Pa
Volume flow (850 °C, 101325 Pa)	30 m ³ h ⁻¹
Monolith dimensions ($l \times w \times h$)	100 × 50 × 50 mm
Cell density	400 CPSI

Regarding mass transport, the governing equation of the model is the differential form of the conservation of mass for incompressible flows:

$$\frac{\partial c}{\partial t} + \mathbf{v} \cdot \nabla c = D \cdot \nabla^2 c \pm S \quad (4)$$

The shown source/sink term S represents the chemical reaction, described by the kinetic equations as optimized on the basis of the experiments. The reactions only occur at the walls, where the catalyst is located. Between the cells in x and y direction, mass transfer occurs via diffusion, resulting from the concentration gradients developing from chemical reaction at the walls. The diffusion coefficients are determined via Maxwell-Stefan diffusion. The model is solved by implementing a finite difference scheme. Advection is accounted for by starting calculations in the first segment, calculating reaction and diffusion, and advancing to the next segment in a loop until the outlet of the channel.

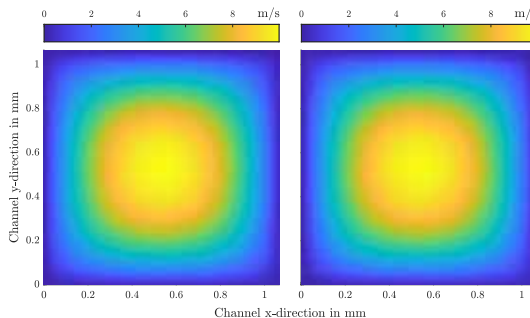
The flow of a fluid is described by the Navier-Stokes equation. Assuming an incompressible fluid, absence of external forces, and constant density ρ and viscosity μ , the following form of the Navier-Stokes equation can be used to describe fluid flow:^[10]

$$\rho \cdot \frac{\partial \mathbf{v}}{\partial t} + \rho \mathbf{v} \cdot \nabla \mathbf{v} = \mu \cdot \nabla^2 \mathbf{v} - \nabla p \quad (5)$$

Assuming a steady state, fully developed laminar flow through a monolith channel, equation 5 is reduced to:

$$0 = \mu \cdot \nabla^2 \mathbf{v} - \nabla p \quad (6)$$

An iterative solver is implemented to determine the velocity profile along the channel. To assess the validity of this approach, the geometry is also simulated in Ansys Fluent. Figure 3 shows both methods sharing general agreement.

Figure 3: Comparison of velocity profiles in channel as calculated with Matlab (left) and Ansys Fluent (right)^[8]

The system is assumed to be adiabatic. If the assumption is made that the resistive heating is not limited and able to directly supply the heat consumed by chemical reaction, the system can be considered isothermal. To determine the needed electrical heating power to sustain the process, the reaction enthalpy is considered. The heating power of the whole monolith is obtained by multiplying the heating power of the single channel by the number of channels in one monolith.

Cascade of monoliths: As given by the assumptions of the model, the whole monolith is described by the single-channel model. In practice the aim is to construct a whole cascade of monoliths, as seen in Figure 4. Each monolith is electrically contacted and therefore, individually heatable. The existing 2D single-channel model is expanded to calculate consecutive monoliths. The preheaters are

monoliths without catalyst. These are intended to preheat the gas to reach the desired 850 °C at the inlet of the first catalyst.

1D vs. 2D model: To determine the effect of diffusive transport from the channel center to the wall and vice versa, a simple 1D model is implemented. By resolving one cell per segment, only average properties across the cross-section are determined, including average velocity and concentrations. In the 1D model, radial mass transport is neglected, assuming no diffusion limitation. The results are then compared to the 2D model, assessing the influence of radial mass transport.

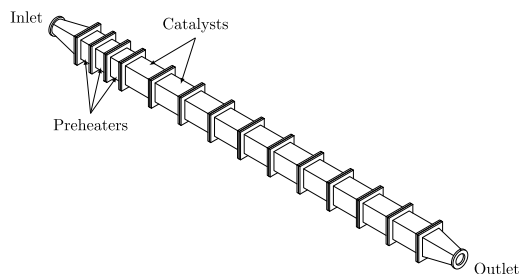


Figure 4: Scheme of cascade of monoliths with preheaters^[8]

Results

The kinetic experiments show that the RWGS reaction can be assumed to operate at equilibrium. Regarding the DRM reaction, the rate is approximately half of the proposed rate of Nguyen et al. Over the whole cascade, the CH₄ conversion can be seen in the bottom part of Figure 5. Each monolith (length of 0.1 m) is meshed with 17 × 17 × 120000 cells. The estimated CH₄ conversion of the 1D model is also shown in the same figure. The top part shows the energy demand resulting from the enthalpy of reaction for each monolith (2D model). The product gas stream is estimated to be 75.7 mol h⁻¹ of H₂ and 260.3 mol h⁻¹ of syngas. The H₂/CO ratio is 0.41.

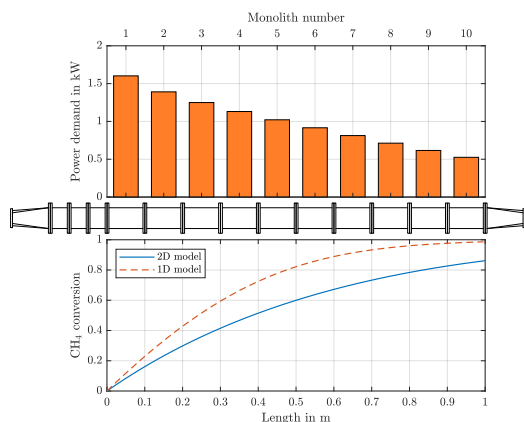


Figure 5: Results of single channel modeling, including heating power (top) and methane conversion (bottom)^[8]

Discussion

In Figure 5, the CH₄ conversion along the cascade is shown. It can be seen that the conversion reaches 86 % at the outlet (2D model). Conversions in this range for an industrial process seem reasonable, as Wismann et al. draw their conclusions of an electrically heated SMR reactor running at 75.4 – 95 % of CH₄ conversion. Their

comparison is a traditional, fired heated SMR plant operated at 75.4 % conversion.^[5] The top part of Figure 5 shows the heating power demand for every monolith. The rate of reaction is highest in the first monolith and reduces subsequently. This is also represented, as expected, in the power demand with the last monolith needing less than a third of the first monolith to maintain its temperature.

The comparison of the two conversion curves of the 1D and the 2D model shows a difference. The 1D model, neglecting all radial mass transport processes, yields a higher conversion than the 2D model, which considers radial diffusion. This underlines the importance of considering the radial transport of educt/product to/from the wall to the center in the process at hand. A qualitatively similar trend can be seen when looking at the comparison of 1D and 2D models in the simulations of a packed bed methanol steam reforming reactor by Zhu et al. Their comparison shows a similar overestimation of the conversion when looking at the 1D case, compared to the 2D model, highlighting the importance of considering radial mass and heat transport for their simulation.^[11]

As an approach to validate the implemented chemical reactions in the model, the simulated cascade is extended. As the residence time is increased, the thermodynamic equilibrium composition should be asymptotically approached. In Figure 6 the composition of the product gas after 15 monoliths is compared to the thermodynamic equilibrium. It can be seen that both of the compositions share good agreement. For an infinitely long reactor, the single-channel model is likely able to predict the thermodynamic equilibrium closely. Remaining differences are likely due to the absence of kinetic terms for other occurring reactions. Here SMR is likely to play a key role:

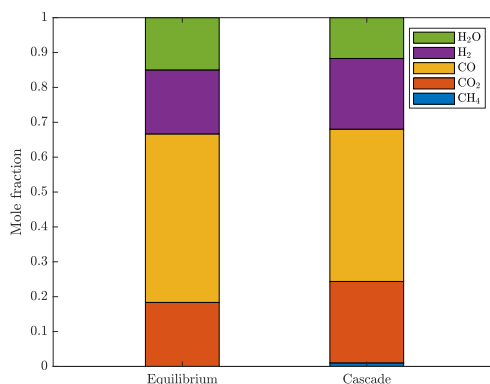
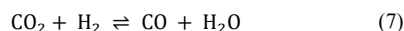


Figure 6: Comparison of cascade with 15 monoliths and thermodynamic equilibrium (components in legend have same order as the stacked bars)

With H₂O being formed through the RWGS reaction, also SMR is becoming relevant. Both reactions, DRM and SMR, consume CH₄ and yield syngas, but with a different composition. Further, reaction kinetics are probably influenced by competitive adsorption between H₂O and CO₂. Investigations including both, modelling and experimental work, are to be conducted to determine the influence of H₂O on the system at hand.

Conclusion

The transition towards electrically heated CH₄ reforming shows a disruptive possibility^[5], drastically reducing reactor sizes and increasing efficiency. A modular system as shown with the cascade of monoliths offers the possibility for easy scalability of plants and differentiated heat supply. The absence of natural gas as heat supply can greatly reduce the overall emissions of the process.

List of references

- [1] European Environment Agency, Total greenhouse gas emissions in the chemical industry (Indicator), 2024
- [2] C. Ampelli, S. Perathoner, and G. Centi, “CO₂ utilization: an enabling element to move to a resource- and energy-efficient chemical and fuel production”, *Philosophical Transactions of the Royal Society A: Mathematical, Physical and Engineering Sciences*, vol. 373, 2015. doi: 10.1098/rsta.2014.0177
- [3] M. Steib, Dry Reforming of Methane – understanding metal support interactions and evaluation of regeneration protocols, PhD thesis, Technische Universität München, 2017
- [4] S. T. Wismann, Electrically heated steam methane reforming, PhD thesis, Technical University of Denmark, 2019
- [5] S. Wismann, J. Engbaek, S. Vendelbo, F. Bendixen, W. Eriksen, K. Aasberg-Petersen, C. Frandsen, I. Chorkendorff, and P. Mortensen, “Electrified methane reforming: A compact approach to greener industrial hydrogen production” *Science*, vol. 364, pp. 756-759, 2019. doi: 10.1126/science.aaw8775
- [6] D. P. Minh, T. J. Siang, D.-V. N. Vo, T. S. Phan, C. Ridart, A. Nzihou, and D. Grouset, “Chapter 4 - Hydrogen Production From Biogas Reforming: An Overview of Steam Reforming, Dry Reforming, Dual Reforming, and Tri-Reforming of Methane”, *Hydrogen Supply Chains*, pp. 111-166, 2018. doi: 10.1016/B978-0-12-811197-0.00004-X
- [7] T. Nguyen, C. L. Luu, H. P. Phan, P. A. Nguyen, and T. T. Van Nguyen, “Methane dry reforming over nickel-based catalysts: insight into the support effect and reaction kinetics”, *Reaction Kinetics, Mechanisms and Catalysis*, vol. 131, pp. 707-735, 2020. doi: 10.1007/s11144-020-01876-8
- [8] L. Nohel, Development and experimental validation of a numeric model for electrically heated monolithic methane reforming catalysts using MATLAB, Master Thesis, MCI The Entrepreneurial School, 2024
- [9] J. Chen, H. Yang, N. Wang, Z. Ring, and T. Dabros, “Mathematical modeling of monolith catalysts and reactors for gas phase reactions”, *Applied Catalysis A: General*, vol. 345, pp. 1-11, 2008. doi: 10.1016/j.apcata.2008.04.010
- [10] R. B. Bird, W. E. Stewart, and E. N. Lightfoot, *Transport phenomena*, Wiley, 2002.
- [11] J. Zhu, X. Cui, and S. S. Araya, “Comparison between 1D and 2D numerical models of a multi-tubular packed-bed reactor for methanol steam reforming”, *International Journal of Hydrogen Energy*, vol. 47, pp. 22704-22719, 2022. doi: 10.1016/j.ijhydene.2022.05.109

Multi-material textile waste as biomass feedstock: using fused filament fabrication to investigate optimal stirrer geometries in non-Newtonian media

D.Ostner-Kaineder^{1,2,*}, C. Strasser¹, M.W. Hlawitschka², C. Burgstaller¹

1: School of Engineering, University of Applied Sciences Upper Austria, Stelzhamerstr. 23, 4600 Wels, Austria

2: Department of Process Engineering, Johannes Kepler University Linz, Austria

* Correspondent author: doris.ostner-kaineder@fh-wels.at

Keywords: rapid prototyping, mixing, non-newtonian flow

Abstract

Processing of blended polyester-cotton waste is difficult using traditional methods. Biocatalytic separation of the fractions via enzymatic hydrolysis of the cellulose fraction offers an alternative approach, resulting in processable polyester and glucose solution as a secondary product. The scale up to intermediate scale (60 l) processing of these shear-thinning non-Newtonian suspensions has been reported, but further investigations of flow properties and optimization of stirrer geometries are required. The aim of this work is the development of optimized stirrer geometries and dimensions via fused-filament fabrication. Mixing times were compared by a computer-assisted optical method and via speed torque assessment.

Introduction

The production of textiles is a resource-intense process, requiring high amounts of land and chemical use. Global fiber production increases yearly, doubling from 2015 to 2020. In 2023, a total of 124MT of fiber was produced. Roughly three quarters consisted of two materials: Polyethylene terephthalate-based polyester (57%) and cotton (19.9%), with no other major material fraction reaching more than 5.4% of the total [1,2]. Blended polyester and cotton (polycotton) textiles are widespread in workwear, home textile and even personal apparel [2]. Differing physical properties (tear strength, thermal melt- and degradation behavior) make blended fabrics unsuitable for the (thermo)mechanical recycling methods already established for the pure material components [3].

To avoid the necessity of landfilling or energy recovery of these materials, separation of the components is necessary. Here, approaches mainly consist of dissolution or degradation of one of the components [3]. Known polyester solvents (such as n-methyl pyrrolidone, phenol/dichlorobenzene, carbon tetrachloride, trichloroacetic acid [4]) are toxic and/or damaging to the environment [5–8]. The polymer can be chemically degraded via a variety of methods, most of which require the use of solvents, catalysts and high temperatures [9]. Advances have been made in the enzymatic hydrolysis of PET, but the corresponding enzymes not commonly available and amorphization of the substrate is required [10]. Cellulose can be dissolved in more environmentally friendly fluids (NMMO, ionic liquids); however, drawbacks of this approach include high costs and sometimes difficult handling [11]. Cellulose degradation is commonly performed via inorganic acids or enzymatic hydrolysis [3,12–14]. The advantages of biocatalysis include low reaction temperatures as well as an absence of organic solvents. Cellulases are commonly used in the food and beverage industry, but also in the digestion of lignocellulose feedstocks for bioethanol production. Pre-prepared catalyst cocktails, optimized for differing cellulose feedstocks, are therefore easily commercially available [15,16].

For processing textile waste, fungal celluloses with an ideal process parameter range of 50-55°C at pH 5 have been applied to great success, allowing complete removal of pre-treated natural fiber components within 24h [14,17]. A respectable body of work has been published for the investigation and optimization of pre-

treatments (both chemical and purely physical) [14]. Further investigations were also published regarding optimal process temperature, enzyme and substrate load [18]. With two notable exceptions, these investigations were performed in glass bottles, using sub-liter to low-liter volumes using some variation of rotary or shaking incubator. Zebec [19] used a 2.5L glass vessel with magnetic overhead stirrer to produce limonene from cellulose-based waste, and Piribauer et al [17] showed a proof-of-concept scaleup of the textile waste separation process to a 60L barrel equipped with a heating coil and electric stirrer. However, while process optimization with regards to the energy requirements and mixing efficiency of the systems used are important parameters for later industrial application, they were not the focus of aforementioned publications.

Enzymatic hydrolysis is a surface process occurring at the solid-liquid interface of the substrate [20]. It is inhibited by excess product concentration [21]. Efficient mixing of the reactant suspension is essential for the efficient and complete removal of residual cellulose. This is especially relevant in the context of textile waste recycling, since extrusion processes of the recycled polyester are highly sensitive to residual contamination. However, mixing of these suspensions is complicated by their non-newtonian flow behavior. Vane rheometry has long been used to investigate the behavior of biomass feedstocks [22]. However, rheometric analysis of textile waste suspensions and especially textile blends was not heretofore a topic of interest. Our investigations show a strong dependence of rheological behavior of the suspension on solid concentration, particle size and polyester content. At 1 wt% they behave as quasi-newtonian particle-in-water mixtures. At 3 and 5 wt%, shear thinning behavior becomes agnostic to solid concentration and only minorly dependent on the other investigated parameters, indicating a minimum concentration of disperse network formation. While higher solid loads are preferable for space-time-efficient catalytic processing, the 3 wt%-minimum is sufficient for analyzing flow behavior.

When investigating stirring processes, material behavior is only half of the equation while the interaction between material and stirrer geometry is the second. Choosing the ideal mixing geometry is a complex combination of empirical guidelines, understanding of the theoretical background, process simulation and laboratory experimentation [23]. The non-newtonian properties of many suspensions, including textile shreds, offers further complications in describing and modelling of these behaviors. To improve the understanding of both mixing behavior and energy consumption concerns, an approach combining rapid prototyping of different impeller geometries and non-intrusive monitoring of opaque agitated suspensions was required.

3D-printing, especially fused-filament fabrication (FFF), offer a quick and relatively low-cost method for the creation of stirring implements, of both simple and complex geometries. Components are designed using computer assisted design software and transformed into g-code, which is readable by printing hardware, by a slicer software. The basic principle behind FFF is the conveying of a polymeric filament through a heated nozzle onto a flat surface. 3-Dimensional products are built using from layer-by layer deposition

of polymer both in the shape of the outline and a given infill geometry. This hollow geometry allows the construction of parts with comparable mechanical properties at much lower density compared to other fabrication techniques such as injection molding. Nozzle temperature and layer height as well as print speed are some of the main parameters affecting the quality of the finished part. The nozzle temperature must be above the melting temperature of the polymer used, since fusion Filament is commonly created from commodity polymers such as poly lactic acid (PLA) or glycol modified polyethylene terephthalate (PETG). When working with aqueous media, both materials are equally resistant to the influence of water. However, PETG also shows excellent resistance to citric acid buffer media, where PLA responds with moderate swelling resulting in decreased stability of the printed part [24]. While mechanical properties of 3D-printed parts can be further finetuned by optimization of infill and printing parameters, chemical resistance may be increased by change of filament material. Chemically inert materials such as POM and PVDF can be processed using FFF, but are significantly more challenging. While this shows the wider applicability of 3DP in chemical (stirrer) applications, for the application of textile hydrolysis, PETG is sufficient.

The aim of this work is to develop a method for rapid stirrer prototyping and assessment of the usability thereof. Therefore, further methodology for evaluation of the flow behavior and mixing efficiency of a given combination of stirrer geometry and suspension is required. Measurement of the applied torque is a cornerstone for many rheological techniques. For the sake of simplicity, simple speed-torque curves were chosen as a preliminary method of evaluating flow behavior.

An important parameter for assessing mixing efficiency is the global mixing time. The investigated fluid is agitated and a tracer is introduced. A tracer, commonly a salt or acid or base solution, and analysis of its distribution is performed using conductivity or pH probes. An alternative approach is computer-assisted colorimetry, as shown by Fitschen et al [25]. This method has the advantage of providing a real-time overview of the entire reactor without (sometimes costly) sensor equipment, with the caveat of being limited to a flat 2D-projection.

Material & Methods

Textile production waste with a cotton content of roughly 20% was provided by Korteks (Bursa, Turkey). Stirrers for mixing geometry optimization were produced from white EcoPLA filament obtained from 3DJake, Austria. An additional stirrer was produced from black PETG by 3DJake for a proof-of-concept measurement in a 40L reaction vessel under real hydrolysis conditions. Mixing time assessments were performed using either a $4 \cdot 10^{-4}$ mol l⁻¹ solution of methylene blue (99%, Riedel de Haan) or a saturated solution of phenolphthalein (pharmaceutical reagent grade, VWR) in 1% ethanol solution.

Stirrer geometries were designed using the Autodesk Fusion 360 software. Gcode was produced using PrusaSlicer 2.7.0. Three different designs – a 6-blade downward pitched turbine (6dPBT), radial impeller (RI) and helical ribbon impeller (HRI)- were produced from PLA using either a Crealiti k1 max (the first two designs) or Prusa MK4 (helical ribbon, PLA and PETG blade impeller for proof-of-concept measurement) printers with a 0.4 mm nozzle, 0.2 mm layer height. The producers recommendation was used for material temperatures and print speeds.

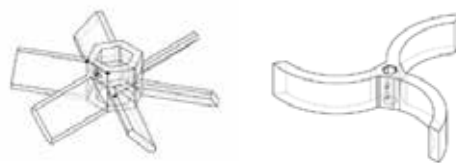


Figure 1: downwards-pumping 6-blade pitched blade turbine (6dPBT, left,) and radial impeller (RI, right) geometries

Printing of the helical ribbon required the use of additional PLA support structure, which was printed from black (for increased ease of separation) PLA from the same source.

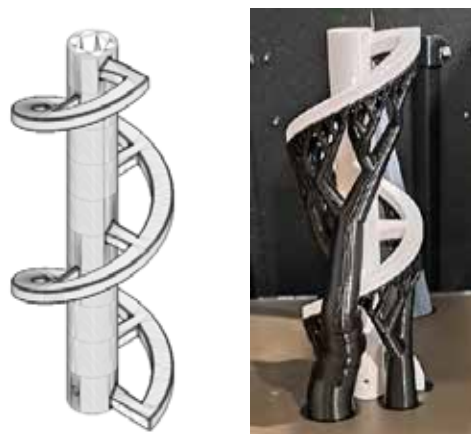


Figure 2: CAD-design (left) and finished print (white) including organic support(black) of the helical ribbon stirrer (right)

The small-scale experiments were conducted in a cylindrical non-baffled 2L double wall glass vessel (Hill Landgraf, Austria) with a rounded bottom. A HeiTorque Ultimate 400 (Heidolph, Germany) motor with integrated torque sensing was used for both speed-torque and mixing experiments. Stirrers were mounted on a 11 mm diameter, 300 mm length hexagonal stainless steel rod using an M4 grubbs screw. Mixing was recorded on a Sony Alpha EZ-10 at a framerate of 50 fps. For illumination, commercially available LED panels were used.

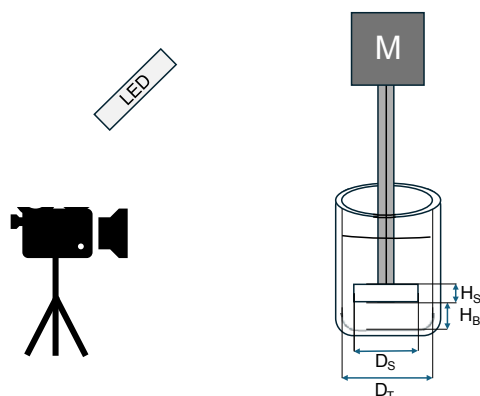


Figure 3: Schematic experimental setup of mixing experiments

All marked dimensions of the stirrers are shown in Table 1:

Table 1: Tank diameter and scale factors of stirrer geometries

	DT / mm	DS	HS	HB
6dPBT	116	0,70·DT	0,10·DS	0,03·DS
RI	116	0,90·DT	0,17·DS	0,18·DS
HRI	116	0,58·DT	2,4·DR	0,2·DS
blade	400	0,45·DT	0,23·DS	0,5·DS

For the flow investigation, a logarithmic ramp with 10 points from 20 to 180 rpm was applied with a duration of 2 minutes per point at 2wt% and 3wt% of textile in deionized water. A reference curve without solids was also recorded and subtracted from the result. An average torque value per shear rate was calculated for each stirrer and substrate concentration. The starting point of the experiment was set to zero.

Mixing experiments were conducted at 3 wt% of textile and 180 rpm. 0.5 mL of colorant (0,03% of the total volume) were added using an automatic pipette. All frames were extracted from the video using ffmpeg. Temporal resolution of the experiments was 0,02 seconds. Average values of each color channel as well as brightness were determined from a selected image area (the mixing vessel) using a python-script. The onset point was determined via frame analysis of the video, while the endpoint of mixing (mixing of a second steady color state) was determined using the first derivative of the curve; smoothing of the data using a LOESS filter was necessary for interpretation of the derivative.

The enzymatic hydrolysis experiments were conducted in a 40 L stainless steel reactor with a conical bottom using the same motor as the small-scale experiments and two separate blade impellers, one from PLA and one from PETG. Hydrolysis was carried out for 48 hours at 50 °C and pH 5.

Results & discussion

The results of the flow experiments are shown in Figure 4.

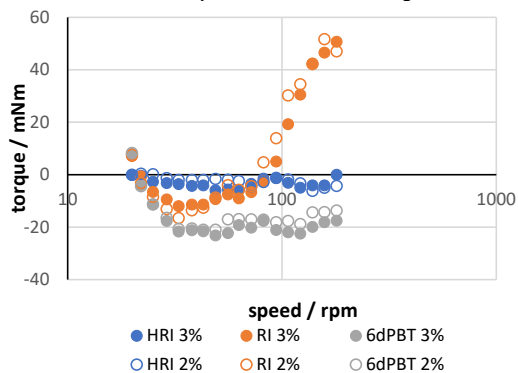


Figure 4: Torque-speed curves for all three stirrer geometries at 2 different concentrations

The torque curves for 2 and 3wt% are relatively similar for each stirrer, showing that the non-Newtonian behavior of the suspension is measurable even at the lower concentration. At higher speeds, the torque increases by 20 mNm from the 6dPBT to the HRI. A much higher increase of 60 mNm is seen from the HRI to the RI, suggesting that this is impeller requires by far the most energy.

The evaluation of the color change for the RI over time is shown in Figure 5. Since the original substrate is white, little to no influence on the blue graph is shown. The green value shows a small decrease, while the red values show the largest decrease. From the way computer graphics portray images, this is inevitable consequence – an increase in one color is achieved by relative decreases of all others. This effect is most pronounced for the opposing primary color.

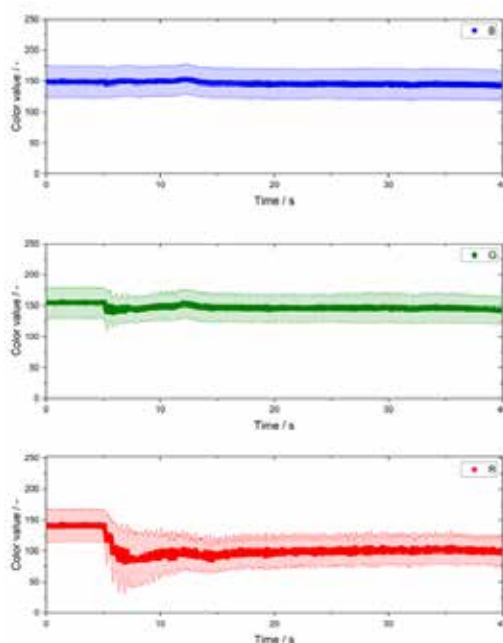


Figure 5: Effect of methylene blue addition on all color changes over time, RI at 3 wt% of textile

The mixing time curve of all three mixing time experiments is shown in Figure 6:

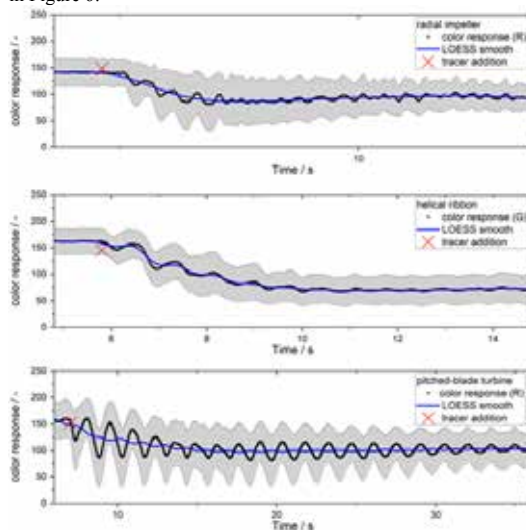


Figure 6: Main color response over video time; mixing time experiments for RI (top), HRI (mid) and 6dPBT (bottom)

The RI and HRI stirrers show relatively flat flow curves when compared to the 6dPBT; for HRI, the green value was evaluated since in this experiment, the base-induced color change of phenolphthalein was used as colorant. The 6dPBT showed a strong quasi-sinusoidal variation fluctuation. This is caused by insufficient dispersion of the substrate, leading to periodically appearing free space in the top third of the vessel, showing both the stirrer shaft as well as a textile-free water-filled area, where the colorant also spread

more efficiently. Mixing response curves, first derivative and first derivative of the smoothed curves are shown in Figure 7:

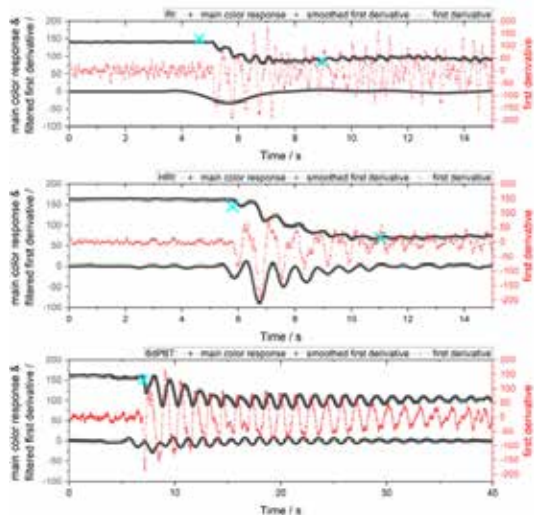


Figure 7: Main color response over time and first derivative of the curve and LOESS-filtered curve for RI (top), HRI (mid) and 6dPBT (bottom); onset and endset marked blue

The onset of mixing is easily discernible in the first derivative of the unfiltered curve; beyond that, the values fluctuate too much for optical endpoint assessment. For the RI and HRI curves, an endpoint could be determined using the filtered first derivative. While fluctuation in the color value of the 6dPBT measurement was drastically reduced at roughly 30 seconds, the value of this assessment may be questionable. The onset, endset and mixing times for all three impellers are shown in Table 2.

Table 2: Results of the mixing time experiments

	onset /s	endset /s	mixing time/s
RI	4.62	8.98	4.36
HRI	5.80	11.02	5.22
6dPBT	7.00	30.00	23.00

While the RI and HRI mixing times appear to be an order of magnitude smaller than the 6dPBT, this may be due to the periodic interference seen in the color response of the latter experiment. This sensitivity to inhomogeneous substrate distribution and the complexity of the endset determination suggest that further optimization of the method is required.

The proof-of-concept experiments in the 40 L reaction vessel showed (via optical assessment of the reactor content and monitoring of vessel- and wall temperatures) that mixing of the material occurred using both the PLA and PETG blade impellers. Complete hydrolysis of the cotton was achieved after 48h using the PETG stirrer, while the PLA stirrer experienced mechanical failure of the blade-shaft interface within the first 24 hours. Production of stirrers for biocatalytic reactions using commodity polymers is possible, but requires a slightly more complex printing material.

Conclusion

Fused filament is an excellent method for low-cost rapid prototyping of different stirrer geometries. The efficiency of three geometries, producing different flow patterns (6dPBT and HRI= axial, RI = radial) were investigated using torque-speed curves and computer-assisted optical mixing time assessment. At low mixing torque and intermediate mixing time, the helical ribbon impeller is the most effective stirrer geometry of the three investigated during the small-scale mixing experiments. Under real hydrolysis conditions, a 3D-printed stirrer performed adequately when switching from one commodity polymer (PLA) to another (PETG), which has higher chemical resistance against citric acid.

References

- [1] UN Environment Program, Unsustainable fashion and textiles in focus for International Day of Zero Waste 2025, 2025. <https://www.unep.org/news-and-stories/press-release/unsustainable-fashion-and-textiles-focus-international-day-zero> (accessed 28 April 2025).
- [2] Textile Exchange, Materials Market Report 2024 - Textile Exchange, 2025. <https://textileexchange.org/knowledge-center/reports/materials-market-report-2024/> (accessed 28 April 2025).
- [3] S. Wang, S. Salmon, Progress toward Circularity of Polyester and Cotton Textiles, *Sustainable Chemistry* 3 (2022) 376–403. <https://doi.org/10.3390/suschem3030024>.
- [4] B.T.I. Ali, N. Widiastuti, Y. Kusumawati, A.L. Ivansyah, J. Jaafar, Solvent selection in membrane preparation from polyethylene terephthalate plastic waste: computational and experimental study, *Mater. Res. Express* 9 (2022) 125302. <https://doi.org/10.1088/2053-1591/aca5f0>.
- [5] PubChem, Trichloroacetic Acid, 2025. <https://pubchem.ncbi.nlm.nih.gov/compound/6421> (accessed 28 April 2025).
- [6] PubChem, Carbon Tetrachloride, 2025. <https://pubchem.ncbi.nlm.nih.gov/compound/Carbon-Tetrachloride#section=Safety-and-Hazards> (accessed 28 April 2025).
- [7] o-Dichlorbenzol/Phenol (Gemisch 1:1) MSDS - 814765 - Merck, 2025. https://www.merckmillipore.com/AT/de/product/msds/MDA_CHEM-814765?Origin=PDP (accessed 28 April 2025).
- [8] PubChem, Methylpyrrolidone, 2025. <https://pubchem.ncbi.nlm.nih.gov/compound/13387> (accessed 28 April 2025).
- [9] T. Muringayil Joseph, S. Azat, Z. Ahmadi, O. Moini Jazani, A. Esmaeili, E. Kianfar, J. Haponiuk, S. Thomas, Polyethylene terephthalate (PET) recycling: A review, *Case Studies in Chemical and Environmental Engineering* 9 (2024) 100673. <https://doi.org/10.1016/j.cscee.2024.100673>.
- [10] N.F.S. Khairul Anuar, F. Huyop, G. Ur-Rehman, F. Abdullah, Y.M. Normi, M.K. Sabullah, R. Abdul Wahab, An Overview into Polyethylene Terephthalate (PET) Hydrolases and Efforts in Tailoring Enzymes for Improved Plastic Degradation, *Int. J. Mol. Sci.* 23 (2022). <https://doi.org/10.3390/ijms232012644>.

- [11] M. Kahoush, N. Kadi, Towards sustainable textile sector: Fractionation and separation of cotton/polyester fibers from blended textile waste, *Sustainable Materials and Technologies* 34 (2022) e00513. <https://doi.org/10.1016/j.susmat.2022.e00513>.
- [12] A. SANKAUSKAITĖ, L. STYGIENĖ, M.D. TUMĖNIENĖ, S. KRAULEDAS, L. JOVAIŠIENĖ, R. PUODŽIŪNIENĖ, Investigation of Cotton Component Destruction in Cotton/Polyester Blended Textile Waste Materials, *ms* 20 (2014). <https://doi.org/10.5755/j01.ms.20.2.3115>.
- [13] G. Buschle-Diller, S.H. Zeronian, N. Pan, M.Y. Yoon, Enzymatic Hydrolysis of Cotton, Linen, Ramie, and Viscose Rayon Fabrics, *Textile Research Journal* 64 (1994) 270–279. <https://doi.org/10.1177/004051759406400504>.
- [14] R.E. Vera, F. Zambrano, A. Suarez, A. Pifano, R. Marquez, M. Farrell, M. Ankeny, H. Jameel, R. Gonzalez, Transforming textile wastes into biobased building blocks via enzymatic hydrolysis: A review of key challenges and opportunities, *Cleaner and Circular Bioeconomy* 3 (2022) 100026. <https://doi.org/10.1016/j.clcb.2022.100026>.
- [15] A. Singh, S. Bajar, A. Devi, D. Pant, An overview on the recent developments in fungal cellulase production and their industrial applications, *Bioresource Technology Reports* 14 (2021) 100652. <https://doi.org/10.1016/j.biteb.2021.100652>.
- [16] U. Ejaz, M. Sohail, A. Ghanemi, Cellulases: From Bioactivity to a Variety of Industrial Applications, *Biomimetics (Basel)* 6 (2021). <https://doi.org/10.3390/biomimetics6030044>.
- [17] B. Piribauer, U. Jenull-Halver, F. Quartinello, W. Ipsmiller, T. Laminger, D. Koch, A. Bartl, Volume 13 - December 2020, *Detritus* (2020) 78–86. <https://doi.org/10.31025/2611-4135/2020.14030>.
- [18] B. Piribauer, A. Bartl, W. Ipsmiller, Enzymatic textile recycling - best practices and outlook, *Waste Manag. Res.* 39 (2021) 1277–1290. <https://doi.org/10.1177/0734242X211029167>.
- [19] Ž. Zebec, M. Poberžnik, A. Lobnik, Enzymatic Hydrolysis of Textile and Cardboard Waste as a Glucose Source for the Production of Limonene in *Escherichia coli*, *Life (Basel)* 12 (2022). <https://doi.org/10.3390/life12091423>.
- [20] T.K. Ghose, V.S. Bisaria, Studies on the mechanism of enzymatic hydrolysis of cellulosic substances, *Biotechnol. Bioeng.* 21 (1979) 131–146. <https://doi.org/10.1002/bit.260210110>.
- [21] A.V. Gusakov, A.P. Sinitsyn, A theoretical analysis of cellulase product inhibition: effect of cellulase binding constant, enzyme/substrate ratio, and beta-glucosidase activity on the inhibition pattern, *Biotechnol. Bioeng.* 40 (1992) 663–671. <https://doi.org/10.1002/bit.260400604>.
- [22] T.C. Nguyen, D. Anne-Archard, L. Fillaudeau, Rheology of Lignocellulose Suspensions and Impact of Hydrolysis: A Review, *Adv. Biochem. Eng. Biotechnol.* 149 (2015) 325–357. https://doi.org/10.1007/10_2015_323.
- [23] A.K. Salho, D.A. Hamzah, A Review of Stirred Tank Dynamics: Power Consumption, Mixing Time and Impeller Geometry, *IJHT* 42 (2024) 1081–1092. <https://doi.org/10.18280/ijht.420335>.
- [24] M. Horak, Prusament (18 October 2021).
- [25] J. Fitschen, S. Hofmann, J. Wutz, A. Kameke, M. Hoffmann, T. Wucherpfeffennig, M. Schlüter, Novel evaluation method to determine the local mixing time distribution in stirred tank reactors, *Chemical Engineering Science: X* 10 (2021) 100098. <https://doi.org/10.1016/j.cesx.2021.100098>.



Tiroler Rohre GmbH

Innovation aus Tradition

SCAN ME



Evaluating pretreatment process impacts in a multi-product wheat straw biorefinery using prospective life cycle assessment

Safdar Abbas^{1*}, Sebastian Serna-Loaiza^{2,1}, Stavros Papadokonstantakis¹

1: Institute of Process Engineering, Environmental Engineering and Technical Biosciences, TU Wien, Vienna, Austria

2: Sphera Solutions GmbH, 70771 Leinfelden-Echterdingen, Germany

* Correspondent safdar.abbas@tuwien.ac.at

Keywords: Ammonia fiber expansion, organosolv, prospective life cycle assessment, integrated assessment model, biorefinery

Abstract

Wheat straw holds significant potential as a renewable resource for a sustainable bioeconomy; however, its complex structure necessitates pretreatment to enable efficient conversion into high-value products. In this study, we investigate four different pretreatment cases to deconstruct the complex structure of wheat straw. Case 1 considers the liquid hot water (LHW) pretreatment method; Case 2, the dilute acid (DA) pretreatment approach; Case 3, the ammonia fiber expansion (AFX); and Case 4, the organosolv (OS) pretreatment method. Each case is designed to preferentially target one of the major biomass components cellulose, hemicellulose, or lignin to enhance the overall efficiency of downstream conversion processes. To assess environmental impacts, we apply prospective life cycle assessment using Activity Browser (AB), an open-source platform designed to perform LCA under evolving future conditions. In this study, we use the open-source BioSTEAM framework for modeling the foreground system. Future background systems are based on regional model of investments and development (REMIND) energy scenarios aligned with the Paris agreement, covering milestone years 2030, 2040, 2050, and beyond. Results show significant reductions in global warming potential when shifting from REMIND-SSP2-Base to REMIND-SSP2-Pkbudg500 in 2030: LHW (59%), DA (54%), AFX (26%), and OS (44%). For 2050, reductions are LHW (43%), DA (35%), AFX (12%), and OS (28%). The goal of this study is to address the gap in understanding how pretreatment processes can be effectively scaled up, with the aim of enhancing the sustainability of emerging processes and materials.

Introduction

The conversion of agroforestry residues into bio-based chemicals and fuels represents a promising pathway toward reducing dependence on fossil resources, while simultaneously creating added value for the agricultural and forestry sectors [1]. In lignocellulosic biomass, cellulose is the predominant and most commercially valuable component; however, a major challenge in its processing lies in the efficient extraction of fermentable sugars from the hemicellulose fraction, while simultaneously enabling the effective utilization of lignin [2]. Therefore, a pretreatment step is essential to enhance cellulose accessibility to hydrolytic enzymes, which convert it into glucose that can then be fermented into biofuels [1]. Various pretreatment methods are available to breakdown lignocellulosic structures, each designed to target specific components such as cellulose, hemicellulose, or lignin. Liquid hot water (LHW) treatment focuses on hydrolyzing hemicellulose, using only water as the reactant, with acetic acid released from the hemicellulose structure acting as a self-promoting catalyst [3]. Dilute acid (DA) pretreatment also hydrolyzes and removes a significant portion of the hemicelluloses, converting them into sugars and furfural [1]. Ammonia fiber expansion (AFX) is a thermochemical pretreatment that improves the accessibility of polysaccharides to enzymes, enabling their hydrolysis into fermentable sugars [4]. Organosolv (OS) is considered one of the most effective methods for enhancing cellulose digestibility and efficiently fractionating biomass components [5]. Wheat straw biorefinery, an emerging technology in its early stages of

development, holds significant potential to facilitate the transition to a circular bioeconomy [6]. However, to ensure its sustainability, it is crucial to conduct a thorough assessment of environmental impacts, such as emissions and resource consumption [7]. This can be effectively achieved through prospective life cycle assessment (pLCA), which helps forecast the long-term environmental implications of the technology [8], [9]. Conducting prospective LCA during the early stages of process development, however, remains challenging due to the limited availability of detailed mass and energy balance data for both the foreground and background systems [10]. In this study, we consider four different pretreatment cases: liquid hot water, dilute acid, ammonia fiber expansion, and organosolv as the foreground system, as shown in Figure 1. For this system, we employ the open-source software BioSTEAM, which enables the simulation of industrial-scale processes even at low technology readiness levels (TRLs), using minimal experimental data [11]. The future background scenarios this study employs the SSP2 narrative, known as the "middle-of-the-road" pathway, serving as a useful starting point for exploring solutions that integrate climate mitigation and adaptation while also addressing broader societal objectives throughout the 21st century [12],[10], [13], [14]. The primary objective of this study is to evaluate each pretreatment case using a prospective LCA approach. Specifically, we present cradle-to-gate results for each biorefinery design to gain deeper insight into the system's potential to produce sustainable bio-based products, including bioethanol, lignin, and biogas.

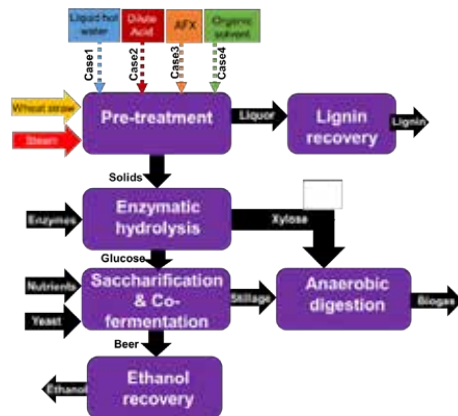


Figure 1: Four different pretreatment case studies: Case 1 uses liquid hot water, Case 2 uses dilute acid, Case 3 uses ammonia fiber expansion, and Case 4 uses the organosolv pretreatment process.

Materials and methods

Foreground modeling is conducted using the open-source BioSTEAM software (version 2.51.4), implemented in Python v3.9 [15]. The pretreatment model is adapted from the Bio-Industrial Park GitHub repository, specifically from the cellulose biorefinery example provided by the software developers [15]. In the four case

studies, only the pretreatment configurations vary, while the downstream processes fermentation, lignin recovery, ethanol purification, and anaerobic digestion remain consistent across all wheat straw biorefinery models [16], [17]. For prospective LCA an open-source LCA tool Activity Browser (AB) is used. The efficacy of the wheat straw biorefinery system is demonstrated through four distinct pretreatment case studies. The descriptions of these foreground case studies are as follows.

Case 1: Liquid hot water Pretreatment

Wheat straw used in this study has the following composition on a dry weight basis: 32.8% glucan, 20.4% xylan, 1.98% arabinan, 0.63% galactan, 0.67% mannan, 16.16% lignin, 19.06% extractives, and 1.01% ash [7]. The moisture content is 7.16 wt% [7]. In this study, we apply BioSTEAM's prebuilt modules and flowsheets for cellulosic biorefineries, particularly those adapted from the corn stover model, to simulate the LHW pretreatment pathway [15], [17], [18]. The LHW pretreatment conditions are based on configurations provided within the BioSTEAM framework and validated by previously published studies [3], [15], [17], [18]. A summary of key life cycle inventory (LCI) data, including material and energy flows, is presented in Table 1. In the simulation, wheat straw at 25 °C is introduced into the LHW pretreatment unit, where it is contacted with hot water at 95 °C and exposed to high-pressure steam at 268 °C and 13.17 bar. The pretreatment reaction occurs within a temperature range of 150–160 °C, facilitating the effective fractionation of biomass components [3], [15], [17], [18]. Following pretreatment, the biomass is separated into two streams: a solid fraction, primarily consisting of cellulose and hemicellulose, and a liquid fraction containing solubilized residual hemicelluloses and lignin. The solid fraction proceeds to enzymatic hydrolysis, where polysaccharides are converted into monomeric sugars. According to the simulation results, the recovery yields are 29% for glucose, 31% for xylose, and 28% for lignin. The glucose-rich hydrolysate then undergoes saccharification and co-fermentation, enabled by microbial inoculation and nutrient addition, to convert sugars into an ethanol-rich beer and stillage. Ethanol is recovered through distillation, while the stillage along with the xylose stream from enzymatic hydrolysis is routed to an anaerobic digestion unit for biogas production. In parallel, the liquid stream from pretreatment is directed to a lignin precipitation unit to recover purified lignin as shown in figure 1. All simulation data, including LCI information and recovery yields, are obtained directly from the BioSTEAM platform using its integrated thermodynamic and chemical property databases [3], [15], [17], [18].

Case 2: Dilute acid Pretreatment

In dilute acid pretreatment process, the wheat straw composition remains the same as in case 1. Hemicellulose carbohydrates present in the wheat straw are primarily converted into soluble sugars via hydrolysis reactions catalyzed by dilute sulfuric acid in the presence of steam [19]. This reaction setup is modeled using the BioSTEAM simulation platform [15], [17], [19]. The life cycle inventory (LCI) data utilized for this scenario are summarized in Table 1 [15], [17], [19]. The pretreatment process facilitates downstream enzymatic hydrolysis by disrupting plant cell wall structures, reducing cellulose crystallinity, and decreasing polymer chain length [19]. However, the hydrolysis also generates sugar degradation by-products such as furfural and 5-hydroxymethylfurfural (HMF), which are toxic to fermenting organisms. To mitigate this, a flash vaporization step is applied to remove these inhibitors [15], [17], [19]. Following pretreatment, the resulting slurry is cooled by dilution water and transferred to a conditioning reactor, where ammonia is used to adjust the pH from approximately 1 to 5 [19]. Although previous studies report the use of lime for pH adjustment (raising the pH to 10, followed by re-acidification to pH 5 with sulfuric acid), this approach poses significant drawbacks [19]. The reaction between

lime and sulfuric acid leads to gypsum precipitation, which not only complicates solid-liquid separation but also contributes to sugar losses due to side reactions at elevated pH or mechanical losses with the gypsum cake [19]. To avoid these issues, ammonia is employed in this simulation for pH control. According to the BioSTEAM model outputs, the hydrolysis step yields 30% glucose, 31% xylose, and 28% lignin. The subsequent downstream processes including saccharification and fermentation, ethanol recovery, lignin recovery, and anaerobic digestion are modeled identically to those described in Case 1 and are illustrated in Figure 1.

Case 3: Ammonia fiber expansion Pretreatment

Ammonia fiber expansion (AFX) pretreatment uses ammonia as the primary reactant to process wheat straw [4], [20]. This method reduces the structural recalcitrance of the biomass and enhances its enzymatic conversion into fermentable sugars [4], [20]. Pretreatment conditions are based on system configurations defined within the BioSTEAM simulation framework [15]. LCI data, including material and energy flows, are presented in Table 1. Wheat straw is introduced at 25 °C, and the pretreatment involves the application of high pressure, high temperature steam at approximately 13.17 bar and 268 °C, supplying 2.44 MJ of thermal energy per kg of wheat straw [15]. Additional inputs include warm water (1.23 kg per kg of wheat straw) and ammonia (0.82 kg per kg of wheat straw) [15]. Within the BioSTEAM simulation, the AFX reaction takes place at temperatures ranging from 120-130 °C [15]. Following pretreatment, the solid stream containing cellulose and hemicellulose proceeds to enzymatic hydrolysis, where enzymes convert structural carbohydrates into glucose and xylose [4], [15], [20]. According to BioSTEAM simulation results, glucose and xylose recovery rates are approximately 45% and 47%, respectively, consistent with values reported in the literature [4], [15], [20]. Downstream processes including saccharification and fermentation, ethanol recovery, lignin recovery, and anaerobic digestion are modeled identically to those in Cases 1 and 2 and are illustrated in Figure 1 [15].

Case 4: Organosolv Pretreatment

The organosolv pretreatment conditions are based on a previous study Serna-Loaiza et al., 2021 [3], [21]. Wheat straw undergoes pretreatment with a mixture of 60 wt% aqueous ethanol at a temperature of 180 °C [3], [21]. After the extraction process is finished, the resulting mixture is separated into liquid and solid fractions. Subsequently, the solid fraction, which contains a higher concentration of glucan, undergoes a washing step. The extracted solid fraction is processed in an enzymatic hydrolysis stage to produce monomeric sugars (hexoses and pentoses). Microorganisms *S.cerevisiae* convert the sugars released during pre-treatment into ethanol through a fermentation process [22]. The liquors stream is sent to the lignin precipitation, where lignin is produced [3], [21]. The xylose, which contains hemicellulose sugars mixed with stillage from the ethanol distillation stage, is fed to an anaerobic digestion stage to obtain biogas as a product as illustrated in figure 1 [3], [21],[15].

Prospective life cycle assessment

Prospective life cycle assessment (pLCA) provides a framework for estimating the environmental performance of technologies under future scenarios by considering technological evolution and systemic changes [10], [23]. It considers changes in the foreground system, such as improvements in the studied technologies (e.g., the four pretreatment case studies presented in this work), as well as developments in the background system, including shifts in raw material supply chains and energy markets. In this study, the prospective background system is modeled by integrating the

ecoinvent life cycle database with integrated assessment models (IAMs), specifically the REMIND model [10], [12], [13]. Two climate change mitigation scenarios from REMIND are evaluated: REMIND-SSP2-Base, which projects a global temperature increase of approximately 3.5 °C under a business-as-usual pathway, and REMIND-SSP2-Pkbugd500, which targets a temperature rise limited to below 1.5 °C in line with the Paris Agreement [10], [12], [13]. These scenarios are aligned with socioeconomic trends and mitigation strategies to enhance the relevance and comparability of the prospective LCA. The open-source LCA tool Activity Browser (AB) is used to automatically modify the ecoinvent database in accordance with each REMIND scenario via its dedicated plugin feature [24]. Following the conventional LCA structure, the pLCA in this study includes goal and scope definition, inventory analysis, impact assessment, and interpretation. The system under investigation aims to convert wheat straw into multiple biorefinery products using different pretreatment processes. Therefore, the functional unit is defined as 1 kg of wheat straw processed. A cradle-to-gate boundary is applied, covering all unit processes involved in the conversion of wheat straw, as shown in Figure 1, with the full biorefinery pathway included within the system boundaries. Foreground life cycle inventory (LCI) data for all conversion processes are detailed in Table 1. For the life cycle impact assessment (LCIA), the ReCiPe Midpoint (H) method version 1.16 is applied, with global warming potential over a 100-year time horizon (GWP100) selected as the key climate change impact indicator [25].

Table 1: LCI data corresponding to the four pretreatment case studies

Materials and energy	Pre-treatment				Units
	LHW	Dilute acid	AFX	Organosolv	
Wheat straw	1	1	1	1	kg FU ⁻¹
Steam	0.85	1.05	2.44	1.72	MJ FU ⁻¹
Warm water	1.61	1.70	1.23	0.11	kg FU ⁻¹
H2SO4	-	0.020	-	-	kg FU ⁻¹
NH3	-	-	0.82	-	kg FU ⁻¹
Organic solvent ^a	-	-	-	0.17	kg FU ⁻¹
Electricity ^b	1.34	1.37	3.73	1.35	kwh FU ⁻¹
Materials and energy	Enzymatic hydrolysis				Units
	LHW	Dilute acid	AFX	Organosolv	
Enzymes	0.022	0.016	0.021	0.010	kg FU ⁻¹
Tap water	1.53	1.13	7.99	1.10	kg FU ⁻¹
NH3	-	0.040	-	-	kg FU ⁻¹
Electricity ^b	0.0047	0.0046	0.0047	0.0047	kwh FU ⁻¹
Materials and energy	Saccharification & Co-fermentation				Units
	LHW	Dilute acid	AFX	Organosolv	
Nutrients	0.038	0.029	0.037	0.025	kg FU ⁻¹
DAP ^c	0.0047	0.0035	0.0045	0.0021	kg FU ⁻¹
Electricity ^b	1.50	1.13	1.46	0.43	kwh FU ⁻¹
Materials and energy	Lignin recovery				Units
	LHW	Dilute acid	AFX	Organosolv	
Steam	0.60	0.58	0.83	0.65	MJ FU ⁻¹
Cooling water	0.001	0.0009	0.0015	0.0012	m ³ FU ⁻¹
Electricity ^b	0.015	0.014	0.021	0.018	kwh FU ⁻¹
Materials and energy	Ethanol recovery				Units
	LHW	Dilute acid	AFX	Organosolv	
Steam	0.28	0.3	0.29	0.28	MJ FU ⁻¹
Cooling water	0.0063	0.0063	0.0062	0.0061	m ³ FU ⁻¹
Electricity ^b	0.094	0.096	0.098	0.090	kwh FU ⁻¹
Materials and energy	Anaerobic digestion				Units
	LHW	Dilute acid	AFX	Organosolv	
Steam	0.10	0.14	0.15	0.12	MJ FU ⁻¹
Tap water	0.09	0.13	0.14	0.11	kg FU ⁻¹
Electricity ^b	0.001	0.001	0.001	0.001	kwh FU ⁻¹

a: Ethanol used as Organic solvents, b: European mix electricity, c: Diammonium phosphate (DAP)

Results and discussions

This section presents the results of the prospective life cycle assessment of a wheat straw biorefinery, evaluated across four different pretreatment case studies. Global warming potential (GWP) is used as the life cycle impact assessment (LCIA) indicator under two prospective background scenarios: REMIND-SSP2-Base and REMIND-SSP2-Pkbugd500, as detailed below.

REMIND-SSP2-Base

Figure 2a illustrates the process-level contributions to the global warming potential (GWP) for four wheat straw pretreatment case studies under the REMIND-SSP2-Base scenario, which projects a global temperature increase of approximately 3.5 °C by 2030, 2040, and 2050. In the year 2030, the liquid hot water (LHW) pretreatment shows a total GWP of 9.91 kg of CO₂-eqFU⁻¹. This total impact is primarily distributed across several unit operations: approximately 9% arises from the pretreatment stage, where wheat straw is separated into solid and liquid fractions; 18% originates from enzymatic hydrolysis, where the cellulose and hemicellulose in the solid fraction are converted into glucose and xylose with the aid of enzymes; and 30% is attributed to saccharification and co-fermentation, which involves the conversion of sugars into beer and stillage. The significant contribution of this stage is due to the addition of nutrients and organic chemicals, as shown in Table 1. Ethanol recovery accounts for 23% of the total GWP due to its high energy requirement, while anaerobic digestion and lignin recovery contribute 17% and 3%, respectively.

For the dilute acid (DA) pretreatment, the total GWP in 2030 is 10.22 kg of CO₂-eqFU⁻¹, slightly higher than that of LHW. The contribution patterns are similar, with 9% from pretreatment, 19% from enzymatic hydrolysis, 30% from saccharification and co-fermentation, 21% from ethanol recovery, 18% from anaerobic digestion, and 3% from lignin recovery. The increased GWP in the DA case is mainly due to the additional use of sulfuric acid in the pretreatment stage and ammonia in the enzymatic hydrolysis unit for pH adjustment. In contrast, the ammonia fiber expansion (AFX) pretreatment shows a much higher total GWP of 52.07 kg of CO₂-eqFU⁻¹. This elevated impact is attributed to the use of liquid ammonia, the high steam demand required to maintain operational temperatures, and significant electricity consumption for ammonia pumping, as reflected in Table 1. The process contributions for AFX are 13% from pretreatment, 22% from enzymatic hydrolysis, 25% from saccharification and co-fermentation, 19% from ethanol recovery, 18% from anaerobic digestion, and 3% from lignin recovery.

The organosolv (OS) pretreatment case study results in a total GWP of 10.26 kg of CO₂-eqFU⁻¹ in 2030. Although its impact is lower than AFX, it is slightly higher than that of the LHW and DA scenarios. The OS process contributions include 12% from pretreatment, 11% from enzymatic hydrolysis, 32% from saccharification and co-fermentation, 25% from ethanol recovery, 16% from anaerobic digestion, and 4% from lignin recovery.

In 2040 and 2050, the distribution of process contributions remains largely consistent with those observed in 2030. However, the total GWP values decline for all four pretreatment strategies due to changes in the background energy system. In 2040, the total GWP values are reduced to 7.35 kg of CO₂-eqFU⁻¹ for LHW, 7.80 kg of CO₂-eqFU⁻¹ for DA, 46.20 kg of CO₂-eqFU⁻¹ for AFX, and 8.30 kg of CO₂-eqFU⁻¹ for OS. By 2050, these values further decrease to 5.02 kg of CO₂-eqFU⁻¹ for LHW, 5.58 kg of CO₂-eqFU⁻¹ for DA, 40.84 kg of CO₂-eqFU⁻¹ for AFX, and 6.51 kg of CO₂-eqFU⁻¹ for OS. The declining GWP trend over time is mainly attributed to the gradual decarbonization of the energy sector projected in the REMIND-SSP2-Base scenario, which reflects a moderate shift toward cleaner

energy sources by 2050.

REMIND-SSP2-Pkbudg500

Figure 2b presents the global warming potential (GWP) outcomes for four pretreatment scenarios in the wheat straw biorefinery system, assessed under the REMIND-SSP2-Pkbudg500 background, which aligns with a stringent climate policy targeting a 1.5 °C global temperature rises by 2100. This scenario represents a highly decarbonized future energy system, resulting in significantly lower GWP values across all case studies compared to the REMIND-SSP2-Base scenario. In 2030, the liquid hot water (LHW) pretreatment exhibits a total GWP of 4.07 kg of CO₂-eqFU⁻¹. The environmental burden is distributed across key process units, including pretreatment (8%), enzymatic hydrolysis (20%), and saccharification/co-fermentation (29%). Ethanol recovery contributes 23%, primarily driven by its heat demand, followed by anaerobic digestion (18%) and lignin recovery (3%).

The dilute acid (DA) pretreatment records a slightly higher GWP of 4.70 kg of CO₂-eqFU⁻¹ in the same year, with a comparable distribution pattern. The increased emissions stem from the inclusion of sulfuric acid in the pretreatment and ammonia for pH control during enzymatic hydrolysis. The percentage breakdown includes 8% from pretreatment, 21% from enzymatic hydrolysis, 30% from saccharification and co-fermentation, 21% from ethanol recovery, 18% from anaerobic digestion, and 3% from lignin recovery.

The ammonia fiber expansion (AFX) process continues to exhibit a notably high environmental impact, with a global warming potential (GWP) of 38.60 kg of CO₂-eqFU⁻¹ projected for 2030. This elevated impact is largely driven by the substantial consumption of steam, liquid ammonia, and electricity for pumping operations. The distribution of GWP across process stages remains relatively stable, with contributions as follows: pretreatment (14%), enzymatic hydrolysis (22%), saccharification and co-fermentation (25%), ethanol recovery (19%), anaerobic digestion (18%), and lignin recovery (3%). A potential strategy to reduce the GWP during the pretreatment stage involves replacing liquid ammonia with volatile (gaseous) ammonia. The use of liquid ammonia often leads to partial flashing, which cools the biomass and necessitates additional heat input to maintain the desired processing temperature. In contrast, volatile ammonia disperses more uniformly throughout the wheat straw and dissolves exothermically into the moisture present in the biomass. This reaction generates heat, promoting rapid and uniform heating of the biomass and thereby reducing the overall energy requirement for pretreatment[4].

For the organosolv (OS) pretreatment pathway, the GWP stands at 5.73 kg of CO₂-eqFU⁻¹. While this is considerably lower than the AFX scenario, it remains moderately higher than LHW and DA. The OS process is characterized by contributions of 13% from pretreatment, 12% from enzymatic hydrolysis, 31% from saccharification and co-fermentation, 24% from ethanol recovery, 16% from anaerobic digestion, and 4% from lignin recovery.

By 2040 and 2050, all four pretreatment scenarios exhibit a consistent downward trajectory in total GWP values, while maintaining similar process-level contribution patterns. In 2040, LHW, DA, AFX, and OS yield total GWP values of 3.06, 3.77, 36.16, and 4.89 kg of CO₂-eqFU⁻¹, respectively. These values further decline by 2050 to 2.88 kg of CO₂-eqFU⁻¹ for LHW, 3.62 kg of CO₂-eqFU⁻¹ for DA, 35.83 kg of CO₂-eqFU⁻¹ for AFX, and 4.70 kg of CO₂-eqFU⁻¹ for OS. This overall reduction is primarily linked to the progressive decarbonization of the energy system assumed in the REMIND-SSP2-Pkbudg500 scenario, which reflects an ambitious transition toward low-carbon energy sources in support of global climate targets.

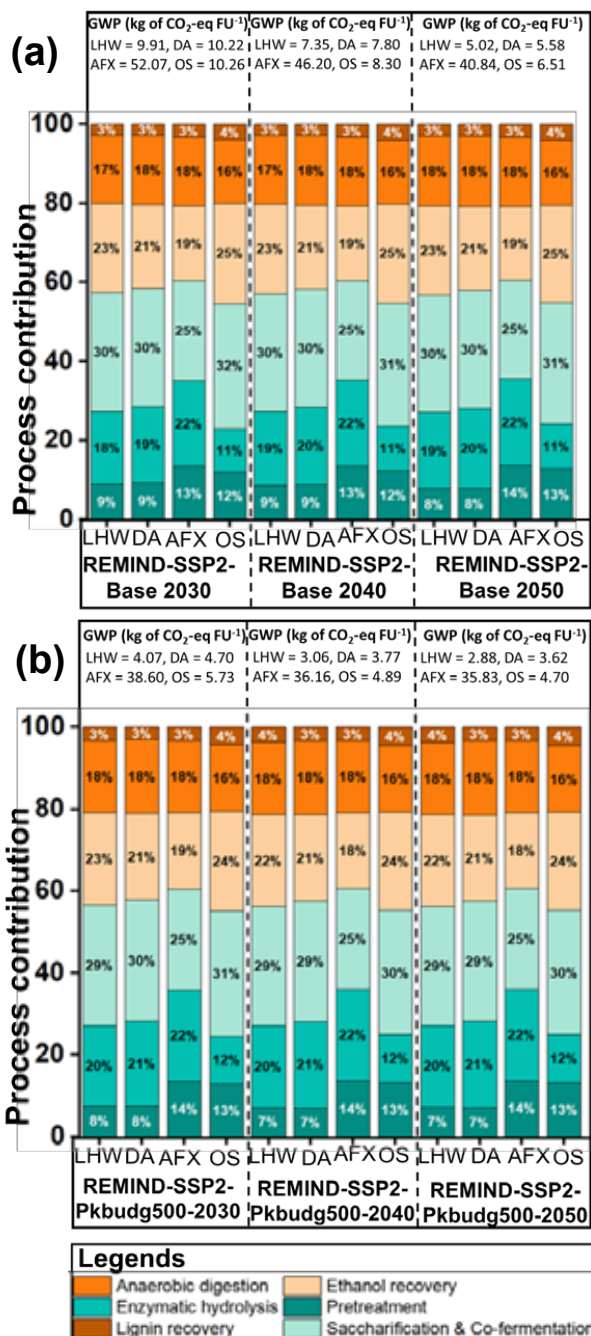


Figure 2: Global warming potential (GWP) contributions of four biomass pretreatment processes Liquid Hot Water (LHW), Dilute Acid (DA), Ammonia Fiber Expansion (AFX), and Organosolv evaluated using the ReCiPe Midpoint (H) method. **a:** REMIND-SSP2-Base scenario as the background system for the years 2030, 2040, and 2050. **b:** REMIND-SSP2-Pkbudg500 scenario as the background system for the same years. The legends in bar graph shows the process contribution for each pretreatment case study.

Conclusions

In this study, we evaluated four different pretreatment methods for wheat straw biorefinery processes using prospective life cycle impact assessments. The environmental performances of the four case studies can be summarized as follows:

- Liquid hot water (LHW) pretreatment demonstrated the best overall environmental performance across both background scenarios (REMIND-SSP2-Base and REMIND-SSP2-Pkbg500) for the years 2030, 2040, and 2050.
- Dilute acid (DA) pretreatment showed a comparable environmental impact to LHW under both background systems, making it a viable alternative in terms of sustainability.
- Ammonia fiber expansion (AFEX) exhibited higher environmental impacts, mainly due to the use of liquid ammonia and the significant demand for steam and electricity. However, AFEX achieved higher glucose and xylose recovery than LHW and DA. Its environmental footprint could be improved through the use of volatile ammonia and by enhancing ammonia recovery. Additionally, a greener energy mix in the future could reduce its global warming potential.
- Organosolv pretreatment also showed improved environmental performance under both background scenarios. While its impact was better than AFEX, it was slightly higher than LHW and DA, primarily due to the use of organic solvents in the process.

Overall, LHW pretreatment emerges as the most environmentally favorable option, particularly due to its use of only heated water. Its performance further improves when the background system shifts toward more sustainable and low-carbon pathways, such as REMIND-SSP2-Pkbg500. On the other hand, although AFEX offers superior glucose and xylose recovery which is advantageous from an economic perspective it comes at a higher environmental cost. This highlights a clear trade-off between environmental sustainability and resource recovery efficiency.

Acknowledgements

We gratefully acknowledge financial support by TU Wien global budget for PhD research.

References

- [1] P. Vergara, M. Wojtusik, E. Revilla, M. Ladero, F. Garcia-Ochoa, and J. C. Villar, "Wheat straw fractionation by ethanol-water mixture: Optimization of operating conditions and comparison with diluted sulfuric acid pretreatment," *Bioresour Technol*, vol. 256, no. January, pp. 178–186, 2018, doi: 10.1016/j.biortech.2018.01.137.
- [2] J. K. Saini, Himanshu, Hemansi, A. Kaur, and A. Mathur, "Strategies to enhance enzymatic hydrolysis of lignocellulosic biomass for biorefinery applications: A review," *Bioresour Technol*, vol. 360, no. April 2022, p. 127517, 2022, doi: 10.1016/j.biortech.2022.127517.
- [3] S. Serna-Loaiza, J. Adamczyk, S. Beisl, M. Miltner, and A. Friedl, "Sequential Pretreatment of Wheat Straw: Liquid Hot Water Followed by Organosolv for the Production of Hemicellulosic Sugars, Lignin, and a Cellulose-Enriched Pulp," *Waste Biomass Valorization*, vol. 13, no. 12, pp. 4771–4784, 2022, doi: 10.1007/s12649-022-01824-8.
- [4] S. P. S. Chundawat and T. Campbell, "Digital Commons @ Michigan Tech Ammonia fiber expansion (AFEX) pretreatment of lignocellulosic biomass," 2020.
- [5] S. C. Rabelo, P. Y. S. Nakasu, E. Scopel, M. F. Araújo, L. H. Cardoso, and A. C. da Costa, "Organosolv pretreatment for biorefineries: Current status, perspectives, and challenges," *Bioresour Technol*, vol. 369, no. November 2022, 2023, doi: 10.1016/j.biortech.2022.128331.
- [6] F. Liu, X. Dong, X. Zhao, and L. Wang, "Life cycle assessment of organosolv biorefinery designs with the complete use of biomass," *Energy Convers Manag*, vol. 246, p. 114653, 2021, doi: 10.1016/j.enconman.2021.114653.
- [7] P. Emeder, "Modelling and Life-Cycle Assessment of Pretreatment Strategies for the Bioconversion of Lignocellulosic Biomass," pp. 1–138, 2021.
- [8] M. Erakca, M. Baumann, C. Helbig, and M. Weil, "Systematic review of scale-up methods for prospective life cycle assessment of emerging technologies," *J Clean Prod*, vol. 451, no. April, p. 142161, 2024, doi: 10.1016/j.jclepro.2024.142161.
- [9] N. Thonemann, A. Schulte, and D. Maga, "How to conduct prospective life cycle assessment for emerging technologies? A systematic review and methodological guidance," *Sustainability (Switzerland)*, vol. 12, no. 3, pp. 1–23, 2020, doi: 10.3390/su12031192.
- [10] R. Sacchi *et al.*, "Prospective Environmental Impact Assessment (premise): A streamlined approach to producing databases for prospective life cycle assessment using integrated assessment models," *Renewable and Sustainable Energy Reviews*, vol. 160, no. April 2021, p. 112311, 2022, doi: 10.1016/j.rser.2022.112311.
- [11] Y. Cortes-Peña, D. Kumar, V. Singh, and J. S. Guest, "BioSTEAM: A Fast and Flexible Platform for the Design, Simulation, and Techno-Economic Analysis of Biorefineries under Uncertainty," *ACS Sustain Chem Eng*, vol. 8, no. 8, pp. 3302–3310, 2020, doi: 10.1021/acssuschemeng.9b07040.
- [12] A. Mendoza Beltran *et al.*, "When the Background Matters: Using Scenarios from Integrated Assessment Models in Prospective Life Cycle Assessment," *J Ind Ecol*, vol. 24, no. 1, pp. 64–79, 2020, doi: 10.1111/jiec.12825.
- [13] R. Sacchi, "Prospective Environmental Impact Assessment," 2024. [Online]. Available: <https://github.com/polca/premise>
- [14] S. Bruhn, R. Sacchi, C. Cimpan, and M. Birkved, "Ten questions concerning prospective LCA for decision support for the built environment," *Build Environ*, vol. 242, no. June, p. 110535, 2023, doi: 10.1016/j.buildenv.2023.110535.
- [15] Y. Cortés-Peña, "BioSTEAM: Biorefinery simulation and techno-economic analysis," 2024.
- [16] Y. Cortes-Peña, D. Kumar, V. Singh, and J. S. Guest, "BioSTEAM: A Fast and Flexible Platform for the Design, Simulation, and Techno-Economic Analysis of Biorefineries under Uncertainty," *ACS Sustain Chem Eng*, vol. 8, no. 8, pp. 3302–3310, 2020, doi: 10.1021/acssuschemeng.9b07040.
- [17] M. Sanchis-Sebastiá, J. Gomis-Fons, M. Galbe, and O. Wallberg, "Techno-economic evaluation of biorefineries based on low-value feedstocks using the BioSTEAM software: A case study for animal bedding," *Processes*, vol. 8, no. 8, 2020, doi: 10.3390/PR8080904.
- [18] D. Humbird *et al.*, "Process Design and Economics for Biochemical Conversion of Lignocellulosic Biomass to Ethanol: Dilute-Acid Pretreatment and Enzymatic

- Hydrolysis of Corn Stover”, doi: 10.2172/1013269.
- [19] R. Davis *et al.*, “Process Design and Economics for the Conversion of Lignocellulosic Biomass to Hydrocarbons: Dilute-Acid and Enzymatic Deconstruction of Biomass to Sugars and Biological Conversion of Sugars to Hydrocarbons,” *National Renewable Energy Laboratory-NREL*, no. October 2013, p. 147, 2013, [Online]. Available: <http://www.osti.gov/servlets/purl/1107470/>
- [20] M. Blümmel *et al.*, “Ammonia Fiber Expansion (AFEX) as spin off technology from 2nd generation biofuel for upgrading cereal straws and stovers for livestock feed,” *Anim Feed Sci Technol*, vol. 236, no. December 2017, pp. 178–186, 2018, doi: 10.1016/j.anifeedsci.2017.12.016.
- [21] S. Serna-Loaiza, F. Zikeli, J. Adamcyk, and A. Friedl, “Towards a wheat straw biorefinery: Combination of Organosolv and Liquid Hot Water for the improved production of sugars from hemicellulose and lignin hydrolysis,” *Bioresour Technol Rep*, vol. 14, no. February, 2021, doi: 10.1016/j.biteb.2021.100667.
- [22] P. Kravanja, K. Könighofer, L. Canella, G. Jungmeier, and A. Friedl, “Perspectives for the production of bioethanol from wood and straw in Austria: Technical, economic, and ecological aspects,” *Clean Technol Environ Policy*, vol. 14, no. 3, pp. 411–425, 2012, doi: 10.1007/s10098-011-0438-1.
- [23] M. Lilja, “Prospective life cycle assessment in environmental analysis of energy transition,” 2023.
- [24] L. C. A. A. Browser, “Activity Browser,” 2024. [Online]. Available: <https://github.com/LCA-ActivityBrowser/activity-browser>
- [25] M. Huijbregts *et al.*, “ReCiPe 2016 - A harmonized life cycle impact assessment method at midpoint and endpoint level. Report I: Characterization,” *National Institute for Public Health and the Environment*, p. 194, 2016, [Online]. Available: <https://www.rivm.nl/bibliotheek/rapporten/2016-0104.pdf>

A continuous particle model for the simulation of direct reduction of iron ore in fluidized beds

Simon Schneiderbauer,^{1,*} Mustafa Efe Kinaci¹

1: Dept. of Particulate Flow Modelling, Johannes Kepler University, Linz, Austria

* Correspondent author: simon.schneiderbauer@jku.at

Keywords: CFD-DEM, continuous particle model (CPM), iron ore reduction, mapping, interpolation

Abstract

Fluidized bed and moving bed reactors are among the most important technologies in various branches of the process industry. For decades, it has been well known that iron can be reduced rapidly and efficiently from iron carrier materials using these technologies. The primary energy sources and reducing agents for this process include natural gas, coal, coke, and pulverized coal, which ultimately release CO₂ and, to a lesser extent, H₂O into the environment. Since iron reduction accounts for approximately 70% of the energy consumed during steelmaking, it presents a significant opportunity for energy savings and CO₂ emission reductions. In particular, the use of green hydrogen as a reducing agent could make a substantial contribution to achieving global climate goals.

Due to the limited accessibility of direct measurements in these systems, simulation methods have become essential tools for optimizing ironmaking processes. While the two-fluid model [1] is a promising candidate for simulating large-scale multiphase processes, it lacks an adequate representation of particle size distribution and the associated physical phenomena. This limitation has led to the development of particle-based approaches, such as the coupling of computational fluid dynamics (CFD) with discrete element methods (DEM) [2], [3]. These approaches effectively handle particle segregation, growth, and mixing. Additionally, chemical reactions can be evaluated on a per-particle basis, eliminating the need to translate these reactions into a continuum representation. However, CFD-DEM methods are computationally expensive and require appropriate coarse-graining techniques to reduce their demands.

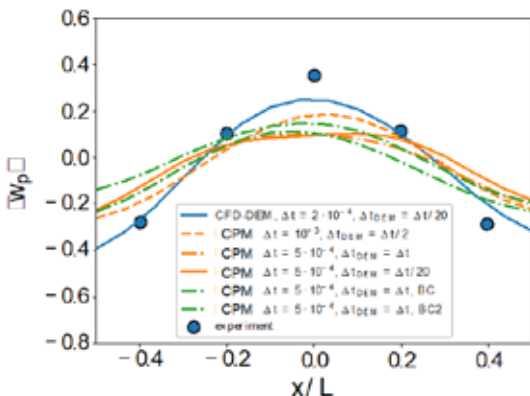


Figure 1: Comparison of CFD-DEM with CFD-CPM and experimental data [4] in the case of a bubbling fluidized bed. $\langle w_p \rangle$ denotes the time-averaged vertical particle velocity.

To address these challenges, we present a continuous particle model (CPM), where ore particles are tracked within a Lagrangian framework, similar to DEM. However, unlike DEM, where particle-particle collisions are explicitly resolved, CPM replaces these

interactions with a particle-stress model. In this approach, individual collisions are substituted by the interpolation of a collisional force, derived as the gradient of the particle stress, at the particle's position [3]. This substitution significantly enhances computational efficiency [5]. Nevertheless, CPM requires advanced mapping and interpolation schemes compared to DEM [6].

Our results demonstrate that CFD-CPM achieves accuracy comparable to CFD-DEM in simulating spouted and bubbling fluidized beds (figure 1). Furthermore, the predictive capability and numerical efficiency of the reactive CFD-CPM approach are validated in a lab-scale fluidized bed. The model accurately predicts the fractional reduction of iron ore and provides detailed insights into temperature distributions and reaction gas consumption during the reduction process.

References

- [1] S. Schneiderbauer, A. Aigner, and S. Pirker, "A comprehensive frictional-kinetic model for gas-particle flows: analysis of fluidized and moving bed regimes," *Chem Eng Sci*, vol. 80, pp. 279–292, 2012, doi: 10.1016/j.ces.2012.06.041.
- [2] C. Kloss, C. Goniva, A. Hager, S. Amberger, and S. Pirker, "Models, algorithms and validation for opensource DEM and CFD-DEM," *Progress in Computational Fluid Dynamics*, vol. 12, no. 2/3, pp. 140–152, 2012, doi: 10.1504/PCFD.2012.047457.
- [3] P. J. O'Rourke and D. M. Snider, "An improved collision damping time for MP-PIC calculations of dense particle flows with applications to polydisperse sedimenting beds and colliding particle jets," *Chem Eng Sci*, vol. 65, no. 22, pp. 6014–6028, Nov. 2010, doi: 10.1016/j.ces.2010.08.032.
- [4] B. Gopalan *et al.*, "Measurements of pressure drop and particle velocity in a pseudo 2-D rectangular bed with Geldart Group D particles," *Powder Technol.*, vol. 291, pp. 299–310, 2016, doi: 10.1016/j.powtec.2015.12.040.
- [5] V. Verma and J. T. Padding, "A novel approach to MP-PIC: Continuum particle model for dense particle flows in fluidized beds," *Chemical Engineering Science: X*, vol. 6, p. 100053, 2020, doi: 10.1016/j.cesx.2019.100053.
- [6] B. Esgandari and S. Schneiderbauer, "On grid-independency of CFD-DEM simulations of cluster-induced turbulence," *International Journal of Multiphase Flow*, vol. 188, p. 105223, Apr. 2025, doi: 10.1016/j.ijmultiphaseflow.2025.105223.

Energy & Process Engineering Posters

Day 1

Bubble-particle interactions: A study on film drainage and particle cutting

E. Enan^{1,2*}, M. Outokesh², M. Saeedipour¹, M. Hlawitschka²

1: Institute of Process Engineering, Johannes Kepler University, Austria

2: Department of Particulate Flow Modelling, Johannes Kepler University, Austria

* Correspondent author: mark.hlawitschka@jku.at

Keywords: Film Drainage, Wetting, Cutting

Predicting the behavior of three-phase flow in a slurry bubble column reactor presents significant challenges, primarily due to the complex interactions between bubbles and solid particles. These bubble-particle interactions influence the system's hydrodynamics [1] and play a crucial role in mass transfer processes. For instance, when a bubble directly contacts a particle, it can reduce the resistance of the liquid film, thereby enhancing the local mass transfer between phases. In this study, a detailed numerical investigation is carried out to predict and analyse the outcomes of bubble-particle interactions at the interface in a liquid medium using the Volume of Fluid (VOF) method, implemented in OpenFOAM v2312.

Various physical properties, such as viscosity and bubble-to-particle ratio, were studied to analyze the bubble's approach to the particle, contact area, film formation, drainage (Fig. 1), and possible particle wetting or cutting. The focus is on examining how various physical parameters - such as viscosity, bubble-to-particle size ratio, and contact angle- affect the bubble's behavior as it approaches the particle, including the contact region, film formation, and drainage dynamics. Particular attention is given to identifying phenomena such as particle wetting and the possibility of bubble cutting during the interaction.

The numerical model captures the evolution of the thin liquid film formed between the bubble and the particle and tracks the contact line dynamics, helping to understand critical behaviors such as film rupture, coalescence, or detachment. The results have been used to develop an initial regime map that categorizes various interaction outcomes based on key dimensionless parameters. The simulation results were validated against the experimental observations involving bubble interactions with a fixed tube to ensure stability and accuracy. Later, results are compared to theoretical and numerical models of film drainage behavior. These validations help build confidence in the simulation framework and provide a pathway for future work.

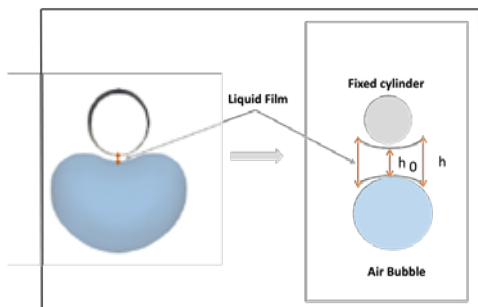


Fig. 1: Formation of a liquid film between the object and the bubble.

List of references:

Journal article: [1] Jiang, W. T., Luo, Q., Liao, H. L., Luo, Y., Qie, F. X., Tan, Q. F., & Qian, Z. (2023). Mechanism of bubble cutting by fibers: Experiment and simulation. *Chemical Engineering Journal*, 478, 147225.

Photocatalyst Development for Water Reclamation: From TiO₂ to Boron Nitride-Based Composites

D. Rattinger^{1,2*}, S. H. Moravej Hariri Paskiabi^{1,3}, V. Rehm⁴, J. Marx¹, M. Spruck¹, H. Schöbel⁴, J. O. Back¹

1: Dept. of Environmental, Process and Energy Engineering, MCI – The Entrepreneurial School, Austria

2: Institute of Analytical Chemistry and Radiochemistry, University of Innsbruck, Austria

3: Dept. of Civil, Chemical, Environmental and Materials Engineering, Alma Mater Studiorum – University of Bologna, Italy

4: Dept. of Biotechnology and Food Engineering, MCI – The Entrepreneurial School, Austria

* Correspondent author: daniel.rattinger@mci.edu

Keywords: Photocatalysis, Water treatment, Titanium dioxide, Boron nitride

The increasing pollution of water resources is one of the most pressing and widespread challenges humanity is facing currently. Even at low concentrations, pollutants are suspected to cause numerous adverse effects to human health, animals and aquatic ecosystems. To address the growing contamination, improvements in wastewater treatment, including the development of novel and effective treatment technologies, are required [1]. Among available approaches, photocatalysis has emerged as promising method where the catalyst material absorbs incoming light and initiates the generation of reactive oxygen species that are responsible for contaminant degradation [2].

The most frequently employed photocatalyst is TiO₂, especially favorable due to its non-toxicity, chemical stability and electrical properties. Challenges arise from its broad bandgap (3.2 eV) and rapid electron-hole-pair recombination during activation [3], [4]. Hexagonal boron nitride (h-BN) has shown potential for photocatalytic applications, however due to its even larger bandgap (5.5 eV) it is a necessity to form composites or heteroatom doped structures with other materials, such as metal oxides. The stabilization of electron-hole-pairs is reported in several different studies with h-BN/TiO₂ composite photocatalysts [3],[5],[6]. Another auspicious strategy is the implementation of a designated carbon source during synthesis, forming boron carbon nitride (BCN) structures, capable of lowering the bandgap and thus shifting activation towards the visible light range. Material modifications with metal oxides among others are reported to enhance the photocatalytic properties even further [7].

Current conducted investigations focus on experimental set-up evaluation of batch and continuous operation with TiO₂ as reference material. The degradation of pharmaceutical trace substances and per- and polyfluoroalkyl substances under UV-A radiation being of interest. Another set of experiments focuses on the inactivation and degradation of *E. coli* bacteria as a preliminary stage for investigating the removal of antibacterial resistant genes and organisms with the developed photocatalysts. The first results for diclofenac (10 mg/l) degradation with TiO₂ (400 mg/l) show fast and effective removal, with reaching concentrations below the detection limit after 20 min in batch mode. However, a mixture of diclofenac, carbamazepine and paracetamol (each 10 mg/l) shows significant residual concentrations of the two latter compounds even after 150 min of irradiation, which highlights the need for improvement.

Ongoing research focuses on synthesizing novel photocatalysts and test them under realistic conditions. The presented findings highlight the potential of photocatalysis for water treatment and emphasize the importance of material development to expand its applicability.

Journal article: [1] Schwarzenbach, R., Escher, B., Fenner, K., Hofstetter, T., Johnson, C., Gunten, U. and Wehrli, B., "The Challenge of Micropollutants in Aquatic Systems," *Science*, vol. 313, pp. 1072-1077, 2006. doi: 10.1126/science.1127291

Book chapter: [2] Ameta, R., Solanki, M.S., Benjamin, S., Ameta, S.C., "Chapter 6 - Photocatalysis," *Advanced Oxidation Processes for Waste Water Treatment*, Academic Press, 2018. doi: 10.1016/B978-0-12-810499-6.00006-1

Journal article: [3] Singh, B., Kaur, G., Singh, P., Singh, K., Sharma, J., Kumar, M., Bala, R., Meena, R., Sharma, K.S., Kumar, A., "Nanostructured BN-TiO₂ composite with ultra-high photocatalytic activity," *New Journal of Chemistry*, vol. 41, pp. 11640-11646, 2017. doi: 10.1039/C7NJ02509B

Journal article: [4] Ganiyu, S.O., van Hellenbusch, E.D, Cretin, M., Esposito, G., Oturan, M.A., "Coupling of membrane filtration and advanced oxidation processes for removal of pharmaceutical residues: A critical review," *Separation and Purification Technology*, vol. 156, part 3, pp. 891-914, 2015. doi: 10.1016/j.seppur.2015.09.059

Journal article: [5] Stengl, V., Henych, J., Slusna, M., "h-BN-TiO₂ Nanocomposite for Photocatalytic Applications," *Journal of Nanomaterials*, 2016. doi: 10.1155/2016/4580516

Journal article: [6] Sheng, Y., Yang, J., Wang, F., Liu, L., Liu, H., Yan, C., Guo, Z., "Sol-gel synthesized hexagonal boron nitride/titania nanocomposites with enhanced photocatalytic activity," *Applied Surface Science*, vol. 465, pp. 154-163, 2019. doi: 10.1016/j.apsusc.2018.09.137

Journal article: [7] Mei, Y., Yuan, N., liu, Y., Zhang, X., Lin, B., Zhou, Y., "Boron Carbon Nitride Semiconductor Modified with CeO₂ for Photocatalytic Reduction of CO₂ with H₂O: Comparative Study," *Carbon Capture Science & Technology*, vol. 1, 2021. doi: 10.1016/j.ccsst.2021.100016

Biosynthesis of silver nanoparticles using *Penicillium ochrochloron* and *Saccharomyces cerevisiae* extracts

L. Colleselli^{1,*}, M. Mutschlechner¹, H. Schöbel¹, P. Vrabl², and S. Zeilinger²

1: Department of Biotechnology and Food Engineering, MCI - The Entrepreneurial School, Austria

2: Institute of Microbiology, Universität Innsbruck, Austria

*Correspondent author: lucia.colleselli@mci.edu

Keywords: Green synthesis, Optimization, Photo-processing, Size-tuning

Silver nanoparticles (AgNPs) are used in many areas of daily life due to their specific size- and shape-dependent antimicrobial, optical and electrical properties [1, 2]. The bio-based production of high-quality and biocompatible nanocomponents represents an environmentally friendly and resource-saving alternative to conventional physicochemical manufacturing [3]. Fungi possess a broad spectrum of enzymes, proteins, cofactors and other metabolites that can serve as important reducing and stabilizing agents, making them promising candidates for the production of NPs.

In this study, AgNPs were generated using extracts of baker's yeast *Saccharomyces cerevisiae* and two different strains of the filamentous fungus *Penicillium ochrochloron* (CBS 123 823 and CBS 123 824) by applying optimization strategies during the cultivation and biosynthesis, respectively. The NP production efficiencies were explored in dependence of environmental factors such as cultivation temperatures or the presence or absence of light. The resulting nanomaterials were characterized by spectrophotometric analysis, scanning electron microscopy, and energy dispersive X-ray spectroscopy.

Our first findings demonstrate that both adaptations in the cultivation and the biosynthesis phase, as well as organism-specific traits, can considerably affect the AgNP yield and the particle size: For example, light-mediated AgNPs synthesis based on *S. cerevisiae* resulted in more than 90 % increased yields and a reduced particle dimension from 130 nm to 100 nm in contrast to dark reaction conditions. Extracts of both *P. ochrochloron* strains resulted in similar high AgNP yields, but strain dependent differences in the AgNP size. The bio-based NP synthesis is a highly sensitive process where key parameters can be identified to modify unique particle properties.

Funding

This work was funded by the Standortagentur Tirol within the K-Regio Project SUPREMEbyNANO (P7440-016-036 to LC)

List of References

- [1] Bamal D, Singh A, Chaudhary G et al. (2021) Silver Nanoparticles Biosynthesis, Characterization, Antimicrobial Activities, Applications, Cytotoxicity and Safety Issues: An Updated Review. *Nanomaterials* (Basel) 11. <https://doi.org/10.3390/nano11082086>
- [2] Kumar JA, Krithiga T, Manigandan S et al. (2021) A focus to green synthesis of metal/metal based oxide nanoparticles: Various mechanisms and applications towards ecological approach. *Journal of Cleaner Production* 324:129198. <https://doi.org/10.1016/j.jclepro.2021.129198>

- [3] Singh P, Garg A, Pandit S et al. (2018) Antimicrobial Effects of Biogenic Nanoparticles. *Nanomaterials* (Basel) 8. <https://doi.org/10.3390/nano812100>

Biosynthese von Silber- & Goldnanopartikeln basierend auf terrestrischen Mikroalgen

L. Colleselli^{1,*}, C. Griesbeck¹, M. Mutschlechner¹, H. Schöbel¹, P. Vrabl², and S. Zeilinger²

1: Department of Biotechnology and Food Engineering, MCI - The Entrepreneurial School, Austria

2: Institute of Microbiology, Universität Innsbruck, Austria

*Correspondent author: lucia.colleselli@mci.edu

Keywords: Screening, wässriges Extrakt, LED, Lichtinduktion

Metallische Nanopartikel werden in vielfältigen Bereichen des Alltags aufgrund ihrer spezifischen antimikrobiellen, optischen und elektrischen Eigenschaften genutzt [1]. Eine bio-basierte Erzeugung von Nanokomponenten mit hoher Qualität und Biokompatibilität stellt eine umweltfreundliche Alternative zu herkömmlichen physikochemischen Herstellungsverfahren dar [2–6]. Einige Mikroorganismen besitzen die Fähigkeit, toxische Metallionen in ihrer Umgebung durch extra- und intrazelluläre Schutzmechanismen zu reduzieren, wodurch die Formation nanoskalierter Partikel stattfindet [7–9]. Mikroalgen weisen aufgrund ihres einzigartigen Adaptionsverhaltens an Umweltbedingungen und der Bereitstellung wertvoller sekundärmetabolischer bioaktiver Substanzen vielversprechendes Potenzial auf, als Reaktanten in der Nanopartikelproduktion zu agieren [10]. Silber- und Goldnanopartikel gehören zu den prominentesten Vertretern metallischer Nanomaterialien, und es wird global an einer Algenvermittelten Synthese geforscht [11]. Die Erforschung der Mechanismen der biotechnologischen Nanopartikelherstellung steht noch am Anfang, jedoch lässt sich durch physikochemische Parameter, wie beispielsweise Bestrahlung mit Licht, die Synthese signifikant beeinflussen und modifizieren.

In dieser Studie wurden Extrakte aus fünf unterschiedlichen terrestrische Mikroalgenstämmen auf das Potenzial der Reduktion von Silber- und Goldionen zu Nanopartikeln untersucht, und der Einfluss von Bestrahlung mit weißem Licht und dunklen Bedingungen auf die Synthese wurde ermittelt. Die Formation von nanoskaligen Silberpartikeln wurde lichtinduziert erzielt, mit Anzeichen der Nanopartikelgenerierung bei Dunkelheit in Abhängigkeit des Pigmentanteils bei einem der fünf untersuchten Algenextrakte. Dem gegenüber konnten Goldnanopartikeln unter dunklen sowie bestrahlten Synthesebedingungen generiert werden. Die resultierenden Nanomaterialien wurden mittels spektrophotometrischer Analyse, Rasterelektronenmikroskopie und energiedispersiver Röntgenspektroskopie charakterisiert. Die sphärischen Silber- und Goldnanopartikelsuspensionen wiesen spezifische Absorptionsmaxima zwischen 400 nm und 440 nm bzw. zwischen 550 nm und 600 nm auf und zeigten eine Tendenz zur Agglomeration mit ansteigender Synthesedauer sowie unter dem Einfluss von Licht. Aufbauend auf diesen Erkenntnissen wird der Fokus zukünftig auf der Untersuchung von Effekten einer Algenkultivierung unter dem abiotischen Stressfaktor UV-A Licht liegen. UV-A Bestrahlung kann die Carotogenese der Mikroalgen beeinflussen [12]. Daher sollen weitere Erkenntnisse über die Auswirkungen eines veränderten Pigmentgehalts der Algenextrakte auf die Biosynthese von Silber- sowie Goldnanopartikel gewonnen werden.

Funding

This work was funded by the Standortagentur Tirol within the K-Regio Project SUPREMEbyNANO (P7440-016-036 to LC)

List of References

- [1] Patel V, Berthold D, Puranik P et al. (2015) Screening of cyanobacteria and microalgae for their ability to synthesize silver nanoparticles with antibacterial activity. *Biotechnol Rep (Amst)* 5:112–119. <https://doi.org/10.1016/j.btre.2014.12.001>
- [2] Nguyen NTT, Nguyen LM, Nguyen TTT et al. (2022) Recent advances on botanical biosynthesis of nanoparticles for catalytic, water treatment and agricultural applications: A review. *Sci Total Environ* 827:154160. <https://doi.org/10.1016/j.scitotenv.2022.154160>
- [3] Gemishev O, Panayotova M, Gicheva G et al. (2022) Green Synthesis of Stable Spherical Monodisperse Silver Nanoparticles Using a Cell-Free Extract of *Trichoderma reesei*. *Materials (Basel)* 15. <https://doi.org/10.3390/ma15020481>
- [4] Ünlüer N, Gül A, Hameş EE (2023) Statistical optimization and characterization of monodisperse and stable biogenic gold nanoparticle synthesis using *Streptomyces* sp. M137-2. *World J Microbiol Biotechnol* 39:223. <https://doi.org/10.1007/s11274-023-03661-w>
- [5] Singh D, Rathod V, Ningangouda S et al. (2014) Optimization and Characterization of Silver Nanoparticle by Endophytic Fungi *Penicillium* sp. Isolated from *Curcuma longa* (Turmeric) and Application Studies against *MDR E. coli* and *S. aureus*. *Bioinorg Chem Appl* 2014:408021. <https://doi.org/10.1155/2014/408021>
- [6] Li X, Xu H, Chen Z-S et al. (2011) Biosynthesis of Nanoparticles by Microorganisms and Their Applications. *Journal of Nanomaterials* 2011:1–16. <https://doi.org/10.1155/2011/270974>
- [7] Salunke BK, Sawant SS, Lee S-I et al. (2016) Microorganisms as efficient biosystem for the synthesis of metal nanoparticles: current scenario and future possibilities. *World J Microbiol Biotechnol* 32:88. <https://doi.org/10.1007/s11274-016-2044-1>
- [8] Bahrulolom H, Nooraei S, Javanshir N et al. (2021) Green synthesis of metal nanoparticles using microorganisms and their application in the agrifood sector. *J Nanobiotechnology* 19:86. <https://doi.org/10.1186/s12951-021-00834-3>
- [9] Mustapha T, Misni N, Ithnin NR et al. (2022) A Review on Plants and Microorganisms Mediated Synthesis of Silver Nanoparticles, Role of Plants Metabolites and Applications. *Int J Environ Res Public Health* 19. <https://doi.org/10.3390/ijerph19020674>
- [10] Sidorowicz A, Fais G, Casula M et al. (2023) Nanoparticles from Microalgae and Their Biomedical Applications. *Mar Drugs* 21. <https://doi.org/10.3390/md21060352>
- [11] Chaudhary R, Nawaz K, Khan AK et al. (2020) An Overview of the Algae-Mediated Biosynthesis of Nanoparticles and Their Biomedical Applications. *Biomolecules* 10
- [12] Mutschlechner M, Walter A, Colleselli L et al. (2022) Enhancing carotenogenesis in terrestrial microalgae by UV-A light stress. *J Appl Phycol* 34:1943–1955. <https://doi.org/10.1007/s10811-022-02772-5>

Renewables

Presentations

Day 1

A novel two stage bubbling fluidized bed gasification process - Practical Insights from gasification of mixed waste wood fractions

M. Kresta^{1,2*}, D. Weilguni¹, J. Krueger³, A. Hofmann^{1,4}, C. Pfeifer²

1: Josef Ressel Centre for the production of powdered activated carbon from municipal residues, Department of Environmental, Process and Energy Engineering, MCI–The Entrepreneurial School, Universitaetsstrasse 15, 6020 Innsbruck, Austria

2: Institute of Chemical and Energy Engineering, University of Natural Resources and Life Sciences, Gregor-Mendel-Straße 33, 1180 Vienna, Austria

3: Syncraft GmbH, Alte Landstraße 7, 6130 Schwaz, Austria

4: Department of Environmental, Process and Energy Engineering, MCI–The Entrepreneurial School, Universitaetsstrasse 15, 6020 Innsbruck, Austria

* Corresponding author: michael.kresta@mci.edu

Keywords: Gasification, Waste Wood, Bubbling Fluidized Bed, Staged Gasification

Abstract

Biomass gasification is a promising technology for sustainable energy generation, particularly when using waste-derived feedstocks. This study investigates the performance of a two-stage bubbling fluidized bed gasifier operated with regionally sourced waste wood of varying qualities, ranging from construction timber to particleboard-rich furniture waste. Experimental trials at 60 kg/h feed rate showed producer gas calorific values of 3.8 to 4.2 MJ/Nm³, with higher values observed for low-quality furniture waste due to elevated methane content. However, this fraction also exhibited reduced gas yields (1.9 Nm³/kg) and lower cold gas (44.7%) and carbon conversion efficiencies (67.3%) compared to higher quality wood waste (2.3 Nm³/kg, 47.7%, and 84.7%, respectively). The increased ash and nitrogen contents in furniture waste led to operational challenges, including slagging and high tar formation. The lean-bed design of the reactor, combined with staged air and steam injection, enabled temperature control (average 800 °C) and minimized slag formation. The results demonstrate that low-grade waste biomass can be converted into energetically valuable gas, though at the cost of lower efficiency. These findings underscore the need for tailored gasifier designs to optimize the conversion of diverse waste wood streams and support the decentralization of renewable energy systems.

Introduction

Biomass is a versatile energy resource that offers practical solutions for greenhouse gas emissions in energy and industrial sectors. Its utilization has expanded in line with international intentions for both energy transition and circular economy [1]. The IEA sees sustainable biomass as an important building block for the decarbonization of the energy sector in all scenarios of the World Energy Outlook 2024 [2], particularly in areas that are difficult to electrify like industrial process heat. Among the available conversion technologies, biomass gasification can play a significant role due to its high efficiency and flexibility in producing a wide range of energy carriers. [3] Gasification is a thermochemical process, which begins with pyrolysis, where biomass decomposes in the absence of oxygen at temperatures between 300°C and 700°C, resulting in volatile gases, tar, and char. At higher temperatures, between 700°C and 1000°C, and with a controlled supply of air, oxygen, or steam, these components are converted into a producer gas (PG), primarily composed of CO, H₂, CH₄, and CO₂. In contrast to conventional combustion, gasification enables the generation of a PG that can be further processed into electricity, heat, hydrogen, synthetic fuels, or chemical feedstocks. Furthermore, the modularity of gasification systems allows decentralized energy production from regionally available residues. [4] The strengthened sustainability criteria of the legislative act of the European Union: Renewable Energy Directive

III (RED III) [5] promote the local use of biomass by supporting regional value chains. This helps to reduce transport emissions and supports the local economy. Building on this, the future of biomass gasification increasingly lies in the use of waste-based feedstocks such as waste wood (WW), agricultural residues, and other biogenic waste materials. [6]

In line with these objectives, the Josef Ressel Centre for the Production of Powdered Activated Carbon from Municipal Residues is dedicated to advancing the utilization of waste-derived biomass for gasification. Established in 2020 at the Department of Environmental, Process and Energy Engineering at the MCI, the centre focuses on developing a process to produce activated carbon from a by-product of wood gasification—powdered biochar. The core of the research is a gasification system that uses regionally sourced WW, such as post-consumer wood, as a sustainable feedstock. The resulting activated carbon is intended for use in local wastewater treatment to remove trace contaminants like pharmaceutical residues. Given the availability of regional biomass, the centre emphasizes small to medium-scale gasification plants (70 kW_{el} to 3 MW_{el}) [7], which facilitate decentralized energy production with minimal transport requirements. However, these smaller systems face specific challenges, including limited economies of scale and constraints in gas cleaning and process efficiency [7–9]. This underscores the importance of optimizing small-scale gasification technologies for effective and sustainable biomass utilization.

This study demonstrates the feasibility of utilizing WW as a resource in small-scale gasification processes. Over the past five years, the Josef Ressel Centre has conducted extensive research on this topic, focusing on the development and optimization of a gasification technology that effectively converts WW into a energetically valuable PG. The findings presented herein encapsulate the outcomes of this research, highlighting the potential of WW gasification in contributing to sustainable energy solutions.

Materials and Methods

The biomass utilized in this research was sourced from the WW collection area at the municipal recycling center in Innsbruck. The WW was classified into categories A1–AIII according to the Ordinance on Requirements for the Recovery and Disposal of Waste Wood [10]. This classification includes natural and treated wood, including materials containing halogenated organic compounds, without wood preservatives or polychlorinated biphenyls (PCBs). Before utilization, the WW underwent processing. Due to the significant presence of metallic impurities, shredders needed to be used, resulting in a wide particle and shape distribution and frayed, needle-like particles. Over the course of the project, three different fractions of WW were processed: (1) CWW waste wood consisting of construction wood waste. This mainly includes solid wood waste and a small amount of chipboard, however, contaminated with

paints, wood preservatives, etc, mostly AI-AII (2) MWW a mixture of CWW and furniture wastes, consisting of chipboard wastes and solid construction wood wastes, AI-AIII (3) FWW waste wood

consisting mainly of chip board furniture waste, mainly AII-AIII. Figure 1 shows pictures of the three different WW fractions used over the course of the research.



Figure 1: Different WW fraction used in the two stage bubbling fluidized bed gasifier

The novel bubbling fluidized bed gasification reactor was designed based on a two-stage concept, with pyrolysis and gasification occurring in locally separated reactors. This design was based on the experimental floating fixed-bed gasification system, collaboratively developed by MCI and SynCraft GmbH. [11] This two-stage configuration offered several advantages, including reduced pressure drop, prevention of channelling and compaction in the char bed, and the production of low-tar PG. [12] Due to the highly heterogeneous nature of WW, maintaining the stability of the floating fixed-bed became unfeasible. This variability led to issues such as channelling and uneven bed compaction.

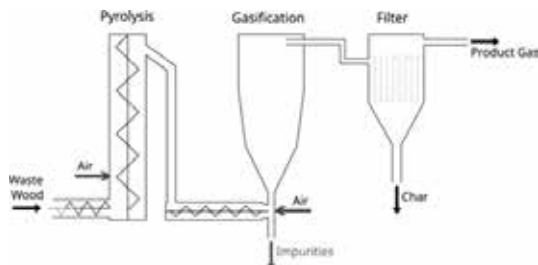


Figure 2: Schematic diagram of the staged gasification process

Consequently, the system was adapted to a fluidized bed configuration, by adjusting the geometry of the reactor with steeper wall angles to accommodate the diverse particle characteristics of WW. Figure 2 shows a schematic layout of the most important process sections. Shredded WW was fed from a container via a sluice system into the pyrolysis unit. This consisted of a vertically aligned auger reactor where particles moved upwards and were pyrolysed simultaneously in an autothermal process. At the top of the pyrolysis gravity caused the pyrolysed particles to fall down into a transport screw, conveying them to the gasification reactor. In the reactor, the pyrolysis products and char particles were entrained and fluidized by the air flow from below. Solid, high-density impurities were separated by gravity and fell out at the bottom of the reactor. The gasification process reduces particle size through thermochemical reactions and abrasion. Reaching a small enough diameter, the

particles were carried out with the PG and separated in the hot gas filter. The collected gasifier char was transferred to a barrel on scales, while the hot PG was sampled for gas composition.

The gasification performance was evaluated using three key indicators: gas yield Y_{gas} , cold gas efficiency (CGE), and carbon conversion efficiency (CCE). Gas yield (Nm^3/kg) quantifies the volume of dry PG generated per kilogram of dry biomass feedstock. CGE (%) is defined as the ratio of the chemical energy in the dry PG to the energy content of the dry feedstock, indicating how efficiently feedstock energy is retained in the gas. CCE (%) measures the fraction of carbon in the biomass that is converted into gaseous carbon species (CO , CO_2 , CH_4), reflecting the extent of carbon utilization.

Results and Discussion

Waste wood characterization

The different WW fractions showed varying elemental and bulk properties. Table 1 shows the characterization based on elemental and proximate composition including the lower heating value H_u (dry). The bulk properties are presented in Table 2. The three WW fractions showed similar carbon and hydrogen contents, which indicated comparable energy potentials. However, the nitrogen and ash contents varied significantly: CWW contained 0.21 % nitrogen and 0.68 % ash, MWW 1.4 % nitrogen and 0.86 % ash, while FWW had the highest values with 3.25 % nitrogen and 2.63 % ash. This could be attributed to the use of nitrogen-containing binders such as urea-formaldehyde resins in chipboard. The high nitrogen and ash content in the FWW lead to challenges in gasification due to the resulting tendency to form slag and high ammonia concentrations in the condensate. As the proportion of particleboard increased from CWW through MWW to FWW, the shredded material yielded progressively finer fragments—evidenced by a d_{50} drop from ~16 mm (CWW) to ~6.3 mm (FWW), a rising share of fines < 8 mm, and a shrinking > 25 mm fraction—which reflects the brittleness and multiple resin-wood interfaces in particleboard. This refinement in particle size enhanced packing efficiency, raising the bulk density from 175 kg/m^3 for CWW to 254 kg/m^3 for FWW.

Table 1: Elemental and proximate composition and lower heating value of WW fraction

Waste wood	wC	wH	wN	wS	W _{ash}	W _{volatile}	W _{fixed carbon}	W _{H2O}	H_u
	/w% (wf)	/w% (wf)	/w% (wf)	/w%	/MJ kg ⁻¹				
CWW	49.9	5.9	0.21	0.032	0.68	81.2	18.1	10.6	18.2
MWW	49.7	6.0	1.4	0.085	0.86	79.3	19.8	8.6	18.5
FWW	48.6	5.8	3.25	0.053	2.63	79.7	17.6	7.0	18.3

Table 2: Bulk properties of WW fractions

Waste wood	ρ_{bulk} /kg m ⁻³	d ₅₀ /mm	<8mm /w%	>25mm /w%
CWW	175.2	15.99	22.7	25.3
MWW	231.2	6.4	29.5	16.3
FWW	254.0	6.33	32.36	18.52

Gasifier development

Fluidized bed gasifiers rely on intense gas–solid mixing and uniform temperatures, achieved by fully suspending an inert bed material (e.g., sand) with the upward gas flow. While this yields high conversion efficiency and consistent PG quality [13], it requires a narrow feed particle size range and substantial energy to keep the bed fluidized [14]—challenges that grow in small- to medium-scale plants using heterogeneous WW, which destabilizes the bed or washes out fines. To overcome these issues, the gasifier concept was modified by eliminating the bed material and using the staged concept with a conical bubbling fluidized bed process. This ‘lean bed’ approach preserved the key advantages of bubbling fluidized beds - strong mixing and temperature uniformity - while allowing the use of highly heterogeneous biomasses like WW.

However, the use of a bubbling bed with low–quality, heterogeneous WW feedstocks made powering gas engines with the PG challenging. Engines require a consistent, high-calorific gas with minimal tars, particulates, and acid gases, necessitating complex cleaning and conditioning systems that add capital and operational costs. Instead, direct thermal utilization of the raw PG was prioritized as high-temperature industrial processes remain heavily dependent on natural gas. PG offers a cleaner combustion profile than burning raw biomass. Using a lean gas burner to supply process heat avoids the stringent gas-treatment requirements of power generation and simplifies plant operation. Out of this reason, the COMET-funded GreenGas developed a multifunctional lean gas burner by DUMAG and BEST in collaboration with SynCraft Engineering GmbH, FRITZ EGGER GmbH & Co OG and Luleå University of Technology, supplying high-temperature industrial heat with the presented pilot plant.

Several operational challenges were encountered during initial commissioning, most notably excessive tar deposition and slag formation in the lower, conical section of the reactor. Slagging was driven by dead zones and localized temperature peaks that caused ash melting and agglomeration. A detailed study of the reactor’s flow regime demonstrated a stable bubbling fluidized bed in the upper section that transitions into fast fluidisation in the constricted lower area—an effect enhanced by the conical geometry, which promotes smooth flow acceleration and uniform fluidization. [15] To mitigate hotspots and prevent slagging, steam was injected and secondary air introduced, flattening the axial temperature profile.

Gasifier performance

In the gasification process, two key parameters could be independently adjusted: the biomass feed rate and the distribution of primary and secondary air flows. In this study, reactor temperature is controlled via the air-to-fuel ratio (λ). Literature indicates that higher gasification temperatures enhance conversion efficiency and PG yield. [16] However, elevated temperatures also increase the risk of slag formation, particularly in the reactor’s lower conical zone. To mitigate this, the reactor’s temperature profile was managed to maintain temperatures below 700 °C in the lower region and prevent exceeding 900 °C in the middle and upper sections. This control strategy results in an average reactor temperature of approximately 800 °C, balancing efficient gasification with the minimization of slag-related issues. Consequently, the biomass feed rate emerged as a pivotal variable influencing gasification performance. Figure 3 illustrates the impact of varying feed rates on key parameters, the lower heating value of the gas LHV, Y_{Gas} , CGE, and CCE, exemplary for the CWW fraction as the medium value of three individual experimental runs.

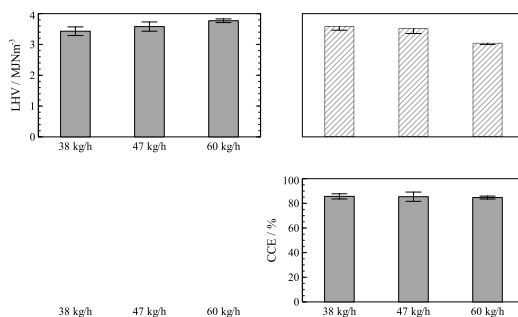


Figure 3: Gasifier performance of CWW at different feeding rates

Increasing the biomass feed rate from 38 kg/h to 60 kg/h elevated the LHV of the PG from 3.4 to 3.8 MJ/Nm³. This improvement stemmed from enhanced thermal efficiency at higher feed. In autothermal gasification, a portion of the biomass is combusted to supply the necessary heat for the endothermic gasification reactions. At lower feed rates, this fixed thermal demand constitutes a larger fraction of the total biomass input, thereby reducing the proportion available for PG production. Consequently, higher feed rates led to a more favorable balance between combustion and gasification, enhancing the overall energy recovery in the form of PG. However, the gas yield remained relatively constant at approximately 2.7 Nm³/kg between 38 and 47 kg/h but declined to 2.3 Nm³/kg at 60 kg/h. To maintain the desired combustion air ratio and reactor temperature at increased biomass throughput, additional air must be introduced, leading to higher gas velocities within the reactor. These elevated velocities reduced the residence time of particles, resulting in incomplete conversion and lower gas yields. This trend was reflected in the CGE, which peaks at 51.6% at 47 kg/h before declining at higher feed rates. Similarly, the CCE decreased with increasing feed rate, underscoring the trade-off between throughput and conversion efficiency in this setup.

Building upon the previous analysis of biomass feed rate effects, the next phase of this study examined the influence of different WW fractions on PG quality. Table 3 presents comparative data from experiments conducted at a consistent feed rate of 60 kg/h, utilizing the three distinct WW fractions. Each dataset represents the average of three experimental runs.

Table 3: Experimental results with different WW fractions at 60kg/h

	CWW	MWW	FWW
$T_{\text{reactor}} / ^\circ\text{C}$	815.0 ± 7.37	808.8 ± 22.8	807.7 ± 7.5
λ_{total}	0.36 ± 0.01	0.34 ± 0.01	0.41 ± 0.01
LHV / MJNm ⁻³	3.8 ± 0.16	3.8 ± 0.13	4.2 ± 0.06
CO / %	14.1 ± 0.20	13.6 ± 0.49	14.5 ± 0.12
CO ₂ / %	14.5 ± 0.31	14.6 ± 0.35	14.1 ± 0.27
CH ₄ / %	1.7 ± 0.09	2.1 ± 0.35	2.7 ± 0.10
H ₂ / %	12.6 ± 0.33	12.1 ± 0.91	12.3 ± 0.07
$Y_{\text{gas}} / \text{Nm}^3\text{kg}^{-1}$	2.3 ± 0.04	2.2 ± 0.05	1.9 ± 0.03
CGE / %	47.7 ± 1.2	44.8 ± 0.57	44.7 ± 0.15
CCE / %	84.7 ± 1.1	70.7 ± 1.0	67.3 ± 0.99

The calorific value of the PG varied only slightly between the fractions. At 4.2 MJ/Nm³, the FWW fraction had a higher calorific value than the other two fractions, due to a higher methane concentration in the PG indicating the lower quality of FWW and its tendency to form tar. The concentrations of CO, CO₂ and H₂ remained similar across all fractions. The observed decrease in gas yield from 2.3 Nm³/kg for CWW to 1.9 Nm³/kg for FWW could be attributed to the physical and chemical properties of the feedstock. FWW, characterized by a higher proportion of fine particles and increased bulk density, tends to require a higher λ to maintain the desired reactor temperature. The resulting higher gas velocities, reduced the residence time of particles within the reactor, thereby

limiting the extent of gasification reactions. Moreover, the higher ash content and presence of additives in FWW contributed to slag formation, further impeding efficient gasification. These combined effects resulted in a lower gas yield compared to feedstocks like CWW. Despite this, when transitioning from CWW to FWW, the CGE remains relatively stable, compensated for the reduced gas volume by increased LHV of the PG. However, the CCE declines with the use of FWW. This reduction was again attributed to the higher proportion of fine particles in FWW.

Pio et al. [17] gives an overview of fluidized bed gasifier performance data in literature. According to the author CGE ranged from 23.5% to 69.0% and CCE between 55.0% and 92.8% for autothermal biomass gasification. The gasification reactor in this study achieved CGE values between 44.7% and 51.6% and CCE values from 67.3% to 84.7% across different WW fractions. These results are notable given the absence of bed material and the challenging nature of the feedstocks used. Furthermore, the LHV of the PG ranged from 3.8 to 4.2 MJ/Nm³, aligning well with the LHV range of 0.1 to 7.8 MJ/Nm³ reported in the literature. The gas yields observed, between 1.9 and 2.3 Nm³/kg, also fall within the typical range reported for bubbling fluidized bed gasifiers. These findings underscore the presented gasification design's capability to efficiently process heterogeneous and low-grade biomass without the need for bed material, maintaining performance metrics comparable to those achieved with higher-quality feedstocks.

Conclusion

This study demonstrates that small-scale gasification of WW fractions of different qualities is technically feasible and can produce a PG suitable for thermal applications in lean gas burners. By adapting the reactor design to a staged, conical bubbling fluidized bed system, stable operation could be maintained despite varying particle characteristics. Although higher biomass feed rates improved the LHV of the gas, they led to lower gas yields and conversion efficiencies due to shorter residence times. Among the tested feedstocks, FWW provided the highest LHV but also presented the greatest operational challenges due to higher nitrogen and ash contents. The performance metrics achieved in this study—such as LHV of the PG of up to 4.2 MJ/Nm³ and CGE between 44–52%—are comparable to values reported in the literature for woody biomass. However, these results were obtained without the use of bed material, in a small-scale system, and using biomass of lower quality, including fractions with high ash and nitrogen contents. This highlights the robustness of the applied reactor design and its suitability for decentralized thermal energy applications based on marginal or waste biomass resources.

Acknowledgement

The financial support by the Austrian Federal Ministry of Labour and Economy, the National Foundation of Research, Technology and Development and the Christian Doppler Research Association as well as the participating companies Syncraft GmbH, Innsbrucker Kommunalbetriebe AG (IBK), Stadtwerke Schwaz (SWS) and Gemeindewerke Telfs (GWT) is gratefully acknowledged.

References

- [1] A. I. Osman et al., "Optimizing biomass pathways to bioenergy and biochar application in electricity generation, biodiesel production, and biohydrogen production," *Environ Chem Lett*, vol. 21, no. 5, pp. 2639–2705, 2023, doi: 10.1007/s10311-023-01613-2.
- [2] International Energy Agency, "World Energy Outlook 2024," International Energy Agency, Paris, 2024. Available: <https://www.iea.org/reports/world-energy-outlook-2024>
- [3] E. Monteiro and S. Ferreira, "Some Perspectives for the Gasification Process in the Energy Transition World Scenario," *Energies*, vol. 16, no. 14, p. 5543, 2023, doi: 10.3390/en16145543.
- [4] D. Fytili and A. Zabaniotou, "Circular Economy Synergistic Opportunities of Decentralized Thermochemical Systems for Bioenergy and Biochar Production Fueled with Agro-industrial Wastes with Environmental Sustainability and Social Acceptance: a Review," *Curr Sustainable Renewable Energy Rep*, vol. 5, no. 2, pp. 150–155, 2018, doi: 10.1007/s40518-018-0109-5.
- [5] The European Parliament and the Council of the European Union, *Directive (EU) 2023/2413 of the European Parliament and of the Council of 18 October 2023 amending Directive (EU) 2018/2001, Regulation (EU) 2018/1999 and Directive 98/70/EC as regards the promotion of energy from renewable sources, and repealing Council Directive (EU) 2015/652*: European Union.
- [6] K. Joshua Abioye, R. Rajamanickam, T. Ogunjinmi, S. Paul, R. Selvasembian, and J. O. Ighalo, "Advancements in biomass waste conversion to sustainable biofuels via gasification," *Chemical Engineering Journal*, vol. 505, p. 159151, 2025, doi: 10.1016/j.cej.2024.159151.
- [7] R. Thomson, P. Kwong, E. Ahmad, and K. Nigam, "Clean syngas from small commercial biomass gasifiers: a review of gasifier development, recent advances and performance evaluation," *International Journal of Hydrogen Energy*, vol. 45, no. 41, pp. 21087–21111, 2020, doi: 10.1016/j.ijhydene.2020.05.160.
- [8] Y. A. Situmorang, Z. Zhao, A. Yoshida, A. Abudula, and G. Guan, "Small-scale biomass gasification systems for power generation (<200 kW class): A review," *Renewable and Sustainable Energy Reviews*, vol. 117, p. 109486, 2020, doi: 10.1016/j.rser.2019.109486.
- [9] S. Heidenreich and P. U. Foscolo, "New concepts in biomass gasification," *Progress in Energy and Combustion Science*, vol. 46, pp. 72–95, 2015, doi: 10.1016/j.pecc.2014.06.002.
- [10] Bundesministerium der Justiz, *AltholzV – Verordnung über Anforderungen an die Verwertung und Beseitigung von Altholz*.
- [11] M. Huber, M. Huemer, A. Hofmann, and S. Dumfort, "Floating-fixed-bed-gasification: From Vision to Reality," *Energy Procedia*, vol. 93, pp. 120–124, 2016, doi: 10.1016/j.egypro.2016.07.159.
- [12] S. Dumfort, M. Huemer, A. Hofmann, M. B. Huber, and J. Krueger, "Tar Decomposition at low Temperatures within staged Gasification Reactors—first Approach towards Mechanisms and Background," *GSTF J Eng Technol*, vol. 3, no. 3, 2015, doi: 10.7603/s40707-014-0024-0.
- [13] F. Scala, Ed., *Fluidized bed technologies for near-zero emission combustion and gasification*. Oxford: WP Woodhead Publ, 2013.
- [14] T. Zhou, S. Yang, Y. Wei, J. Hu, and H. Wang, "Impact of wide particle size distribution on the gasification performance of biomass in a bubbling fluidized bed gasifier," *Renewable Energy*, vol. 148, pp. 534–547, 2020, doi: 10.1016/j.renene.2019.10.059.
- [15] M. Kresta, D. Gurtner, L. Nohel, A. Hofmann, and C. Pfeifer, "Experimental study and characterisation of a novel two stage bubbling fluidised bed gasification process utilising municipal waste wood," *Fuel Processing Technology*, vol. 266, p. 108156, 2024, doi: 10.1016/j.fuproc.2024.108156.
- [16] E. Madadian, V. Orsat, and M. Lefsrud, "Comparative Study of Temperature Impact on Air Gasification of Various Types of Biomass in a Research-Scale Down-draft Reactor," *Energy & Fuels*, vol. 31, no. 4, pp. 4045–4053, 2017, doi: 10.1021/acs.energyfuels.6b03489.
- [17] D. T. Pio, L. Tarelho, and M. Matos, "Characteristics of the gas produced during biomass direct gasification in an autothermal pilot-scale bubbling fluidized bed reactor," *Energy*, vol. 120, pp. 915–928, 2017, doi: 10.1016/j.energy.2016.11.145.

Evaluation of an electrically heated bubbling fluidized bed gasification reactor

T. Brunauer^{1,*}, G. Karte¹, C. Pfeifer¹, T. Pröll¹, T. K. Hann^{1,2}, F. Benedikt¹

1: Institute of Chemical and Energy Engineering, BOKU University, Muthgasse 107/1, A-1190 Vienna, Austria

2: BEST – Bioenergy and Sustainable Technologies GmbH, Inffeldgasse 21b, A-8010 Graz, Austria

* Correspondent author: theresa.brunauer@boku.ac.at

Keywords: electric heating elements, heat transfer, biomass gasification, modeling and simulation

This study examines the thermodynamic aspects of an internally electrically heated fluidized bed gasifier. The reactor design features a vertically installed silicon carbide (SiC) heating element enclosed within a protective tube, positioned inside a bubbling fluidized bed gasifier, which is usually operated with biomass fuel. Heat transfer from the heating element to the protective tube occurs through radiation. The wall-to-bed heat transfer coefficient (α) is determined between the surface of the protective tube and the particles within the fluidized bed. The aim is to analyse the heat transfer properties and the maximum thermal fuel power of the reactor. Through modelling and simulation, the effects of various parameters, such as heat transfer coefficients and heating power on reactor performance are evaluated. The maximum achievable thermal biomass fuel power is estimated based on the supplied electrical heat input. Using electrical energy to supply high temperature heat to the reactor allows for efficient utilization of surplus renewable electricity and may contribute to the decarbonization of industrial processes that rely on gaseous fuels. The results provide a foundation for the further development of electrically heated fluidized bed reactors and highlight their potential for renewable gas production.

Introduction

Fluidized bed gasifiers convert carbonaceous materials, such as biomass or coal into a gas mixture – the product gas respectively synthesis gas (syngas). They are often heated through fossil fuel combustion [1]. A study conducted by the Austrian Energy Agency estimated that, by 2040, the total annual potential of biomass residues available for the production of renewable CH₄ will amount to approximately 20.3 TWh [2]. A significant increase in energy efficiency in the production of renewable gas via thermochemical conversion methods could further increase the renewable CH₄ amount.

One approach enhancing efficiency is to introduce additional energy into the process through electrical heating. Thereby, surplus electricity can be converted to chemical energy in the form of product gas/syngas. Using renewable and sustainable electricity to heat the fluidized bed can thus contribute to industrial decarbonization. Improved temperature and process control is expected for electrically heated gasifiers compared to conventional systems. However, electric supply of high temperature heat in harsh environments such as fluidized bed comes with material and design challenges and electrically heated fluidized beds barely exist [1].

This study will carry out initial evaluations of an electrically heated bubbling fluidized bed (BFB) gasification reactor. Although there are various options for electrification [1], the focus lies on internal Joule heating.

Methodology

An existing bubbling fluidized bed reactor (Figure 1) is planned to be equipped with additional heating elements within the fluidized bed. The aim is to directly and efficiently introduce additional energy into the experimental reactor. Given the limited diameter of the reactor ($d_r = 90$ mm), it will be equipped with a single silicon carbide (SiC) heating element ($d_{he} = 25$ mm), enclosed in a protective tube that is 1.5 times larger ($d_{pt} = 37.5$ mm). The heating element has an immersed length of 250 mm. The cylindrical cross section of the empty reactor is 64 cm². When the heating element, along with its protective tube, is installed, the cross-section of the fluidized bed is

reduced by 17 %, resulting in a new cross-sectional area of 53 cm². The reactor is externally trace heated, to reduce the heat losses due to limited insulation as well as a bed surface-to-volume ratio, using four heating elements attached to the wall surface. The initial calculations assume that these heating elements are sufficient to compensate for the heat losses via the outer surface.

Calcium carbonate (CaCO₃) is used as bed material, with steam ($T_s = 400$ °C) acting as the fluidization and gasification medium. For the reference case, a particle size of $d_p = 350$ μm, a bed temperature of $T_{bed} = 840$ °C and a heating element temperature of $T_{he} = 1200$ °C is selected. The fuel conveyor screw for fuel addition is designed to handle a maximum capacity of 5 kg/h of wood pellets, which are used as the fuel in the initial calculations and correspond to a thermal fuel power of 20 kW. This fuel mass flow can be partially replaced by electric heating.

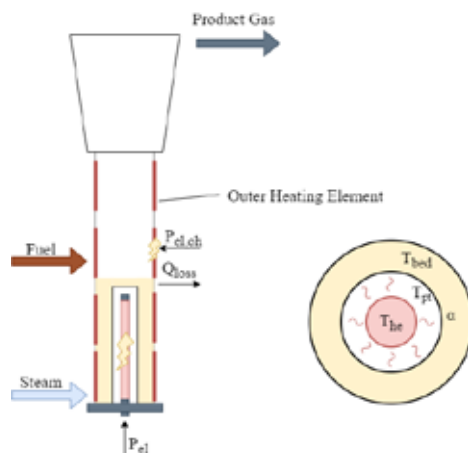


Figure 1: Basic principle of the electrically heated bubbling fluidized bed, with outer heating of the reactor (left) and cross section of the reactor (right).

Heat Transfer

One of the main advantages of fluidized beds is their ability to provide excellent heat transfer and temperature uniformity. An important specification is the surface-to-bed heat transfer (α) as defined in equation (1). The heat transfer coefficient consists of a particle convective component (α_p), a gas convection term (α_g) and a radiative term (α_r). The radiative component is often neglected [3], [4].

$$\alpha = \dot{Q} / (A_{pt} \cdot (T_{st} - T_{bed})) = \alpha_p + \alpha_g + \alpha_r \quad (1)$$

There are different correlations proposed to calculate the heat transfer coefficient in bubbling fluidized beds. Nevertheless, none of them reflects all dependencies [5]. Three common models were selected for the estimation of the heat transfer coefficient and implemented in a Matlab model. The fluid properties are calculated

with CoolProp [6].

The first two models are calculations of the maximum heat transfer coefficient and do not depend on the fluidization velocity. A straightforward solution is proposed by Zabrodsky. His empirical formula depends on the thermal conductivity of the gas, the particle diameter and the particle density [7]. Martin proposes a single particle model, which is based on a conception comparable to the molecular kinetic theory of gases [7]. The third model implemented, is proposed by Molerus et al. It predicts the heat transfer coefficient based on the physical properties and the gas velocity [5].

The heating element primarily transfers heat to the protective tube via radiation. This heat is then transferred from the protective tube to the fluidized bed by thermal conduction. In the calculation model, the thickness of the protective tube is neglected. The electrical power of the heating element can be determined by using equation (2) and equation (3) [3], [8]. For the heating element material, an emissivity of $\epsilon_{he} = 0.9$ is assumed, while for the protection tube, an emissivity of $\epsilon_{pt} = 0.7$ is considered [9].

$$P_{el} = \alpha \cdot A_{pt} \cdot (T_{pt} - T_{bed}) = C_{12} \cdot A_{be} \cdot (T_{be}^4 - T_{pt}^4) \quad (2)$$

$$C_{12} = \sigma / (1/\epsilon_{he} + A_{bed}/A_{pt} \cdot (1/\epsilon_{pt}) - 1) \quad (3)$$

Process Simulation

The process simulation of the biomass steam gasification in the fluidized bed reactor is carried out using the commercial steady-state equation solver IPSEpro. The gasifier model is based on the mass and energy balances formulated by Pröll and Hofbauer [10].

The gasifier model assumes the complete conversion of the fuel, with no combustion occurring. The energy required for the conversion process is supplied entirely by electrical energy. For the simulation, the energy loss through the reactor wall is assumed to be zero (adiabatic reactor), based on the premise that the outer heating can fully compensate for any losses. The simulation is intended as an initial evaluation of the achievable thermal fuel power (P_{th}), based on the lower heating value as seen in equation (4).

$$P_{th} = \dot{m}_f \cdot LHV \quad (4)$$

The cold gas efficiency is defined based on lower heating values and includes the electric heating on the input side as shown in equation (5).

$$\eta_{cg} = (\dot{V}_{a,PG} \cdot LHV_{PG}) / (\dot{m}_f \cdot LHV + P_{el}) \quad (5)$$

The main simulation process parameters for the bubbling fluidized bed gasifier are summarized in Table 1. Fuel composition and product gas composition are derived from the experiments conducted by Mayerhofer et al. [11]. The gasification experiments were carried out with wood pellets in a bubbling fluidized bed at a temperature of 840 °C and a steam-to-fuel ratio of 0.83 [11]. For an initial evaluation of the system, this case of allothermal wood gasification was selected as reference process.

Table 1: Main simulation process parameters [11]

Process parameter	Symbol	Set value	Unit
Bed temperature	T_{bed}	840	°C
Heat loss	Q_{loss}	0	W
Steam-to-fuel ratio	φ_{SF}	0.83	-
Moisture	$W_{H_2O,F}$	4.84	wt.%
Ash content	$W_{Ash,F}$	0.12	wt.% _{db}
Carbon (C)	$W_{C,F}$	49.84	wt.% _{db}
Hydrogen (H)	$W_{H,F}$	6.74	wt.% _{db}
Nitrogen (N)	$W_{N,F}$	0.10	wt.% _{db}
Oxygen (O)	$W_{O,F}$	43.12	wt.% _{db}
Sulphur (S)	$W_{S,F}$	0.08	wt.% _{db}
Hydrogen (H ₂)	$y_{H_2,PG}$	45.8	vol.% db
Carbon dioxide (CO ₂)	$y_{CO_2,PG}$	19.2	vol.% _{db}
Methane (CH ₄)	$y_{CH_4,PG}$	6.9	vol.% _{db}
Tar Content	C_{tar}	4	g/Nm ³ _{db}

The share of CO is not set to not overdetermine the system of equations of the model. Mayerhofer et al. report a CO concentration of 21.1 vol.%_{db}, which is in reasonable agreement with the simulation result of 22.6 vol.%_{db} [11]. The remaining composition is assumed to consist of C₂H₄ in the simulation. For the calculations, tar is modelled as pure naphthalene, which consists of 94 wt.%_{db} carbon (C) and 6 wt.%_{db} hydrogen (H). The product gas composition is close to the equilibrium of the CO shift reaction.

Results and Discussion

The results for the estimation of the heat transfer coefficient (α) using all applied models are presented in Figure 2. From the reference case, ($T_{bed} = 840$ °C, $d_p = 350$ μ m), the effects of varying bed temperature and particle size are examined. Using the equations from Molerus et al., a curve of the fluidization degree u/u_{mf} can be plotted [5]. Additionally, the maximum values for α from the calculations according to Martin and Zabrodsky are provided [7]. The maximum heat transfer coefficient values obtained from the equations by Molerus et al. align closely with those determined using Martins method.

All models indicate that the heat transfer coefficient is influenced by both the temperature and the particle size of CaCO₃. The particle diameter influences the trend of α as a function of u/u_{mf} .

For all particle classes, α increases significantly after reaching the minimum fluidization velocity and then flattens around $u/u_{mf} = 10$. The smaller particles ($d_p = 250$ μ m) achieve α_{max} at $u/u_{mf} > 60$. However, α remains at a comparably high level both in the preceding and subsequent ranges. In contrast, the larger particles ($d_p = 450$ μ m) achieve α_{max} significantly earlier, but then the heat transfer coefficient decreases again at higher u/u_{mf} . For smaller particles, particle convective heat transfer is the prevailing effect, whereas for larger particles, gas convection becomes the dominant factor [5].

On the other hand, the influence of temperature is less significant in the studied range. Increasing the temperature shifts the curve upwards, but the curves overall shape remains unchanged.

As previously mentioned, α increases significantly at $u/u_{mf} > 1$. For this reason, it is important to ensure that the chosen fluidization point allows for sufficient heat transfer performance. For a BFB steam gasification u/u_{mf} is usually in the range of 5 to 10 [12]. Considering larger particles, the optimum operational range regarding α is narrower compared to the reference case.

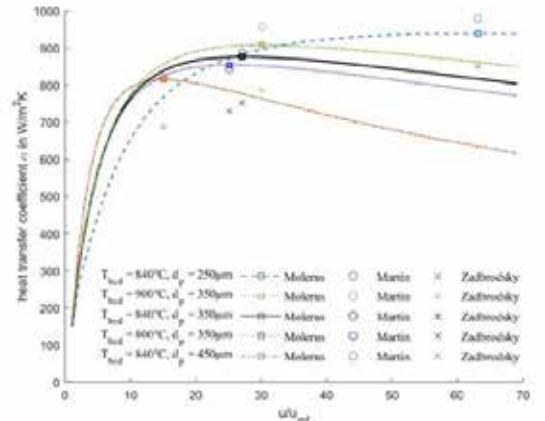


Figure 2: Results of α model according Molerus over u/u_{mf} and α_{max} according to Martin and Zabrodsky.

For the experimental reactor, a heat transfer coefficient in the range of 750 to 850 W/(m²K) can be expected when calcium carbonate is used as bed material. Based on this assumption, the electrical power of the heating element ($T_{he} = 1200$ °C) is calculated by varying the

heat transfer coefficient. The results presented in Table 2 indicate that the power of the heating element decreases as the heat transfer coefficient decreases. Since energy dissipation is more efficient at a higher heat transfer coefficient, the temperature of the protective tube decreases, while the surface load increases. The surface load is defined as the power output per unit area of the heating element surface. If the heat transfer coefficient falls below the expected value, the power output of the system decreases. For instance, at $\alpha = 400 \text{ W/(m}^2\text{K)}$, the system achieves a heat output of only 1.8 kW. Accordingly, an accurate estimation of the heat transfer coefficient is of great importance for the design of the heating elements.

Table 2: Electrical power dependant on α at $T_{bed} = 840 \text{ }^\circ\text{C}$.

Heat transfer coefficient	α	W/(m ² K)	850	800	400
Temperature HE	T_{he}	°C	1200	1200	1200
Electrical power	P_{el}	kW	2.13	2.11	1.80
Surface load	q_s	W/m ²	10.9	10.7	8.9
Temperature PT	T_{pt}	°C	923	927	986

The dependency on the heating element temperature at $\alpha = 800 \text{ W/(m}^2\text{K)}$ and $T_{bed} = 840 \text{ }^\circ\text{C}$ is presented in Table 3. The impact of the temperature difference between the heating element and the bed on the electrical power is considerably more significant. If the heating element temperature is reduced to $1000 \text{ }^\circ\text{C}$, a temperature difference of $160 \text{ }^\circ\text{C}$ between the heating element and the bed results in a power output of less than 1 kW. This means that the heating element temperature and the temperature difference have a significantly greater influence on the power output than the α itself.

Table 3: Electrical power dependant on heating element temperature at $T_{bed} = 840 \text{ }^\circ\text{C}$.

Temperature HE	T_{he}	°C	1200	1100	1000
Heat transfer coefficient	α	W/(m ² K)	800	800	800
Electrical power	P_{el}	kW	2.11	1.35	0.73
Surface load	q_s	W/cm ²	10.7	6.9	3.7
Temperature PT	T_{pt}	°C	927	896	870

It can be deduced that the heating element temperature, and thus the temperature difference to the bed, has a greater influence on the supplied power than changes in the heat transfer coefficient. Nevertheless, an accurate prediction of the heat transfer coefficient is essential for the design of an electrically heated fluidized bed. When selecting the heating element and its protective tube, it is essential to ensure that the chosen materials withstand the operational demands and meet the required specifications.

With knowledge of the heat transfer and the resulting power of the heating element, the electrically heated gasification reactor can be analysed and evaluated using process simulation with IPSEpro. In Table 4, the key results of the simulation are presented. Based on a $u/u_{mf} = 11$ (resulting from the reactor cross-section and the steam demand), a heat transfer coefficient $\alpha = 788 \text{ W/(m}^2\text{K)}$ is assumed (Figure 2). The thermal fuel power is determined using the lower heating value (LHV) and the fuel mass flow rate.

Thus, with an electrical heat input of 2.1 kW, 8.7 kW of thermal fuel power can be converted based on the given LHV. The cold gas efficiency is 0.87. To utilize the full feed capacity (5 kg/h corresponding to 25 kW_{th} in case of the studied pellets) of the conveyor screw, 6 kW of electrical power input from the heater would be required.

Table 4: Key results of the process simulation of the electrically heated gasifier.

Process parameter	Symbol	Result	Unit
Heat transfer coefficient	α	788	W/(m ² K)
Mass flow steam	\dot{m}_{st}	1.3	kg/h
Mass flow fuel	\dot{m}_f	1.75	kg/h
Normal volume flow PG	$\dot{V}_{n,PG}$	3.7	Nm ³ /h
Fluidization	u/u_{mf}	11	
Lower heating value fuel	LHV	17.98	MJ/kg
Lower heating value PG	LHV _{PG}	13.83	MJ/Nm ³
Electrical heat input	P_{el}	2.1	kW
Thermal fuel power	P_{th}	8.7	kW
Cold gas efficiency	η_{cg}	0.87	

Conclusion and Outlook

This study provides a first evaluation of electrically heated bubbling fluidized bed reactors, focusing on their heat transfer properties and thermal performance. The performance of electrically heated bubbling fluidized bed reactors is influenced by several key factors. The heating element temperature plays a critical role, as a higher temperature difference between the heating element and the bed leads to greater specific power output. For instance, reducing the heating element temperature from $1200 \text{ }^\circ\text{C}$ to $1000 \text{ }^\circ\text{C}$ decreases the electrical power from 2.11 kW to 0.73 kW. Additionally, the wall-to-bed heat transfer coefficient is a decisive parameter, with higher α values enabling more efficient heat transfer. The heat transfer coefficient is affected by particle size, fluidization velocity, and bed temperature, with smaller particles and higher fluidization velocities promoting better heat transfer in certain regions. The particle size determines whether particle convection or gas convection dominates. Lastly, achieving an optimal fluidization velocity is essential, as the heat transfer coefficient increases significantly beyond the minimum fluidization velocity. Based on the conducted heat transfer calculations, the potential capacity of an electrically heated pilot-scale allothermal biomass steam gasification reactor is determined. With an installed electric heating power of 2.1 kW, a thermal fuel power of 8.7 kW and a cold gas efficiency of 87 % can be achieved.

Future work should focus on experimental validation of the simulation results. It is important to examine heat transfer more precisely under different operating conditions. An open issue is also the durability of the protective tube during the gasification process and the lifespan of the heating elements.

Optimizing these factors is crucial for maximizing the efficiency and performance of electrically heated fluidized bed reactors, paving the way for their effective application in renewable gas production and industrial decarbonization. By integrating surplus renewable and sustainable electricity into the process, electrically heated fluidized bed reactors might offer a promising pathway for industrial decarbonization and the efficient utilization of biomass residues for renewable energy production.

Acknowledgement

This research was conducted in the course of and funded by the FFG project I/O-Gas (Integration und Optimierung der Produktion von erneuerbarem Gas aus biogenen Reststoffen), FO999915024.

Nomenclature

A_{he}	Surface heating element	m^2
A_{pt}	Surface protection tube	m^2
c_{tar}	Tar content	g/Nm^3
d_{he}	Heating element diameter	m
d_r	Reactor diameter	m
d_p	Particle diameter	m
d_{pt}	Protection tube diameter	m
\dot{m}	Mass flow	kg/h
P_{el}	Electrical power	kW
q_s	Surface load	W/cm^2
T_{bed}	Bed temperature	$^{\circ}C$
T_{he}	Heating element temperature	$^{\circ}C$
T_{pt}	Protection tube temperature	$^{\circ}C$
T_{st}	Steam temperature	$^{\circ}C$
u	Fluidization velocity	m/s
u_{mf}	Minimum fluidization velocity	m/s
\dot{V}_n	Normal Volume Flow	Nm^3/h
w	Mass fraction	$wt\%$
y	Volume fraction	$vol\%$
α	Heat transfer coefficient	$W/(m^2K)$
α_g	Gas convection heat transfer coefficient	$W/(m^2K)$
α_r	Radiation heat transfer coefficient	$W/(m^2K)$
α_p	Particle convection heat transfer coefficient	$W/(m^2K)$
ε	Emissivity of a surface	-
η_{cg}	Cold gas efficiency	-
σ	Stefan-Boltzmann constant	$W/(m^2K^4)$
$\varphi_{S/F}$	Steam-to-fuel ratio	-
BFB	Bubbling fluidized bed	
db	Dry basis	
HE	Heating element	
LHV	Lower heating value fuel (organic, water, ash)	
LHV _{PG}	Lower heating value of the product gas (without organic loadings, water free)	
PG	Product gas	
PT	Protection tube	

References

- [1] I. Ahmed, M. Duchesne, Y. Tan, and D. Y. Lu, 'Electrically Heated Fluidized Beds—A Review', *Ind. Eng. Chem. Res.*, vol. 63, no. 10, pp. 4205–4235, Mar. 2024, doi: 10.1021/acs.iecr.3c04232.
- [2] 'Studie Grünes Gas: AEA - Österreichische Energieagentur'. Accessed: May 01, 2025. [Online]. Available: <https://www.energyagency.at/aktuelles/studie-gruenes-gas>
- [3] E. Tsotsas, 'M5 Wärmetübergang in Wirbelschichten', in *VDI-Wärmeatlas*, P. Stephan, S. Kabelac, M. Kind, D. Mewes, K. Schaber, and T. Wetzel, Eds., in Springer Reference Technik., Berlin, Heidelberg: Springer Berlin Heidelberg, 2019, pp. 1719–1730. doi: 10.1007/978-3-662-52989-8_100.
- [4] J. Grace, X. Bi, and N. Ellis, Eds., *Essentials of Fluidization Technology*, 1st ed. Wiley, 2020. doi: 10.1002/9783527699483.
- [5] O. Molerus, A. Burschka, and S. Dietz, 'Particle migration at solid surfaces and heat transfer in bubbling fluidized beds—II. Prediction of heat transfer in bubbling fluidized beds', *Chem. Eng. Sci.*, vol. 50, no. 5, pp. 879–885, Mar. 1995, doi: 10.1016/0009-2509(94)00446-X.
- [6] I. H. Bell, J. Wronski, S. Quoilin, and V. Lemort, 'Pure and Pseudo-pure Fluid Thermophysical Property Evaluation and the Open-Source Thermophysical Property Library CoolProp', *Ind. Eng. Chem. Res.*, vol. 53, no. 6, pp. 2498–2508, Feb. 2014, doi: 10.1021/ie4033999.
- [7] H. Martin, 'Heat Transfer between Gas Fluidized Beds of Solid Pkticles and the Sutiaces of Immersed Heat Exchanger Elements, Part II'.
- [8] S. Kabelac and D. Vortmeyer, 'K1 Wärmestrahlung technischer Oberflächen', in *VDI-Wärmeatlas*, P. Stephan, S. Kabelac, M. Kind, D. Mewes, K. Schaber, and T. Wetzel, Eds., in Springer Reference Technik., Berlin, Heidelberg: Springer Berlin Heidelberg, 2019, pp. 1183–1199. doi: 10.1007/978-3-662-52989-8_68.
- [9] T. Chun, S. Kim, J. Chung, and H. Lee, 'Numerical study on temperature and thermal stress behaviors in silicon carbide heating elements within high-temperature annealing furnaces', *Appl. Therm. Eng.*, vol. 260, p. 125047, Feb. 2025, doi: 10.1016/j.applthermaleng.2024.125047.
- [10] T. Pröll and H. Hofbauer, 'Development and Application of a Simulation Tool for Biomass Gasification Based Processes', *Int. J. Chem. React. Eng.*, vol. 6, no. 1, Oct. 2008, doi: 10.2202/1542-6580.1769.
- [11] M. Mayerhofer, P. Mitsakis, X. Meng, W. De Jong, H. Spliethoff, and M. Gaderer, 'Influence of pressure, temperature and steam on tar and gas in allothermal fluidized bed gasification', *Fuel*, vol. 99, pp. 204–209, Sep. 2012, doi: 10.1016/j.fuel.2012.04.022.
- [12] J. Karl and T. Pröll, 'Steam gasification of biomass in dual fluidized bed gasifiers: A review', *Renew. Sustain. Energy Rev.*, vol. 98, pp. 64–78, Dec. 2018, doi: 10.1016/j.rser.2018.09.010.

Computational analysis of carbon-neutral biofuels pyrolysis and combustion

Sh. Saberi^{1,2}, C. Spijker¹, Z. Raonic¹, M. Gruber³

1: Chair of Thermal Processing Technology, Montanuniversität Leoben, Franz Josef-Straße 18, 8700 Leoben, Austria

2: Area 2, Decarbonization and Sector Coupling, K1-MET GmbH, Stahlstraße 14, 4020 Linz, Austria

3: RHI Magnesita GmbH, 8700 Leoben, Austria

* Correspondent author: Shekoofeh.saberi@k1-met.com

Keywords: Biomass combustion, carbon-neutral biofuels, CFD modeling, Discrete phase model

Abstract

The growing demand for sustainable energy sources has established biomass as one of the key alternatives to fossil fuels. This study investigates the combustion characteristics of carbon-neutral biofuels using Computational Fluid Dynamics (CFD). A detailed multiphase combustion model was developed in ANSYS Fluent to simulate the thermal degradation processes of carbon-neutral particles in a non-premixed flame environment, including drying, pyrolysis, and char oxidation. The model incorporates experimentally derived kinetic parameters and tracks particle behavior and the evolution of gas-phase species. Results reveal a staged mass loss pattern associated with moisture evaporation, volatile release, and char oxidation, accompanied by the production of major combustion gases such as CO, CO₂, CH₄, and H₂O. The simulations reveal a noticeable cooling effect due to endothermic processes and provide valuable insights into the feasibility of carbon-neutral biomass as a renewable fuel. These findings contribute to the optimization of biomass combustion systems and the development of efficient low-emission energy technologies.

1. Introduction

The global transition toward renewable energy is driven by the urgent need to reduce greenhouse gas emissions and decrease reliance on fossil fuels. Among the various renewable options, biomass offers unique advantages as a carbon-neutral, widely available, and dispatchable energy source. Biomass can be derived from agricultural waste, forestry residues, or dedicated energy crops, making it an essential part of sustainable energy systems. In particular, agricultural byproducts such as biological substitution fuels have attracted growing attention for their potential as solid biofuels. These residues are not only abundant and cost-effective, but also exhibit favorable thermochemical properties, such as high volatile content and low ash fraction, which make them suitable for clean and efficient energy conversion [1].

Using carbon-neutral biofuels in combustion systems contributes to waste reduction and supports circular economy goals. However, to fully harness their energy potential, it is important to understand thermal degradation behavior, including key processes such as drying, pyrolysis, and char oxidation. These processes are strongly influenced by the material's composition, structure, and operating conditions within the combustion system [2]. Compared to more extensively studied fuels like wood pellets, biological substitution fuels are less represented in the literature, and their combustion behavior under realistic conditions remains relatively underexplored.

Due to the complex nature of biomass combustion—characterized by coupled heat transfer, chemical reactions, and mass transport between the phases—experimental investigations are often difficult, expensive, and limited in scope. As a result, Computational Fluid Dynamics (CFD) has become an increasingly valuable tool for simulating and analyzing biomass combustion processes. CFD models enable detailed predictions of temperature distribution, species concentrations, and reaction rates, providing insights that are difficult to obtain through experiments alone [3], [4].

CFD has been widely applied to assess both small-scale systems and industrial biomass boilers, particularly for fuels like wood pellets, olive stones, and almond shells [3]. These models help

optimize combustion chamber design and air supply strategies, which are critical for enhancing thermal efficiency and reducing emissions of CO, NO_x, and unburned hydrocarbons [4]. Furthermore, open-source and commercial CFD tools allow researchers to evaluate different combustion regimes and reactor geometries under variable conditions, which would otherwise require extensive physical prototyping [2].

Although previous studies have explored the behavior of lignocellulosic biomass in updraft and fixed-bed reactors, carbon-neutral biofuels remain underrepresented in numerical modeling efforts. Their use as fuel in CFD simulations is a relevant step toward assessing practical viability and understanding the specific parameters that affect performance in real-world systems. CFD-based analysis combined with thermogravimetric and spectroscopic data can also reveal the formation of intermediate species and emissions during pyrolysis [1], which is essential for evaluating environmental impacts and optimizing process conditions.

This study presents a CFD-based investigation into the combustion characteristics of carbon-neutral biomass fuels in a non-premixed flame environment. A detailed multiphase model was developed using ANSYS Fluent, where biomass particles undergo drying, pyrolysis, and char oxidation. The model incorporates experimentally derived kinetic parameters and simulates the thermochemical conversion process under realistic combustion conditions. The simulations focus on temperature distribution, gas species evolution, and energy release during combustion.

The results provide new insights into the behavior of carbon-neutral biomass as a renewable fuel and demonstrate its feasibility for sustainable energy applications. This work contributes to ongoing efforts to improve biomass combustion systems, reduce environmental impacts, and support the development of cleaner and more efficient energy technologies.

2. Methods

This study utilizes Computational Fluid Dynamics (CFD) modeling to investigate the thermal degradation and combustion characteristics of carbon-neutral biofuel in a non-premixed combustion setup. The simulations are conducted using ANSYS Fluent, incorporating advanced turbulence and combustion models alongside user-defined functions (UDFs) to account for the specific behavior of biomass particles.

2.1 Geometry and computational domain

The computational domain represents an axisymmetric combustion chamber with dimensions of 1.6 m in length and 0.4 m in width. The boundary domain consists of the pilot flame, jet injector, coflow, outlet, and rotational axis. The coflow was later excluded in post-processing due to its observed cooling effect on particle temperatures.

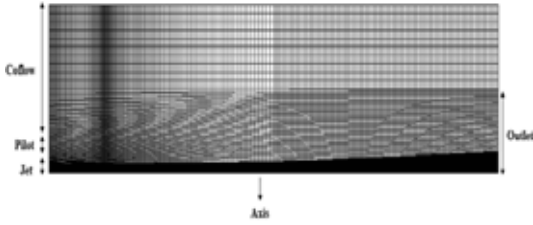


Figure 1. Geometry of the combustion chamber

2.2 Turbulence and combustion modeling

Flow turbulence was simulated using the standard $k-\epsilon$ model with standard wall functions [5]. Combustion reactions were modeled using the Eddy Dissipation Concept (EDC) [6], which couples turbulence and chemical reaction rates. DRM-19 [7] the reaction mechanism was applied, suitable for hydrocarbon combustion, including light volatiles released during pyrolysis.

2.3 Particle injection and composition

Carbon-neutral biofuels were modeled as multicomponent particles, injected into the domain with the following mass fractions:

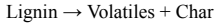
- Lignin (volatile compounds + char): 90.7%
- H₂O (moisture): 6.5%
- Ash: 2.8%

These components undergo sequential thermal processes, including drying, pyrolysis, and char oxidation, as the particle moves through the combustion zone. During combustion, the lignin component decomposed into various gaseous products, including: H₂O (g), CO, CO₂, CH₄, and Char (solid carbon).

2.4 Thermal conversion reactions

a. Pyrolysis

Pyrolysis is the thermal decomposition of lignin components in the absence of oxygen, resulting in the release of volatiles and the formation of solid char. It is represented by:



The rate of pyrolysis was modeled as a temperature- and composition-dependent reaction, expressed as:

$$R_{\text{pyr}} = A \cdot \exp\left(-\frac{T_a}{T_p}\right) \cdot X_{\text{Lignin}}^n \cdot m_p$$

where T_p is the particle temperature, X_{Lignin} is the lignin mass fraction, and m_p is the particle mass. The model uses a pre-exponential factor $A = e^{13.1}$, activation temperature $T_a = 10748$ K, and reaction order $n = 2$. This form allows for a more physically representative pyrolysis behavior by linking the rate to both temperature and the remaining volatile material in the particle.

b. Drying

Drying is modeled as a thermal phase-change process triggered when the particle temperature T_p exceeds the boiling point of water (373 K). The mass of evaporated moisture m_{evp} is calculated from the available heat above the boiling point within the time step:

$$h_{\text{evp}} = (T_p - T_{\text{boil}}) \cdot m_p \cdot C_p$$

$$m_{\text{evp}} = \frac{h_{\text{evp}}}{(h_{\text{lat}}) \cdot \Delta T}$$

Where:

- h_{evp} : Sensible heat used for evaporation [J]
- m_{evp} : Water mass evaporated during the time step [kg/s]

- T_p : Particle temperature [K]
- $T_{\text{boil}} = 373$ K: Boiling point of water
- m_p : Particle mass [kg]
- C_p : Particle heat capacity [J/kg·K]
- Time step [s]
- $h_{\text{lat}} = 2.2564 \times 10^6$ J/kg: Latent heat of vaporization

c. Char reactions

The residual char formed during pyrolysis undergoes heterogeneous gas–solid reactions with gas-phase species such as CO₂, H₂O, and H₂. The following reactions are considered [8]:

- Reaction 1 (Boudouard reaction): $\text{C(s)} + \text{CO}_2 \rightarrow 2\text{CO}$

$$R_{\text{BR}} = A_{\text{BR}} e^{-\frac{E_{a,\text{BR}}}{RT}} \left(\frac{Y_{\text{CO}_2}}{M_{\text{CO}_2}} - \frac{Y_{\text{CO}}}{M_{\text{CO}} K_{\text{BR}}} \right) \rho_g RT$$

- Reaction 2 (Water-gas reaction): $\text{C(s)} + \text{H}_2\text{O} \rightarrow \text{H}_2 + \text{CO}$

$$R_{\text{HW}} = A_{\text{HW}} e^{-\frac{E_{a,\text{HW}}}{RT}} \left(\frac{Y_{\text{H}_2\text{O}}}{M_{\text{H}_2\text{O}}} - \frac{Y_{\text{CO}} Y_{\text{H}_2}}{M_{\text{CO}} M_{\text{H}_2} K_{\text{HW}}} \right) \rho_g RT$$

- Reaction 3 (Methanation): $\text{C(s)} + 2\text{H}_2 \rightarrow \text{CH}_4$

$$R_{\text{M}} = A_{\text{M}} e^{-\frac{E_{a,\text{M}}}{RT}} \left(\left(\frac{Y_{\text{H}_2}}{M_{\text{H}_2}} \right)^2 \rho_g RT - \frac{Y_{\text{CH}_4}}{M_{\text{CH}_4} K_{\text{M}}} \right)$$

- A : Pre-exponential factor (reaction constant)
- E_a : Activation energy [J/mol]
- R : Universal gas constant [J/mol·K]
- T : Temperature [K]
- Y_i : Species mass fraction in the gas phase
- M_i : Molecular weight [kg/kmol]
- K : Equilibrium constant
- ρ_g : Gas density [kg/m³]

3. Results and Discussion

The initial flame temperature, measured before particle injection, served as a reference for evaluating the thermal impact of the injected carbon-neutral particles. After the injection and subsequent pyrolysis, drying, and char conversion reactions, the flame temperature showed a noticeable decrease. This cooling effect can be attributed to two factors:

- The endothermic nature of the drying and devolatilization processes.
- Evaporation of moisture in the biomass consumes a significant amount of thermal energy.

Furthermore, the co-flow effect was intentionally excluded in this simulation to avoid its influence on the particle temperatures due to the cooling effect. This decision enables better isolation and analysis of the particle reaction effects. Figure 2 shows the comparison of flame temperature before and after biofuels injection, highlighting the thermal impact of drying and devolatilization.

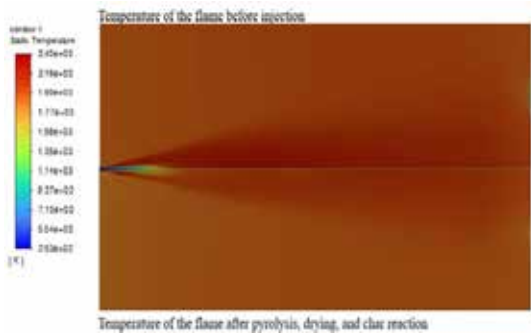


Figure 2. Flame temperature before and after particle injection

Following the injection, the particle temperature increased rapidly due to heat transfer from the surrounding hot gas, reaching levels sufficient for drying and pyrolysis. This thermal behavior, well captured by the implemented heat and mass transfer model, coincided with a steady decline in particle mass driven by moisture evaporation, volatile release, and progressive char consumption through gas–solid reactions. Figures 3 and 4 illustrate the particle temperature and particle mass, respectively.

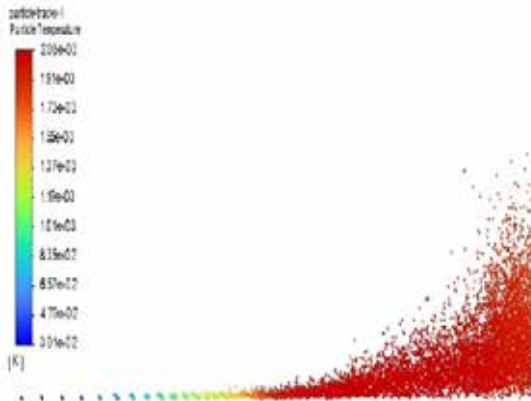


Figure 3. Particle temperature

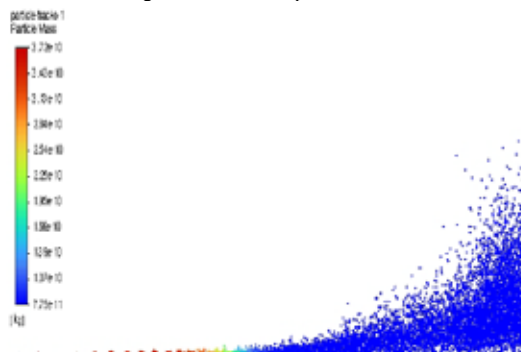


Figure 4. Particle mass

conversion. Char continued to decrease through surface reactions with CO_2 , H_2O , and H_2 . Ash stayed constant because it was considered non-reactive. The mass fractions of each particle component are shown in the Figures below.

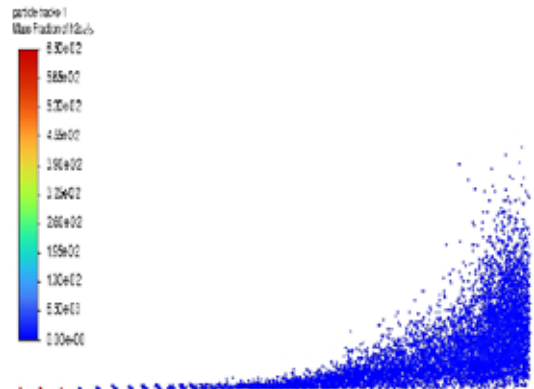


Figure 5. Water mass fraction

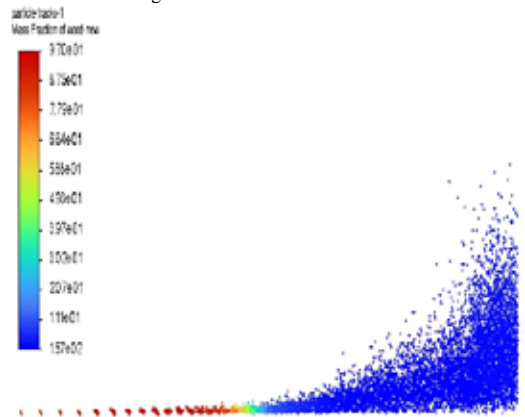


Figure 6. Lignin mass fraction

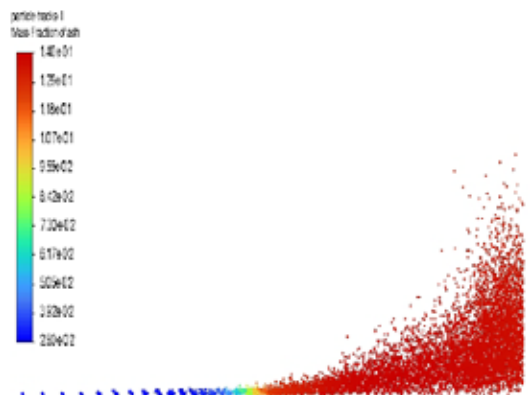


Figure 7. Ash mass fraction

The evolution of each particle component was monitored in the simulation. Water content decreased sharply once the temperature went above the boiling point (373 K) since part of the heat was used for evaporation, which slightly delayed the start of pyrolysis. The lignin component (volatiles + char) showed a two-stage decrease, first due to volatile release, then a slower reduction from char

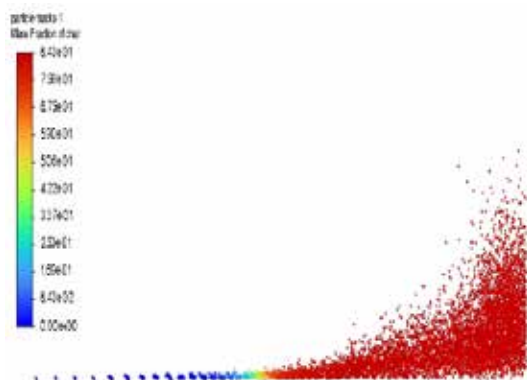


Figure 8. Char mass fraction

4. Conclusion

This study employed CFD modeling to investigate the combustion behavior of carbon-neutral biofuels. The results demonstrated their potential as a viable alternative energy source. After injection, the particles heated up rapidly, which led to moisture evaporation, pyrolysis, and char reactions.

The particle mass decreased in stages: initially due to water loss, followed by volatile release, and finally from char consumption. Gas species like CO, CO₂, CH₄, and H₂O were produced in amounts consistent with those reported in the literature [9], confirming that the reaction models worked well.

Overall, biological substitute fuels demonstrated strong potential as a renewable energy source. The simulation provided valuable insights into their combustion behavior and energy release mechanisms. Future work will focus on experimental validation and the incorporation of additional physical effects, such as radiation, to improve the model further.

5. Acknowledgements

The authors gratefully acknowledge the financial support provided by K1-MET GmbH, the metallurgical competence center. This research was conducted within the framework of the K1-MET Competence Center, funded under the COMET – Competence Centers for Excellent Technologies – program by the Austrian Federal Ministry for Climate Action, Environment, Energy, Mobility, Innovation and Technology, and the Federal Ministry for Digital and Economic Affairs.

5. References

- [1] J. Silva, S. Teixeira, and J. Teixeira, “A Review of Biomass Thermal Analysis, Kinetics and Product Distribution for Combustion Modeling: From the Micro to Macro Perspective,” Sep. 01, 2023, *Multidisciplinary Digital Publishing Institute (MDPI)*. doi: 10.3390/en16186705.
- [2] G. García-Sánchez, J. Chacón-Velasco, D. Fuentes-Díaz, J. Jaramillo-Ibarra, and J. Martínez-Morales, “CFD modelling of biomass boilers - a review of the state of the art,” *Respuestas*, vol. 25, no. 3, Sep. 2020, doi: 10.22463/0122820x.2462.
- [3] G. F. García Sánchez *et al.*, “Biomass Combustion Modeling Using OpenFOAM: Development of a Simple Computational Model and Study of the Combustion Performance of Lippia origanoides Bagasse,” *Energies (Basel)*, vol. 16, no. 6, Mar. 2023, doi: 10.3390/en16062932.
- [4] S. Khelifi, M. Lajili, P. Perré, and V. Pozzobon, “A Numerical Study of Turbulent Combustion of a Lignocellulosic Gas Mixture in an Updraft Fixed Bed Reactor,” *Sustainability (Switzerland)*, vol. 14, no. 24, Dec.

2022, doi: 10.3390/su142416587.

- [5] B. E. Launder and D. B. Spalding, “THE NUMERICAL COMPUTATION OF TURBULENT FLOWS,” 1974.
- [6] B. F. Magnussen, “On the structure of turbulence and a generalized eddy dissipation concept for chemical reaction in turbulent flow,” *American Institute of Aeronautics and Astronautics, Aerospace Sciences Meeting*, vol. 7, pp. 12–15, Jan. 1981.
- [7] Kazakov A and Frenklach M, “DRM19,” <http://www.me.berkeley.edu/drm/>.
- [8] Y. Wang and C. M. Kinoshita, “KINETIC MODEL OF BIOMASS GASIFICATION,” 1993.
- [9] W. C. Park, A. Atreya, and H. R. Baum, “Experimental and theoretical investigation of heat and mass transfer processes during wood pyrolysis,” *Combust Flame*, vol. 157, no. 3, pp. 481–494, Mar. 2010, doi: 10.1016/j.combustflame.2009.10.006.

Simulation of a novel steam gasification process with in-situ char separation via an overflow pipe to generate negative emission syngas from biomass

T. Rasl^{1*}, G. Karte¹, T. Hannl^{1,2}, T. Pröll¹, C. Pfeifer¹, F. Benedikt¹

1: Institute of Chemical and Energy Engineering, BOKU University, Muthgasse 107/I, A-1190 Vienna, Austria

2: BEST – Bioenergy and Sustainable Technologies GmbH, Inffeldgasse 21b, A-8010 Graz, Austria

* Correspondent author: Gregor.karte@boku.ac.at

Keywords: Sorption enhanced gasification (SEG), Electric heating, Negative emissions, Biochar

Abstract

This sorption enhanced gasification (SEG) concept with an inherent carbon sink is an advancement of the classical SEG process in a dual fluidized bed (DFB) steam gasification process consisting of a gasification and a combustion reactor. The classical reactor design employs limestone to capture CO₂ from the product gas during the gasification of biomass, which enhances the hydrogen (H₂) concentration in the product gas, making it more suitable for most downstream synthesis applications. Whereas this adaptation additionally integrates an overflow pipe for separating the carbon.

About 50 % of the fuel carbon content is found in the remaining char, which can be separated in the gasification reactor based on density differences. In the proposed concept, the char is led out of the process via an overflow pipe. The heat required to sustain the gasification reactions, typically provided by the char combustion taking place in the combustion reactor, is instead supplied by electrical heating elements in the combustion reactor. This design leverages surplus energy from the electricity grid, allowing the system to utilize fluctuating renewable energy sources to power these heating elements.

Mass and energy balances of the novel concept were calculated for a pilot plant with 150 kW fuel power input based on the lower heating value. At maximum char separation rate, the system requires 65 kW of electrical power. However, the overall efficiency of the system decreases as the chemical energy in the separated char remains unreleased. Even without CO₂ separation, 16.8 kW of electrical heating is necessary to sustain the endothermic devolatilization and steam gasification reactions. At a 100 % char separation rate, 0.33 kg of carbon in the char can be recovered per kg of carbon in the biomass. This corresponds to a cold gas efficiency of 49.6 % and a remaining carbon content in the flue gas of 0.26 kg per kg of biomass.

Introduction

The steady rise in global energy consumption has been accompanied by a corresponding increase in CO₂ levels in the atmosphere. To mitigate this trend, key technologies such as renewable energy systems including photovoltaics, wind turbines, and biomass play a crucial role in reducing CO₂ emissions. In particular, sustainably grown biomass offers unique opportunities for capturing CO₂ from the atmosphere, enabling the achievement of negative emissions [1].

The sorption enhanced gasification (SEG) process is based on the dual fluidized bed (DFB) gasification, in which gasification and the combustion take place in two separate reactors. In the gasification reactor (GR) the biomass is converted into product gas (PG) using steam to generate a PG with minimal N₂ content. The biomass undergoes drying, devolatilization and gasification, whereby volatile gas fractions are released in the form of PG. The energy demand for drying, devolatilization and gasification is provided by the bed material, which is heated in the combustion reactor (CR) through combustion of the remaining char of the gasification process. Unlike conventional DFB gasification, which employs inert bed materials

that do not significantly chemically react in the GR, the SEG process utilizes bed materials suitable for CO₂ chemisorption, such as limestone, to enhance the process by capturing CO₂ in the GR and releasing it in the CR [2]. The CO₂ removal additionally leads to an increased H₂ content in the PG that can be explained by a shift of the equilibrium composition according to the water-gas shift reaction [3]. This process results in a product gas with a lower CO₂ content compared to that produced by conventional DFB steam gasification. The CO₂ released in the CR is carried out of the combustion reactor via the FG. In both the classical DFB gasification and SEG processes, CO₂ is emitted via the flue gas and the product gas.

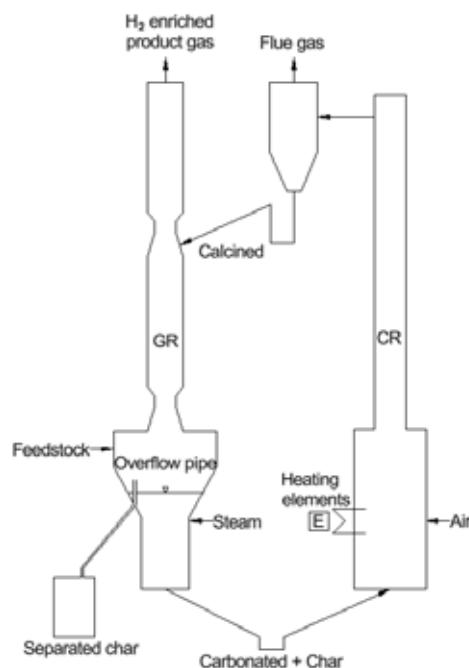


Figure 1: Schematic diagram of the SEG reactor with in-situ char separation

The proposed novel SEG reactor, however, partially replaces the use of char as a heat source with an electric heating system installed at the CR, as shown in Figure 1. By utilizing surplus electricity generated from renewable energy sources, the electric heating system meets the thermal requirements of the GR while enabling the separation and potential sequestration of char, yielding negative CO₂ emissions. The separation of the bed material and char in the GR is achieved based on their density differences. The floating char is drained from the GR via an overflow pipe. However, the char could also be separated in an external reactor located between GR and CR, similarly to carbon strippers in chemical looping combustion systems [4].

The wall-to-bed heat transfer coefficient is significantly higher in a bubbling fluidized bed than in a circulating fluidized bed reactor [5]. Therefore, to ensure efficient heat transfer from the heating elements to the bed material, a larger cross-section is incorporated at the bottom of the CR which is operated in the bubbling regime. This design provides sufficient space to integrate the required heat transfer surface.

Methodology

The simulation of the novel SEG system is performed using IPSEpro, an equation-oriented flowsheet simulation solver. The process model comprises mass and energy balances of the two reactors (unit models) which are connected with each other via solid streams. The model is on the one hand used to set the dimensions of the reactors, on the other hand the implications of the integration of the electric heat source shall be studied. The volume flows resulting from the simulation are used to calculate the cross-sections of the different reactors based on fluidization criteria from literature. Furthermore, the fluidization points of the in- and output of the gasification reactor as well as the output of the combustion reactor are drawn in a Grace diagram [6] to show in which regime the different reactors operate. Equations to calculate the dimensionless numbers describing the fluidized gas-solid system were taken from Schmid [7].

The composition of the product gas is determined as a function of temperature, based on data from [3][8], while the lower heating value (LHV) of the biomass feedstock is calculated using its composition based on softwood from [8]. The heat loss of the reactor is estimated based on [8]. The main set parameters for the simulation are shown in Table 1.

Table 1: Set process parameters for calculation of mass and energy balances

Process parameter	Symbol	Set value	Unit
Fuel power of biomass	P_{BM}	150	kW
Biomass moisture content	W_{H_2O}	7.2	wt. %
Steam to fuel ratio GR	φ_{SF}	0.4	kg/kg
Temperature GR	T_{GR}	700	°C
Steam temperature input	T_{Steam_GR}	450	°C
Temperature CR	T_{CR}	900	°C
CR superficial velocity	v_{CR}	5	m/s
Air temperature input	T_{Air_CR}	450	°C
Overall thermal loss	\dot{Q}_{loss_total}	30	kW
Air–fuel equivalence ratio	λ	1.15	-
Char output gasifier	\dot{m}_{char_GR}	5.63	kg/h

The reactor is assumed to operate with softwood pellets at 150 kW fuel power input based on the LHV, fed into the GR. The impact of the char separation rate is studied by varying it incrementally from 0 % to 100 %. No char separation (0 %) represents the classical SEG operation, where the total amount of residual char exiting the GR is burnt in the CR. 100 % char separation indicates the ideal case that all char exiting the GR is separated and no char is burnt in the CR.

The fraction of biomass converted to PG is assumed to be independent of the char separation efficiency. Due to the variation of the char separation, different flue gas volume flows result and therefore different superficial velocities in the CR. If the air supply to the combustion reactor is controlled to keep the air–fuel equivalence ratio constant, the superficial velocity in the CR is at the limit for the turbulent fluidization at 85 % char separation efficiency.

This results in an upper limit of the operation range where it cannot be ensured that the particles are sufficiently entrained out of the CR to ensure circulation.

To ensure continuous operation, the superficial velocity in the CR within the model is maintained constant at 5 m/s. At 0% char separation rate, a minimum air–fuel equivalence ratio of 1.15 is set, as the entire char mass flow is transported to the CR. As the char separation efficiency increases, the air–fuel equivalence ratio also rises because the airflow is adjusted to maintain the set velocity in the CR. In an industrial application, the gas velocity in the CR could be kept constant via recirculation of flue gas to keep the CO₂ concentration high in the FG for potential CO₂ separation. In oxyfuel mode (char combustion with pure oxygen), a concentrated CO₂ stream would be emitted. The amount of CO₂ chemically bound in limestone in the gasification reactor is limited by the equilibrium of partial pressure of CO₂.

Relevant key performance indicators (KPIs) to describe the process efficiency are introduced in the following. If the cold gas efficiency is calculated in the classical way, it fails to account for the additional electrical energy required to replace the separated char. This omission would result in artificially high cold gas efficiency values that would not accurately reflect the actual performance of the process. As a result, the equation has been adjusted in a way to consider the electrical power according to Eq. 1.

$$\eta_{CGEel} = \frac{P_{PG}}{P_{BM} + P_{el}} \cdot 100 \quad \text{Equation 1 Cold gas efficiency}$$

The carbon separation efficiency of char in Eq. 2 indicates how much carbon is captured in relation to the carbon that is available in the fuel. A higher separation efficiency indicates that more carbon is captured, since the carbon in the biomass is assumed to be constant.

$$\eta_{C,sep} = \frac{\dot{m}_{c,char,sep}}{\dot{m}_{c,BM}} \quad \text{Equation 2 Carbon separation efficiency of char}$$

Eq. 3 defines the share of carbon exiting via the FG, considering the changes in char feed to the CR due to the separation of carbon in the GR and the CO₂ released through calcination of the bed material in the CR.

$$\eta_{C,FG} = \frac{\dot{m}_{c,FG}}{\dot{m}_{c,BM}} \quad \text{Equation 3 Carbon separation efficiency of FG}$$

Furthermore, Eq. 4 defines the relative electrical energy demand required for the biomass conversion process.

$$\phi_{el} = \frac{P_{el}}{P_{BM}} \quad \text{Equation 4 Electricity to fuel ratio}$$

Results & Discussion

Using the process parameters from Table 1 and the criteria outlined in [9], the actual diameters and the U/U_{mf} ratios occurring in the process were calculated based on the volume flows from the simulation. The volume flows of the different fluids are calculated at 1 bar absolute pressure and the respective temperature of the reactors.

Table 2: Results of the simulation in IPSEpro

Parameter	Unit	GR in	GR out	CR out
Fluid	-	Steam	PG	FG
Diameter	m	0.2	0.2	0.125
Volume flow	Nm ³ /h	11.8	35.2	60.9
U/U_{mf} criteria	-	5-10	5-10	-
U/U_{mf} calculated	-	8.1	19.9	-
Velocity criteria	m/s	-	-	4-8
Velocity calculated	m/s	-	-	5.00

Table 2 shows the volumetric flow rates at the inlet and outlet of the GR, as well as at the outlet of the CR, plotted in a Grace diagram to illustrate the operating regime (Figure 2). The inlet and outlet of the gasification reactor were calculated with the different fluids according to Figure 2 and lie within the bubbling fluidization regime. Through the gasification of the biomass the volatile components emerge, which increases the volume flow. The CR lies on the border to the fast fluidization regime. As comparably low solid circulation rates are required in the SEG process, the CR fluidization being on the lower edge of the fast-fluidized bed regime seems reasonable.

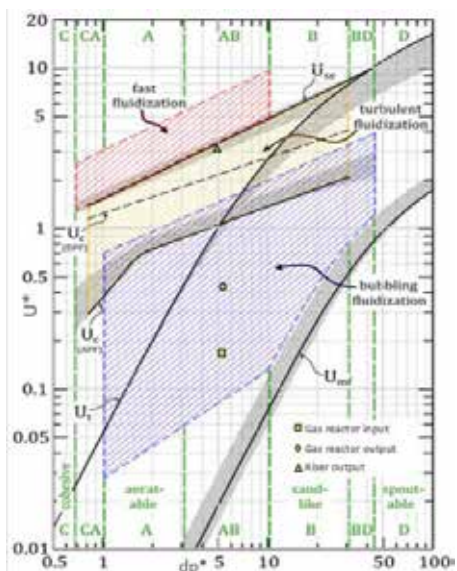


Figure 2: Grace diagram to show the fluidization regimes in the investigated reactor system

As the degree of char capture increases, along with the C bound within it, more electrical heating is required to compensate for the heat previously provided by the char to the bed material. However, as the demand for additional heating rises, the overall efficiency of the system decreases.

Figure 3 shows how the cold gas efficiency is related to the char separation rate of the GR. With the increasing separation rate, more electricity is required to compensate for the lower amount of char burnt in the CR. At 0 % separation efficiency a cold gas efficiency of 63.9 % can be observed. It should be mentioned that even when no char is separated, an additional electric heat demand of 16.8 kW is required to maintain the endothermic reactions in the GR and to compensate for the heat losses of the simulated pilot plant. In this case, the additional heating demand is covered by electric heating elements. However, the heating requirement could also be covered with additional fuel, but the resulting CO₂ would produce additional emissions or would increase the energy demand of a downstream CO₂ capture step. With a maximum electrical output of the heating elements of 65 kW and a 100 % char separation rate, the cold gas efficiency decreases to 49.6 %. Compared to 0 % separation rate, a difference of 14.3 % in cold gas efficiency can be observed. Therefore, with an increase in electrical power a higher separation rate can be achieved which results in a lower cold gas efficiency. The carbon separation efficiency in the flue gas is steadily decreasing with an increase of the electricity to fuel ratio. At 100 % separation rate an electricity-to-fuel ratio of 0.43 results in 0.28 kg carbon exiting via the flue gas per kilogram carbon input as biomass. At 0 % separation efficiency this value increases to 0.61 kg due to the carbon released via char combustion.

At the same time at 100 % char separation rate 0.33 kg carbon per kg carbon in the biomass can be separated via the char. As the char separation rate decreases, the amount of carbon captured in the form of char per kilogram of biomass also decreases. At 0 % char separation rate, no carbon is captured.

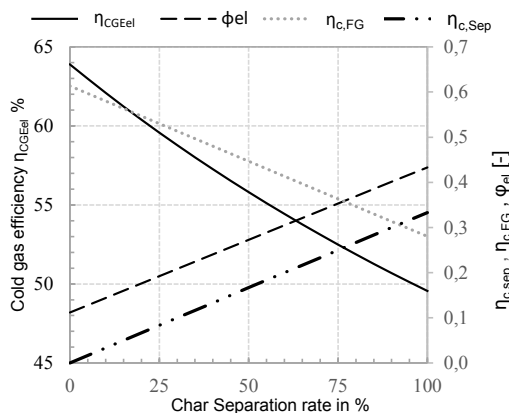


Figure 3: Comparison of KPIs with a variation of char separation

Conclusion & Outlook

This simulation study for a 150-kW sorption enhanced gasification pilot plant with in-situ char separation demonstrates the potential of a negative emissions technology for syngas production. The reduction in emissions is only possible if surplus energy from the electricity grid is used, as this energy comes from renewable sources and has a low CO₂ footprint.

As these are only initial calculations, they still need to be validated experimentally at a pilot plant which is currently designed and engineered. Considerations regarding the fluidization regimes already revealed limitations regarding the reactor dimensions varying the carbon separation with the overflow pipe. Furthermore, there are still unanswered questions about the pressure profile of the system which would have a significant impact on the operation of the reactor system. The implementation of electrical heating in fluidized beds seems highly suitable due to the high heat transfer properties but also needs to be proven experimentally.

Acknowledgements

This research was conducted in the course of and funded by the EU project CarbonNeutralLNG (Horizon Europe Grant Agreement 101084066).

Nomenclature

\dot{m}	Mass flow rate	kg/h
P_{el}	Electrical power	kW
P_{BM}	Fuel power based on LHV	kW
T	Temperature	°C
\dot{V}	Volume flow rate	Nm ³ /h
v	Velocity	m/s
w	Mass fraction	wt. %
φ_{SF}	Steam to fuel ratio	kg/kg
ϕ_{el}	Electricity to fuel ratio	-
Q_{loss_total}	Heat loss	kW
X_C	Carbon rate	kg/kg
U/U_{mf}	U to U_{mf} ratio of superficial velocity	-
d	Diameter	m
η_{CGEet}	Cold gas efficiency	-
SEG	Sorption enhanced gasification	
DFB	Dual fluidized bed	
PG	Product gas	
CR	Combustion reactor	
GR	Gasification reactor	
FG	Flue gas	

References

- (1) Kemper, J. (2015). "Biomass and carbon dioxide capture and storage: A review". *International Journal of Greenhouse Gas Control*, Volume 40, Pages 401-430, <https://doi.org/10.1016/j.IJGGC.2015.06.012>
- (2) Berger, R., Hein, K.R.G., Weimer, T., Specht, M., (2003), High temperature CO₂-absorption. A process offering new prospects in fuel chemistry, *Proceedings of the 5th International Symposium on Coal Combustion*, pp. 547-549
- (3) Fuchs, J., Schmid, J. C., Müller, S., Mauerhofer, A. M., Benedikt, F., & Hofbauer, H. (2020), "The impact of gasification temperature on the process characteristics of sorption enhanced reforming of biomass." *Biomass Conversion and Biorefinery*, 10(4), Volume 10, pages 925–936, <https://doi.org/10.1007/s13399-019-00439-9>
- (4) Gong, Y., Wang, X., Chen, D., & Al-Qadri, B. M. H. (2021). "Retrospect and prospect of carbon stripper technology in solid-fuel chemical looping combustion." *Fuel Processing Technology*, Volume 221, 106920, <https://doi.org/10.1016/j.FUPROC.2021.106920>
- (5) Di Natale, F., Nigro, R., & Scala, F. (2013), "Heat and mass transfer in fluidized bed combustion and gasification systems.", *Fluidized Bed Technologies for Near-Zero Emission Combustion and Gasification*, 2013, Pages 177-253, <https://doi.org/10.1533/9780857098801.1.177>
- (6) Grace, J. R. (1986), "Contacting modes and behaviour classification of gassolid and other two-phase suspensions.", *The Canadian Journal of Chemical Engineering*, Volume 64 Issue 3, Pages 353-363, <https://doi.org/10.1002/cjce.5450640301>
- (7) Schmid, J. C. (2014), "Development of a novel dual fluidized bed gasification system for increased fuel flexibility.", <https://doi.org/10.34726/hss.2014.25397>
- (8) Schmid, J. C., Benedikt, F., Fuchs, J., Mauerhofer, A. M., Müller, S., & Hofbauer, H. (2021), "Syngas for biorefineries from thermochemical gasification of lignocellulosic fuels and residues 5 years' experience with an advanced dual fluidized bed gasifier design. ", *Biomass Conversion and Biorefinery*, Volume 11, Pages 2405-2442, <https://doi.org/10.1007/s13399-019-00486-2>
- (9) Karl, J., Pröll, T., (2018), "Steam gasification of biomass in dual fluidized bed gasifiers: A review", *Renewable and Sustainable Energy Reviews*, Volume 98, Pages 64-78, <https://doi.org/10.1016/j.rser.2018.09.010>

Techno-economic assessment of CO₂ capture technologies in SNG upgrading from biomass steam gasification

A. Biebighäuser, F. Benedikt*, C. Pfeifer, T. Pröll, B. Fleiß

Institute of Chemical and Energy Engineering, BOKU University, Muthgasse 107/I, A-1190 Vienna, Austria

* Correspondent author: antonia.biebighauser@boku.ac.at

Keywords: methane slip, adsorption technologies, scrubbing technologies, membrane separation, cryogenic separation, biogas purification, dual fluidized bed gasification

This study presents a comprehensive techno-economic assessment of various CO₂ capture technologies for Synthetic Natural Gas (SNG) upgrading applications. The production of SNG from biogenic feedstocks represents a promising pathway for decarbonizing energy systems. However, raw SNG from gasification processes converting biomass typically contains a variety of gases (e.g., H₂, CO, H₂S, ...), with a specifically high concentration of CO₂ (40-60 %) [1], [2]. To ensure a high calorific value of the SNG, an upgrading step of the biogas is required to meet natural gas grid specifications (typically <3 % CO₂ in Austria) [3]. This research evaluates nine CO₂ capture technologies, based on their technical performance, operational requirements, environmental impacts, and economic viability. The assessment reveals that mature technologies like High Pressure Water Scrubbing (HPWS) and Pressure Swing Adsorption (PSA) offer advantages for smaller-scale applications, while alternative technologies such as the Benfield Process and Temperature Swing Adsorption (TSA) demonstrate promising potential for improved performance and reduced costs, particularly when integrated with existing energy systems.

Introduction

As part of the European Green Deal, the EU aims to reduce greenhouse gas emissions by at least 55 % by 2030 compared to 1990 levels [4]. To achieve this goal, Austria has proposed the Renewable Gas Act (Erneuerbares-Gas-Gesetz), which mandates that by 2030, 9.75 % or at least 7.5 TWh of fossil natural gas should be replaced by domestically produced renewable gas [5]. Starting from 2024, annually increasing green gas quotas were implemented, with suppliers facing penalties of €150/MWh for non-compliance [5]. This creates both a regulatory imperative and economic opportunity for improving SNG production systems. However, so far no political agreement has been achieved and therefore an entry into force of the proposed legislation is still missing.

Projects demonstrating SNG production from woody biomass using dual fluidized bed gasification have been successfully implemented in Güssing, Austria (1 MW), Gothenburg, Sweden ('GoBiGas', 20 MW), and Lyon, France ('GAYA', 500 kW), proving the technical feasibility of the technology [6], [7], [8], [9]. However, wider implementation has been hindered by economic factors, particularly for smaller-scale biomass plants where the methanation and upgrading technologies (especially CO₂ capture) derived from refinery technology are too complex and cost-intensive.

The I/O-Gas project ('Integration and Optimization of Renewable Gas Production from Biogenic Residues') addresses these challenges by seeking to develop more efficient technologies across the entire process chain. A critical focus area is the optimization of CO₂ capture technologies, which represent a significant portion of capital expenditures, operational costs in SNG production facilities and the possibility of generating additional revenues via selling the biogenic CO₂ [10]. Selecting the most suitable CO₂ removal

technology is essential for reducing costs, improving energy efficiency, and making SNG production economically viable under currently prevailing conditions.

Methodology

This study evaluates nine technologies for CO₂ removal from SNG streams: Pressure Swing Adsorption (PSA), Temperature Swing Adsorption (TSA), Amine Scrubbing (AS), High Pressure Water Scrubbing (HPWS), Organic Physical Scrubbing (OPS), Hot Potassium Carbonate (HPC, also known as the Benfield Process), Membrane Separation (MS), Cryogenic Separation (CS), and Calcium Looping (CaL).

For each technology, several key performance indicators were evaluated:

1. **Technical parameters:** methane purity, methane loss, technology readiness level (TRL)
2. **Operational requirements:** operating temperature, pressure, and energy consumption
3. **Environmental impacts:** greenhouse gas potential and resource consumption
4. **Economic factors:** capital expenditure (CAPEX), operational expenditure (OPEX), and lifecycle costs

The assessment methodology follows a multi-criteria approach where technologies are ranked based on weighted scores across these parameters. Special consideration is given to methane slip due to its significant environmental and economic implications. The Technology Readiness Level (TRL) is also factored in to assess deployment readiness, with scores ranging from 1 (basic principles observed) to 9 (proven system in operational environment).

SNG upgrading can be achieved through various procedures, depending on the specific process employed. In the I/O-Gas project, the process flow is illustrated in *Figure 1*. It begins with gas generation, which can be integrated with hydrogen produced via electrolysis during periods of surplus electricity. Following this, the gas undergoes a series of treatment steps, including heat exchange, filtration, biodiesel scrubbing, and activated carbon adsorption, before proceeding to methanation. Although sorption enhanced reforming (SER) is generally favoured for SNG production – since it enables nearly complete methanation due to the higher hydrogen concentration of the product gas – the conventional dual fluidized bed (DFB) gasification with olivine as bed material has advantages in the carbon utilization rate. Compared to SER, during DFB gasification less CO₂ is transported to the flue gas and as a result, a more concentrated green CO₂ stream is obtained in the product gas, which is separated directly after methanation and can be utilized for other applications (highlighted in red in *Figure 1*), while ensuring the final SNG meets pipeline quality requirements.

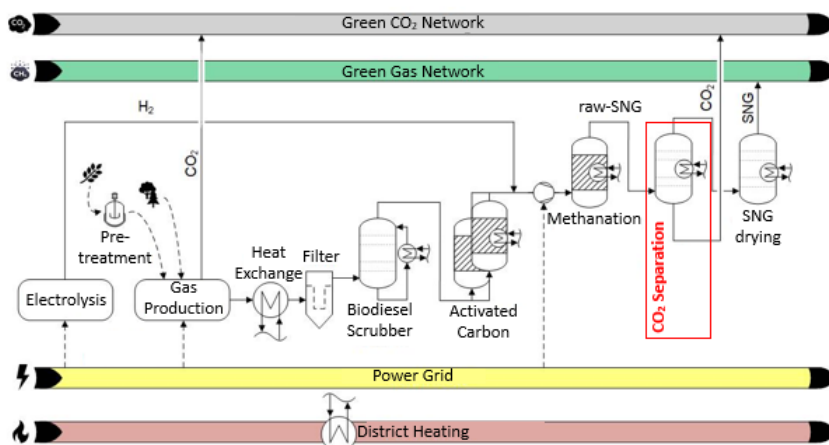


Figure 1: process chain for producing SNG in the I/O-Gas project with renewable electricity and biogenic CO₂ production, including CO₂ separation after raw-SNG production. **Highlighted in red.**

Technical Analysis of CO₂ Capture Technologies (see Table 1)

Adsorption Technologies

Pressure Swing Adsorption (PSA) operates by adsorbing CO₂ at solid materials under elevated pressure (1-10 bar – or even higher) and ambient temperatures (10-30 °C). CO₂ desorption occurs at temperatures of 20-50°C and atmospheric or lower pressure, with vacuum-PSA increasing desorption efficiency. With a Technology Readiness Level (TRL) of 9, PSA represents a mature technology capable of achieving methane purities of 90-99 %. However, it typically suffers from relatively high methane losses (1-5 %). The process offers advantages through rapid regeneration cycles and the absence of chemical additives but requires significant electrical energy (0.18-0.60 kWh/Nm³) primarily for gas compression. [11], [12]

Temperature Swing Adsorption (TSA) presents an emerging alternative to PSA (TRL 6/7) with improved adsorption performance, utilizing temperature rather than pressure for adsorbent regeneration. TSA employs heating to 80-120 °C (or up to 200 °C) using hot inert gas or steam, while achieving methane purities of >98 % at an energy consumption of 0.68 kWh/Nm³. [13]

Scrubbing Technologies

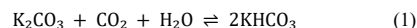
Various scrubbing technologies utilize different solvents to absorb CO₂ from gas streams. Amine Scrubbing (AS), operating at a TRL of 9, employs chemical absorption with amine solvents such as MEA, DEA, MDEA, or aMDEA¹. This technology achieves a methane purity of 96-99.5 % with minimal methane losses (0.03-0.1 %), resulting in the lowest greenhouse warming potential (GWP) among all assessed technologies. However, AS poses environmental concerns related to amine usage, including volatile organic compound (VOC) emissions, potential for nitrosamine formation, and degradation products that can be hazardous to aquatic environments. AS is particularly advantageous for facilities that already have steam production infrastructure (such as refineries), as the waste steam can be utilized for solvent regeneration, since thermal energy for solvent regeneration is relatively high (0.30-0.75 kWh/Nm³). [11], [12], [14]

High Pressure Water Scrubbing (HPWS), also at TRL 9, exploits CO₂'s higher solubility in pressurized water (6-10 bar) compared to CH₄. It operates on principles similar to AS but uses water as a

physical solvent rather than chemical absorption, resulting in lower CO₂ solubility. This lower solubility necessitates higher flow rates and pressures, increasing energy consumption for compression (0.19-0.55 kWh/Nm³ total electrical energy). The technology offers high methane recovery (95-99.9 %) with moderate methane losses (0.5-3 %) and can simultaneously remove contaminants like H₂S and NH₃. It presents advantages through relatively low operating costs and the absence of hazardous chemicals. [11], [15]

Organic Physical Scrubbing (OPS) employs organic solvents like Selexol® or Genosorb®, which offer 5-6 times higher CO₂ solubility than water. Operating at TRL 8/9, OPS achieves methane purities of around 97 % but suffers from high methane losses (4 %) and complex solvent regeneration requirements [11] Notably, while operational costs in €/Nm³ are documented for other CO₂ separation technologies, no peer-reviewed €/Nm³ values specific to OPS were identified in the literature.

The Benfield Process (HPC) utilizes a hot potassium carbonate solution (15-30 % K₂CO₃) as the absorbent, which reacts with CO₂ to form potassium bicarbonate (KHCO₃). The reaction mechanism is:



This reversible reaction involves carbonation (forward reaction) and regeneration (reverse reaction at higher temperatures). Operating at elevated temperatures (85-105 °C) and pressures (20-30 bar), this TRL 7 technology demonstrates promising performance with very low methane slip (<0.1 %) and moderate energy consumption (0.25-0.53 kWh/Nm³ with potential heat recovery). The process offers advantages through low-toxicity solvents and excellent methane retention, but faces challenges related to corrosion and contaminant accumulation. [14]

Other Technologies

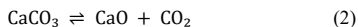
Membrane Separation (MS) systems can leverage both physical and chemical transport mechanisms, that permit faster diffusion of either CO₂ or CH₄. At TRL 6/7, current membrane systems can achieve methane purities in the range of 85-98 % with moderate methane losses (1 %). Multi-stage membrane configurations have shown improved performance, potentially reaching 99.5 % methane recovery by using multiple membrane stages in series and recycling streams between stages. This configuration allows rejected gas from

¹ aMDEA = combination of MDEA with an activator (e.g., piperazine), which enhances kinetics while maintaining MDEA's low regeneration energy requirements

later stages to be processed in earlier stages, minimizing methane losses at the cost of increased complexity and capital expenditure. Despite advantages in terms of compact design and moderate energy requirements (0.19-0.77 kWh/Nm³ electrical), MS faces challenges related to scalability and membrane durability [11]. Although Gkotis et al. (2023) claim high scale-up flexibility, issues arise from the need for proportionally larger membrane areas as flow rates increase, leading to permeance drops, exponentially higher costs, and more complex manifolding systems [16]. Additionally, membranes are susceptible to fouling, plasticization, and aging effects that can reduce separation efficiency over time. [11], [12], [14], [15]

Cryogenic Separation (CS) employs extreme cooling to exploit the different condensation temperatures of gas components. While effective at producing high purity biomethane (98 % with 0.65 % CH₄ loss), this TRL 6 technology requires substantial energy for cooling (>0.42 kWh/Nm³) and presents the highest total costs among all evaluated technologies. However, liquefied CO₂ produced by CS is already in a suitable state for transport, making it advantageous for carbon capture and storage (CCS) applications where pipeline infrastructure is limited and truck transport is required. [11]

Calcium Looping (CaL), at TRL 6/7, represents an emerging technology for CO₂ capture that uses limestone (CaCO₃) as a sorbent. The reaction mechanism involves calcination (forward reaction at ~850-950 °C) and carbonation (reverse reaction at ~600-700 °C) [17]:



This cycle allows for both CO₂ capture and the potential for thermochemical energy storage via the heat released during carbonation. While potentially offering advantages through nonproblematic sorbent materials and the possibility of integrating waste heat recovery, limited technical and economic data are currently available for biogas upgrading applications. [17]

Results and Discussion

Energy Requirements and Environmental Impact

Energy consumption significantly impacts both operational costs and carbon footprint of upgrading facilities. Among the evaluated technologies, AS demonstrates the highest total energy consumption (0.35-1.31 kWh/Nm³) due to substantial thermal energy requirements for solvent regeneration [11], [12]. If used in industries with abundant steam production (such as refineries), this heat can be efficiently reused, reducing the net energy penalty. However, this disadvantage is partially offset by very low methane losses. In contrast, HPWS and PSA consume only electrical energy (0.19-0.55 and 0.18-0.60 kWh/Nm³, respectively), avoiding thermal energy needs but typically resulting in higher methane losses [11], [12].

From an environmental perspective, technologies with lower methane slip generally demonstrate better greenhouse gas performance. Considering methane's global warming potential (GWP, 28 times higher than CO₂), even small reductions in methane slip can yield significant environmental benefits. AS and the Benfield Process show the smallest GWP due to their minimal methane losses (0.03-0.1 % and <0.1 %, respectively), while PSA has the highest GWP due to significant methane losses in the range of 1-5 % [11], [14], [15]. However, AS faces challenges with VOC emissions, especially in decentralized SNG plants without emission control capabilities. In this case, HPWS demonstrates a better holistic performance despite higher methane slip [14].

Water consumption and chemical usage represent additional environmental considerations. HPWS requires substantial water input, although recirculation systems can reduce freshwater demand to 0.01-0.6 l/Nm³ [12]. Chemical scrubbing processes, including AS, involve potentially hazardous substances, with amine-based systems raising concerns regarding toxicity. The Benfield Process offers an advantage in this respect, as potassium carbonate has significantly lower toxicity compared to amines.

Economic Analysis

The economic assessment of CO₂ capture technologies must consider both capital expenditure (CAPEX) and operational expenditure (OPEX). CAPEX varies significantly between technologies, influenced by factors such as process complexity, equipment requirements, and construction materials. For most technologies, CAPEX decreases substantially with increasing plant capacity, indicating economies of scale.

The CAPEX analysis² across biogas upgrading technologies demonstrates economies of scale effects as plant capacity increases. MS technology exhibits the most favourable economics at small scales, with specific CAPEX of 6.6 kUSD/(m³/h) at 100 m³/h capacity, compared to AS (10.5), HPWS (11.4), and OPS (10.7 kUSD/(m³/h)). All technologies demonstrate substantial CAPEX reductions with increasing capacity, though the HPWS scaling pattern presents irregularities, particularly the reduction from 11.4 to 1.22 kUSD/(m³/h) between 100 and 250 m³/h followed by an increase to 3.9 kUSD/(m³/h) at 500 m³/h, suggesting potential data inconsistencies or technology-specific operational factors [16]. The convergence effect becomes evident at industrial scales, where CAPEX differences narrow considerably at 1000 m³/h capacity, ranging from 2.0 kUSD/(m³/h) for HPWS to 2.6 kUSD/(m³/h) for AS, with PSA and MS both achieving 2.2 kUSD/(m³/h). This analysis indicates that while MS technology provides economic advantages for small-scale applications, technology selection criteria should incorporate operational parameters such as methane slip rates and energy efficiency at larger scales, where CAPEX differentials become less significant. The data also highlights the importance of comprehensive datasets across all capacity ranges for robust technology assessment, particularly given the absence of small-scale PSA data, lack of data for HPC, CS, TSA, and CaL technologies, and the irregular HPWS scaling behaviour. [11]

OPEX is primarily determined by energy consumption, maintenance requirements, and replacement of consumables (e.g., membrane modules, adsorbent/solvent replacement). Energy costs represent a substantial portion of OPEX for most technologies, with electricity typically accounting for 7-14 % of total upgrading costs. AS and the Benfield Process incur additional costs for thermal energy, although this can be mitigated through heat integration with other processes [11].

Methane losses contribute significantly to OPEX, as they represent lost revenue. Technologies with lower methane slip (AS, Benfield Process) demonstrate clear economic advantages in this respect. For instance, over a 20-year plant lifetime, methane loss costs can decrease from 540,000 to 55,000 euros when switching from MS to the Benfield Process [14].

² Notable data limitations include the complete absence of CAPEX information for HPC, CS, TSA, and CaL technologies, which restricts the scope of comparative analysis across the full spectrum of available biogas upgrading options. Additionally, MS technology lacks intermediate-scale

data for 250 and 500 m³/h capacities, and OPS data is unavailable for 600 m³/h. Also, no data concerning CAPEX of PSA at 100 m³/h was available.

Table 1: Comparative analysis of CO₂ separation technologies, detailing TRL, energy inputs (kWhel/kWhth per Nm³), CH₄ purity (%) with loss, and costs (€/Nm³). Ranges reflect study variability; "/" for non-applicable parameters, "N/A" for unavailable data

Technology	TRL	Energy Requirements (kWh/Nm ³)		Product Purity (CH ₄ , %)	Costs (€/Nm ³ biogas)
		kWh _{el} /Nm ³	kWh _{th} /Nm ³		
PSA	9	0.18-0.60 for gas compression	/	90-99 with 1-5 % CH ₄ loss	0.26-0.40
MS	6/7	0.19-0.77	/	85-99.5 % with 1% CH ₄ loss	0.12-0.26
AS	9	0.05-0.56	0.30-0.75	96-99.5 with 0.03-0.1 % CH ₄ loss	0.17-0.33
HPWS	9	0.19-0.55 for compression	/	95-99.9 with 0.5-3% CH ₄ loss	0.13-0.16
OPS	8/9	0.4-0.511	/	97 with 4% CH ₄ loss	N/A
HPC	7	0.20-0.25	0.42-0.65	97.6-98.6 with <0.1% CH ₄ loss	N/A
CS	6	>0.42 for extreme cooling	/	98 with 0.65% CH ₄ loss	0.17-0.52
TSA	6/7	0.68 (when thermal energy available)	/	98 with minimal CH ₄ loss	N/A
CaL	6/7	N/A	N/A	N/A	N/A

Technology Selection for Implementation

Based on this assessment, MS, CS, and CaL were explicitly excluded from further consideration, due to scalability challenges within the project, high costs and energy consumption, and limited available data, respectively. The following technologies were selected for further testing through process simulation within the I/O-Gas project:

- 1. PSA** - Despite relatively high methane losses, PSA represents a mature, widely deployed technology with moderate energy requirements and well-understood operation.
- 2. Scrubbing Technologies** - All four scrubbing methods (AS, HPWS, OPS, and HPC) will be evaluated further due to their complementary strengths and weaknesses. AS offers minimal methane losses but high thermal energy requirements; HPWS provides readily available solvent and low environmental toxicity; OPS offers enhanced absorption capabilities; and HPC demonstrates excellent methane retention with moderate energy consumption.
- 3. TSA** - Despite its lower TRL, TSA shows promising performance characteristics and potential economic advantages, particularly when integrated with processes that generate excess heat.

Conclusion and Outlook

The techno-economic assessment of CO₂ capture technologies for SNG upgrading is a critical component of the I/O-Gas project's goal to make renewable gas production from biogenic residues more efficient and economically viable. This assessment aligns with the European Green Deal's target of reducing greenhouse gas emissions by 55 % by 2030 and supports Austria's Renewable Gas Act, to replace 7.5 TWh of fossil natural gas with renewable gas by 2030.

By identifying and optimizing suitable CO₂ capture technologies, the project contributes to several key objectives: reducing SNG production costs to less than half of the proposed penalty payments of €150/MWh, increasing the carbon utilization rate compared to the current state of the art, and enabling better integration with energy systems through appropriate sector coupling. These advancements are essential for expanding the use of biogenic residues in SNG production, which could add approximately 11 TWh of renewable gas capacity in Austria from straw-like biomass alone.

The selection of appropriate CO₂ capture technologies must balance technical performance, environmental impact, and economic considerations. While mature technologies like AS and PSA offer proven reliability, emerging alternatives such as the Benfield Process and TSA show promising potential for improved performance and reduced costs, particularly when integrated with other energy systems.

Further research and development efforts, as outlined in the I/O-Gas project, will focus on optimizing these technologies and evaluating their performance in the context of the complete process chain from biomass pre-treatment to SNG grid injection.

Acknowledgement

This research was conducted in the course of and funded by the FFG

project I/O-Gas (Integration und Optimierung der Produktion von erneuerbarem Gas aus biogenen Reststoffen), FO999915024.

Nomenclature

AS	Amine Scrubbing
CaL	Calcium Looping
CAPEX	Capital Expenditure
CS	Cryogenic Separation
DEA	Diethanolamine
GWP	Global Warming Potential
HPC	Hot Potassium Carbonate (Benfield Process)
HPWS	High Pressure Water Scrubbing
MDEA	Methyldiethanolamine
MEA	Monoethanolamine
MS	Membrane Separation
OPS	Organic Physical Scrubbing
OPEX	Operational Expenditure
PSA	Pressure Swing Adsorption
SER	Sorption Enhanced Reforming
SNG	Synthetic Natural Gas
TRL	Technology Readiness Level
TSA	Temperature Swing Adsorption

References

- Sustainable Natural Gas production through gasification. 2022
- Thermodynamic investigation of SNG production based on dual fluidized bed gasification of biogenic residues. 2021
- GB210 Richtlinie - Gasbeschaffenheit. 2021
- The European Green Deal - European Commission. 2021
- Erneuerbares-Gas-Gesetz | Servicestelle Erneuerbare Gase. 2025
- First ever large-scale demonstration biogas plant goes on-stream in Sweden with technology from Topsoe. 2025
- BioSNG—process simulation and comparison with first results from a 1-MW demonstration plant. 2011
- Production of Bio-Methane from Woody Biomass using the MILENA Gasification Technology. 2015
- Gaya: Production of SNG from Biomass and Waste Pyrogasification in France. 2022
- I/O-Gas. <https://projekte.ffg.at/projekt/5125926>. 2024
- Biogas as a renewable energy fuel – A review of biogas upgrading, utilisation and storage. 2017
- Techno-economic and environmental assessment of the main biogas upgrading technologies. 2020
- Effiziente Aufbereitung von Biogas zu Biomethan mittels kontinuierlicher Temperaturwechselsorption. 2019
- CO₂/CH₄ separation by hot potassium carbonate absorption for biogas upgrading. 2019
- Biogas upgrading technologies – Recent advances in membrane-based processes. 2023
- SNG-electricity cogeneration through MSW gasification integrated with a dual chemical looping process. 2019
- Membrane gas separation technologies for biogas upgrading. 2015

Renewables

Posters

Day 1

Project “Reallabor Holzgas” - Biomass Syngas Methanation from a 10 kW Prototype to the planned 5 MW Pilot Plant

M. Jeremić^{1,*}, A. Krammer¹, M. Lehner¹

¹: Chair of Process Technology and Environmental Protection, Montanuniversität Leoben, Austria

* Correspondent author: marija.jeremic@unileoben.ac.at

Keywords: Biomass gasification, Catalytic methanation, BioSNG, Fixed-bed reactor, Process simulation

Introduction

The project “Reallabor Holzgas” (eng. “wood gas real-world lab”) aims to contribute to the decarbonization of Austria’s agricultural and forestry sectors by converting biogenic residues into renewable fuels, specifically synthetic natural gas (bio-methane) and “wood diesel”, through an integrated biorefinery approach. Thermochemical conversion technologies form the backbone of the process.

The core element is the installation of a dual fluidized bed (DFB) gasification system (5-8 MW) in Zeltweg, Styria, converting solid biomass into a product gas rich in hydrogen (~ 41 vol.%), carbon monoxide (~ 24 vol.%), carbon dioxide (~ 23 vol.%), methane (~ 10 vol.%), and light hydrocarbons (~ 2 vol.%).

Downstream of gasification, the gas is cleaned and conditioned for further conversion via Fischer-Tropsch synthesis or catalytic methanation with subsequent CO₂ separation.

The Chair of Process Technology and Industrial Environmental Protection at Montanuniversität Leoben supervises, optimizes, and develops the methanation process to ensure high efficiency, stability, and economic feasibility under realistic conditions.

Methods

For the methanation of biomass-derived synthesis gas, both catalytic fixed-bed and fluidized-bed reactor technologies are under investigation. These technologies are being assessed for their technical viability and process integration potential within the overall biomass-to-fuel value chain.

In this context, a laboratory-scale methanation plant with fixed-bed reactor has been developed and operated. The setup includes thermal oil-cooled shell-and-tube reactors equipped with a nickel-based catalyst. This design allows for precise thermal management and stable operating conditions, which are crucial for the highly exothermic methanation reactions.

The experiments focus on evaluating the influence of key process parameters, such as gas composition, pressure, oil temperature, and GHSV on reaction performance and methane concentration. The obtained experimental data are further used to calibrate and validate process models in Aspen Plus. This enables the identification of technically and economically optimal process configurations for large-scale implementation.

Results

Figure 1 shows a selection of experimental results from the methanation of biomass gasification product gas in a thermal oil-cooled shell-and-tube reactor with a nickel fixed-bed catalyst. The experiments were conducted at an operating pressure of 4 to 10 bar and a gas hourly space velocity (GHSV) of 6000 to 20000 h⁻¹.

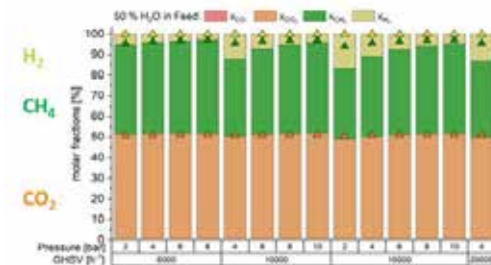


Figure 1. Experimental results of methanation of biomass gasification product gas as a function of pressure and GHSV

These results show that CO is almost completely converted in a single reactor stage, and at higher pressure. Due to a lack of hydrogen, the CO₂ conversion is not sufficient to produce grid-compatible bioSNG, therefore subsequent CO₂ separation is needed.

Outlook and next steps

In the coming months, the fixed-bed experiments will be further expanded regarding variations in feed gas concentration and process conditions, in order to demonstrate, for example, sufficient conversion even at a low pressure of around 2 bar. Based on the experimental results, simulations will be carried out in Aspen Plus to compare fixed-bed and fluidized-bed technologies within the overall process context. The influence of methanation operating conditions – such as the number of reactor stages and the respective operating pressure – on the energy efficiency and investment costs of the planned plant will be analyzed in detail. Ultimately, the purpose of the process simulation is to identify the most economical process configuration in order to demonstrate sustainable, climate-neutral energy supply from biogenic residues on a megawatt scale.

References

- [1] Hanchate, N., Ramani, S., Mathpati, S., C., Dalvi, H., V., “Biomass gasification using dual fluidized bed systems: A review”, *Journal of Cleaner Production*, 2020, doi: <https://doi.org/10.1016/j.jclepro.2020.123148>
- [2] Krammer, A., Salbrechter, K., Lehner, M., “High-capacity CO/CO₂ methanation reactor design strategy based on 1D PFR modelling and experimental investigation”, *Journal of CO₂ Utilization*, vol. 80, 2024, doi: <https://doi.org/10.1016/j.jcou.2023.102661>

A Multi-Component Learning Curve Framework for Estimating SAF Production Costs Using Solar-Assisted Fast Pyrolysis

S. Zervopoulou^{1,*}, S. Papadokonstantakis¹

¹: Institute of Chemical, Environmental and Bioscience Engineering, Vienna University of Technology, Austria

* Correspondent author: stavroula.zervopoulou@tuwien.ac.at

Keywords: Sustainable Aviation Fuel, Learning Curves, CAPEX reduction, EU ReFuelEU targets

To tackle the rising CO₂ emissions from the aviation sector, the European Union has implemented the ReFuelEU Aviation Regulation, designed to accelerate the adoption of Sustainable Aviation Fuel (SAF). Beginning in 2025, aviation fuel suppliers will be mandated to ensure a minimum SAF blend of 2% at EU airports, with the target gradually increasing to 6% by 2030 and 70% by 2050. Of the 2050 target, 35% is expected to be met through synthetic aviation fuels (e-fuels). This regulation is anticipated to reduce CO₂ emissions from aviation by over 60% by 2050 compared to 1990 levels, marking a key milestone in the EU's overall climate and decarbonization strategy [1].

This study presents a forward-looking techno-economic framework for estimating the production costs of Sustainable Aviation Fuel (SAF) derived from EU-sourced second-generation biomass as listed in the REDII (2018/2001) [2], using solar-assisted fast pyrolysis and solar hydrogen upgrading.

The production costs of SAF currently remain higher than those of conventional fossil-based jet fuels. A major contributor to these costs is Capital Expenditures (CAPEX), particularly for SAF production technologies that serve the aviation sector. These costs, along with feedstock expenses, significantly influence the overall economic viability of SAF.

Therefore, estimating the potential for cost reduction through research and development (R&D) and cumulative deployment, from first-of-a-kind (FOAK) to nth-of-a-kind (NOAK) production facilities, is essential. SAF production processes typically involve a combination of mature and emerging technologies, each with distinct cost-reduction trajectories. This study adopts a methodological framework based on learning curve theory to estimate cost reduction. The proposed approach employs a multi-component learning curve model [3] that disaggregates the SAF production value chain into major subsystems/units into its technological elements to identify where cost reductions are most likely, using techno-economic data. This bottom-up modelling captures first-of-a-kind (FOAK) to next-of-a-kind (NOAK) cost transitions for scaling scenarios targeting 0,1 Mt SAF production in 2030 and 5 Mt by 2040.

The framework incorporates scenario-based analysis to evaluate the effects of technological maturity, deployment scale, and future capacity expansion on production costs.

This work supports informed policy and investment decisions to accelerate the deployment of climate-aligned aviation fuels in the EU, highlighting the potential for significant long-term cost reductions in emerging SAF production technologies.

References

- [1]. European Parliament and Council of the European Union. Regulation (EU) 2023/2405 of the European Parliament and of the Council of 18 October 2023 on ensuring a level playing field for sustainable air transport (ReFuelEU Aviation). Official Journal of the European Union, L202, 1–378 (2023).
- [2]. REDII. (2018/2001). Directive (EU) 2018/2001 of the European Parliament and of the Council of 11 December 2018 on the promotion of the use of energy from renewable sources (recast).
- [3]. Ferioli, F., Schoots, K and van der Zwaan; B.C.C. (2009): Use and Limitations of Learning Curves for Energy Technology

Policy: A Component-Learning Hypothesis. Energy Policy,37, 2009, 2525-2535.

Sustainable Aviation Fuels (SAF)

E. Komatz¹, S. Sendlhofer¹, M. Lehner¹, C. Markowitsch^{1,*}

1: Chair of Process Technology and Industrial Environmental Protection, Technical University of Leoben, Austria

* Correspondent author: christoph.markowitsch@unileoben.ac.at

Keywords: Sustainable Aviation Fuel, Alcohol-to-Jet, Carbon Capture and Utilization (CCU), Machine learning

The decarbonization of the aviation sector depends on the large-scale implementation of Sustainable Aviation Fuels (SAF) [1]. The motivation originates from the ReFuelEU Aviation regulation, which mandates minimum SAF blending shares of 2% by 2025, 6% by 2030, and 70% by 2050 [2]. To achieve these targets, sustainable fuel must be designed to match the specifications of Jet A-1 (ASTM D1655), which requires a specific hydrocarbon composition to ensure suitable freezing points, energy density and material compatibility [3]. Best practice SAF pathways include Hydroprocessed Esters and Fatty Acids (HEFA), Fischer–Tropsch synthesis (FT), and Alcohol-to-Jet (AtJ) upgrading [4]. These processes utilize diverse renewable feedstocks (e.g. oils, biomass, or alcohols) to produce drop-in fuels that comply with ASTM D7566 and meet the Jet A-1 specifications defined in ASTM D1655.

Current sustainable aviation fuels are based on Synthetic Paraffinic Kerosene (SPK), predominantly composed of normal- and iso-paraffins and require supplementation with Synthetic Aromatic Kerosene (SAK) due to SPK's low aromatic content [5]. The composition of Jet A-1 fuel is approximately 20 wt.-% n-alkanes, 30 wt.-% iso-alkanes 32 wt.-% cycloalkanes and 18 wt.-% aromatics [1]. Maintaining this composition is essential to meet the properties required for a “drop-in” use of synthetic fuels [3].

At the Technical University of Leoben, a new research initiative focuses on catalyst development and SAF production process development. A multipurpose pilot plant is established to process various feedstocks such as methanol, higher alcohols, and biomass-derived intermediates into SAF precursors. Machine learning models are employed for kinetic research, while techno-economic assessments and Multiphysics simulations support process optimization and scale-up.

References

- [1] U.S. Department of Energy, *Sustainable Aviation Fuel: Review of Technical Pathways*. [Online]. Available: <https://www.energy.gov/sites/default/files/2020/09/t78/beto-sust-aviation-fuel-sep-2020.pdf>
- [2] *REGULATION (EU) 2023/2405: ReFuelEU Aviation*, 2023. [Online]. Available: <https://eur-lex.europa.eu/eli/reg/2023/2405/oj>
- [3] *ASTM D1655: Specification for Aviation Turbine Fuels*, D02 Committee, West Conshohocken, PA.
- [4] *ASTM D7566: Specification for Aviation Turbine Fuel Containing Synthesized Hydrocarbons*, D02 Committee, West Conshohocken, PA.
- [5] Bundesministerium für Klimaschutz, Umwelt, Energie, Mobilität, Innovation und Technologie (BMK), *SAF-Roadmap: Strategie zur Einführung nachhaltiger Kraftstoffe im Flugverkehr in und aus Österreich*. [Online]. Available: https://www.bmimi.gv.at/dam/jcr:ea56f660-1bf7-4a6a-bcbf-6e95bb2cc728/BMK_SAF_Roadmap_UA.pdf

Hydrogen and its Applications

Presentations

Day 2

Direct-Fired Furnace for Steel Strip Reheating: High-Fidelity CFD Analysis of Pure H₂ versus Austrian Pipeline Natural Gas Firing

A. Aghajanianpour*^{1,2}, C. Spijker¹, H. Raupenstrauch¹, E. Wimmer², M. Witzan², G. Zellinger²

1: Chair of Thermal Processing Technology, Montanuniversität Leoben, Austria

2: voestalpine Stahl GmbH, Linz, Austria

* Correspondent author: abdo@leoben.ac.at

Keywords: Direct-Fired Furnace, Hydrogen Combustion, Steel Reheating, CFD Simulation, Radiative Heat Transfer, Decarbonization

1. Introduction

The steel industry is actively exploring hydrogen as a key enabler for industrial decarbonization, driven by the need to reduce carbon emissions from high-temperature processes. This study investigates the technical feasibility and thermal performance of fully substituting Austrian pipeline natural gas with pure hydrogen in an industrial-scale direct-fired furnace (DFF) used for steel strip reheating. Through high-fidelity computational fluid dynamics (CFD) analysis, the impacts on furnace operation and heat transfer efficiency are comprehensively evaluated to support the transition toward sustainable steel manufacturing.

2. CFD Solver and Physical Models

In this study, a sophisticated Computational Fluid Dynamics (CFD) framework was developed to analyze combustion in a twelve-level Direct-Fired Furnace (DFF). Numerical simulations utilized ANSYS Fluent 2024 R1, a validated solver for industrial combustion. Governing equations were solved under fully compressible conditions to effectively model density variations from high-temperature combustion. Simulations employ double precision to reduce truncation errors and improve robustness in resolving fine-scale gradients in temperature, species concentration, and velocity across the domain.

2.1 Turbulence Modelling

Turbulence from low-swirl burners and high Reynolds number conditions was modeled using the Realizable k - ϵ turbulence model [1]. The Realizable variant enhances predictions of swirling flows and rotational effects, essential for flame stabilization in swirl-stabilized burners. It dynamically adjusts turbulent viscosity based on local flow characteristics, providing a more accurate representation of turbulence-chemistry interactions. The turbulence closure utilized standard wall functions to resolve near-wall behaviors in boundary layers. A turbulent Prandtl number of 0.85 was adopted for energy transport, aligning with the best industrial practices for high-temperature combustion simulations.

2.2 Combustion Chemistry

The combustion process was analyzed using the Eddy Dissipation Concept (EDC). The EDC model integrates turbulence and chemical kinetics by positing that reactions primarily take place in fine turbulent structures with well-mixed reactants. This method offers substantial benefits over basic eddy dissipation models, especially in complex combustion scenarios [2]. A reduced 19-species global reaction mechanism, derived from GRI-MECH 1.2, was employed to simulate the oxidation of methane-hydrogen mixtures in the combustion domain [3]. This detailed chemical kinetic scheme includes key species such as OH, H, O₂, CO, CO₂, and H₂O, allowing for accurate representation of major combustion pathways while significantly reducing computational cost compared to full detailed mechanisms. The mechanism consists of 84 elementary reactions and was selected specifically for its proven reliability in methane-

and hydrogen-containing fuel systems. By balancing computational efficiency with chemical fidelity, this mechanism enables robust prediction of flame speed, pollutant formation, and thermal energy release, essential for analyzing the impact of fuel switching in industrial direct-fired furnace operation.

2.3 Radiative Heat Transfer

Since over 70% of heat transfer in a DFF is radiative, precise radiation modelling was essential. The Discrete Ordinates (DO) method was employed for radiative heat transfer analysis, effectively solving the Radiative Transfer Equation (RTE) in participating media [4]. A 3×3 angular discretization scheme was utilized, providing 9 discrete directions per spatial cell, balancing computational efficiency with directional accuracy of radiative intensity.

Spectral variations in gas absorption-emission were modeled using the Weighted-Sum-of-Gray-Gases Model (WSGGM) [5]. This model, based on Solovjov and Bord's formulation, addresses the CO₂-H₂O mixture in methane combustion and the predominant H₂O radiation in hydrogen combustion. The WSGGM approximates the spectral behavior of the participating medium as a weighted sum of gray gases, enhancing computational efficiency while ensuring accuracy. In wall emissivity modeling, temperature-dependent emissivity data were integrated for refractory walls and steel strip surfaces, accounting for emissivity degradation at high temperatures, thus providing a physically consistent radiative boundary condition.

2.4 Additional Numerical Considerations

The Coupled algorithm with pseudo-transient under-relaxation was utilized to maintain numerical stability in high-temperature combustion flows within the Direct-Fired Furnace (DFF). Second-order upwind schemes were employed for spatial discretization to minimize numerical diffusion while accurately resolving flame fronts and thermal gradients essential for combustion dynamics. A staged initialization strategy was adopted to ensure flame stabilization and prevent numerical divergence during start-up. Elevated initial temperatures of 800 K for combustion air and fuel were set to facilitate rapid ignition and early flame stabilization. Additionally, burner components were preheated with the burner dish at 3000 K and the nozzle at 2000 K to provide necessary thermal energy for igniting the fuel-air mixture.

After establishing the flame, the elevated temperatures were removed, and boundary conditions were adjusted to standard operational values, reducing fuel and air inlets to 300 K. The simulation then progressed towards a steady state under fully adiabatic conditions. Stringent convergence criteria were upheld throughout the simulation, requiring scaled residuals for continuity, momentum, and species transport equations to be below 10⁻⁶, while energy and radiation transport equations were held to stricter standards of 10⁻⁸ for accurate thermal resolution. Integral parameters such as total heat input, surface temperature distribution, and combustion product concentrations were continuously monitored,

ensuring that the numerical solution achieved true physical convergence and the reliability of the simulation results.

3. Geometry and Meshing

The computational domain was established utilizing proprietary engineering plans from voestalpine Stahl GmbH, facilitating an accurate reconstruction of the twelve-level Direct-Fired Furnace (DFF) for steel strip reheating. The geometric model encompasses the entire furnace length, integrating essential structural and functional elements, including 132 low-swirl burners and a continuously moving steel strip of 1.5 mm thickness and 1.6 m width, and velocity equal to 1.6 m per second.

The furnace's twelve levels were categorized into two sections for effective computational administration: Block 1 (Levels 1-6) and Block 2 (Levels 7-12). Burners were asymmetrically positioned on both sides of the strip at each level, with one side containing five single burners and the other six; this pattern was alternated at subsequent levels to enhance heating uniformity and reduce lateral thermal gradients. The moving steel strip was modelled as a solid wall boundary with a defined longitudinal velocity to accurately simulate its movement through heating zones, enabling precise predictions of convective and radiative heat transfer between the combustion gases and the strip surface.

An unstructured polyhedral mesh was created to discretize the intricate furnace geometry, consisting of approximately 24.8 million control volumes. Polyhedral cells were chosen for their advantageous numerical characteristics, such as diminished numerical diffusion and enhanced convergence rates, essential for ensuring solution precision in turbulent, high-temperature combustion scenarios. Local mesh refinement was applied in critical areas, including burner nozzles, flame zones, and surfaces adjacent to the strip and walls, to accurately resolve sharp gradients in velocity, temperature, and chemical species concentrations. This comprehensive geometric and meshing approach establishes a solid framework for effectively simulating the multiphase and multi-physics interactions that dictate heat transfer, combustion dynamics, and strip heating efficacy in both hydrogen and natural gas firing conditions.

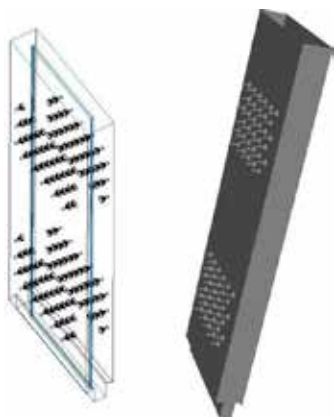


Figure 1 – General configuration of 132 single burners of the DFF

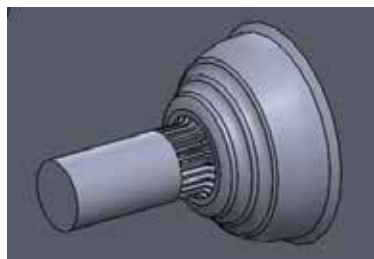


Figure 2 – Geometry of an arbitrary single burner

Radiative heat transfer, a key component of the furnace's energy transport, was effectively modeled using temperature-dependent emissivity for the strip and refractory walls. The furnace's outer casing was modeled as adiabatic to represent substantial insulation. The high-quality mesh coupled with precise geometric representation establishes a solid computational basis for elucidating the intricate multi-physics interactions that influence the performance of hydrogen and natural gas combustion modes in the industrial DFF.

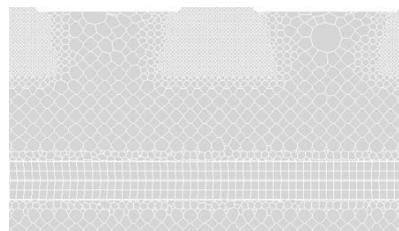


Figure 3 - Mesh around any arbitrary burner dish and the steel strip (shadow layer)

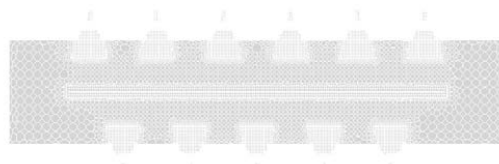


Figure 4 - Mesh over any arbitrary levels of the DFF (1 to 12)

4. Boundary Conditions

The boundary conditions for numerical simulations were defined to replicate full-load operation of the Direct-Fired Furnace (DFF), facilitating a reliable assessment of natural gas versus hydrogen firing scenarios. The air-to-fuel equivalence ratio (λ) was fixed at 0.91, indicating a 9% sub-stoichiometric combustion environment. This fuel-rich condition aligns with industrial practices aimed at optimizing radiative heat transfer efficiency while ensuring stable combustion. Specific fuel compositions were established for the two combustion scenarios to reflect industrial feedstock characteristics. The natural gas (NG) composition adhered to Austrian specifications, comprising 90.15% CH₄, 0.11% C₂H₆, 0.011% CO₂, 70.9% N₂, and 18.82% O₂ by mole fraction. In contrast, the hydrogen (H₂) scenario utilized a blend of 31.58% H₂, 54.05% N₂, and 14.37% O₂, representing suitable blending strategies for equivalent combustion conditions. The mass flow rates were precisely adjusted to 1.9685 kg/s for NG and 2.0274 kg/s for H₂, ensuring identical nominal thermal power output.

A shielding gas system was implemented to protect the steel strip from surface oxidation. The protective mixture, HNX, consisting of 3% H₂ and 97% N₂, was injected at 993 K with a total mass flow rate of 0.24 kg/s along the strip faces. This shielding gas was crucial in reducing oxygen ingress, preventing oxidation, decarburization, and quality degradation of the reheated strip. At the furnace outlet, a

pressure-outlet boundary condition was established to simulate the mild underpressure typical of industrial exhaust systems, enhancing gas flow consistency. Radiative boundary conditions were implemented for the furnace refractory walls and the moving steel strip, incorporating temperature-dependent emissivities to capture the intricate radiative heat exchange within the furnace.

5. Results

5.1 Temperature Fields

The replacement of natural gas with hydrogen significantly altered the thermal dynamics of the Direct-Fired Furnace. The maximum internal gas temperature surged by 10.8%, from 2268 K to 2514 K, due to hydrogen's superior combustion properties. This increase is linked to hydrogen's higher adiabatic flame temperature, resulting from its lower molecular weight and enhanced energy release. Additionally, temperature profiles for the steel strip demonstrated a notable rise, with surface temperatures increasing by 7.6% from 893 K to 961 K. The temperature increase was uniformly distributed along the furnace, preventing localized thermal issues that could adversely affect metallurgy. The findings underscore the intricate relationship between gas combustion dynamics and solid heating mechanisms, affirming hydrogen's capacity to improve thermal efficiency.

annealing. The improved furnace gas temperatures, radiative energy exchange, and enhanced surface heating highlight hydrogen's superior thermophysical performance, emphasizing its viability as a clean, efficient alternative fuel in high-temperature industrial applications.

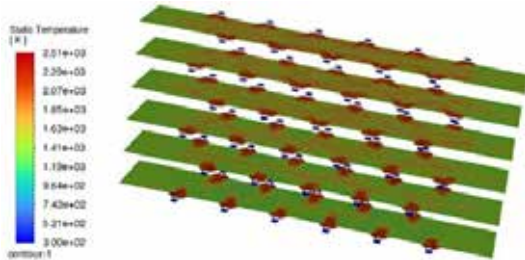


Figure 5 - "NG" Case - Temperature of the gas - Block 2 (scaled)

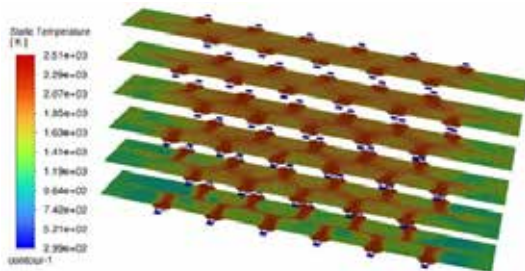


Figure 6 - "NG" Case - Temperature of the gas - Block 1 (scaled)

5.2 Heat Transfer

The rise in furnace temperatures with hydrogen firing significantly improved heat transfer to the steel strip. The radiative heat flux on the strip's surface rose by about 37% compared to natural gas. This improvement is due to higher furnace gas temperatures and changes in the radiative properties of combustion products. The composition of flue gas under hydrogen combustion shifts toward an H₂O-rich environment, as carbon is absent in the fuel. Water vapor acts as a potent emitter and absorber in the mid-infrared region, enhancing radiative heat transfer to the strip. As a result, the total heat input to the strip increased by roughly 40% when transitioning from natural gas to hydrogen combustion. This significant enhancement in energy transfer is advantageous for industrial processes, potentially increasing heating rates or reducing energy consumption for production targets.

Additionally, greater radiative heat transfer under hydrogen conditions promotes uniform strip heating, essential for maintaining metallurgical specifications in downstream processes like rolling or

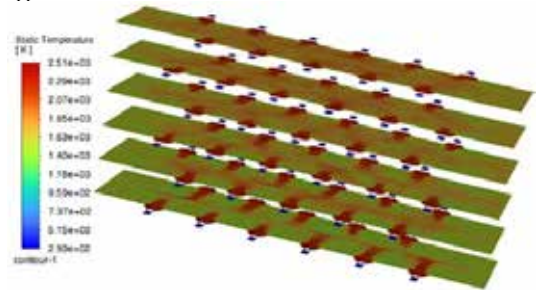


Figure 7 - "H₂" Case - Temperature of the gas - Block 2

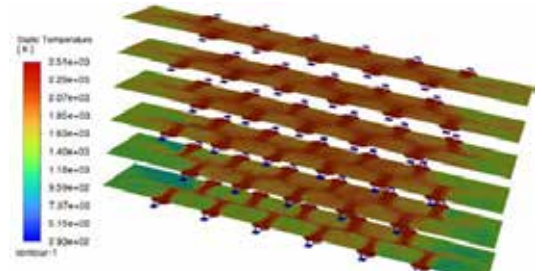


Figure 8 - "H₂" Case - Temperature of the gas - Block 1



Figure 9 - "NG" Case - Temperature of the steel strip (scaled)



Figure 10 - "H₂" Case - Temperature of the steel strip

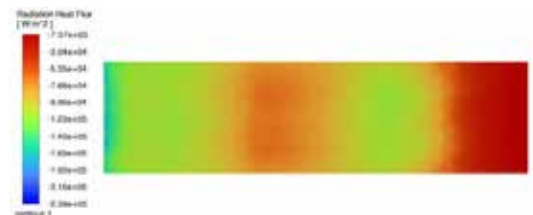


Figure 11 - "NG" Case - Radiation heat flux of steel strip (scaled)

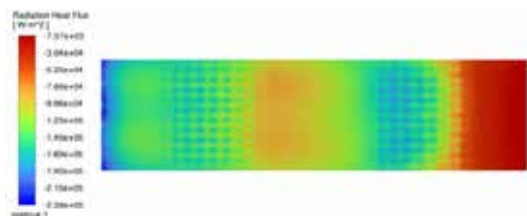


Figure 12 - "H₂" Case - Radiation heat flux of steel strip

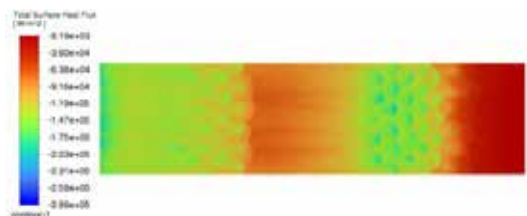


Figure 13 - "NG" Case - Total surface heat flux of steel strip (scaled)

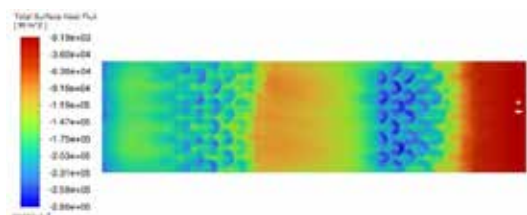


Figure 14 - "H₂" Case - Total surface heat flux of steel strip

6. Conclusion

This research illustrates that pure hydrogen can effectively substitute natural gas as a combustion fuel in industrial Direct-Fired Furnaces without compromising performance metrics. The hydrogen substitution led to elevated furnace gas and strip surface temperatures, significantly enhancing radiative heat flux due to water vapor's superior radiative characteristics compared to carbon dioxide. These enhancements provide substantial benefits in increasing production efficiency or decreasing energy usage, aiding decarbonization efforts. Consistent combustion performance was observed throughout the study, affirming the durability of the burner and furnace design under hydrogen conditions. Nevertheless, the findings highlight the importance of meticulous shielding gas management to mitigate edge oxidation, particularly at the elevated thermal intensities from hydrogen combustion. In summary, hydrogen emerges as a technically feasible and environmentally advantageous substitute for natural gas in industrial strip reheating, facilitating the transition to more sustainable steel production.

References

- [1] ANDRITZ Metals. (n.d.). Continuous Galvanizing Line Furnaces. Retrieved April 30, 2025, from <https://www.andritz.com/products-en/metals/furnaces/continuous-strip-processing/galvanizing-line-furnaces>
- [2] Launder, B. E., and Spalding, D. B., "The numerical computation of turbulent flows," *Computer Methods in Applied Mechanics and Engineering*, vol. 3, no. 2, pp. 269–289, 1974. doi:10.1016/0045-7825(74)90029-2
- [3] Magnussen, B. F., "On the structure of turbulence and a generalized eddy dissipation concept for chemical reaction in

turbulent flow," 19th AIAA Aerospace Meeting, St. Louis, Missouri, USA, 1981. doi:10.2514/6.1981-42

[4] Smith, G. P., Golden, D. M., and Frenklach, M., "GRI-Mech 1.2: Natural Gas Combustion Mechanism," Gas Research Institute, 1994. [Online]. Available: <http://combustion.berkeley.edu/drm/drm19.dat>

[5] Chui, E. H., and Raithby, G. D., "Computation of radiant heat transfer on a nonorthogonal mesh using the discrete ordinates method," *Numerical Heat Transfer, Part B: Fundamentals*, vol. 23, no. 3, pp. 269–288, 1993. doi:10.1080/10407799308955848

[6] Solovjov, V. P., and Bord, S. A., "An improved weighted-sum-of-gray-gases model for air–H₂O–CO₂ mixtures," *International Journal of Heat and Mass Transfer*, vol. 49, no. 19–20, pp. 4511–4524, 2006. doi:10.1016/j.ijheatmasstransfer.2006.04.037

[7] Scarpa, F., Boon-Brett, L., and Buttner, W., "Combustion properties and safety aspects of hydrogen," *International Journal of Hydrogen Energy*, vol. 46, no. 5, pp. 3892–3905, 2021. doi:10.1016/j.ijhydene.2020.10.148

Methanation of Biogenic CO₂ vs. Fossil CO₂ from Industrial Point Sources: A Techno-Economic and Feedstock Comparison

S. Sendlhofer¹, A. Krabichler-Mark¹, E. Komatz¹, C. Markowitsch^{1,*}

¹: Department of environmental and energy process engineering, TU Leoben, Franz-Josef-Straße 18, 8700 Leoben, Austria

* Correspondent author: christoph.markowitsch@unileoben.ac.at

Keywords: Power-to-Gas, ASPEN Plus, Carbon Capture and Utilization

Introduction

The urgency to mitigate climate change and limit the rise in global average temperature to below 2 °C compared to pre-industrial levels (1990) requires significant reductions in greenhouse gas emissions across all sectors [1]. Within this context, the mineral industry faces considerable challenges. This is particularly evident in cement production, where a significant proportion of CO₂ emissions are considered "unavoidable" due to the calcination process inherent in clinker production [2]. In Austria, cement plants emitted approximately 3 Mt CO₂ in 2022, despite a decline in production volume compared to 2021 [3].

The European Emissions Trading System (EU-ETS) and Austria's national CO₂ tax further increased the economic pressure on carbon-intensive industries by raising the cost of greenhouse gas emissions [4]. Consequently, carbon capture and utilization (CCU) technologies offer promising pathways for the valorization of unavoidable CO₂ emissions. Among CCU technologies, the catalytic methanation of CO₂ shows great potential [5].

Catalytic CO₂ methanation involves converting CO₂ into synthetic methane (CH₄) using hydrogen (H₂). The synthetic CH₄ can be stored in the existing natural gas infrastructure, enabling the indirect storage of excess renewable electricity and its use as a versatile energy carrier for future demands or immediate consumption [6].

Accordingly, this work investigates how CO₂ from heavy emitting industrial sources can serve as a feedstock for Power-to-Gas (PtG) applications via catalytic methanation to synthetic methane (SNG). It further evaluates the performance of a PtG plant based on a techno-economic analysis (TEA) and a life cycle assessment (LCA) by comparing three scenarios with different feedstocks:

- Scenario 1: Fossil CO₂ from cement plant off-gas
- Scenario 2: Biogas from anaerobic digestion of biomass
- Scenario 3: Pyrolysis gas-derived from biomass

All scenarios are scaled to a uniform synthetic methane output of

approx. 34 t_{CH₄}/h, corresponding to an annual production of approximately 270,439 tons of CH₄. A cement plant, emitting 750,000 tons of CO₂ annually, with 100,000 tons of biogenic origin, serves as a case study for scenario 1 [7].

The main objectives of this work are (i) the comparison of mass and energy balances, (ii) the evaluation of the techno-economic viability, (iii) the assessment of the process related CO₂ emissions for each route and (iv) the calculation of the respective biomass demand.

Methodology

The aim of this study is to compare three distinct CO₂ methanation pathways. To achieve a meaningful comparison, all scenarios were scaled to achieve the same methane output. The methodology covers process modeling of the methanation plant in ASPEN Plus V14®, an economic assessment focusing on the net production costs (NPC, in EUR/kg_{CH₄}), and a life cycle assessment (LCA) using the open-source software openLCA® to determine the carbon footprint (in kg_{CO₂}/h).

The assessment was performed under the boundary condition that the product gas must comply with the Austrian gas grid standards (ÖVGW B210) [8]. To meet these standards, the product gas must contain >90 mol-% methane, <10 mol-% hydrogen, and <2.5 mol-% CO₂. Figure 1 shows the scope of the comparison in the form of a block flow diagram, highlighting the main process steps of each scenario as well as the system boundaries.

Process Modeling

The process simulations were conducted in ASPEN Plus V14® under steady-state conditions. The flow sheet of the simulation is shown in Figure 2. Each scenario integrates two major units: an electrolysis system and a two-stage methanation unit. Hydrogen production follows the reaction given in equation 1.

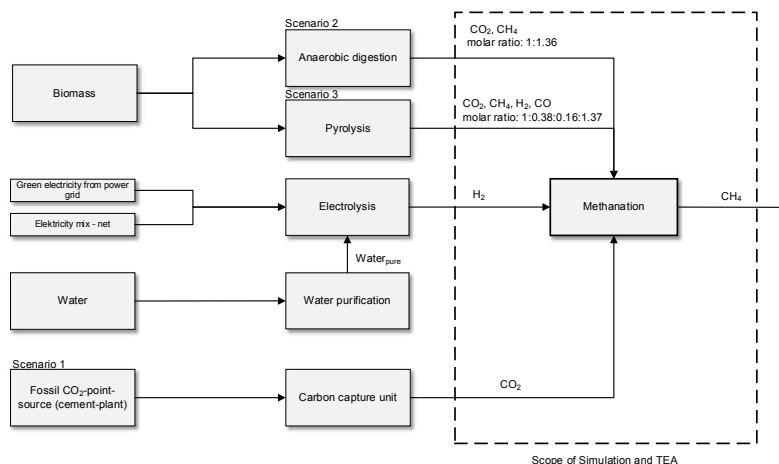


Figure 1: Block flow diagram for the production of methane from two different feedstocks with three distinct feed gas compositions

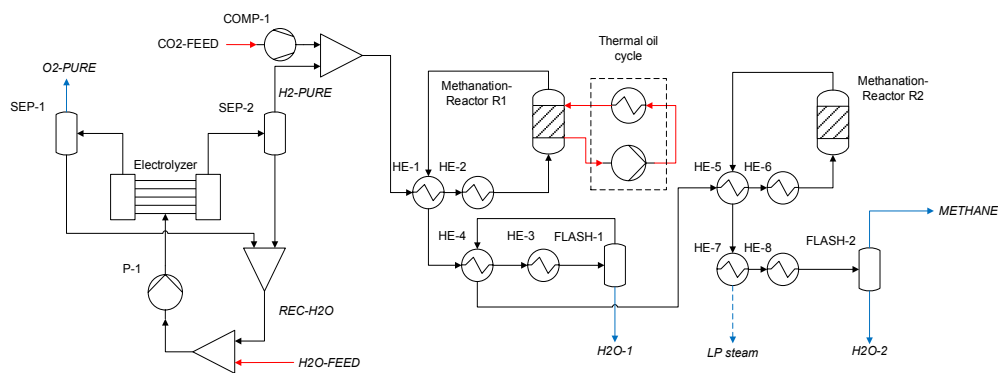
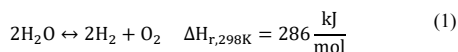
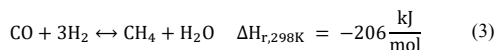


Figure 2: Flow sheet of the methanation process simulated in ASPEN Plus V14 ®

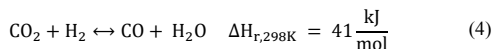


The electrolyzer is modeled as an alkaline system with a specific energy consumption of 4.7 kWh/Nm³H₂ and investment costs of 1000 EUR₂₀₂₄/kW [9–11].

The methanation process consists of two catalytic plug flow reactors (RPlug) in series. Reactor 1 (R1) operates at 350 °C and 8 bara, while Reactor 2 (R2) operates adiabatically at an inlet temperature of 270 °C and 7 bara. In the methanation process, CH₄ is formed along with H₂ from CO or CO₂ according to the reaction shown in equation 2 and equation 3, respectively. The underlying reaction kinetics follow the model of Rönsch et al. [12].



The reverse water-gas shift reaction (rWGS) couples the two reactions according to equation 4:



Economic Assessment

The economic evaluation of the different methanation scenarios was conducted with the approach from Peters et al. by calculating and comparing the Net Production Costs (NPC), expressed in EUR per kilogram of produced synthetic methane (\dot{m}_{CH_4}) as shown in equation 5 [13]. The annualized capital costs (ACC in EUR/year), required to set up the PtG plant, were estimated based on the fixed capital investment (FCI in EUR) e.g. equipment costs and are taken from the Aspen Process Economic Analyzer V14® (APEA).

$$\text{NPC} = \frac{\text{ACC} + \text{OPEX} + \text{ARC}}{\dot{m}_{\text{CH}_4}} \quad (5)$$

For a plant lifespan of 20 years (PL) and an interest rate of 7 % (IR) and working capital (WC), which is assumed to be 10 % of the FCI, the ACC are calculated according to equation 6 [13,14]:

$$\text{ACC} = (\text{FCI} + \text{WC}) * \frac{\text{IR} * (1 + \text{IR})^{\text{PL}}}{(1 + \text{IR})^{\text{PL}} - 1} - \frac{\text{WC}}{\text{PL}} \quad (6)$$

The operational expenditures (OPEX) were calculated by factoring in costs for raw materials, electricity, water, catalyst replacement, labor, maintenance, and any associated by-product

revenues. In addition, the annual replacement costs (ARC in EUR/year) were also considered for a more precise evaluation of the electrolysis unit.

Life Cycle Assessment and Biomass Demand

The Life Cycle Assessment (LCA) was conducted using the software openLCA® and includes the electrolysis unit and the methanation systems. The primary objective of the LCA was to compare the CO₂ emissions during methane production across the three scenarios, with particular focus on the source of CO₂, either fossil or biogenic emissions. The key metric used in the comparison are the process related CO₂ emissions per hour (in kgCO₂/h). To ensure a meaningful comparison, the LCA evaluates the environmental impact of utilizing green electricity as an alternative to the current Austrian energy mix on greenhouse gas emissions. Additionally, it assesses the potential benefits of process heat recovery.

For a detailed analysis, two main calculations are performed:

1. Baseline scenario: This scenario assumes the use of Austria's current energy mix, which had an emission factor of 127 gCO₂-eq./kWh in 2022 [15].
2. Green Electricity scenario: This scenario assumes the electricity used in the process originates entirely from renewable sources, resulting in a lower emission factor of 30 gCO₂-eq./kWh [16].

In addition to the carbon footprint, this study calculates the biomass quantity which would be necessary in scenario 2 and 3, along with the corresponding land area needed to achieve the same methane output as in scenario 1, where fossil CO₂ is used.

Results and Discussion

In scenario 1, the hydrogen demand is the highest with 17,604 kg/h, and the total electricity consumption is 845 MW, primarily due to the pure CO₂ feed. Scenario 2 (biogas) requires significantly less hydrogen (7,450 kg/h) and has the lowest electricity demand (354 MW) because of the higher methane content in the feed gas. In scenario 3 (pyrolysis gas), the hydrogen demand is 12,703 kg/h, and the total electricity consumption is 566 MW, as the mixed feed consisting of CO₂, CO, CH₄ and H₂ requires more hydrogen than biogas but less than scenario 1.

The mass and energy balances are listed in table 1 and 2. It can also be seen that the feed-in capability is achieved for all three scenarios.

Table 1: Mass balance of the methanation process for each route

Mass balance			Scenario		
Methanation			1	2	3
Inlet					
H ₂ -PURE	H ₂	kg/h	17,604	7,450	12,703
CO ₂ -FEED	CO ₂	kg/h	95,129	40,259	34,494
	CO	kg/h			30,114
	CH ₄	kg/h		19,845	4,707
	H ₂	kg/h			247
Outlet					
H2O-1	H ₂ O	kg/h	75,473	31,618	46,063
	H ₂	kg/h	1	0	1
	CH ₄	kg/h	123	63	87
	CO ₂	kg/h	108	30	48
H2O-2	H ₂ O	kg/h	1,650	823	1,059
	CH ₄	kg/h	2	1	2
	METHANE	CH₄	kg/h	34,302	34,302
Feed-in capability	CO	kg/h	45	22	21
	CO ₂	kg/h	507	357	297
	H ₂	kg/h	295	149	195
	H ₂ O	kg/h	227	189	190
	CH ₄	mol.-%	97	96	95
Feed-in capability	H ₂	mol.-%	1	3	4
	CO ₂	mol.-%	1	1	0

The results of the life cycle assessment (LCA) show significant differences in CO₂ emissions and biomass requirements across the analyzed scenarios, depending on the energy source, the implementation of heat recovery, and the type of feedstock used.

In scenario 1, CO₂ emissions are the highest, with 216 tCO₂/h without heat recovery, which decreases slightly to 202 tCO₂/h when heat recovery is implemented. Switching to 100% renewable electricity significantly reduces emissions to 120 tCO₂/h and further decreases to 117 tCO₂/h with heat recovery. In scenario 2 (biogas), emissions are much lower, with 12 tCO₂/h when using renewable electricity, compared to 52 tCO₂/h under the current electricity mix. Heat recovery further reduces emissions slightly to 11 tCO₂/h. scenario 3 (pyrolysis gas) shows a similar trend, with emissions

starting at 87 tCO₂/h under the current mix and reducing significantly to 21 tCO₂/h when using renewable electricity. The impact of heat recovery is minimal, reducing emissions further to 17 tCO₂/h.

Figure 4 provides a summarized comparison of the CO₂ emissions across all scenarios. The biomass demand for scenario 2 and scenario 3 was calculated based on their respective feedstock compositions (see table 1). In scenario 2, to produce the same methane output as scenario 1, 4.2 million tons of biomass per year are required, corresponding to 72% of Austria's annual biogas production [17]. In scenario 3, the biomass demand is 3.3 million tons per year, which translates to the deforestation of approximately 418 hectares annually, based on the average forest density in Austria [18].

The economic performance of each scenario was evaluated using the NPC. Based on the produced methane quantity (34,302 kg/h, Table 1), the NPC of 3.8 EUR/kg confirms that scenario 1 is the most cost intensive, compared to scenario 2 (1.9 EUR/kg) and scenario 3 (2.7 EUR/kg).

Table 2: Summarized energy balance of the methanation plant

Energy balance methanation		Scenarios		
		1	2	3
Total process electricity demand	MW	845	354	566
Comp-1	MW	4	4	5
P-1	kW	24	24	24
Electrolysis	MW	936	384	655
HE-2	MW	14	6	9
HE-6	MW	3	3	3
Steam generation (-) ¹	MW	-112	-43	-106
Total product energy content	MW	486	481	483
CH ₄	MW	476	476	476
CO ₂	MW	-	-	-
CO	MW	0	0	0
H ₂	MW	10	5	7

¹Steam generated from excess heat is seen as an energetic byproduct and therefore subtracted from the total energy demand.

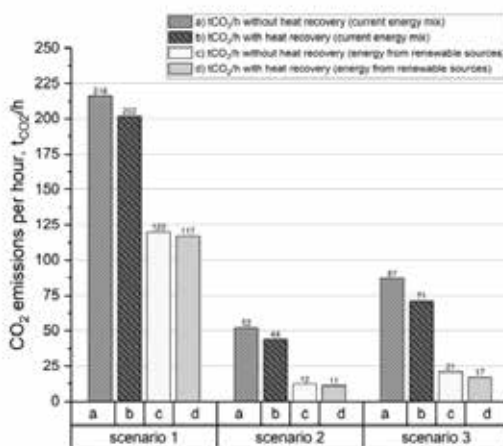


Figure 3: Summarized comparison of the CO₂ emissions in tCO₂ per hour for all scenarios 1-3, with a distinction of heat recovery and energy sources

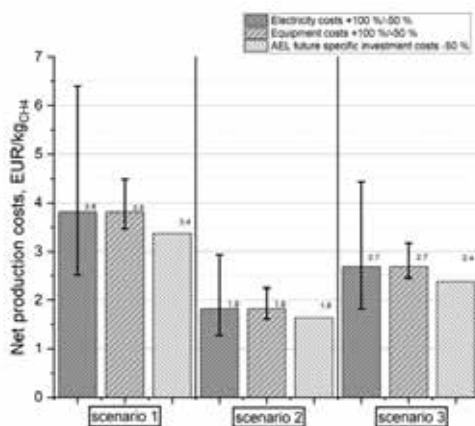


Figure 4: Sensitivity analysis of the scenarios analyzed related to the equipment costs, electricity price and future predicted AEL electrolyzer investment costs

It is apparent that the OPEX costs of the electrolysis unit are significantly lower for scenarios 2 and 3 compared to scenario 1 due to the reduced H₂ demand (see Table 1), which is a key factor in contributing to the substantially lower NPC in these scenarios. A sensitivity analysis was conducted to understand the impact of these key cost factors on the NPC. The results are shown in figure 3. The most significant factor influencing the cost of synthetic methane production was the electricity price, which accounts for a large share of operational costs, particularly in scenario 1. An increase of 100% of electricity costs would lead to a 71% higher NPC, from 3.8 EUR/kg_{CH₄} to nearly 6.5 EUR/kg_{CH₄}. Conversely, a -50% reduction in electricity prices could lower the NPC to approximately 2.5 EUR/kg_{CH₄}.

Additionally, variations in electrolyzer investment costs also affected the overall economics. A reduction in investment costs for the electrolyzer system from 1000 EUR/kW to 500 EUR/kW resulted in a slight decrease in NPC (from 3.8 EUR/kg CH₄ to 3.4 EUR/kg CH₄). On the other hand, a doubling of investment costs to 2000 EUR/kW led to a rise in NPC, reaching 4.5 EUR/kg CH₄.

Looking ahead, biomass-based CO₂ methanation will not be able to reach the scale of fossil-based CO₂ methanation systems due to limited and competing biomass availability in Austria. Future efforts must therefore prioritize the utilization of unavoidable process emissions and the direct use of renewable electricity, combined with process heat recovery and efficient CO₂ capture technologies.

References

- [1] 'Pariser Klimaschutzübereinkommen', <https://www.consilium.europa.eu/de/policies/climate-change/paris-agreement/>, accessed February, 2024
- [2] Mauschitz, G.: 'Emissionen aus Anlagen der österreichischen Zementindustrie: Endbericht', 2022
- [3] 'AUSTRIA'S ANNUAL GREENHOUSE GAS INVENTORY 1990–2022', <https://www.umweltbundesamt.at/fileadmin/site/publikationen/rep0892.pdf>, accessed July, 2024
- [4] 'Ökosoziales Steuerreformgesetz 2022 Teil I – ÖkoStRefG 2022 Teil I | Parlament Österreich', <https://www.parlament.gv.at/gegenstand/XXVIII/1293>, accessed March, 2025
- [5] Schmidt, M., Schwarz, S., Stürmer, B., Wagener, L., Zuberbühler, U.: 'Technologiebericht 4.2a Power-to-Gas (Methanisierung chemisch-katalytisch)', (2018)
- [6] Salbrechter, K., Lehner, M., Grimm, S.: 'Standardisierte Biogasaufbereitung und Methanisierung' (2021)
- [7] 'C2PAT-Partner setzen auf groß-industrielle Lösungen für CO₂-Management', <https://www.holcim.at/nachhaltigkeit/mit-c2pat-plus-zur-klimaneutralitaethttps://www.holcim.at/newsroom/detailsicht/c2pat-partner-setzen-auf-gross-industrielle-loesungen-fuer-co2-management>, accessed May, 2024
- [8] 'ÖVGW G B210', 06.2021
- [9] Albrecht, F.G., König, D.H., Baucks, N., Dietrich, R.-U.: 'A standardized methodology for the techno-economic evaluation of alternative fuels – A case study', *Fuel*, 2017, **194**, pp. 511–526
- [10] Saba, S.M., Müller, M., Robinus, M., Stolten, D.: 'The investment costs of electrolysis – A comparison of cost studies from the past 30 years', *International Journal of Hydrogen Energy*, 2018, **43**, (3), pp. 1209–1223
- [11] Davies, J., Dolci, F., Weidner, E.: 'Historical analysis of FCH 2 JU electrolyser projects: Evaluation of contributions towards advancing the state of the art' (Publications Office of the European Union, Luxembourg, 2021)
- [12] Rönsch, S., Köchermann, J., Schneider, J., Matthischke, S.: 'Global Reaction Kinetics of CO and CO₂ Methanation for Dynamic Process Modeling', *Chem Eng & Technol*, 2016, **39**, (2), pp. 208–218
- [13] MS Peters, KD Timmerhaus, RE West: 'Plant design and economics for chemical engineers' (2003)
- [14] Herz, G., Rix, C., Jacobasch, E., et al.: 'Economic assessment of Power-to-Liquid processes – Influence of electrolysis technology and operating conditions', *Applied Energy*, 2021, **292**, p. 116655
- [15] 'AGGREGATED EMISSIONS FOR 2022', <https://www.nowtricity.com/country/austria/>, accessed July, 2024
- [16] 'GHG Emission Factors for Electricity Consumption', <http://data.europa.eu/89h/919df040-0252-4e4e-ad82-c054896e1641>, accessed July, 2024
- [17] 'Implementation of bioenergy in Austria – 2021 update', https://www.ieabioenergy.com/wp-content/uploads/2021/11/CountryReport2021_Austria_fina.pdf#:~:text=URL%3A%20https%3A%2F%2Fwww.ieabioenergy.com%2Fwp, accessed July, 2024
- [18] 'Forest cultural heritage in Germany', <https://www.deutschland.de/en/topic/environment/how-large-are-germanys-forests-facts-and-figures>, accessed July, 2024

Hydrogen and its Applications

Posters

Day 2

BIOcubed: Biosynthesis of Green Hydrogen Using a Newly Discovered Microorganism

Selina Haller^{1*}, Andreas Wagner², Mira Mutschlechner¹, Harald Schöbel¹

1: Department Food Science & Biotechnology, MCI International University of Applied Sciences GmbH, Innsbruck, Austria

2: Department of Microbiology, Universität Innsbruck, Innsbruck, Austria

* Correspondent author: selina.haller@mci.edu

Keywords: Biohydrogen production, *Thermoactinomyces mirandus*, dark fermentation, process optimization, climate neutrality

In order to achieve the objective of climate neutrality by 2040, the Austrian government is placing an increasing emphasis on the expansion of renewable energy sources [1]. Hydrogen (H₂) plays a pivotal role in this strategy as a clean energy carrier with the potential to replace fossil fuels and facilitate the decarbonization of various sectors [2]. Among the methods for biological H₂ production, dark fermentation using anaerobic bacteria has gained significant attention [3]. Recently, *Thermoactinomyces mirandus*, a thermophilic bacterium first isolated in 2015 from a biogas plant in Tyrol, Austria, has shown promise for H₂ production under anaerobic conditions [4]. To explore the potential of *T. mirandus* in H₂ production, the BIOcubed project was launched to develop an efficient and economical process for generating H₂ from lactose-containing biomass and other renewable resources by leveraging the bacterium's unique properties.

The primary objective of the present study was to optimize H₂ biosynthesis by *T. mirandus* in small-scale systems, focusing on cultivation conditions to maximize H₂ yield. Standard anaerobic media preparation and cultivation were performed in serum bottles (50 mL working volume) under controlled conditions: pH 7.2 ± 0.1, temperature 51.4 ± 0.2 °C, and defined nutrient concentrations with lactose as the carbon source (0.8 g C/L) and yeast extract as the nitrogen source (0.04 g N/L).

Experimental results revealed that yeast extract combined with fructose or xylose produced significantly higher H₂ yields compared with yeast extract and lactose. Further optimization of the carbon-to-nitrogen (C:N) ratio demonstrated that reduced carbon concentrations (0.8 g C/L) improved substrate utilization and enhanced H₂ production. For each carbon source and concentration, a specific C:N ratio optimum was determined. Additionally, the influence of initial pH and temperature on H₂ yield was systematically evaluated, with optimal conditions established for maximizing H₂ production. Metabolite analysis using HPLC-RID revealed succinate, lactate, acetate, and ethanol as key fermentation (by)products, aligning with mixed acid fermentation pathways characteristic of H₂-producing bacteria. This study further investigated potential inhibitory factors affecting H₂ production, such as acidification of the medium and elevated H₂ partial pressure. The findings demonstrated that pH regulation and gas-phase sparging with nitrogen significantly improved H₂ yields.

The study established a reproducible and optimized process, while further characterizing *T. mirandus* in terms of its functional and metabolic properties. The results provide a solid foundation for upscaling the process to laboratory scale and adapting it to use waste products as substrates to enhance sustainability according to the principles of a circular economy.

- [1] Bundesministerium für Klimaschutz, Umwelt, Mobilität, Innovation und Technologie BMK; Klima- und Energiefonds, Ed., 'Energiewende im Praxistest - Reallabore für die klimaneutrale Energieversorgung', vol. 3, 2023.
- [2] Bundesministerium für Klimaschutz, Umwelt, Mobilität, Innovation und Technologie BMK; Klima- und Energiefonds, Ed., 'Wasserstoff für die Energiewende - Forschung und Technologieentwicklung in Österreich', *Energy innovation austria*, vol. 4, 2023.
- [3] Y. Cao, H. Liu, W. Liu, J. Guo, and M. Xian, 'Debottlenecking the biological hydrogen production pathway of dark fermentation: insight into the impact of strain

improvement', *Microb Cell Fact*, vol. 21, no. 1, Art. no. 1, Aug. 2022, doi: 10.1186/s12934-022-01893-3.

- [4] M. Mutschlechner, N. Lackner, R. Markt, W. Salvenmoser, C. A. Dunlap, and A. O. Wagner, 'Proposal of *Thermoactinomyces mirandus* sp. nov., a filamentous, anaerobic bacterium isolated from a biogas plant', *Antonie van Leeuwenhoek*, vol. 114, no. 1, Art. no. 1, Jan. 2021, doi: 10.1007/s10482-020-01497-0.

Hydrogen Storage in Magnesium-Based Metal Powders: Influence of Production and Activation Methods

E. Vigl^{1*}, J. Eisbacher-Lubensky², C. Weiß¹, S. Gneiger³, S. Edinger⁴, M. Dopler⁵, P. Schäffler⁶

1: Chair of Process Technology and Industrial Environmental Protection, Montanuniversität Leoben, Austria

2: Chair of Ferrous Metallurgy, Montanuniversität Leoben, Austria

3: LKR Light Metals Technologies, AIT Austrian Institute of Technology, Austria

4: Center for Energy, Power and Renewable Gas Systems, AIT Austrian Institute of Technology GmbH, Austria

5: Metalpine GmbH, Austria

6: non ferrum GmbH, Austria

* Correspondent author: elias.vigl@unileoben.ac.at

Keywords: hydrogen storage, activation methods, metal hydrides, magnesium-based materials

The magnesium/magnesium hydride system is a promising candidate for hydrogen storage, offering high gravimetric and volumetric storage capacities of up to 7.7 wt.% and 110 gL⁻¹ [1]. To enhance gas-solid interaction, these storage materials are typically utilized in the form of fine-grained metal powders.

Powder production techniques vary: mechanical methods such as crushing, scratching, grinding, and milling achieve size reduction, while gas atomization involves melting the metal and dispersing it finely using an inert gas at high cooling rates to obtain the desired powder characteristics. Additionally, chemical synthesis from precursor substances, such as organic magnesium compounds, has been explored [2,3].

Due to the low standard potential of magnesium metal, its alloys exhibit high reactivity, which can lead to passivation effects such as the formation of oxide and hydroxide surface layers when exposed to humid air [4]. These layers act as diffusion barriers for hydrogen and make initial activation a challenging process [5]. Consequently, selecting an effective activation strategy is crucial for the technical applicability of magnesium-based hydrogen storage materials [6].

This study examines the influence of powder production processes on the hydrogenation and dehydrogenation behavior of Mg-based powders, as well as the effects of activation methods (mechano-thermal and homogeneous catalytic techniques). The absorption and desorption properties were evaluated using Sieverts experiments, including Pressure-Composition-Isotherms (PCI) and non-equilibrium absorption experiments. To quantify the hydride content and estimate dehydrogenation kinetics, Simultaneous Thermal Analysis (STA) was applied. Additionally, phase composition was analyzed via X-ray powder diffraction (XRD), with further characterization conducted through scanning electron microscopy (SEM) and specific surface measurements (BET method).

The results demonstrate that initial hydrogenation dynamics are significantly influenced by both the powder production technique and the selected activation method. These variations are attributed to differences in microstructure, dislocation density, and passivation layer characteristics. Notably, chemical activation enabled substantial hydrogenation rates at room temperature, even for pure magnesium powders.

Ultimately, optimal powder activation is key to ensuring the technical feasibility of hydrogen storage, making it a critical consideration in the design of effective storage systems.

[4] Abreu, J. B., et al., "The interfacial chemistry of the Grignard reaction: The composition of the film formed on air-exposed magnesium," *Journal of Colloid and Interface Science*, vol. 206, pp. 247–251, 1998. doi:10.1006/jcis.1998.5681

[5] Xinglin, Y., et al., "Progress in improving hydrogen storage properties of Mg-based materials," *Materials Today Advances*, vol. 19, 100387, 2023. doi:10.1016/j.mtadv.2023.100387

[6] Klopčič, N., et al., "A review on metal hydride materials for hydrogen storage," *Journal of Energy Storage*, vol. 72, 108456, 2023. doi:10.1016/j.est.2023.108456

[1] Hirscher, M. (Ed.), *Handbook of Hydrogen Storage: New Materials for Future Energy Storage*, 1st ed., Weinheim: Wiley-VCH, 2010.

[2] Bogdanović, B., et al., "Catalytic synthesis of magnesium hydride under mild conditions," *Angewandte Chemie International Edition in English*, vol. 19, pp. 818–819, 1980. doi:10.1002/anie.198008181

[3] Bogdanovic, B., "Magnesium anthracene systems and their application in synthesis and catalysis," *Accounts of Chemical Research*, vol. 21, pp. 261–267, 1988. doi:10.1021/ar00151a002

Platinum-cobalt ORR Catalyst Degradation in LT-PEFCs: Effects of Anode-Cathode Humidity Gradients

J.M. Edjokola^{1,*}, Viktor Hacker¹, M. Bodner¹

¹: Institute of Chemical Engineering and Environmental Technology, Graz University of Technology, Austria

* Correspondent author: joel.edjokola@tugraz.at

Keywords: ORR catalyst, degradation, relative humidity, gradient

Low-temperature polymer electrolyte fuel cells (LT-PEFCs) are a promising clean energy technology, particularly for transportation, where their high efficiency and fast start-up are clear advantages [1]. To support their continued adoption, it is essential to deepen our understanding of how catalyst materials behave under realistic operating conditions. While the degradation behavior of Pt-based catalysts has been widely investigated under controlled and uniform humidity conditions, the effects of dynamic and spatially asymmetric humidity, characteristic of real-world fuel cell operation, remain underexplored. In this study, we examine the degradation mechanisms of Pt₃Co alloy catalysts subjected to relative humidity (RH) gradients using an accelerated stress testing protocol recommended by the U.S. Department of Energy [2].

Two operating scenarios are tested [3]: a baseline with uniform 100% RH at both electrodes and a humidity gradient condition with 30% RH at the anode and greater than 100% RH at the cathode. Under gradient conditions, the Pt₃Co catalyst exhibited a 77% drop in fuel cell performance and significant losses in electrochemical surface area, indicating greater structural vulnerability compared to pure Pt systems. Morphological and structural analyses using small-angle X-ray scattering and scanning electron microscopy revealed particle coarsening, catalyst layer heterogeneities, and membrane thinning. These physical changes are consistent with degradation mechanisms dominated by Ostwald ripening and further accelerated by dealloying, surface area loss, and increased charge and mass transport resistances. Our findings highlight the detrimental impact of humidity gradients on Pt-alloy stability and emphasize the importance of water management strategies in maintaining fuel cell performance over time. By revealing the distinct degradation behavior of Pt₃Co under non-uniform RH, this work advances the understanding of alloy catalyst resilience and informs the design of more robust materials and operational protocols for next-generation LT-PEFC systems.

Acknowledgements

This research was supported in part by the Austrian Research Promotion Agency (FFG) through the projects Hermes-FCV and AlpeDHues. The authors also acknowledge contributions within the framework of IEA Hydrogen TCP Task 30.

References

- [1] Lafforgue C., Toudret P., Micoud F., Heitzmann M., Blachot J-F, Chatenet M. Manufacturing of carbon-supported platinum cathodes for proton exchange membrane fuel cell using the doctor blade process: Microstructure and performance. *Journal of Power Sources* 2025(627):23581. <https://doi.org/10.1016/j.jpowsour.2024.23581>.
- [2] Strategy Advisory Committee of the Technology Roadmap for Energy Saving and New Energy Vehicles. *Hydrogen Fuel Cell Vehicle Technology Roadmap* 2015.
- [3] Edjokola J.M., Bogar M., Grandi M., Taccani R., Amenitsch H., Marinšek M. et. al. Humidity-Induced Degradation Mapping of Pt₃Co ORR Catalyst for PEFC by In-Operando Electrochemistry and Ex Situ SAXS. Small (Weinheim an der Bergstrasse, Germany) 2024;20(51):e2407591. <https://doi.org/10.1002/sml.202407591>.

Lifecycle Greenhouse Gas Emissions and Energy Efficiency of Fuel Cell Electric Trucks in Alpine Applications

Lucas Schuchter^{1,*}, Anna Holzkecht¹, Martin Spruck¹

¹: Dept. of Environmental, Process & Energy Engineering, MCI Management Center Innsbruck, Austria

* Correspondent author: lucas.schuchter@mci.edu

Keywords: Fuel Cell Electric Trucks (FCET), Alpine Transport, Life Cycle Assessment (LCA), Energy Efficiency

Introduction

Decarbonizing mobility is a major concern in setting up sustainable energy systems. Transport is responsible for 41 % of greenhouse gas (GHG) emissions in the federal state of Tyrol, Austria, thus being the largest emitter [1]. Heavy duty freight transport is considered harder to decarbonize through electrification than passenger transport. Fuel Cell Electric Trucks (FCET) and Battery Electric Trucks (BET) are projected to make up 30 % and 70 %, respectively, of heavy duty transport in Tyrol by 2050 [2]. While the applicability, environmental sustainability and energy efficiency of FCET in urban areas is well studied, their deployment in alpine regions is underrepresented in research.

As part of the project H2Alpin the aim of this study is to estimate and quantify GHG emissions and energy efficiency of FCET and compare them to BET and conventional Internal Combustion Engine Diesel Trucks (ICET).

Methodology

To calculate life cycle environmental impacts, the methodology of life cycle assessment (LCA) according to the ISO standards 14040/14044 is applied. The functional unit is the transport of one metric ton of unspecified goods over a distance of one kilometer. The system is modelled as cradle-to-grave, also including estimates of the end-of-life emissions of material disposal. *Umberto II* by *iPoint systems* was applied as an LCA modelling tool. Background data was obtained from *ecoinvent 3.9.1*.

In inventory analysis, material balances for the vehicles' construction were taken from literature [3] and fitted accordingly to *ecoinvent* data. Well-to-wheel analyses were conducted for different technologies of electricity and hydrogen production. For BEV the Austrian grid electricity mix, electricity from a representative renewable electricity mix for Tyrol and electricity from run-of-river (RoR) hydropower plants were used. For hydrogen production scenarios for yellow hydrogen produced from the Austria grid electricity mix, green hydrogen from a representative renewable energy mix for Tyrol and hydrogen produced from RoR via direct line were modeled. Well-to-wheel data for Diesel was directly obtained from the *ecoinvent* database. To model alpine routes, two representative routes have been chosen. As a route with moderate slope, the route Kufstein-Brenner Pass has been modeled with slopes between 0 and 2 % [4]. As a second scenario the route Innsbruck-Kühtai has been modeled as a route with strong alpine characteristics. Slopes were calculated to be in the range of -1.54 % to 13.99 %.

For Impact Assessment two impact categories have been selected, namely Climate Change (CC) expressed as an amount of emissions in kg CO₂-eq t⁻¹ km⁻¹ and the Cumulative Energy Demand (CED) as MJ-eq t⁻¹ km⁻¹.

Results and Interpretation

While the impacts are only marginally larger in case of the route Kufstein-Brenner Pass, due to 2/3 of the route being in the flat and with moderate slope afterwards, a heavy increase in environmental impacts is observed in case of the route Innsbruck-Kühtai. With an

average slope of 4 % and a steepest slope up to 13.99 %, demands for power provision are strongly increased (Figure 1).

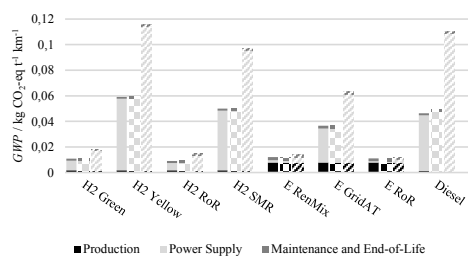


Figure 1: GWP of heavy duty transportation modes. Scenarios: 0% slope - solid, Kufstein-Brenner Pass - chequered, Innsbruck-Kühtai - dashed

As for the technologies, the need for renewable power as energy source is highlighted. When using grid electricity for power and hydrogen supply, the GHG emissions of BET and FCET are even higher than those of ICET. When renewable electricity is used, results for CC and CED are heavily reduced. As for the use phase, BEV overall show slightly lower impacts than FCEV when renewables are used. However, with the use of renewables, BET's advantage shrinks or vanishes, as emissions from vehicle production make up a higher fraction of overall impacts.

Conclusion

The results show, that alpine conditions influence the environmental impacts of heavy duty freight transport. BEV and FCEV show strong potential for emission reduction on alpine routes through higher energy efficiency by recuperation and low renewable energy environmental impacts. Next steps should look at other environmental impacts such as particulate matter formation, as preliminary research showed potential drawbacks for BEV and FCEV through additional weight. Primary and measured consumption data for FCEV is planned to be integrated from demonstration phases within the project H2Alpin.

List of References

- [1] Stampfer, C., Egg, J., Goertz, S., Dobler, C., Salcher, P., „Tiroler Nachhaltigkeits- und Klimastrategie – Monitoring Bericht 2024,“ Amt der Tiroler Landesregierung, Innsbruck, 2024.
- [2] Ebenbichler, R., Gleirscher, R., Hertl, A., Hofmann, A., Schaaf, N., Streicher, W., Tosatto, A., Mailer, M., Neugebauer, D., „Energie-Zielszenario Tirol 2025 – Aktualisierung 2024,“ Amt der Tiroler Landesregierung, Abteilung Wasser-, Forst- und Energierecht, Innsbruck, 2024.
- [3] Wolff, S., Seidenfus, M., Gordon, K., Álvarez, S., Kalt, S., Lienkamp, M., „Scalable Life-Cycle Inventory for Heavy-Duty Vehicle Production,“ *Sustainability*, 12(13), 5396, 2020. doi: 10.3390/su12135396
- [4] Sedlacek, N., „Entwicklung der Energieeffizienz des transitierenden Güterverkehrs am Brennerkorridor in Tirol,“ Amt der Tiroler Landesregierung, Abteilung Mobilitätsplanung, 2023.



TINEXT

Innovative und nachhaltige Energielösungen für Tirol

Zur Erreichung der Klimaziele wird Wasserstoff ein zentraler Baustein des künftigen Energiesystems sein. TINEXT unterstützt diese Ziele mit der Umsetzung von nachhaltigen sowie bedarfs- und anforderungsgerechten Wasserstoffprojekten.



Circular Economy & Recycling Presentations

Day 2

Producing Packaging Paper from Post-Consumer Textile Waste

T. Harter¹, A. Wagner¹, A. Weissensteiner¹ and U. Hirn^{1,*}

¹ Institute of Bioproducts and Paper Technology, Graz University of Technology, Inffeldgasse 23, 8010 Graz, Austria

* Correspondent author: ulrich.hirn@tugraz.at

Keywords: Textile Recycling, Circularity, Packaging Paper, Cellulose

Introduction

Fast fashion is driving a surge in textile consumption, leading to significant waste generation, with 92 million tons of textile waste produced globally in 2017 (Amicarelli & Bux, 2022). The majority of this waste is disposed of in landfills or subjected to thermal recovery (Niinimäki et al., 2020), rather than being recycled. In Europe, a total of 6.95 million tons of textile waste was generated in 2020, with 72.5% ending up in mixed household waste, making it highly likely to be landfilled or incinerated (Deckers et al., 2024). More recent estimates indicate an even higher waste volume of 11 million tons annually, with 80% of it being disposed of through landfilling or thermal recovery (Napolano et al., 2025). Added to this is the 1.7 million tons of used textiles, of which nearly 90% are exported to Africa and Asia in an unsorted state, with a significant portion ultimately ending up in disposal sites. Cotton is an excellent fiber source for paper production due to its long fibre length and biodegradability underscoring the importance of recovering it from waste streams.

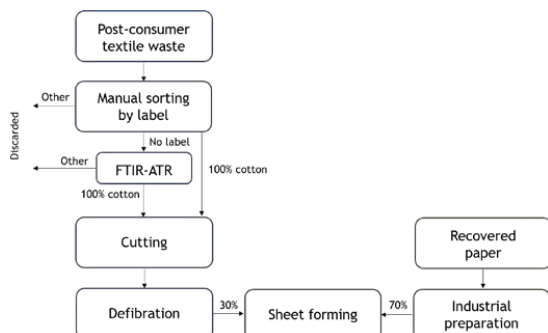


Figure 1. Scheme of the preparation of handsheets made as mixture of post-consumer waste and recycled paper.

This study proposes a recycling pathway for post-consumer textile waste by integrating it into the packaging paper industry. While most existing textile recycling technologies focus on post-production waste (Baloyi et al., 2024), the majority of post-consumer textiles are currently landfilled or incinerated. We propose integrating low-quality textile waste and other underutilized cotton waste streams into the highly circular paper packaging cycle. In the following we will demonstrate that post-consumer textiles are a suitable raw material for producing corrugating liner (containerboard) and folding boxboard (cartonboard). We will describe a process to convert post-consumer cotton textiles from a commercial supplier to papermaking pulp. This pulp is then used to produce packaging paper on the lab scale.

Materials and Methods

A waste management and recycling company supplied actual post-consumer textile waste consisting of a 26kg mix of clothing and home textiles in post-collection condition. The packaging paper raw stock was sourced from two European industrial packaging paper manufacturers. The textiles used in this study were analyzed with FTIR-ATR spectroscopy, only textile samples composed of 100%

cotton were selected. An in-house developed cutting device equipped with 60 mm rotary cutter blades was used to cut the textiles to patches of 5×5 mm², 10×10 mm², and 20×20 mm². The defibration process was carried out using a valley beater (ABB, Switzerland) mostly following ISO 5264-1, with some adaptations to accommodate the processing of textile fibres. For each defibration experiment, 360g (oven-dry) of cut textile slices were used. The material was diluted with deionized water to achieve a suspension consistency of 1.5%. The valley beater was equipped with a 5500g weight mounted on the lever, applying a constant force to a plate pressing onto the rotating grinder. A commercial anti-foaming agent Glanapon 6233 (Bussetti, Austria) based on fatty acids was used at a concentration of 0.15 g/L to avoid foaming during defibration.

Before sheet forming, the pulp was disintegrated according to ISO 5263-1:2004. Then sheets with a grammage of 80g/m² were produced using a Rapid-Köthen handsheet former RK-4A (PTI Instruments, Germany), following EN-ISO 5269-2:2004. The fibre dimensions of the pulps were assessed using an L&W Fibertester+ image analyser according to ISO 16065-2. Drainability of the pulp suspensions in terms of the Schopper-Riegler (SR) number was determined according to EN ISO 5267-1. Paper tensile strength was measured in accordance with ISO 1924-2. Paper bending stiffness was evaluated following ISO 5628:2019, assessing the resistance of the sheets to bending deformation. The compressive strength of the sheets was determined using the short-span compression test (SCT) performed on a universal testing machine proline Z010 (ZwickRoell, Germany) according to ISO 9895.

Results and Discussion

Fiber morphology is highly relevant for good mechanical properties of the resulting paper (Horn, 1974). The average length-weighted fibre lengths for different defibration times of textiles, as shown in Figure 2, do not exhibit a clear trend concerning the cut size of the fabric slices. However, it seems, the 10x10mm² slices mostly have the maximum fibre length.

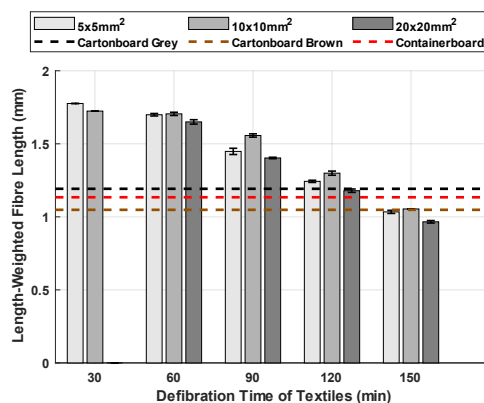


Figure 2. Length-weighted fibre length for different textile cut sizes at different defibration times. Dotted lines indicate reference values for the industrial paper stock. Error bars represent twice the standard deviation.

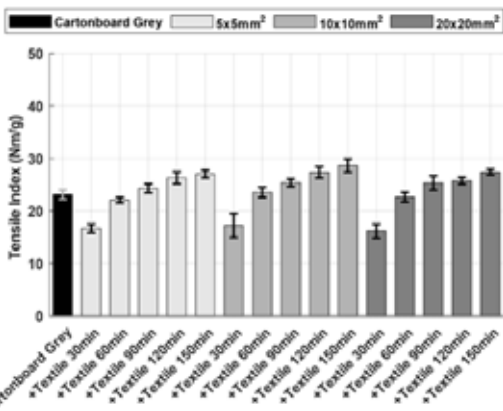


Figure 3. Tensile index of paper sheets composed of 70% grey cartonboard stock and 30% textile fibre suspension. The leftmost bar (black) represents pure industrial paper stock without textile fibres. Bars to the right represent mixtures containing textile fibres, grouped by textile cut size (5×5 mm² – light grey, 10×10 mm² – grey, and 20×20 mm² – dark grey).

Figure 3 shows the tensile index of the sheets for both cartonboard mixed with 30% textile waste fibres. A clear trend is observed with increasing valley beater defibration time, leading to an enhancement in the tensile index. This improvement can be attributed to increased external fibrillation, higher fiber flexibilization and fines generation, which contribute to denser fibre networks and enhanced fibre-fibre bonding. A defibration time of 60 minutes resulted in a tensile index comparable to that of sheets made entirely from cartonboard grey pulp.

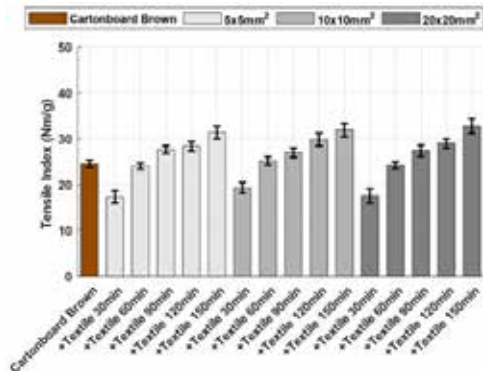


Figure 4. Tensile index of paper sheets composed of 70% brown cartonboard stock and 30% textile fibre suspension. The leftmost bar (brown) represents pure industrial paper stock without textile fibres.

Bending stiffness is the most crucial parameter for cartonboard, as it determines the structural integrity and resistance of the material against folding or deformation during handling and packaging applications (Fellers & Carlsson, 2001). The results in Figure 5, show that bending stiffness for mixtures of cotton fibres and recycled pulps remained comparable to or higher than that of pure industrial pulps for defibration times up to 120 minutes.

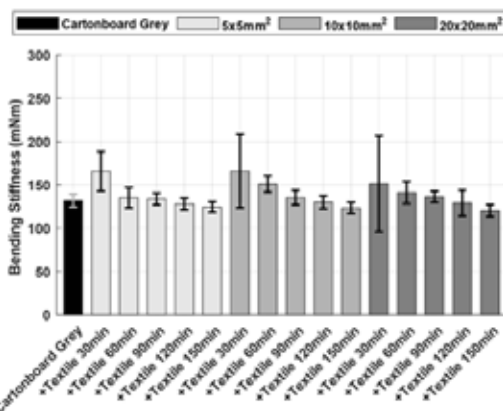


Figure 5. Bending stiffness of cartonboard (grey and brown) mixtures. The leftmost bar (black or brown) represents pure industrial paper without textile fibres. Bars to the right represent mixtures containing textile fibres, grouped by textile cut size (5×5 mm² – light grey, 10×10 mm² – grey, and 20×20 mm² – dark grey).

The key mechanical property of hence is the in-plane compressive strength of the material (Bronkhorst & Benett, 2001), measured by the short span compression test (SCT). SCT measurements were conducted on both the industrial paper stock and its mixtures with textile fibres, as shown in Figure 6. Here, apart from the sample defibrated for 30 minutes, comparable SCT results were achieved when incorporating textile waste into containerboard pulp.

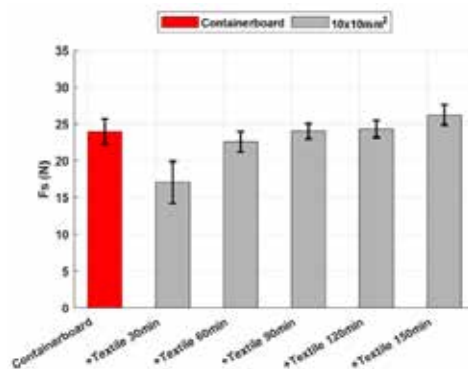


Figure 6. Short-span compression strength (SCT) of containerboard mixtures with 10x10mm² cut textiles. The leftmost bar (red) represents pure recycled paper without textile fibres.

Conclusions

In this study, we demonstrated a straightforward-to-implement process for conversion of post-consumer textile waste into a papermaking suspension. The resulting fibre suspension was benchmarked against industrial papermaking stock collected from large scale linerboard- and cartonboard mills. Best results were achieved for a 10x10mm² cut size of the patches and 60-90 minutes of mechanical defibration. The resulting textile suspension had superior fibre length and a good dewatering ability, which is necessary for industrial paper production. By incorporating 30% textile suspension into the industrial fibre stock, we demonstrated that paper produced from this suspension had equal or even better mechanical properties. The key performance indicators for these packaging grades – tensile strength, bending stiffness (for cardboard) and short span compression strength SCT (for linerboard) – met or even exceeded the industrial benchmarks. These findings

confirm that cotton fibres can be successfully extracted from textile rags and fibrillated to serve as a quality fibre source for paper packaging. This opens the potential for utilizing a wide range of cotton textile waste grades – both, pre- and post-consumer – within the packaging paper recycling loop. Further research will focus on upscaling the process.

References

Amicarelli, V., & Bux, C. (2022). Quantifying textile streams and recycling prospects in Europe by material flow analysis. *Environmental Impact Assessment Review*, 97, 106878. <https://doi.org/10.1016/j.eiar.2022.106878>

Baloyi, R. B., Gbadeyan, O. J., Sithole, B., & Chunilall, V. (2024). Recent advances in recycling technologies for waste textile fabrics: a review. *Textile Research Journal*, 94(3–4), 508–529. <https://doi.org/10.1177/00405175231210239>

Bronkhorst, C. A., & Benett, K. A. (2001). Deformation and Failure Behavior of Paper. In *Handbook of Physical Testing of Paper* (2nd ed., pp. 313–428). CRC Press.

Fellers, C., & Carlsson, L. A. (2001). Bending Stiffness, with Special Reference to Paperboard. In *Handbook of Physical Testing of Paper* (2nd ed., pp. 233–256). CRC Press.

Horn, R. A. (1974). Morphology of wood pulp fiber from softwoods and influence on paper strength (Vol. 242). US Department of Agriculture, Forest Service, Forest Products Laboratory,.

Napolano, L., Foschi, J., Caldeira, C., Huygens, D., & Sala, S. (2025). Understanding textile value chains: Dynamic Probabilistic Material Flow Analysis of textile in the European Union. *Resources, Conservation and Recycling*, 212, 107888. <https://doi.org/10.1016/j.resconrec.2024.107888>

Niinimäki, K., Peters, G., Dahlbo, H., Perry, P., Rissanen, T., & Gwilt, A. (2020). The environmental price of fast fashion. *Nature Reviews Earth & Environment*, 1(4), 189–200. <https://doi.org/10.1038/s43017-020-0039-9>

*Den
ersten
Kuss vergisst
man nie.*



Numerical development of thermal pre-treatment for Li-ion battery recycling

E. E. Barros de Souza^{1,2,*}, C. Spijker²

1: K1-MET GmbH, Austria

2: Chair of Thermal Processing Technology, Montanuniversität Leoben, Austria

* Correspondent author: emerson.barros@k1-met.com

Keywords: Lithium-ion battery, Recycling, Pre-treatment, CFDEMcoupling

Introduction

The use of lithium-ion batteries (LIBs) has been extensively studied for their applications in electronic products, electric vehicles (EVs), and various energy storage devices due to lithium's high energy density, low self-discharge rate, and lack of memory effect [1]. Given that the service life of EV batteries typically ranges between five and eight years, the number of spent batteries is expected to increase significantly as current EVs become obsolete [2], with global end-of-life EV battery capacity projected to reach 174 GWh by 2030, surpassing the total installed EV battery capacity of 136.3 GWh in 2020 [3]. Motivated by carbon neutrality goals, the European Union has introduced regulations requiring target collection rates for portable batteries and light means of transport (LMT) batteries [4], with lithium recovery rates set to rise from 50% in 2027 to 80% by 2031. Furthermore, predictions indicate a significant increase in demand for battery cathode materials, particularly lithium, with supply estimated to reach 1,000 tons by 2030, while demand is expected to soar to approximately 2,750 tons, potentially leading to significant deficits in these elements [3].

The use of lithium-ion batteries (LIBs) is essential for achieving carbon neutrality in energy storage, ensuring a sustainable and climate-neutral transport system, and supporting the energy transition [5]. Establishing large-scale recycling and securing the necessary raw materials are essential to meet the rising energy demand. Currently, hydro- and pyrometallurgical routes dominate the industrial LIB recycling processes for recovering valuable metals, with the bio-metallurgical route also emerging as a potential method. To improve recovery rates while ensuring safety, battery deactivation is a viable strategy, preventing the formation of harmful hydrofluoric acid, reducing gas emissions, and mitigating risks such as thermal runaway, fires, and explosions [6]. This process enhances material separability in subsequent recycling steps by involving dismantling, discharging, electrolyte evaporation, and mechanical processing [7].

The present study focuses on thermal deactivation pre-treatment for LIB recycling, exploring its potential to improve the recovery of precious metals. It is divided into experimental and simulation components: the experimental part involves replicating the thermal deactivation of batteries on a small scale to collect data on temperature and off-gases during thermal runaway, while the simulation part uses this data to model the process and identify key variables, with the goal of proposing improvements to maximize material recovery in large-scale industrial applications.

Methodology

Thermal deactivation experiments

An experiment was designed to replicate the thermal deactivation process. The goal is to simulate, on a small scale, the conditions of thermal deactivation under controlled temperature conditions. A schematic of the experimental setup is shown in Figure 1.

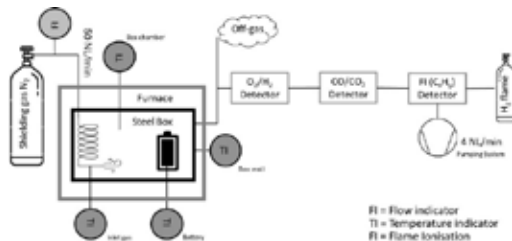


Figure 1. Flowchart of the thermal deactivation experiment

The battery was placed inside a steel box, with four thermocouples positioned at various locations to monitor the temperature throughout the experiment. The box was then sealed and placed inside a furnace, which was set to heating mode. Nitrogen was introduced into the steel box to create forced convection and facilitate gas transport to the detectors. The laboratory furnace was programmed to heat at a rate of 9 K/min. At approximately 220–230 °C, the battery reaches the thermal runaway, releasing off-gases and thermal energy. The gases were collected by a pumping system, which directed them through a series of gas analyzers to measure the concentrations of specific chemical species. The battery's state of charge was kept as received from the manufacturer.

Thermal deactivation modelling

A numerical model combining computational fluid dynamics (CFD) and the discrete element method (DEM) was used to simulate the battery deactivation process. This approach incorporates three software components: OpenFOAM for CFD, LIGGGHTS [8] for DEM, and CFDEMcoupling [9] to link the two methods. The CFD component simulates the gas phase, while the DEM component models the solid particle phase (battery). CFDEMcoupling connects these solvers, ensuring the interaction variables from both the CFD and DEM models are properly accounted for.

Governing equations – Gas phase

The mass conservation for the gas phase can be described by the Equation (1) [10]:

$$\frac{\partial(\alpha_f \rho_f)}{\partial t} + \nabla \cdot \alpha_f \rho_f \mathbf{u}_f = S_{\text{massThermalRunaway}} \quad (1)$$

where α_f represents the fluid (gas) void fraction, ρ_f is fluid density and \mathbf{u}_f is the fluid velocity vector. The source term on the right-hand side represents the mass generated during thermal runaway of the battery. The momentum conservation for the gas phase is given in Equation (2) [10]:

$$\frac{\partial(\alpha_f \rho_f \mathbf{u}_f)}{\partial t} + \nabla \cdot \alpha_f \rho_f \mathbf{u}_f \mathbf{u}_f = -\alpha_f \nabla p + \rho_f \mathbf{g} + \mathbf{R}_{fs} \quad (2)$$

where the first term at the right-hand side represents the pressure

gradient, \mathbf{g} is gravitational acceleration, and \mathbf{R}_{fs} is the momentum exchange term with the solid phase, expressed as:

$$\mathbf{R}_{fs} = \frac{1}{\Delta V_c} \sum_{i=1}^n \mathbf{f}_{d,i} \quad (3)$$

where n is the number of particles in the CFD cell, V_c is the cell volume, and $\mathbf{f}_{d,i}$ is the drag force acting on particle i . The Gidaspow correlation was used to model the drag force [11]. The energy equation for the gas phase, accounting for particle interactions, is given by Equation (4) [10]:

$$\begin{aligned} \frac{\partial(\alpha_f \rho_f E)}{\partial t} + \nabla \cdot \alpha_f \rho_f \mathbf{u}_f E &= -\nabla \cdot (\alpha_f p_f \mathbf{u}_f) \\ -\alpha_f \frac{\lambda_f}{c_{p,f}} \nabla \cdot \mathbf{e} + S_q & \end{aligned} \quad (4)$$

where E is the total energy (internal energy e plus kinetic energy), λ_f is the thermal conductivity, and $c_{p,f}$ is the specific heat capacity of the gas. The heat source term S_q includes contributions from convection and chemical reactions:

$$S_q = Q_{conv} + Q_{react} \quad (5)$$

The convective heat transfer is given by:

$$Q_{conv} = h A_p (T_f - T_p) \quad (6)$$

where A_p is the particle surface area, T_f , T_p are the fluid and particle temperatures, respectively. The convective heat transfer coefficient h is defined as:

$$h = \frac{\lambda_f N_p}{d_p} \quad (7)$$

where d_p is the particle diameter and N_p is the Nusselt number, given by the correlation [12]:

$$\begin{aligned} N_p &= (7 - 10\alpha_f + 5\alpha_f^2)(1 + 0.7Re_p^{0.2}Pr^{1/3}) \\ &+ (1.33 - 2.4\alpha_f + 1.2\alpha_f^2)Re_p^{0.7}Pr^{1/3} \end{aligned} \quad (8)$$

where the term Re_p is the particle Reynolds number given by:

$$Re_p = \frac{d_p \alpha_f |\mathbf{u}_f - \mathbf{u}_p|}{\nu_f} \quad (9)$$

where ν_f is the kinetic viscosity. The Prandtl number is defined as:

$$Pr = \frac{c_{p,f} \mu}{k} \quad (10)$$

with μ is the fluid viscosity and k the thermal conductivity. The heat generated by chemical reactions during thermal runaway is modeled as:

$$Q_{react} = H_{thermalRunaway} \frac{dm_p}{dt} \quad (11)$$

where $H_{thermalRunaway}$ is the energy released per unit mass and m_p is the particle mass. Species conservation is described by Equation (12) [10]:

$$\frac{\partial(\rho_f \alpha_f Y_i)}{\partial t} + \nabla \cdot \alpha_f \rho_f \mathbf{u}_f Y_i = \nabla \cdot \alpha_f \rho_f D_f \nabla Y_i + S_{Y_i} \quad (12)$$

where Y_i mass fraction of the species i and the source term S_{Y_i} is the source term representing mass generation or consumption of species i . The Schmidt number is related to D_f as:

$$Sc = \frac{\mu_f}{\rho_f D_f} \quad (13)$$

Governing equations – Particle phase

In this study, a single particle representing the battery is kept stationary in the domain, consistent with the thermal runaway experiment. Therefore, particle motion is not solved. The battery mass change due to gas release is described by:

$$\frac{\partial m_p}{\partial t} = \sum rr_{i,g} \quad (14)$$

As a consideration the mass of the particle in the domain was held constant. The reaction rate is defined by Equation (15) below:

$$rr_{i,g} = A \exp\left(\frac{T_b}{T_{battery}}\right) \left(\frac{X_i}{X_{i,0}}\right)^n \quad (15)$$

where $rr_{i,g}$ denotes the reaction rate, A is the frequency factor, $T_{battery}$ and T_b are the actual battery temperature and activation temperature, respectively. X_i and $X_{i,0}$ are the current and initial gas contents, and n is the reaction order. The values of the constants used are provided in Table 1 for CO and CO₂.

Table 1: Parameters for reaction rate model

Species	$X_{i,0}$ (kg)	A (kg/s)	T_b (K)	n (-)
CO	6.69E-04	4.75	933	1
CO ₂	5.60E-03	1.37	603	1

The battery temperature evolution is governed by:

$$\frac{\partial T_p}{\partial t} m_p c_{p,p} = S_{thermalRunaway} + S_{conv} \quad (16)$$

where the source terms are related to the energy source term S_q from Equation (5). The total energy released during thermal runaway is modeled as [13]:

$$H_{thermalRunaway} = m_p c_{p,p} (T_{max} - T_{thermalRunaway}) \quad (17)$$

where the T_{max} is the maximum temperature reached during thermal runaway and $T_{thermalRunaway}$ is the temperature at which the thermal runaway begins. The values used for Equation (17) can be seen in Table 2, which were derived from the experiments.

Table 2: Values of variables for thermal runaway

Variable	Value	Unit
$H_{thermalRunaway}$	13286	J
m_p	70	g
$c_{p,p}$	730	J/(kg·K)
T_{max}	764	K
$T_{thermalRunaway}$	504	K

Results and Discussion

The comparison between the experimental and simulation results for battery temperature and chemical species is shown in Figures 2 and 3, respectively.

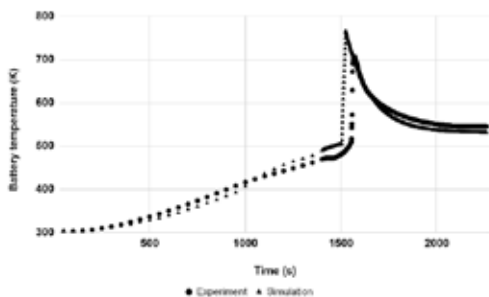


Figure 2. Comparison experiment/simulations: battery temperature

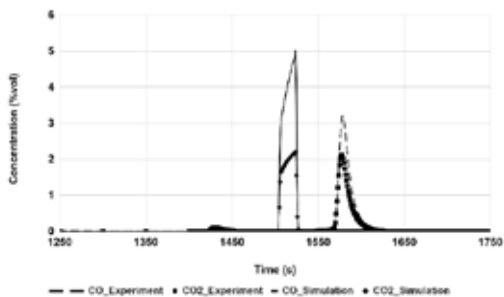


Figure 3. Comparison experiment/simulation: chemical species

As seen in the plots, there is a reasonable agreement between the methods. The battery temperature plot illustrates the transition from room temperature to thermal runaway, followed by cooling to the laboratory furnace temperature after all the energy has been released from the battery. The maximum temperatures and thermal runaway temperatures (where the rate $dT/dt > 1$) reached in the simulations were 765 K and 706 K, respectively, while the experimental values were 504 K and 507 K.

For the chemical species considered, a time delay between the curves is noticeable. This difference can be attributed to the experimental setup, where the gas must be transported to the detectors. Overall, the model was able to reproduce the experimental data with a reasonable degree of accuracy. Figure 4 below shows the simulation domain containing the battery particle in a cylindrical shape at the center of a box domain, designed to replicate the experimental setup.

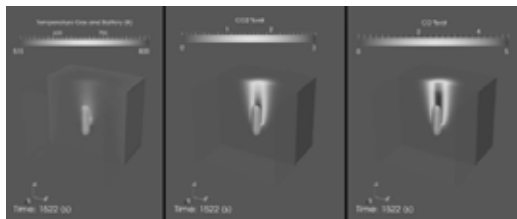


Figure 4. Simulation domain showing the temperature distribution and chemical species concentrations at the thermal runaway

The figure displays the time step relative to thermal runaway, where the increase in temperature and the release of chemical species are visible. The data used to plot the comparison in Figures 2 and 3 were sampled from the upper center surface of the domain, where the particle is located. This sampling point was chosen to closely match the conditions observed in the experimental setup, ensuring an accurate comparison between the experimental and simulation results.

Conclusion

This study developed a model for battery recycling through thermal deactivation. The energy and species release processes were characterized using experimental data, which formed the basis for the model's formulation. Comparisons between experimental results and simulation outputs demonstrated that the model was able to accurately replicate the thermal runaway curve. However, further refinements are needed to enhance its predictive capabilities and improve the overall accuracy of the model.

Acknowledgement

This study received funding from the module FuLiBatter which is supported by COMET (Competence Center for Excellent Technologies), the Austrian programme for competence centres. COMET is funded by the Federal Ministry for Climate Action, Environment, Energy, Mobility, Innovation and Technology, the Federal Ministry for Labour and Economy, the Federal States of Upper Austria, and Styria as well as the Styrian Business Promotion Agency (SFG). Furthermore, Upper Austrian Research GmbH continuously supports KI-MET. Besides the public funding from COMET, this research project is partially financed by the scientific partners acib GmbH, Coventry University, Montanuniversität Leoben, University of Natural Resources and Life Sciences, UVR-FIA GmbH, and the industrial partners AUDI AG, BRAIN Biotech AG, Ebner Industrieofenbau GmbH, RHI Magnesita GmbH, Saubermacher Dienstleistungen AG, TÜV SÜD Landesgesellschaft Österreich GmbH, voestalpine High Performance Metals GmbH and VTU Engineering GmbH.

References

- [1] Y. Wang, N. An, L. Wen, L. Wang, X. Jiang, F. Hou, Y. Yin, and J. Liang, 'Recent progress on the recycling technology of Li-ion batteries', *Journal of Energy Chemistry*, vol. 55, pp. 391–419, 2021. doi: 10.1016/j.jechem.2020.05.008.
- [2] P. Li, S. Luo, L. Zhang, Q. Liu, Y. Wang, Y. Lin, C. Xu, J. Guo, P. Cheali, and X. Xia, 'Progress, challenges, and prospects of spent lithium-ion batteries recycling: A review', *Journal of Energy Chemistry*, vol. 89, pp. 144–171, 2024, doi: 10.1016/j.jechem.2023.10.012.
- [3] J. Jung, P.-C. Sui, and J. Zhang, *Hydrometallurgical Recycling of Lithium-Ion Battery Materials*. CRC Press, 2023.
- [4] D. Aschermayr, S. Kadne, L. Risch, J. Simböck, A. Braunfels, B. Dixon, S. Herrmann, J. Jäger, C. Kühn, S. Schenk, et al., "Battery Passport Content Guidance-Achieving Compliance with the EU Battery Regulation and Increasing Sustainability and Circularity," Battery Pass consortium, Project Report, 2023. [Online]. Available: https://thebatterypass.eu/assets/images/content-guidance/pdf/2023_Battery_Passport_Content_Guidance.pdf. [Accessed: April 29, 2025].
- [5] J. Lin, X. Zhang, E. Fan, R. Chen, F. Wu, and L. Li, 'Carbon neutrality strategies for sustainable batteries: from structure, recycling, and properties to applications', *Energy Environ. Sci.*, vol. 16, no. 3, pp. 745–791, 2023, doi: 10.1039/D2EE03257K.
- [6] L. An, *Recycling of Spent Lithium-Ion Batteries: Processing Methods and Environmental Impacts*. Springer Nature, 2019.
- [7] H. Pinegar and Y. R. Smith, 'Recycling of End-of-Life Lithium-Ion Batteries, Part II: Laboratory-Scale Research Developments in Mechanical, Thermal, and Leaching Treatments', *J. Sustain. Metall.*, vol. 6, no. 1, pp. 142–160, 2020, doi: 10.1007/s40831-020-00265-8.
- [8] C. Kloss, C. Goniva, A. König, S. Amberger, and S. Pirker, 'Models, algorithms and validation for opensource DEM and CFD-DEM', *Progress in Computational Fluid Dynamics*, vol. 12, pp. 140–

152, 2012, doi: 10.1504/PCFD.2012.047457.

[9] C. Goniva, C. Kloss, N. G. Deen, J. A. M. Kuipers, and S. Pirker, 'Influence of rolling friction on single spout fluidized bed simulation', *Particuology*, vol. 10, no. 5, pp. 582–591, 2012, doi: 10.1016/j.partic.2012.05.002.

[10] T. B. Anderson and R. Jackson, 'Fluid Mechanical Description of Fluidized Beds. Comparison of Theory and Experiment', *Ind. Eng. Chem. Fund.*, vol. 8, no. 1, pp. 137–144, 1969, doi: 10.1021/i160029a022.

[11] D. Gidaspow, *Multiphase Flow and Fluidization: Continuum and Kinetic Theory Descriptions*. Academic Press, 1994.

[12] D. J. Gunn, 'Transfer of heat or mass to particles in fixed and fluidised beds', *International Journal of Heat and Mass Transfer*, vol. 21, no. 4, pp. 467–476, 1978, doi: 10.1016/0017-9310(78)90080-7.

[13] C.-Y. Jhu, Y.-W. Wang, C.-M. Shu, J.-C. Chang, and H.-C. Wu, 'Thermal explosion hazards on 18650 lithium ion batteries with a VSP2 adiabatic calorimeter', *J Hazard Mater*, vol. 192, no. 1, pp. 99–107, 2011, doi: 10.1016/j.jhazmat.2011.04.097.

QualiCheese – Haltbarkeitsoptimierung von Schnittkäse in ökologisch nachhaltigen Verpackungen

A. L. Rudolph^{1,*}, S. Petersen¹, C. Borsum¹

1: KLEVERTEC, Hochschule Kempten, Deutschland

* Correspondent author: anton.rudolph@hs-kempten.de

Keywords: semi-hard cheese, sustainable packaging, shelf-life optimization, gas permeability in food packaging

Einleitung

Lebensmittelverpackungen spielen eine zentrale Rolle in der modernen Lebensmittelversorgung. Sie ermöglichen empfindliche Produkte über längere Zeiträume hinweg frisch und genießbar zu halten. Dadurch leisten sie einen entscheidenden Beitrag zur Reduktion von Lebensmittelverschwendung – ein zentrales Problem im globalen Ernährungssystem, das nicht nur ökonomische, sondern auch ökologische Auswirkungen hat. Indem sie Lebensmittel vor mikrobieller Verunreinigung, Feuchtigkeit, Sauerstoff und Licht schützen, tragen Verpackungen wesentlich dazu bei, die Haltbarkeit zu verlängern und die Qualität der Produkte während Transport und Lagerung zu sichern. Damit leisten sie einen essentiellen Beitrag zum Umweltschutz, da weniger verderbliche Lebensmittel letztlich entsorgt werden müssen.

Gleichzeitig stehen Lebensmittelverpackungen zunehmend in der Kritik: Sie sind mit heutigen Recyclingmethoden nur sehr schwer oder gar nicht stofflich verwertbar, da sie häufig aus sogenannten Multilayer- oder Verbundmaterialien – komplexen Kombinationen aus verschiedenen funktionalen Kunststoffschichten – bestehen, und machen etwa die Hälfte des Kunststoffabfalls im Meer aus [1]. In diesem Spannungsfeld zwischen Beitrag zur Nachhaltigkeit durch Verlängerung der Haltbarkeit und gleichzeitiger Mitverursachung von Umweltverschmutzung und Abfallaufkommen bewegen sich unsere heutigen Lebensmittelverpackungen.

Vor diesem Hintergrund formuliert die Europäische Union im Rahmen ihres Green Deals immer ambitioniertere Vorgaben an Kunststoffe und insbesondere an Verpackungen, die in Verkehr gebracht werden sollen. Ziel ist es, die Kreislauffähigkeit zu erhöhen und den CO₂-Fußabdruck zu senken. Ein zentrales Instrument dafür ist die Einführung verbindlicher Vorgaben für Design-for-Recycling und den Einsatz von Rezyklaten, also recyceltem Kunststoffmaterial. So sollen gemäß den aktuellen Plänen bis zum Jahr 2030 alle Kunststoffverpackungen im europäischen Binnenmarkt durchschnittlich mindestens 30 % Rezyklat enthalten [2]. Dies stellt nicht nur technische, sondern auch wirtschaftliche Herausforderungen für die Industrie dar. Parallel wird auch der Einsatz alternativer Materialien wie biobasierter Kunststoffe oder biologisch abbaubarer Verpackungskomponenten diskutiert, wobei hier Aspekte wie Kompostierbarkeit, Entsorgungsinfrastruktur und tatsächlicher ökologischer Nutzen genau geprüft werden müssen.

Verpackungen, die diese neuen Anforderungen erfüllen, basieren häufig auf innovativen Materialien oder neuartigen Kombinationen bewährter Komponenten. Zahlreiche Forschungsprojekte haben bereits verschiedenste nachhaltige Verpackungslösungen entwickelt, doch die industrielle Umsetzung verläuft bislang schleppend. Ein wesentlicher Grund dafür liegt in den technologischen Eigenschaften klassischer Kunststoffverbunde, die über Jahre hinweg hinsichtlich ihrer Barrierewirkung, Bedruckbarkeit, Siegelbarkeit und Maschinengängigkeit perfektioniert wurden. Bei der Umstellung auf neue Materialien drohen Unternehmen, dieses Know-how zu verlieren und in aufwändige Umrüstungen investieren zu müssen – sowohl technisch als auch prozessual.

Darüber hinaus ist nicht absehbar, wie sich neue Verpackungsmaterialien langfristig auf die verpackten Lebensmittel auswirken. Über mehrere Monate hinweg können Wechselwirkungen zwischen Produkt und Verpackung auftreten, die

die Haltbarkeit oder sensorische Eigenschaften negativ beeinflussen. Geruch, Geschmack, Textur und Farbe könnten sich verändern, was wiederum die Akzeptanz durch Verbraucherinnen und Verbraucher beeinträchtigen kann. Deshalb ist es von entscheidender Bedeutung, die spezifischen Herausforderungen und Potenziale dieser neuen Materialien frühzeitig zu erkennen und systematisch zu untersuchen – idealerweise unter realitätsnahen Bedingungen über die gesamte Lagerdauer hinweg.

Das Forschungsprojekt **QualiCheese** widmet sich genau dieser Fragestellung – speziell am Beispiel von Käseverpackungen. Ziel ist es, Verpackungslösungen zu identifizieren, die nicht nur in ökologischer Hinsicht überzeugen, sondern auch unter verschiedenen Lagerbedingungen die Eigenschaften des Käses in gewohnter Qualität erhalten – eventuell sogar über einen längeren Zeitraum. Dabei stehen sowohl monomaterialbasierte als auch neuartige biobasierte Verpackungslösungen im Fokus. Im Rahmen des Projekts wurden bislang drei Langzeit-Lagerversuche durchgeführt. Zwei dieser Versuche sind bereits abgeschlossen, während der dritte im April 2025 gestartet wurde. Die Erkenntnisse aus diesen Tests liefern wichtige Hinweise darauf, welche nachhaltigen Verpackungskonzepte auch unter industriellen Bedingungen langfristig funktionieren und am Markt bestehen können.

Material und Methoden

In den ersten beiden Langzeit-Lagerversuchen wurde Tiroler Bergkäse in ganzen Stücken unter standardisierten Bedingungen getestet, um die Auswirkungen unterschiedlicher Verpackungsmaterialien auf die Produktqualität über einen verlängerten Zeitraum zu analysieren. Als Verpackungslösungen kamen zum einen ein biobasierter und kompostierbarer Cellulose-Stärkeblend-Verbund (CS) sowie als Referenzmaterial ein Polyamid-Polyethylen-Verbund (PA-PE) zum Einsatz. Der Käse wurde dabei in einem sogenannten Scheinvakuum verpackt. Dabei wird die Verpackung beim Abpacken mit 100 % CO₂ gefüllt. Dieses löst sich dann im Wasser, das der Käse enthält, sodass das gesamte freie Gasvolumen verschwindet und eine Verpackung entsteht, die einer Vakuumverpackung entspricht.

Im zweiten Lagerversuch wurde die Untersuchung des CS-Verbunds vertieft, indem zwei unterschiedliche Materialstärken – 50 µm – zusätzlich verglichen wurden. Ziel war es, zu analysieren, ob sich die Dicke der Folie signifikant auf die Schutzfunktion gegenüber Umwelteinflüssen wie die Wasserdampf- oder die Sauerstoffbarriere auswirkt. Darüber hinaus wurde der Einfluss unterschiedlicher Lagerbedingungen überprüft, insbesondere im Hinblick auf Luftfeuchtigkeit. Hierfür wurden zwei Lagerumgebungen mit stark voneinander abweichender relativer Luftfeuchtigkeit gewählt: 30 % als trockene Umgebung und 85 % als feuchte Umgebung. Diese extremen Bedingungen sollten unter anderem Aufschluss darüber geben, ob erste Anzeichen einer biologischen Zersetzung des kompostierbaren Materials während der Lagerung auftreten könnten – etwa durch frühzeitigen Materialabbau oder veränderte Barriereigenschaften.

Der dritte Lagerversuch unterscheidet sich hinsichtlich Käseart, Schnittform und Verpackungsmaterialien deutlich von den ersten beiden Tests. In diesem Fall wurde industriell hergestellter Allgäuer

Emmentaler in Scheiben verwendet. Die Scheiben wurden entweder in Mono-PET (Polyethylenterephthalat) oder in Mono-PP (Polypropylen) verpackt. Durch die Verwendung von nur einem Polymer (Monomaterial) wird eine Rezyklierung überhaupt erst ermöglicht, da dafür sortenreine Materialien nötig sind, was sie zu einer nachhaltigen Alternative zu Multilayer-Verpackungen macht, wobei sie hinsichtlich Sauerstoff- und Wasserdampfdurchlässigkeit unterschiedliche Eigenschaften aufweisen. Auch hier wurde die relative Luftfeuchtigkeit als Einflussfaktor in die Versuchsanordnung integriert, um Rückschlüsse auf Verpackungintegrität und Produkthalbarkeit unter verschiedenen klimatischen Bedingungen ziehen zu können.

Die Lagerung des Käses erfolgte beziehungsweise erfolgt in allen drei Versuchsreihen bei einer Temperatur von 6 °C – ein Wert, der typischen Kühlkettenbedingungen im Handel entspricht. Die Lagerdauer wurde auf 125 % des deklarierten Mindesthaltbarkeitsdatums (MHD) ausgeweitet, was je nach Käsesorte einer Zeitspanne von rund drei bis vier Monaten entspricht. Diese verlängerte Lagerung dient dazu, auch eine potenzielle Optimierung der Haltbarkeit über das MHD hinaus erfassen zu können.

Die Analysen des Käses erfolgen zu Beginn und am Ende der Lagerperiode und dazwischen in regelmäßigen Intervallen von 25 % des deklarierten MHDs. Dabei wurden vom KLEVERTEC der pH-Wert, der Wasseraktivitätswert (a_w -Wert) sowie der absolute Wassergehalt des Käses untersucht. Dieser Parameter erlaubt Rückschlüsse auf physikalische Veränderungen des Käses während der Lagerzeit. Ergänzend dazu wurden zu Beginn der Lagerung und zum Zeitpunkt des MHDs auch die verwendeten Verpackungsmaterialien analysiert. Hierbei lag der Fokus auf den Barriereigenschaften gegenüber Sauerstoff und Wasserdampf – zwei Faktoren, die maßgeblich die Haltbarkeit und Qualität verpackter Lebensmittel beeinflussen.

Weitere Untersuchungsschwerpunkte wurden durch die Projektpartner abgedeckt, die unter anderem die mikrobielle Belastung des Produkts analysierten. Dazu gehören sowohl klassische mikrobiologische Parameter wie Gesamtkeimzahl als auch der Nachweis sensorisch relevanter Veränderungen, die bei einem neuen Material auftreten können.

Da zum jetzigen Zeitpunkt lediglich die ersten beiden Lagerversuche vollständig abgeschlossen und ausgewertet sind, konzentrieren sich die vorliegenden Ergebnisse auf diese beiden Versuchsanordnungen. Der dritte, derzeit noch laufende Lagerversuch wird bis zum Zeitpunkt des geplanten Symposiums deutlich weiter fortgeschritten sein, sodass dann auch neue Erkenntnisse aus diesem Versuch vorgestellt werden können. Diese Daten werden insbesondere im Hinblick auf recyclingfähige Monomaterialien von großem Interesse sein und könnten wichtige Impulse für die Weiterentwicklung nachhaltiger Verpackungslösungen im Bereich geschnittener Käseprodukte liefern.

Ergebnisse

Der Tiroler Bergkäse, der in den ersten beiden Versuchsreihen jeweils am Stück in verschiedenen Verpackungsmaterialien gelagert wurde, zeigte im Verlauf der Lagerdauer Veränderungen, die unabhängig vom eingesetzten Verpackungstyp auftraten. Sowohl der Wassergehalt als auch der a_w -Wert (Wasseraktivität) des Produkts nahmen im Verlauf der Lagerung sukzessive ab, was auf eine Austrocknung bzw. einen Wasserverlust hindeutet. Beim pH-Wert konnte keine Veränderung festgestellt werden, die über die Standardabweichung hinausgeht (siehe Abbildung 1). Diese Entwicklung war sowohl bei der konventionellen PA-PE-Verpackung als auch bei dem biobasierten, kompostierbaren Cellulose-Stärke-Verbund (CS) festzustellen und trat auch unabhängig von der relativen Feuchte während der Lagerung auf.

Dennoch traten zwischen den beiden Verpackungssystemen geringe Unterschiede in der Stabilität dieser Parameter auf: So zeigte der Käse, der in der klassischen PA-PE-Folie verpackt war, im Vergleich zum Käse in der nachhaltigen CS-Verpackung ein stärker schwankendes Verhalten über die Lagerzeit hinweg. In der biobasierten CS-Verpackung verliefen die Veränderungen dagegen gleichmäßiger und ohne größere Ausschläge. Trotz dieser Unterschiede im Detail konnte im Gesamtbild – also in der vergleichenden Betrachtung aller physikalisch-chemischen Parameter über den gesamten Zeitraum und bei unterschiedlichen Lagerbedingungen – kein eindeutiger oder signifikanter Unterschied eines der beiden Verpackungstypen festgestellt werden. Die vom KLEVERTEC untersuchten Parameter lassen somit keine klare Präferenz zugunsten eines Materials hinsichtlich der Erhaltung der Grundparameter von Qualität und Haltbarkeit erkennen. Dies spricht insofern für die CS-Verpackung, da sich Produzent und Konsument nachhaltigere Verpackungen wünschen, ohne Änderungen am bekannten System in Kauf nehmen zu müssen.

Auch aus mikrobiologischer Sicht fiel das Ergebnis überwiegend unauffällig aus: Über den Großteil der Lagerdauer wurde bei keinem der getesteten Käseproben – unabhängig von der jeweiligen Verpackungsart oder den gewählten Lagerbedingungen – ein Schimmelbefall dokumentiert. Eine Ausnahme stellte lediglich der Käse dar, der in PA-PE-Folie verpackt war und bei hoher relativer Luftfeuchte von 85 % gelagert wurde. In diesem Fall kam es etwa nach Erreichen von 75 % der vorgesehenen Lagerzeit (entspricht ca. 2,5 Monaten) zu einer Schimmelbildung auf der Käsoberfläche und in den Falten in der Verpackung. Zusätzlich sammelte sich auffällig viel Wasser in der Verpackung – und das trotz augenscheinlich intaktem Vakuum. Dieses Ergebnis weist auf mögliche Schwächen des PA-PE-Materials unter sehr feuchten Lagerbedingungen hin, was mit einer verringerten Barrierefunktion bei hoher Feuchtigkeit zusammenhängen könnte.

Deutlich ausgeprägter waren die Unterschiede zwischen den getesteten Verpackungsmaterialien jedoch beim Ausschuss, also dem Anteil an Verpackungseinheiten, die bereits bei der Produktion oder im Verlauf der Lagerung kein Vakuum bildeten. Hier zeigte sich, dass der Ausschuss bei der biobasierten CS-Verpackung

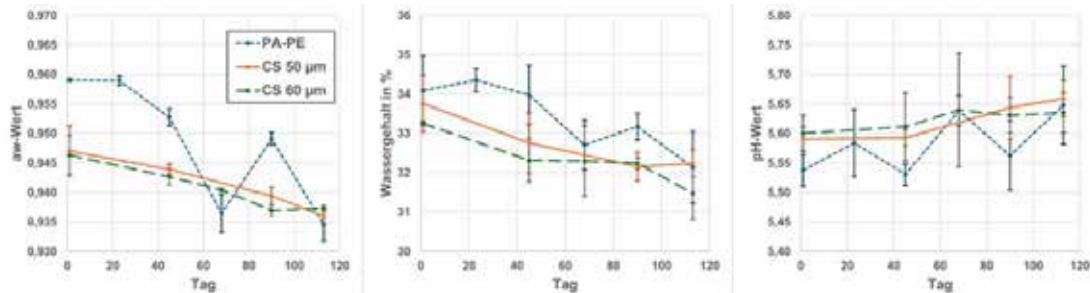


Abbildung 1: Entwicklung des a_w -Werts, des Wassergehaltes und des pH-Wertes des Bergkäses während der Lagerdauer von 113 Tagen in 2 biobasierten Verpackungen (CS) und einer PA-PE-Referenzverpackung.

deutlich höher lag – mit Werten zwischen 40 und 60 %, während er bei der konventionellen PA-PE-Verpackung lediglich 10 % betrug. Ob dieser erhebliche Ausschuss auf materialimmanente Schwächen des biobasierten Films zurückzuführen ist oder ob suboptimale Einstellungen oder fehlende Kompatibilität mit der verwendeten Verpackungsmaschine eine Rolle spielten, ließ sich im Rahmen der Untersuchungen nicht abschließend klären. Hinweise auf maschinentechnische Probleme zeigten sich aber bereits während der Abpackversuche: Die CS-Folie erwies sich als deutlich weniger maschinengängig, was sich in Knicken und Mikrorissen in der äußeren Schicht der Folie äußerte. Entgegen der Erwartung wiesen viele der Verpackungen, bei denen kein vollständiges Vakuum erreicht wurde, trotzdem über den gesamten Lagerzeitraum hinweg keinen sichtbaren Schimmelbefall auf.

Des Weiteren konnten im Rahmen sensorischer Analysen, die von Projektpartnern durchgeführt wurden, bei Käseproben aus der CS-Verpackung vereinzelt geschmackliche Veränderungen festgestellt werden. Teilnehmende beschrieben diese als „kunststoffartig“, was auf Migrationen von Verpackungsbestandteilen in das Produkt hindeutet. Eine solche sensorische Beeinträchtigung ist aus Konsumentensicht als nicht akzeptabel zu bewerten. Allerdings konnte nicht eindeutig festgestellt werden, ob diese sensorische Veränderung durch die Materialzusammensetzung an sich oder durch unsachgemäße Lagerbedingungen verursacht wurde. Eine abschließende Bewertung, ob es sich um ein grundsätzliches Problem des CS-Materials handelt oder um ein Problem der spezifischen Marge und ihrer Lagerbedingungen, blieb offen.

Die begleitenden Materialanalysen ergaben, dass es bei der biobasierten CS-Verpackung unter hoher Luftfeuchtigkeit zu einem Quellen des Materials kommt. Dennoch zeigten die Messungen Wasserdampf- und Sauerstoffpermeation keine Veränderungen, zumindest nicht unter standardisierten Bedingungen. Es konnte aber während der Messung Trocknungseffekte beobachtet werden, die sich darin äußerten, dass sich die Permeationsrate erst nach langer Messdauer auf einem niedrigen Wert stabilisierte (siehe Abbildung 2). Dies legt nahe, dass äußere Materialveränderungen nicht zwingend mit funktionalen Einbußen bei der Schutzwirkung einhergehen oder reversibel sind.

Im Gegensatz dazu zeigte die PA-PE-Verpackung bei Messungen unter erhöhter Luftfeuchtigkeit eine deutliche Veränderung: Die

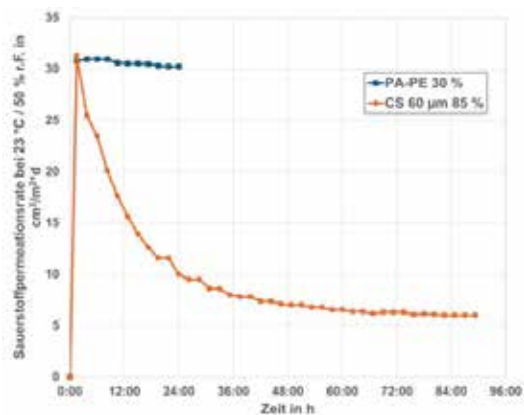


Abbildung 2: Veränderung der Sauerstofftransmissionsrate im Verlauf der Permeationsmessung mit sichtbaren Trocknungseffekten der bei 85 % gelagerten CS-Verpackung.

Sauerstoffpermeation verdreifachte sich unter diesen Bedingungen, was auf eine feuchtesensible Eigenschaft dieses Materials hinweist. Diese Beobachtung ist insbesondere für Produkte mit hoher Empfindlichkeit gegenüber Sauerstoff – wie Schnittkäse – von großer Relevanz.

Diskussion

Die bislang durchgeführten Lagerversuche liefern erste aufschlussreiche Erkenntnisse über die Praxistauglichkeit biobasierter Verpackungslösungen im Vergleich zu herkömmlichen, auf fossilen Rohstoffen basierenden Kunststoffverpackungen. Konkret wurde Tiroler Bergkäse am Stück über eine verlängerte Lagerdauer hinweg sowohl in einem biobasierten Cellulose-Stärkeblend-Verbund (CS) als auch in einem klassischen PA-PE-Mehrschichtsystem gelagert und hinsichtlich Haltbarkeit und Verpackungsperformance untersucht. Die Ergebnisse deuten darauf hin, dass die biobasierte CS-Verpackung – sofern die Verpackung technisch einwandfrei und luftdicht ausgeführt wurde – hinsichtlich der Lagerstabilität des Käses vergleichbare Resultate erzielt wie die herkömmliche Verpackung. Es konnte kein signifikanter Unterschied im physikalischen oder mikrobiologischen Verhalten des Käses während der Lagerung festgestellt werden. Die Haltbarkeit des Produkts war in beiden Fällen bis über das deklarierte Mindesthaltbarkeitsdatum (MHD) hinaus gegeben, was auf eine grundsätzlich ausreichende Schutzwirkung beider Verpackungstypen schließen lässt.

Besonders bemerkenswert ist, dass unter Bedingungen erhöhter Luftfeuchtigkeit die Sauerstoffbarriere des biobasierten CS-Materials sogar besser ist, als die des Referenzmaterials. Dies ist insofern relevant, als Sauerstoff einen maßgeblichen Einfluss auf mikrobielle Stabilität und oxidative Prozesse im Käse hat. Trotz des beobachteten Quellens der Cellulose-Stärke-Folie bei hoher Umgebungsfeuchte konnte in den durchgeführten Barriereanalysen kein nachteiliger Einfluss auf die Sauerstoff- oder Wasserdampfdurchlässigkeit festgestellt werden. Die Verpackung blieb in ihrer Schutzwirkung stabil und effektiv. Auch eine potenzielle Zersetzung oder ein Kompostierungsprozess der biobasierten Folie während der Lagerdauer wurde nicht beobachtet, obwohl Feuchtigkeit eine Voraussetzung für Kompostierung ist. Damit konnte die zuvor formulierte Hypothese, dass ein Kompostierungsprozess bereits im Lagerzeitraum einsetzt, nicht bestätigt werden.

Im Gegensatz dazu zeigten sich bei der herkömmlichen PA-PE-Verpackung unter denselben klimatischen Bedingungen deutliche Schwächen: Bei Lagerung bei 85 % relativer Luftfeuchtigkeit kam es zu einer signifikanten Erhöhung der Sauerstoffpermeation. In Folge dessen verschlechterte sich die Haltbarkeit des Produkts messbar, was auf eine Schwächung der Barrierewirkung zurückgeführt wird. Es wird vermutet, dass die Polyamid-Komponente im Verbund bei Feuchteeinwirkung aufquillt und dadurch die dichte Matrixstruktur durchlässiger wird. Dies verändert die Diffusionswege für Gase und beeinträchtigt die Schutzwirkung der Verpackung gegenüber Sauerstoff. Allerdings bleibt offen, wie praxisrelevant dieses Verhalten tatsächlich ist – derartige hohe Luftfeuchten treten in mitteleuropäischen Logistik- und Verkaufsstrukturen normalerweise nur bei gravierenden Lagerfehlern auf. Dennoch unterstreichen diese Ergebnisse die Notwendigkeit, auch etablierte Materialien unter realitätsnahen Extrembedingungen zu bewerten, um ihre Leistungsgrenzen besser zu verstehen.

Trotz dieser positiven Befunde hinsichtlich der Schutzwirkung der CS-Verpackung muss festgestellt werden, dass die praktische Anwendbarkeit dieser biobasierten Alternative durch erhebliche technische Probleme während des Verpackungsprozesses stark eingeschränkt war. Ein besonders kritischer Punkt ist die im Vergleich zur PA-PE-Verpackung signifikant erhöhte Ausschussquote. Während bei der konventionellen Verpackung nur etwa 10 % der Einheiten als fehlerhaft aussortiert werden mussten, lag der Ausschuss bei Verwendung der biobasierten CS-Folie zwischen 40 und 60 %, also bis zu dem Sechsfachen. Rechnet man diese Ausschussraten mit den geringeren Emissionen einer biobasierten Verpackung gegen, fällt die CO₂-Bilanz der CS-Verpackung um den Faktor 167 schlechter aus. Damit wird der Nachhaltigkeitsansatz der Verpackung ad absurdum geführt.

Die Ursachen für diese hohe Ausschussrate konnten nicht

eindeutig identifiziert werden. Während der Versuche wurde beobachtet, dass vereinzelt Mikrorisse oder Faltenbildungen in der Folie auftraten. Diese Probleme könnten auf mangelnde Kompatibilität des Materials mit der bestehenden Verpackungsanlage hindeuten. Weiterhin sind die Siegelnähte eine offensichtliche mögliche Fehlerquelle bei mangelnder Kompatibilität zwischen Material und Maschine beziehungsweise falschen Parametern. Verschiedene Messungen zur Gaspermeation und Dichtheitsprüfung konnten jedoch zu keinem Zeitpunkt eine klar identifizierbare Fehlerquelle festmachen. Das deutet darauf hin, dass mehrere Faktoren – darunter Prozessparameter wie Temperatur, Druck und Siegelzeit – in ihrer Wechselwirkung für die mangelhafte Performance verantwortlich sein könnten. Nur weitergehende Prozessoptimierungen könnten hier Abhilfe schaffen.

Auch die sensorische Qualität des verpackten Käses stellte sich als Ausschlusskriterium für die Marktfähigkeit der CS-Verpackung heraus. In sensorischen Prüfungen durch Projektpartner wurde bei einigen Proben ein deutlich wahrnehmbarer Fremdgeschmack festgestellt. Ob dieser Effekt durch Materialbestandteile selbst, durch Wechselwirkungen zwischen Produkt und Verpackung oder durch die Lagerbedingungen verursacht wurde, blieb bislang ungeklärt. Auch hier könnten weitere Untersuchungen mit gezielter Variation der Einflussgrößen Aufschluss geben.

Aufgrund dieser bislang widersprüchlichen Befunde ergibt sich zum aktuellen Stand des Projekts kein eindeutiges Bild hinsichtlich der Eignung der biobasierten CS-Verpackung als nachhaltige Alternative zu herkömmlichen Kunststoffverbunden. Die genannten Schwächen – insbesondere die hohe Ausschussrate und die sensorischen Probleme – sprechen gegen eine sofortige Implementierung. Gleichzeitig ist es nicht ausgeschlossen, dass diese Schwächen prozessbedingt sind und durch gezielte technische Optimierungen überwunden werden können. Die prinzipielle Eignung des Materials als kompostierbare, biobasierte Lösung bleibt also weiterhin Gegenstand der Untersuchung und kann zum gegenwärtigen Zeitpunkt weder bestätigt noch ausgeschlossen werden.

Schließlich stellt sich – über die rein technische Betrachtung hinaus – die Frage, ob eine biobasierte, kompostierbare Verpackung wie der CS-Verbund tatsächlich einen ökologischen Vorteil gegenüber anderen als nachhaltig geltenden Alternativen bietet. Insbesondere Monomaterialverpackungen, die recyclingfähig sind und in etablierten Wertstoffkreisläufen verarbeitet werden können, gelten aktuell als bevorzugte Lösung im Sinne der Kreislaufwirtschaft. Bei kompostierbaren Verpackungen hingegen gehen die eingesetzten Ressourcen im Kompostierungsprozess in der Regel verloren, insbesondere wenn keine kontrollierte industrielle Kompostierung erfolgt. Zudem ist die Kompostierung solcher Verpackungen in Ländern wie Deutschland oder Österreich regulatorisch eingeschränkt und technisch kaum verbreitet. In der Praxis endet die Verwertung solcher Materialien daher häufig nicht auf dem Kompost, sondern in der thermischen Abfallbehandlung, was den Nachhaltigkeitsgedanken infrage stellt.

Um eine fundierte und belastbare Bewertung der Umweltwirkung verschiedener Verpackungsoptionen zu ermöglichen, ist daher eine umfassende Lebenszyklusanalyse (LCA) unerlässlich. Eine solche Analyse wird im Rahmen des Forschungsprojekts **QualiCheese** derzeit durch die beteiligten Projektpartner durchgeführt. Sie soll klären, inwiefern sich die ökologischen Auswirkungen der CS-Verpackung im gesamten Lebenszyklus – von der Rohstoffgewinnung über Produktion und Nutzung bis zur Entsorgung – im Vergleich zu anderen Verpackungsoptionen darstellen. Ebenso wird die Analyse der Lagerversuche mit recyclingfähigen Monomaterialien noch ausstehen, sodass weitere Daten notwendig sind, um fundierte Aussagen über die langfristige Nachhaltigkeit verschiedener Verpackungssysteme treffen zu können.

Quellen

- [1] European Commission, “Packaging waste: EU rules on packaging and packaging waste, including design and waste management.”, [europa.eu](https://environment.ec.europa.eu/topics/waste-and-recycling/packaging-waste_en), Zugriff: 30.04.2025, [Online.] Verfügbar: https://environment.ec.europa.eu/topics/waste-and-recycling/packaging-waste_en
- [2] European Parliament and Council of the European Union, *Regulation (EU) 2025/40 of 19 December 2024 on packaging and packaging waste, amending Regulation (EU) 2019/1020 and Directive (EU) 2019/904, and repealing Directive 94/62/EC (Text with EEA relevance)*, Official Journal of the European Union, 2025.

Shelf Life Optimization of Cheese Considering Ecologically Sustainable Packaging

J. Müller^{1,*}, D. Gottardi², M. Moravek³, M. Knödseder³, F. Patrignani², C. Huck⁴, K. Bach¹,

1: Department of Food Technology & Nutrition, Management Center Innsbruck (MCI), 6020 Innsbruck, Austria

2: Department of Agricultural and Food Sciences, University of Bologna, Piazza Gabriele Goidanich 60, 47521 Cesena, Italy

3: muva kempten GmbH, 87437 Kempten, Germany

4: Institute of Analytical Chemistry and Radiochemistry, University of Innsbruck, 6020 Innsbruck, Austria

* Correspondent author: Johanna.Mueller@mci.edu

Keywords: Bergkäse, food packaging, Shelf-life, cheese microbiota

Abstract

Tiroler Bergkäse, a Protected Designation of Origin (PDO) semi-hard cheese produced in the alpine regions of Tyrol, Austria, was analysed to assess the effect of different packaging materials on product quality during refrigerated storage. Seven Tyrolean mountain cheese samples were analysed, including five packaged cheeses and two unpackaged cheeses. The packaged samples were stored in either a conventional multilayer film (LDPE/PA) or a compostable, cellulose- and starch-based film. Microbiological quality, pH, organic acid composition, microbiota dynamics and sensory properties were analysed using standardised culture methods, high-performance liquid chromatography (HPLC) and next-generation sequencing (NGS). The results showed no significant differences between the packaging types in terms of total microbial counts, the development of yeasts and moulds, pH stability, or the occurrence of pathogenic bacteria. The dominant microorganisms in all samples were *Lactobacillus delbrueckii* and *Streptococcus salivarius*, with minor differences in diversity observed between packaging conditions. The organic acid profiles showed typical levels of lactic and acetic acid. No significant differences were identified in the sensory analysis. Overall, it was demonstrated that compostable cellulose-starch packaging preserved the microbiological, chemical and sensory properties of Tiroler Bergkäse comparably well to conventional plastic films, making it a promising sustainable alternative. Further analyses are planned.

Introduction

Austria is renowned for its diverse culinary traditions. It places a strong emphasis on cheese in daily nutrition. In recent decades, cheese consumption has risen significantly: today, the average Austrian consumes 22.5 kilograms of cheese per year, equivalent to approximately 63 grams per day [1]. Austria also maintains a high level of self-sufficiency in cheese production, reflecting the sustainable availability and preference for local varieties. In 2023, the country produced 200,265 tonnes of cheese, around 16% of which was organic. In 2023, dairy products, including cheese, accounted for 9.3% of Austria's agricultural exports, with hard cheeses making up 24% of total cheese production [2]. Tiroler Bergkäse holds particular significance among Austria's traditional cheeses. Produced exclusively in the alpine regions of North and East Tyrol, it is manufactured according to strict specifications under the Protected Designation of Origin (PDO) framework (EU Regulation 1065/97 [3]). Tiroler Bergkäse is made from raw cow's milk obtained from animals fed primarily on fresh grass and hay from alpine pastures, following a silage-free diet to preserve the natural aromatic profile imparted by the alpine flora. The transportation of the milk must be limited to short distances, and its processing is undertaken without the incorporation of additives, preservatives, emulsifiers, stabilisers, thickeners, colourants, or artificial flavours. Only natural calf rennet is permitted for coagulation. The PDO certification guarantees that production

occurs entirely within the designated Tyrolean region, employing traditional techniques that ensure the preservation of unique sensory properties, food safety, and cultural heritage. The link between the alpine landscape, traditional animal feeding practices, and artisanal processing is considered essential for the authenticity and quality of Tiroler Bergkäse [4].

Traditionally, multilayer plastic films have been used to protect cheeses during storage, providing high barrier properties against oxygen and moisture [5]. Packaging plays a critical role in preserving the quality, safety, and shelf life of food products by minimising exposure to environmental factors that can lead to spoilage, chemical degradation, and microbial contamination. [6]. Without adequate protection, cheeses are particularly vulnerable to moisture loss, oxidation, and microbial spoilage, all of which can compromise sensory attributes and food safety [7, 8]. However, multilayer packaging systems often present recyclability challenges due to the combination of incompatible polymer layers, raising environmental concerns within the context of circular economy goals [9]. In response, bio-based and compostable packaging alternatives, such as cellulose-starch films, have been introduced to reduce the environmental footprint of food packaging [10]. Previous studies on traditional cheeses, such as Kashar, have shown that storage conditions and the type of packaging atmosphere (vacuum versus non-vacuum) play a crucial role in the development of organic acids and biogenic amines during ripening [11]. Building on these findings, more recent research on semi-hard cheeses like Montasio has further highlighted the importance of packaging, demonstrating that a shift from conventional multilayer plastic systems to recyclable mono-material films can significantly impact microbial stability, oxidation processes, and overall shelf life [12]. While these results are promising, the impact of such novel packaging materials on the preservation of long-ripened, microbiologically complex cheeses remains largely unexplored. Given that packaging not only serves a protective function but also actively influences the physicochemical and microbial stability of the product, it may have critical implications for maintaining quality attributes essential for PDO certification.

Homofermentative species are characterised by the production of lactic acid as their predominant product, whereas heterofermentative species are known to generate an array of other compounds. These include acetic, formic, lactic and propionic acids, as well as acetaldehyde, ethanol and CO₂ [13]. The organic acids contribute significantly to the flavour of matured cheese [14]. The use of next-generation sequencing (NGS), have enabled a deeper understanding of the complex microbial communities associated with traditional cheeses. Unlike classical cultivation methods, NGS allows for comprehensive profiling of both culturable and non-culturable microorganisms, providing insights into microbial diversity, succession during ripening, and the effects of packaging on microbial stability [15]. Furthermore, monitoring the pH value provides insights into ripening dynamics and microbial activity during cheese maturation. Sensory analysis is also essential for

evaluating the effects of packaging on critical quality attributes such as appearance, texture, aroma, and flavour, which determine consumer acceptance [8].

Materials and Methods

Cheese samples

A total of seven Tiroler Bergkäse PDO cheeses (Table 1) all of which are commercially available, were obtained from two manufacturers located in Tyrol, Austria. All cheese samples were produced using microbial rennet, with differences observed in manufacturing dates and producers.

Table 1: Overview of Cheese Samples

Date of manufacture	Ripening time in days	Packaging date	Packaging material
16 Feb 2024	101 – 248	27 May 2024	LDPE/PA
16 Feb 2024	101 – 248	27 May 2024	Cellulose/starch (50 µm)
17 Aug 2024	100 – 187	25 Nov 2024	LDPE/PA
17 Aug 2024	100 – 187	25 Nov 2024	Cellulose/starch (50 µm)
17 Aug 2024	100 – 187	25 Nov 2024	Cellulose/starch (60 µm)
31 Oct 2022	123	unpacked	unpacked
02 Dec 2022	125	unpacked	unpacked

Two types of packaging materials were tested: a multilayer plastic film (Südpack Multipeel P 60/200; LDPE/PA) and compostable cellulose-starch-based films (Repaq RPQ-CBST 50 and RPQ-CBST 60). In Table 2, details on the material composition and barrier properties according to the manufacturer's specifications are summarized. After packaging, all samples were stored at 5 °C and 55 % relative humidity.

Table 2: Compositional and barrier properties of packaging material

Film	Material	Thickness in µm	OTR ¹	WVTR ²
Südpack Multipeel P 60/200	LDPE	45	35	8
	PA	12		
Repaq RPQ-CBST 50	Cellulose	50	4.1	22
	Starch			
RPQ-CBST 60	Cellulose	60	4.1	22
	Starch			

LDPE: low-density polyethylene; PA: polyamide

¹ Oxygen Transmission Rate (cm³(STP)/(m² × 24 h), at 23 °C, 0 % RH and 0.1 MPa partial pressure).

² Water Vapor Transmission Rate (g/(m² × 24 h), at 38 °C and 90 % RH).

HPLC

Organic acids in cheese samples, including lactic, citric, acetic, propionic, and butyric acid, were quantified by high-performance liquid chromatography (HPLC, Thermo Scientific UltiMate 3000) using a Rezex ROA-Organic Acid H⁺ column (300 × 7.8 mm, 8 µm; Phenomenex) with a refractive index detector operated at 55 °C. Samples were prepared using a modification of the method of Zeppa et al. [16] and Ahmed et al. [17]. Sample preparation involved homogenizing 5 g of chopped cheese with 25 ml of 0.1 % formic acid preheated to 70 °C, followed by stomacher treatment for 10 min. After centrifugation at 3.000 rpm for 15 min, the fat layer was removed, and the supernatant was sequentially filtered through cellulose filter paper (Rotilabo® Type 601P) and a 0.2 µm regenerated cellulose syringe filter (Rotilabo® Mini-Tip).

The mobile phase consisted of 0.1 % formic acid in RO water, run isocratically at 0.5 ml/min and 70 °C. Quantification was performed using external calibration with certified standards. Duplicate analyses were performed on all the samples.

Microbiological analysis

The number of mesophilic aerobic bacteria was determined using Plate Count Agar (PCA) according to DIN ISO 4833-1:2013 [18]. A surface inoculation of 50 µl was applied and the plate was incubated at 30 °C for 72 ± 2 h under aerobic conditions. All other microbiological analyses were carried out by our project partners muva. Yeasts and moulds were analysed by surface inoculation (100 µl), followed by incubation at 25 °C for 120 h under anaerobic conditions, in accordance with ASU §64 LFGB and DIN 10186:2005-10 [19]. Furthermore, *Listeria monocytogenes* (DIN EN ISO 11290-1 [20]), coagulase-positive *Staphylococcus* spp. (DIN EN ISO 6888-1 [21]), *Salmonella* spp. (DIN EN ISO 6579-1 [22]), *Escherichia coli* (DIN ISO 16649-2 [23]) and *Enterobacteriaceae* (DIN EN ISO 21528-2 [24]) were detected in accordance with the relevant international standards.

pH

The pH of the cheese samples was determined by MUVA using an electrometric method in accordance with VDLUFA [25].

NGS

NGS were carried out by the University of Bologna. DNA was extracted from 200 mg of crushed cheese using the Qiacube HT and the Qiagen DNeasy 96 PowerSoil Pro kit, with a specific pre-treatment for cheese matrices. Samples were mixed with 2 % sodium citrate, incubated at 45 °C, and centrifuged to separate the microbial pellet from the fat layer. After mechanical lysis with zirconium beads and a Tissue Lyzer, DNA was extracted from 550 µl of the supernatant according to the manufacturer's protocol.

5 µl of DNA were amplified using modified Takahashi primers. Amplicons were purified, indexed with Nextera XT adapters, normalized, pooled, and sequenced on a MiSeq platform using V3 chemistry (2 × 300 bp).

Reads (n = 703,965) were processed using Qiime2 (v2023.7) and DADA2, resulting in 98 ASVs across 9 samples after quality filtering and rarefaction to 39,089 reads per sample. Taxonomy was assigned using GreenGenes2 v2024.09 and Silva v138.2 databases.

Sensory analysis

The sensory evaluation was conducted by MUVA using a trained panel of five assessors following the principles of Quantitative Descriptive Analysis (QDA). The panel evaluated the samples based on the attributes appearance (surface and interior), odor, taste, and texture, using a 5-point scale (5 = excellent, 1 = poor).

Statistical analysis

Statistical evaluation was not possible for all samples at this stage. Additional data will be collected and analyzed in future work.

Results and Discussion

At the beginning of storage, the total bacterial count in cellulose-packaged samples was 2.01×10^7 CFU/g, while conventionally packaged samples showed a slightly lower value of 1.18×10^7 CFU/g. During the storage period a decrease in viable cell counts was observed in both packaging types. The gradual decrease in total bacterial counts observed during storage can be attributed to nutrient depletion, accumulation of inhibitory metabolites such as organic acids, reduced oxygen availability due to packaging conditions, and the natural microbial succession occurring during cheese ripening

[26]. Throughout the storage period, the pH values of all samples remained relatively stable, ranging between 5.5 and 5.9. No substantial differences between conventional and cellulose packaging were observed throughout the storage period for both cheeses produced on 17 August 2024 (Figure 1) and 16 February 2024 (Figure 2). Overall, packaging material did not exert a significant influence on the dynamics of yeast and mould development in either batch. Furthermore, no pathogenic microorganisms such as *Listeria monocytogenes*, *Salmonella* spp., or coagulase-positive *Staphylococcus* were detected in any sample.

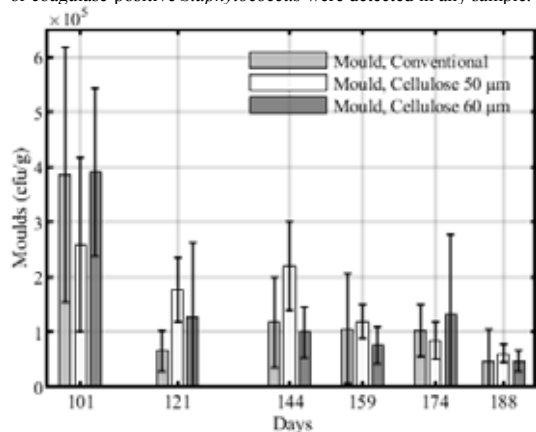


Figure 1: Moulds during storage (Production Date: 17 Aug 2024)

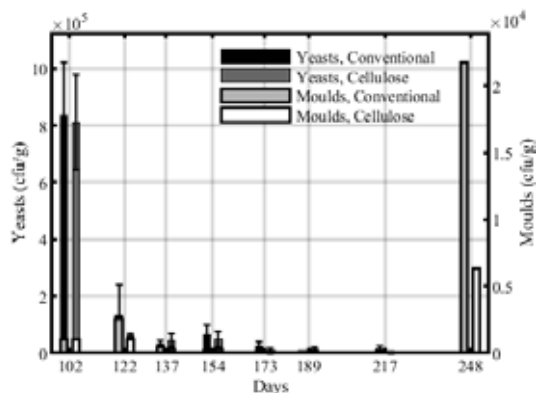


Figure 2: Yeasts and Moulds during storage (Production Date: 16 Feb 2024)

The microbiota of Tiroler Bergkäse samples was predominantly composed of *Lactobacillus delbrueckii* and *Streptococcus salivarius*. Microbial composition remained relatively stable across conventional and cellulose/starch packaging, although some samples exhibited higher species diversity and minor contributions from *Enterobacteriaceae*, *Pseudomonadaceae*, and *Corynebacteriaceae*. Overall, cheeses packaged in cellulose/starch films exhibited microbial diversity comparable to or slightly higher than those packaged conventionally.

The presence of distinct peaks in the HPLC chromatogram (Figure 3), corresponding to lactic acid, acetic acid, and propionic acid, was confirmed through spiking experiments and comparison with certified standards. Two additional peaks at 10.06 min and 10.26 min, identified as lactose and citric acid, exhibited partial overlap under the framework of refractive index detection.

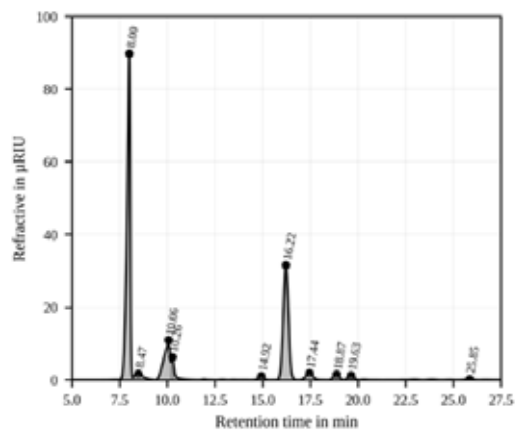


Figure 3: Chromatogram of the prepared cheese (Production Date: 17 Aug 2024)

In order to enhance separation and facilitate reliable quantification, the utilisation of a UV detector is recommended, given its superior selectivity for these compounds. [16, 17, 27]. Quantification is currently in progress and will be reported in future work.

Sensory analysis showed no differences between the cheeses.

Conclusion and Outlook

This study demonstrated that compostable cellulose-starch packaging preserved the microbiological, physicochemical, and sensory properties of Tiroler Bergkäse comparably to conventional LDPE/PA multilayer films. Throughout refrigerated storage, no significant differences in total bacterial counts, yeast and mould development, or pH were observed between the two packaging types. The microbiota composition remained relatively stable, with *Lactobacillus delbrueckii* and *Streptococcus salivarius* dominating across all samples.

The quantification of organic acids revealed the presence of lactic acid, acetic acid, and propionic acid in several samples. However, due to the limited number of quantified results, it is not possible to determine the influence of packaging material or storage time at this stage. In general, the analytical method requires further optimization. Furthermore, comprehensive method validation is imperative to ensure analytical reliability. This encompasses the determination of limits of detection (LOD), limits of quantification (LOQ), linearity, repeatability, and recovery.

From a sustainability perspective, cellulose-based packaging is considered an attractive ecological alternative due to the renewable nature of the raw materials utilised in its production. Nevertheless, challenges persist regarding industrial composting infrastructure, which limits its end-of-life management compared to recyclable monomaterials like polypropylene [28, 29]. Despite the fact that multilayer LDPE/PA films continue to demonstrate excellent barrier properties, which are crucial for maintaining cheese quality, their poor recyclability contradicts the objectives of the circular economy [30].

Acknowledgments

The supervision of my doctoral thesis by Christian Huck, the collaboration within the project with Manuel Kessel (MCI), Swantje Petersen (HS Kempten), and Amelie Reinold (Bioalpin), as well as financial support from the Interreg project QualiCheese (BA0100106), are gratefully acknowledged.

References

- [1] Statistik Austria, *Versorgungsbilanzen für tierische Produkte*. [Online]. Available: https://www.statistik.at/fileadmin/user_upload/SB_1 (accessed: Apr. 26 2025).
- [2] AgrarMarkt Austria, *Marktbericht MILCH UND MILCHPRODUKTE. 12. Ausgabe*. [Online]. Available: https://www.ama.at/getattachment/8733a278-0896-4cc0-9e89-d1fc0cc2717a/MB_12.pdf (accessed: Apr. 26 2025).
- [3] *Regulation on geographical indications for wine, spirit drinks and agricultural products, as well as traditional specialities guaranteed and optional quality terms for agricultural products, amending Regulations (EU) No 1308/2013, (EU) 2019/787 and (EU) 2019/1753 and repealing Regulation (EU) No 1151/2012*, Regulation (EU) 2024/1143, European Parliament and of the Council of the European Union. [Online]. Available: https://agriculture.ec.europa.eu/farming/geographical-indications-and-quality-schemes/geographical-indications-and-quality-schemes-explained_en#pdo
- [4] Bundesministerium für Land- und Forstwirtschaft, Klima- und Umweltschutz, Regionen und Wasserwirtschaft (BMLUK), *Tiroler Bergkäse g. U.* [Online]. Available: https://www.bmluk.gv.at/themen/lebensmittel/trad-lebensmittel/kaese/tiroler_bergkaese.html (accessed: Apr. 26 2025).
- [5] S. Ebnesajjad, Ed., *Plastic films in food packaging: Materials, technology and applications*. Oxford: William Andrew, 2013. [Online]. Available: <https://www.sciencedirect.com/science/book/9781455731121>
- [6] K. Marsh and B. Bugusu, "Food packaging—roles, materials, and environmental issues," *Journal of food science*, vol. 72, no. 3, R39-55, 2007, doi: 10.1111/j.1750-3841.2007.00301.x.
- [7] C. Spreafico and D. Russo, "A sustainable cheese packaging survey involving scientific papers and patents," *Journal of Cleaner Production*, vol. 293, p. 126196, 2021, doi: 10.1016/j.jclepro.2021.126196.
- [8] P. F. Fox, *Fundamentals of Cheese Science*, 2nd ed. Boston, MA: Springer, 2017.
- [9] N. Peelman *et al.*, "Application of bioplastics for food packaging," *Trends in Food Science & Technology*, vol. 32, no. 2, pp. 128–141, 2013, doi: 10.1016/j.tifs.2013.06.003.
- [10] P. R. Salgado, L. Di Giorgio, Y. S. Musso, and A. N. Mauri, "Recent Developments in Smart Food Packaging Focused on Biobased and Biodegradable Polymers," *Front. Sustain. Food Syst.*, vol. 5, 2021, doi: 10.3389/fsufs.2021.630393.
- [11] S. Andiç, Y. Tunctürk, and H. Gençcelep, "The effect of different packaging methods on the formation of biogenic amines and organic acids in Kashar cheese," *Journal of dairy science*, vol. 94, no. 4, pp. 1668–1678, 2011, doi: 10.3168/jds.2010-3586.
- [12] N. Renoldi, S. Calligaris, M. C. Nicoli, M. Marino, A. Rossi, and N. Innocente, "Effect of the shifting from multi-layer systems towards recyclable mono-material packaging solutions on the shelf-life of portioned semi-hard cheese," *Food Packaging and Shelf Life*, vol. 46, p. 101363, 2024, doi: 10.1016/j.fpsl.2024.101363.
- [13] O. Erkmen and T. F. Bozöglü, *Food microbiology: Principles into practice*. Chichester, West Sussex, Hoboken, NJ: John Wiley & Sons, 2016. [Online]. Available: <https://onlinelibrary.wiley.com/doi/book/10.1002/9781119237860>
- [14] U. Rehn, F. K. Vogensen, S.-E. Persson, K. Hallin Saedén, B. F. Nilsson, and Y. Ardö, "Influence of microflora on texture and contents of amino acids, organic acids, and volatiles in semi-hard cheese made with DL-starter and propionibacteria," *Journal of dairy science*, vol. 94, no. 3, pp. 1098–1111, 2011, doi: 10.3168/jds.2010-3146.
- [15] N. M. Quijada, M. Hernández, and D. Rodríguez-Lázaro, "High-throughput sequencing and food microbiology," *Advances in food and nutrition research*, vol. 91, pp. 275–300, 2020, doi: 10.1016/bs.afnr.2019.10.003.
- [16] M. E. Ahmed *et al.*, "Measurement of carbohydrates and organic acids in varieties of cheese using high-performance liquid chromatography," *Food science & nutrition*, vol. 11, no. 5, pp. 2081–2085, 2023, doi: 10.1002/fsn3.2438.
- [17] G. Zeppa, L. Conterno, and V. Gerbi, "Determination of organic acids, sugars, diacetyl, and acetoin in cheese by high-performance liquid chromatography," *J. Agric. Food Chem.*, vol. 49, no. 6, pp. 2722–2726, 2001, doi: 10.1021/jf0009403.
- [18] *Microbiology of the food chain—Horizontal method for the enumeration of microorganisms—Part 1: Colony count at 30 °C by the pour plate technique*, ISO 4833-1:2013, ISO, Geneva, Switzerland, 2013.
- [19] *Microbiological analysis of milk - Enumeration of yeasts and moulds - Reference method*, DIN 10186:2005-10, ISO, Berlin, 2005.
- [20] *Microbiology of the food chain - Horizontal method for the detection and enumeration of Listeria monocytogenes and of Listeria spp. - Part 1: Detection method*, ISO 11290-1:2017, ISO, 2017.
- [21] *Microbiology of the food chain - Horizontal method for the enumeration of coagulase-positive staphylococci (Staphylococcus aureus and other species) - Part 1: Method using Baird-Parker agar medium (ISO 6888-1:2021)*, DIN EN ISO 6888-1:2022-06, ISO, 2022.
- [22] *Microbiology of the food chain - Horizontal method for the detection, enumeration and serotyping of Salmonella - Part 1: Detection of Salmonella spp. (ISO 6579-1:2017 + Amd.1:2020)*, DIN EN ISO 6579-1:2020-08, ISO, 2020.
- [23] *Microbiology of food and animal feeding stuffs - Horizontal method for the enumeration of β-glucuronidase-positive Escherichia coli - Part 2: Colony-count technique at 44 °C using 5-bromo-4-chloro-3-indolyl β-D-glucuronide (ISO 16649-2:2001)*, DIN ISO 16649-2:2020-12, ISO, 2020.
- [24] *Microbiology of the food chain - Horizontal method for the detection and enumeration of Enterobacteriaceae - Part 2: Colony-count technique (ISO 21528-2:2017, Corrected version 2018-06-01); German version EN ISO 21528-2:2017*, DIN EN ISO 21528-2:2019-05, ISO, 2019.
- [25] Verband Deutscher Landwirtschaftlicher Untersuchungs- und Forschungsanstalten, *Methodenbuch / Verband Deutscher Landwirtschaftlicher Untersuchungs- und Forschungsanstalten. Hrsg. von Rolf Bassler*, 4th ed. Darmstadt: VDLUFA-Verl., 1985.
- [26] A. Szosland-Faltyn, N. Maciejewska, and B. Bartodziejska, "Effect of Ripening Temperature on Microbial Safety and Biogenic Amine Levels in Rennet Cheeses Produced from Raw Cow Milk," *Journal of food protection*, vol. 88, no. 5, p. 100476, 2025, doi: 10.1016/j.jfp.2025.100476.
- [27] *ISO/TS 19046-2: Cheese — Determination of propionic*, International Dairy Federation. [Online]. Available: <https://standards.iteh.ai/catalog/standards/sist/fcb71e58-ed88-4cd4-a959-b3357ec062f9/iso-ts-19046-2-2017>
- [28] M. Seier, V.-M. Archodoulaki, T. Koch, B. Duscher, and M. Gahleitner, "Prospects for Recyclable Multilayer Packaging: A Case Study," *Polymers*, vol. 15, no. 13, 2023, doi: 10.3390/polym15132966.
- [29] P. Tamizhdurai *et al.*, "A state-of-the-art review of multilayer packaging recycling: Challenges, alternatives, and outlook," *Journal of Cleaner Production*, vol. 447, p. 141403, 2024, doi: 10.1016/j.jclepro.2024.141403.
- [30] V. Siracusa, M. D. Rosa, S. Romani, P. Rocculi, and U. Tylewicz, "Life Cycle Assessment of multilayer polymer film used on food packaging field," *Procedia Food Science*, vol. 1, pp. 235–239, 2011, doi: 10.1016/j.profoo.2011.09.037.

Recovery of polyolefins from mixed waste in Tyrol: Status, qualities and critical parameters for recycling

A.-M. Lipp^{1,*}; D. Blasenbauer¹; J. H. Stipanovic²; G. Koinig²; A. Tischberger-Aldrian²; J. Lederer¹

1: Christian Doppler Laboratory for a Recycling-based Circular Economy, Institute of Chemical, Environmental and Bioscience Engineering (ICEBE), TU Wien, Getreidemarkt 9/166, 1060 Vienna, Austria

2: Waste Processing Technology and Waste Management, Department of Environmental and Energy Process Engineering, Montanuniversität Leoben, Franz-Josef-Straße 18, 8700 Leoben, Austria

* Correspondent author: anna-maria.lipp@tuwien.ac.at

Keywords: Circular economy, Municipal solid waste, Plastic waste, Recycling, Material recovery facility, Automated waste sorting

Introduction

Globally, vast amounts of plastics are being incinerated, landfilled, littered or dumped [1] while the demand for plastic continues to increase [2]. Although plastic waste collection, recovery, and recycling are well-established practices in industrialized nations, recycled plastics currently meet only ~ 10 % of Europe's total plastic demand [3], highlighting a significant reliance on primary raw materials. Separate waste collection and connected capture rates of plastic waste were shown to have limited success, especially in urban centers and areas with extensive tourism due to spatial constraints and various socio-economic reasons [4], [5], [6]. Thus, substantial quantities of plastics are still found in mixed municipal solid waste (MSW) [7].

While waste separation performance in the city of Innsbruck and Tyrol as a whole is relatively strong compared to the broader EU context [8], a considerable untapped potential remains. To harness these plastic resources, sensor-based sorting, i.e., near-infrared (NIR) technologies, can be implemented within material recovery facilities (MRFs) [9]. Thereby, shortwave NIR light with a wavelength of 800 - 2,500 nm is directed onto a particle and its material-specific transmission spectrum is analyzed by a detector [10] and, if applicable, sorted by means of compressed air. The extraction of polyolefins (PO) shows particular potential, as these polymers account for a large proportion of total plastics production with various application cases. They are not subject to a deposit scheme, such as polyethylene terephthalate (PET). PO are semi-crystalline thermoplastics polymerized from alkenes; the most important resins, polyethene (PE) and polypropylene (PP), account for approx. 63 % of the global plastics production volume [11]. Typical use cases include packaging, pipes or automotive applications [11].

This paper deals with the technical aspects, quantities and qualities of PO recovery from the mixed MSW in terms of recycling. The districts of Innsbruck-Stadt, Innsbruck-Land and Schwaz are investigated through testing upgrades to the local MRF with NIR technology, thereby contributing to the Tyrol's shift toward circularity.

Material and Methods

The investigated MRF, Recyclingzentrum (RZ) Ahrental, is located in Innsbruck-Vill and treats approximately 80,000 t_{yr}⁻¹ of mixed MSW and bulky waste of household and commercial origin. After shredding and screening (40 – 250 mm), the waste is subjected to a ballistic separator as well as magnets and eddy current separators, as seen in Figure 1. This results in two metal fractions (magnetic and non-ferrous) for recycling and three mixed fractions for thermal utilization with different calorific values. This includes a low calorific value fraction (LCVF; < 40 mm), as well as a medium (MCVF; 40 - 250 mm, 2D) and high calorific value fraction (HCVF; 40 - 250 mm, 3D).

NIR Processing Trials for PO Recovery

In order to perform technical assessments of PO recoveries for the proposed NIR upgrades, two processing trials have been conducted. Therefore, ~ 1,000 kg of HCVF and ~ 520 kg MCVF were

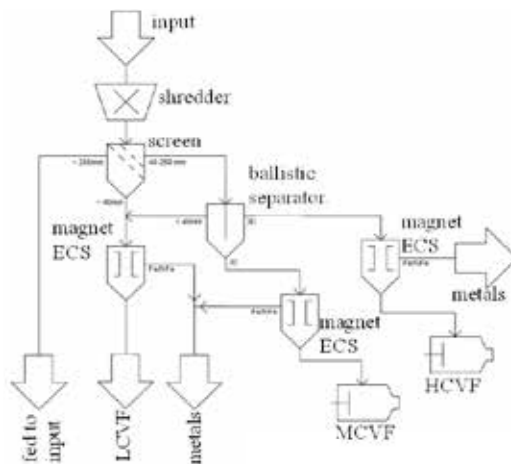


Figure 1: Simplified process schematic of the RZ Ahrental with a shredder, screen, ballistic separator, magnets, eddy current separators (ECS) and balers.

representatively sampled and subjected to a two-stage rough-cleaner NIR setup at the Digital Waste Research Lab at the Chair of Waste Processing Technology and Waste Management of the Montanuniversität Leoben in St. Michael in Upper Styria. PO were positively sorted in both NIR stages, and the eject and reject streams were continuously sampled. All outputs were sorted manually and with the help of Fourier transform infrared (FTIR) spectroscopy; to further determine PO contents, the plastic fractions were shredded to 15 mm particle size and a sink-float analysis was conducted with subsamples of 100 g in 18 l water tanks at 25 °C for 48 h. PO exhibit densities lower than 1 kg l⁻¹; hence, floating fractions were considered PO after being dried at 60 °C and weighed. Finally, the technical indicators of mass recovery rate (R), purity (P) and yield (Y) have been calculated via Equations (1), (2) and (3), respectively, whereas m denotes the total mass and c the PO content of the stream.

$$R = \frac{m_{out}}{m_{in}} \quad (1)$$

$$P = \frac{m_{PO,out}}{m_{in}} = c_{PO,out} \quad (2)$$

$$Y = \frac{m_{PO,out}}{m_{PO,in}} = \frac{m_{out} \cdot c_{PO,out}}{m_{PO,in} \cdot c_{PO,in}} \quad (3)$$

Material Flow Analysis and Heating Values

To assess the overall impact on the waste management system in the region, six different scenarios were modeled using material flow analysis (MFA) with the software STAN 2.6.801 in accordance with ÖNORM S 2096 [12]. MFA provides a framework for mapping and evaluating material stocks and flows over time and space, grounded in the law of mass conservation [13], [14]. All main municipal PO

streams - mixed MSW and separately collected lightweight packaging waste (LWP) - were modeled within the area. Processes include the RZ Ahrental and the MRF for LWP, as well as a simulated recycling plant. Data were received from local municipalities, plant operators and packaging waste collection and recycling companies. In addition to the status quo, three scenarios were implemented; for scenario description, see Table 1.

Scenario	Description	Upgrade	NIRs
Status quo	No PO Recovery	none	none
I	PO Recovery I	HCVF	two
II	PO Recovery II	MCVF	two
III	Maximum Recovery	both	four

Table 1: Scenario description for the potential recovery of polyolefins (PO) in the service area of the RZ Ahrental.

Since PO, being saturated hydrocarbons consisting only of carbon and hydrogen, exhibit particularly high heating values, typically between 40 - 43 MJ kg⁻¹ [15], the extraction of such is expected to impact thermal utilization and refuse-derived fuels (RDFs). For this reason, the heating value of the remaining streams was determined based on the chemical elemental composition of the individual fractions, according to Kost [16], which represents a variant of *Dulong's formula* adapted for RDF. Here, the raw lower heating value (LHV) is calculated following Equation (4) from the total content of carbon (C), oxygen (O), hydrogen (H) and water (W).

$$LHV = 33.146 C - 10.384 O + 103.469 H - 2.441 W \quad (4)$$

Results and Discussion

NIR Processing Trials for PO Recovery and Mechanical Recycling

In trial 1, about 17 % of the total input of HCVF was recovered as PO concentrate during the initial NIR sorting stage, as seen in Figure 2. This material had an approximate mono-plastic purity of 40 % and a technical purity of around 60 %, as perceived by the NIR sorter, which also accounts for compounds and textiles. Following a second sorting step, the PO concentrate comprised roughly 11 % of the total input mass, with an improved mono-plastic purity of about 60 % and technical purity of around 70 %.

Challenges were particularly evident by the presence of composite materials in the feedstock - items such as polyurethane foams layered with textiles or plastic components combined with metals introduced by bulky waste. Lower yields can largely be attributed to these compound and composite materials, which force a trade-off between maximizing purity and maintaining overall yield. In terms of product stream composition, all PO streams show a significant proportion of non-packaging content.

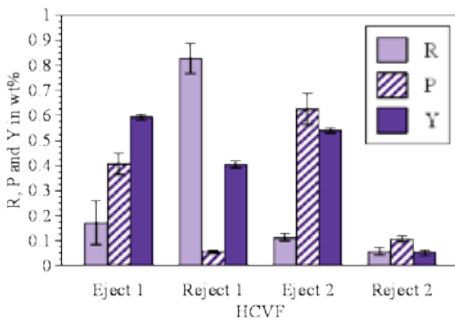


Figure 2: Mass recovery rate (R), purity (P) and yield (Y) for the Polyolefin (PO) recovery from the high calorific value fraction (HCVF) of the RZ Ahrental in trial 1. Values are depicted as mean \pm standard deviation of a normal distribution.

In trial 2 (MCVF), the initial NIR sorting stage yielded about 26 % of the total input mass as PO output. A second round of sorting resulted in about a 15 % mass recovery rate. Within those streams,

the mono-plastic purity was enhanced from a first level of roughly 20 % to over 30 %. However, the technical purity remained steady at around 55 % throughout both steps, with no notable improvement. All calculated technical indicators for trial 2 are displayed in Figure 3. The MCVF feedstock comprised a greater proportion of film plastics, which complicate sorting. As films tend to overlap and behave unpredictably due to their characteristics, such as being lightweight and thin, they are challenging to categorize and separate accordingly by state-of-the-art NIR sorters [10].

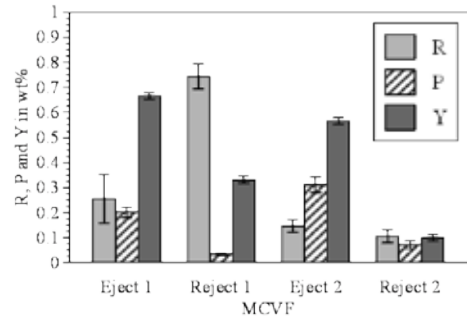


Figure 3: Mass recovery rate (R), purity (P) and yield (Y) for the Polyolefin (PO) recovery from the high calorific value fraction (MCVF) of the RZ Ahrental in trial 2. Values are depicted as mean \pm standard deviation of a normal distribution

The gap between mono-plastic and technical purity observed in the trials is primarily driven by the substantial presence of compounds and textile materials in the waste streams, which is also the case with other MRFs. There, one notable issue is the misclassification of polyester textiles: These textiles are often wrongly identified by NIR systems as PET, leading to contamination of PET fractions in LWP MRFs. Whether such contamination is acceptable depends on the specific end-use and requirements of downstream recyclers [17]. A similar pattern was evident in the processing trials, where PO-based textiles contributed notably to contamination levels. These textiles, widely found in products like sportswear, shoes and carpets [18], [19], are commonly discarded with mixed MSW. When present, they interfere with mechanical PO recycling processes, diminishing the quality of the final product. Hence, a reduction of these objects in the streams should take place *a priori*. The EU's revised Waste Framework Directive will require separate textile collection starting in 2025 [20], a move expected to reduce textile contamination in the investigated waste streams. However, the regulation does not clearly define what qualifies as textile waste or specifies the required quality of collected materials. For example, in Austria, collection efforts mostly target clothing suitable for reuse, while damaged textiles are still disposed of in mixed MSW [21].

Although the technical viability of PO recovery from mixed waste has been demonstrated across multiple studies [22], [23], [24], [25], investment remains limited. In contrast, Dutch MRFs have shown that plastics recovered from MSW can meet quality standards, prompting regulatory acceptance of such recyclates in national recycling targets, a precedent Austria may need to follow [9], [26]. Mechanically recycled PO from MSW generally shows comparable properties to that from separately collected streams [14], [27]. However, recyclate suitability depends on the final application [28], and contamination safety and odor remain an underexplored area [14], [22]. The upcoming EU Packaging and Packaging Waste Regulation [29], which introduces mandatory minimum recycled content, is expected to boost recyclate demand, also for secondary materials less suited for high-end uses.

Chemical Recycling of Recovered PO

To address contamination issues in mechanical recycling, thermochemical methods like pyrolysis offer a promising

complementary approach due to their higher tolerance in plastics processing types (rigids, flexibles, foams...) within the feedstock [30], [31]. In Austria, the OMV ReOil® plant, operational since 2024 with a capacity of 16,000 t_{yr}⁻¹ [9], realizes such chemical recycling of PO. The process involves heating a blend of PO melt and a solvent to below 500 °C in a tubular reactor, breaking down polymers into short-chain hydrocarbons, which are then separated via distillation [32], [33]. Heavier fractions and unconverted material are recirculated, producing usable liquid hydrocarbons alongside minor gas and coke residues [32], [33]. Despite its flexibility, pyrolysis requires relatively clean feedstock and struggles with PVC contamination, which is particularly present in 3D material [31]. Here, the HCVF PO Eject 2 stream contained approximately 1.2 % PVC (excluding compounds), while the MCVF equivalent remained under 0.01 %.

Material Flow Analysis and Heating Values

The MFA indicates that installing two NIR sorters for the HCVF stream could increase regional PO recycling by 5.7 % (Scenario I) while upgrading the MCVF stream alone would result in a 10 % boost (Scenario II), in absolute terms. Applying NIR sorting to both outputs (Scenario III) yields the highest gain, with a combined 16 % increase.

Annual variation in lower heating values (LHV) of material flows designated for incineration were also assessed. Due to the waste heterogeneity, results show an uncertainty of approximately ± 10 %. Therefore, no significant differences across the scenarios are evident, as illustrated in Figure 4. Nonetheless, a consistent decline in heating value is expected following PO removal. In comparison, sampling errors contributed less to the overall uncertainty.

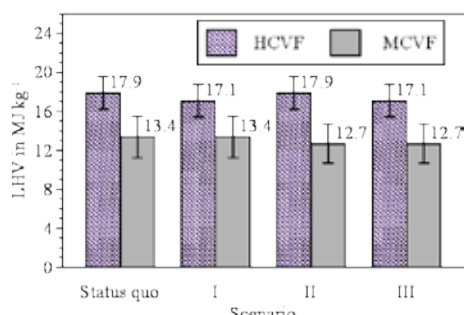


Figure 4: Lower heating values (LHV, raw) of the remaining high (HCVF) and medium calorific value fraction (MCVF) in the different scenarios. Values are depicted as mean ± standard deviation of a normal distribution.

Research has shown that enhancing separate collection efforts leads to lower plastic and textile content in RDF streams [34]. Such development is expected to continue, especially if PO is increasingly extracted from mixed MSW at scale. While the exact effect on heating values is still uncertain, a decline is likely due to the removal of plastics characterized by higher heating values.

Austria, currently a net exporter of RDF [35], could expand PO recovery without facing domestic shortages. However, reduced RDF availability may have cross-border consequences, potentially increasing dependence on fossil fuels in other countries. Striking the right balance between recycling and RDF production remains an open question, requiring further study. Region-specific case studies are essential to better understand and quantify the interactions between material recovery and energy recovery and to guide future decision-making.

Conclusion

Regardless of the well-established waste collection system in the districts of Innsbruck-Stadt, Innsbruck-Land and Schwaz, plastic capture rates have plateaued, leaving considerable recoverable material in mixed MSW. The local MRF focuses on metal recovery,

with outstanding investments in plastics recovery due to insufficient data on material quality and quantity. This study highlights the potential for PO sorting, showing that a two-step NIR sorting process can achieve 50 - 70 % purity and boost regional recycling rates by an absolute 6 - 16 % without significantly affecting heating values of residual streams.

Nevertheless, regulatory support is essential to offset the economic disadvantage of recycled plastics over virgin materials. Small-scale MRF upgrades can yield acceptable purities, but balancing recovery rates with contamination remains challenging. Furthermore, the classification of mixed MSW as non-recoverable limits its perceived value, while odor and chemical safety concerns require further investigation.

Ultimately, while mixed MSW recovery supports circularity, it must complement and not replace separate collection. Ongoing research is needed to understand how expanding recovery from mixed MSW might affect household sorting behavior and the integrity of existing collection systems.

Acknowledgements

The financial support from the Austrian Federal Ministry for Labour and Economy, the National Foundation for Research, Technology and Development and the Christian Doppler Research Association is gratefully acknowledged. Furthermore, we greatly acknowledge the financial and non-financial support of our company partners, which are, in alphabetical order: Ahrental GmbH, Altstoff Recycling Austria AG, Brantner Österreich GmbH, Holding Graz Kommunale Dienstleistungen GmbH, Lenzing Aktiengesellschaft, Linz Service GmbH, Mayr-Melnhof Board and Paper AG, OMV Downstream GmbH, Wien Energie GmbH, and Wopfinger Transportbeton Ges.m.b.H. In addition, we thank our strategic partner Magistratsabteilung MA 48, responsible for Waste Management, Street Cleaning and Vehicle Fleet Management in the City of Vienna.

Disclaimer

This conference paper refers to the following unpublished journal article: A.-M. Lipp, D. Blasenbauer, H. Stipanović, G. Koinig, A. Tischberger-Aldrian and J. Lederer, "Technical Evaluation and Recycling Potential of Polyolefin and Paper Separation in Mixed Waste Material Recovery Facilities" *Waste Manag.*, [Manuscript Submitted], 2025

References

- [1] M. Dokl *et al.*, "Global projections of plastic use, end-of-life fate and potential changes in consumption, reduction, recycling and replacement with bioplastics to 2050," *Sustain. Prod. Consum.*, vol. 51, pp. 498–518, Nov. 2024, doi: 10.1016/j.spc.2024.09.025.
- [2] A. T. Williams and N. Rangel-Buitrago, "The past, present, and future of plastic pollution," *Mar. Pollut. Bull.*, vol. 176, p. 113429, Mar. 2022, doi: 10.1016/j.marpolbul.2022.113429.
- [3] Plastics Europe, "Plastics – the Facts 2022," 2022. Accessed: Jul. 17, 2023. [Online]. Available: <https://plasticseurope.org/knowledge-hub/plastics-the-facts-2022-2/>
- [4] D. Schuch, J. Lederer, J. Fellner, and C. Scharff, "Separate collection rates for plastic packaging in Austria – A regional analysis taking collection systems and urbanization into account," *Waste Manag.*, vol. 155, pp. 211–219, Jan. 2023, doi: 10.1016/j.wasman.2022.09.023.
- [5] A. Feil, T. Pretz, M. Jansen, and U. Thoden van Velzen, "Separate collection of plastic waste, better than technical sorting from municipal solid waste?," *Waste Manag. Res.*, vol. 35, no. 2, pp. 172–180, Feb. 2017, doi: 10.1177/0734242X16654978.
- [6] G. Obersteiner, S. Gollnow, and M. Eriksson, "Carbon footprint reduction potential of waste management strategies in tourism," *Environ. Dev.*, vol. 39, p. 100617, Sep. 2021, doi: 10.1016/j.envdev.2021.100617.
- [7] T. Karak, R. M. Bhagat, and P. Bhattacharyya, "Municipal solid

- waste generation, composition, and management: The world scenario,” *Crit. Rev. Environ. Sci. Technol.*, vol. 42, no. 15, pp. 1509–1630, 2012, doi: 10.1080/10643389.2011.569871.
- [8] J. Lederer *et al.*, “A review of recent trends to increase the share of post-consumer packaging waste to recycling in Europe,” *Detritus*, vol. Volume 19-June 2022, p. 3, Jun. 2022, doi: 10.31025/26111-4135/2022.15198.
- [9] D. Blasenbauer, A.-M. Lipp, J. Fellner, A. Tischberger-Aldrian, H. Stipanovic, and J. Lederer, “Recovery of plastic packaging from mixed municipal solid waste. A case study from Austria,” *Waste Manag.*, vol. 180, pp. 9–22, May 2024, doi: 10.1016/j.wasman.2024.02.040.
- [10] H. Stipanovic *et al.*, “Influence of Different Measuring Backgrounds on the Classification of Multilayer Polyolefin Films Using a Near-Infrared Handheld Spectrometer,” *Appl. Spectrosc.*, p. 00037028241307034, Dec. 2024, doi: 10.1177/00037028241307034.
- [11] W. Posch, “2 - Polyolefins: Plastics Engineering Encyclopedia,” in *Applied Plastics Engineering Handbook (Third Edition)*, M. Kutz, Ed., in Plastics Design Library., William Andrew Publishing, 2024, pp. 29–56. doi: 10.1016/B978-0-323-88667-3.00012-6.
- [12] O. Cencic and H. Rechberger, “Material Flow Analysis with Software STAN,” *J. Environ. Eng. Manag.*, vol. 18, no. 1, pp. 3–7, 2008.
- [13] P. H. Brunner and H. Rechberger, *Handbook of Material Flow Analysis: For Environmental, Resource, and Waste Engineers*, 2nd ed. Boca Raton: CRC Press, 2016. doi: 10.1201/9781315313450.
- [14] A.-M. Lipp, J. Schlossnikl, I. Gentgen, T. Koch, V.-M. Archodoulaki, and J. Lederer, “Recycling Rigid Polypropylene from Mixed Waste: Does the Origin Affect Mechanical Recyclate Quality?,” *Waste Manag. Res.*, vol. [Manuscript Accepted with Revisions], 2025.
- [15] R. Fehringer and P. H. Brunner, *Kunststoffflüsse und Möglichkeiten der Kunststoffverwertung in Österreich*. in Monographien / Umweltbundesamt, no. Bd. 80. Wien: Umweltbundesamt, 1997.
- [16] T. Kost, “Brennstofftechnische Charakterisierung von Haushaltsabfällen,” Dissertation, Technische Universität Dresden, 2001.
- [17] I. Antonopoulos, G. Faraca, and D. Tonini, “Recycling of post-consumer plastic packaging waste in the EU: Recovery rates, material flows, and barriers,” *Waste Manag.*, vol. 126, pp. 694–705, 2021, doi: <https://doi.org/10.1016/j.wasman.2021.04.002>.
- [18] Y. Kim, “The use of polyolefins in industrial and medical applications,” in *Polyolefin Fibres*, S. C. O. Ugbole, Ed., in Woodhead Publishing Series in Textiles., Woodhead Publishing, 2009, pp. 133–153. doi: 10.1533/9781845695552.1.133.
- [19] M. Ouederni, “Polyolefins in Textiles and Nonwovens,” in *Polyolefin Compounds and Materials: Fundamentals and Industrial Applications*, M. Al-Ali AlMa’adeed and I. Krupa, Eds., Cham: Springer International Publishing, 2016, pp. 231–245. doi: 10.1007/978-3-319-25982-6_9.
- [20] EU, “Directive (EU) 2018/851 of the European Parliament and of the Council of 30 May 2018 amending Directive 2008/98/EC on waste,” *OJ L*, vol. 150, pp. 109–140, May 2018.
- [21] BMSGPK, “Recycling von Alttextilien: Was in Österreich gilt.” Konsumentenfragen. Accessed: Mar. 11, 2025. [Online]. Available: <https://www.konsumentenfragen.at/konsumentenfragen/Aktuelles/Konsumentenfragen/Recycling-von-Alttextilien-Was-in-Oesterreich-gilt.html>
- [22] A. Cabanes, M. Strangl, E. Ortner, A. Fullana, and A. Buettner, “Odorant composition of post-consumer LDPE bags originating from different collection systems,” *Waste Manag.*, vol. 104, pp. 228–238, Mar. 2020, doi: 10.1016/j.wasman.2020.01.021.
- [23] B. Luijsterburg and H. Goossens, “Assessment of plastic packaging waste: Material origin, methods, properties,” *Resour. Conserv. Recycl.*, vol. 85, pp. 88–97, Apr. 2014, doi: 10.1016/j.resconrec.2013.10.010.
- [24] S. Möllnitz, M. Feuchter, I. Duretek, G. Schmidt, R. Pomberger, and R. Sarc, “Processability of Different Polymer Fractions Recovered from Mixed Wastes and Determination of Material Properties for Recycling,” *Polymers*, vol. 13, no. 3, Art. no. 3, Jan. 2021, doi: 10.3390/polym13030457.
- [25] U. Thoden van Velzen, S. Chu, F. Alvarado Chacon, M. T. Brouwer, and K. Molenveld, “The impact of impurities on the mechanical properties of recycled polyethylene,” *Packag. Technol. Sci.*, vol. 34, no. 4, pp. 219–228, Apr. 2021, doi: 10.1002/pts.2551.
- [26] C. Picuno, E. Van Eygen, M. T. Brouwer, K. Kuchta, and U. Thoden van Velzen, “Factors Shaping the Recycling Systems for Plastic Packaging Waste—A Comparison between Austria, Germany and The Netherlands,” *Sustainability*, vol. 13, no. 12, Art. no. 12, Jan. 2021, doi: 10.3390/su13126772.
- [27] U. Thoden van Velzen, I. Smeding, M. Brouwer, and E. Maaskant, “Comparison of the quality of mechanically recycled plastics made from separately collected and mechanically recovered plastic packaging waste,” in *Conference: Waste to Resources*, Hanover, May 2021. [Online]. Available: https://www.researchgate.net/publication/351746182_Comparison_of_the_quality_of_mechanically_recycled_plastics_made_from_separately_collected_and_mechanically_recovered_plastic_packaging_waste
- [28] M. Golkaram *et al.*, “Quality model for recycled plastics (QMRP): An indicator for holistic and consistent quality assessment of recycled plastics using product functionality and material properties,” *J. Clean. Prod.*, vol. 362, p. 132311, Aug. 2022, doi: 10.1016/j.jclepro.2022.132311.
- [29] EU, “Regulation (EU) 2025/40 of the European Parliament and of the Council of 19 December 2024 on packaging and packaging waste, amending Regulation (EU) 2019/1020 and Directive (EU) 2019/904, and repealing Directive 94/62/EC (Text with EEA relevance),” *OJ L*, pp. 1–124, Dec. 2024.
- [30] M. Kusenberg *et al.*, “Towards high-quality petrochemical feedstocks from mixed plastic packaging waste via advanced recycling: The past, present and future,” *Fuel Process. Technol.*, vol. 238, p. 107474, Dec. 2022, doi: 10.1016/j.fuproc.2022.107474.
- [31] K. Ragaert, L. Delva, and K. Van Geem, “Mechanical and chemical recycling of solid plastic waste,” *Waste Manag.*, vol. 69, pp. 24–58, Nov. 2017, doi: 10.1016/j.wasman.2017.07.044.
- [32] A. Lechleitner, D. Schwabl, T. Schubert, M. Bauer, and M. Lehner, “Chemisches Recycling von gemischten Kunststoffabfällen als ergänzender Recyclingpfad zur Erhöhung der Recyclingquote,” *Österr. Wasser- Abfallwirtsch.*, vol. 72, no. 1, pp. 47–60, Feb. 2020, doi: 10.1007/s00506-019-00628-w.
- [33] T. Schubert, M. Lehner, T. Karner, W. Hofer, and A. Lechleitner, “Influence of reaction pressure on co-pyrolysis of LDPE and a heavy petroleum fraction,” *Fuel Process. Technol.*, vol. 193, pp. 204–211, Oct. 2019, doi: 10.1016/j.fuproc.2019.05.016.
- [34] R. Sarc, I. Seidler, L. Kandlbauer, K. Lorber, and R. Pomberger, “Design, quality and quality assurance of solid recovered fuels for the substitution of fossil feedstock in the cement industry – Update 2019,” *Waste Manag. Res.*, vol. 37, no. 9, pp. 885–897, Sep. 2019, doi: 10.1177/0734242X19862600.
- [35] BMK, “Die Bestandsaufnahme der Abfallwirtschaft in Österreich - Statusbericht 2024 (Referenzjahr 2022),” Bundesministerium für Klimaschutz, Umwelt, Energie, Mobilität, Innovation und Technologie, Wien, 2024. [Online]. Available: https://www.bmk.gv.at/themen/klima_umwelt/abfall/aws/bundes_awp/bawp2023.html

Circular Economy & Recycling

Posters

Day 2

Glass recovery from fluidized bed bottom ashes from municipal solid waste incineration

J. Mühl^{1,*}, J. Lederer¹

1: Christian Doppler Laboratory for a Recycling-based Circular Economy, Institute of Chemical, Environmental and Bioscience Engineering, TU Wien, Austria

* Correspondent author: julia.muehl@tuwien.ac.at

Keywords: waste incineration, glass recycling, mechanical waste treatment, incineration bottom ash

The increasing emphasis on circular economy demands the recovery of valuable materials from waste streams that were traditionally destined for disposal. In Austria, approximately 5% of mixed municipal solid waste (MSW) consists of glass, which, if not captured through separate collection, enters the waste-to-energy process [1]. After incineration of MSW, incineration bottom ashes (IBAs) remain as solid residues of the process. These IBAs are either landfilled or recycled in the construction sector. However, large amounts of glass can be found in these IBAs. Especially in IBA from fluidized bed combustion up to nearly 50% glass in IBA were found in a previous study [2,3]. This glass is not recovered from IBA hitherto and thus lost for a closed-loop recycling.

In course of the CD Laboratory for a Recycling-based Circular Economy at TU Wien the potential for recovering and recycling glass from MSW bottom ash deriving from two different fluidized bed combustion plants was investigated in detail [4]. The glass was removed from the IBA by an industrial mechanical treatment process based on sensor-based sorting. Subsequently, the material was further upgraded experimentally by removal of extraneous material. Since glass fractions recovered from IBAs contain extraneous material in the form of metals, ceramics, stones, building material and other, the glass is not directly suitable for recycling in the packaging industry. To reduce the content of these contaminants, upgrading was conducted in two comparative setups. One upgrading setup included multiple sensor-based sorting runs of glass recovered from the IBA. The second upgrading setup consisted of sieving and single-step contaminant removal from the glass fraction 8-16 mm.

By means of material flow analysis and manual sorting of all fractions produced, the quality of the upgraded glass could be assessed and the upgrading itself could be evaluated. Moreover, the glass fractions were milled to <500 µm for XRF analysis of the material.

The results show that sensor-based sorting substantially reduces extraneous material. Yet, significant glass losses occur, especially if the material is sieved previously, but also through missorting. For example, only 51% and 64%, respectively of the glass originally contained in the glass fractions could be recovered after the upgrading setup including sieving. Better results were determined for the multi-step treatment, where 66% and 83%, respectively, of the glass were recovered in the end. Regarding the XRF analysis, the most important results were detected for Pb. Multi-step upgrading could clearly reduce the Pb concentrations to below 200 mg/kg, which is the threshold set by the packaging glass industry [5]. However, despite these improvements, the final glass fractions exceeded the extraneous material contents required by the packaging glass industry, since these thresholds are very strict.

This study examined the recyclability of glass recovered from fluidized bed IBA. It could be shown that significant glass amounts can be found in and technically separated from fluidized bed IBA. Since closed-loop glass recycling reduces energy and raw material usage, this can enable a more circular economy. Nevertheless, further research is necessary to improve the upgrading setups for glass. Additionally, other recycling paths for the glass should be assessed, such as utilization in the foam glass industry.

Acknowledgements

The financial support from the Austrian Federal Ministry of Economy, Energy and Tourism, the National Foundation for Research, Technology and Development and the Christian Doppler Research Association is gratefully acknowledged. Furthermore, we greatly acknowledge the financial and non-financial support of our company partners, which are, in alphabetical order: Abfallbehandlung Ahrental GmbH, Altstoff Recycling Austria AG, Brantner Österreich GmbH, Holding Graz - Kommunale Dienstleistungen GmbH, Lenzing Aktiengesellschaft, Linz Service GmbH, MM Board & Paper, Wien Energie GmbH, and Wopfinger Transportbeton Ges.m.b.H. In addition, we thank Magistratsabteilung MA 48, the public waste management provider of Vienna, for its non-financial support and Binder+Co AG for their experimental support.

References

- [1] Bernhardt, A., Brandstätter, C., Broneder, C., Gold, C., Neubauer, C., Oliva, J., Roll, M., Schaffernak, A., Stoifl, B., Tesar, M., Wankmüller-Tista, M., Walter, B., Weissenbach, T., 2024. Die Bestandsaufnahme der Abfallwirtschaft in Österreich, Statusbericht 2024. Bundesministerium für Klimaschutz, Umwelt, Energie, Mobilität, Innovation und Technologie, Wien, 274 pp. https://www.bmk.gv.at/dam/jcr:7119f610-1180-4337-8837-f5c45e73b4b5/BAWP_Statusbericht_2024.pdf (accessed 4 June 2024).
- [2] Mühl, J., Skutan, S., Stockinger, G., Blasenbauer, D., Lederer, J., 2023. Glass recovery and production of manufactured aggregate from MSWI bottom ashes from fluidized bed and grate incineration by means of enhanced treatment. *Waste Management* 168, 321–333. <https://doi.org/10.1016/j.wasman.2023.05.048>.
- [3] Huber, F., Blasenbauer, D., Aschenbrenner, P., Fellner, J., 2020. Complete determination of the material composition of municipal solid waste incineration bottom ash. *Waste management (New York, N.Y.)* 102, 677–685. <https://doi.org/10.1016/j.wasman.2019.11.036>.
- [4] Mühl, J., Mika, S., Tischberger-Aldrian, A., Lederer, J., 2025. Upgrading and Characterization of Glass Recovered from MSWI Bottom Ashes from Fluidized Bed Combustion. *Recycling* 10, 63. <https://doi.org/10.3390/recycling10020063>.
- [5] Bundesverband Glasindustrie e.V.; BDE Bundesverband der Deutschen Entsorgungs-, Wasser- und Rohstoffwirtschaft e. V.; bvse-Bundesverband Sekundärrohstoffe und Entsorgung e.V., 2014. Leitlinie „Qualitätsanforderungen an Glasscherben zum Einsatz in der Behälterglasindustrie“: Standardblatt T 120 [Guideline "Quality requirements for glass cullet for the use in the packaging glass industry"]. https://www.bvse.de/dateien2020/2-PDF/03-Themen_Ereignisse/FV_Glas/Standardblatt_T_120_2014-08-14_2.pdf.

Aufwertung von Bierhefe-Abfällen zur Biosynthese von Silbernanopartikel

Lydia Challandes^{1,*}, Lucia Colleselli², Thomas Senfter¹, Harald Schöbel²

1: Studiengang Umwelt-, Verfahrens- und Energietechnik, MCI - Die Unternehmerische Hochschule, Österreich

2: Studiengang Bio- und Lebensmitteltechnologie, MCI - Die Unternehmerische Hochschule, Österreich

* Korrespondierender Autor: lydia.challandes@mci.edu

Stichwörter: Grüne Synthese, *S. cerevisiae*, Silbernanopartikel, Bestrahlung, VIS-Licht

Im Jahr 2024 erreichte die Bierproduktion in Österreich 9,48 Mio. hl, wobei durchschnittlich 2,1 kg Hefebiomasse pro hl erzeugt werden^[1,2]. Dies entspricht ca. 20.000 Tonnen Abfall jährlich. Neben der Verwertung in der Futter- und Lebensmittelindustrie sowie der Biogaserzeugung bietet sich die Biosynthese von Metallnanopartikel als eine innovative Alternative zur Nutzung von Hefe-Abfällen an. Metallnanopartikel weisen aufgrund ihrer hohen Oberflächenenergie und ihres großen Flächen-zu-Volumen-Verhältnisses überlegene physikochemische Eigenschaften im Vergleich zum Bulkmaterial auf. Gerade Silbernanopartikel (AgNPs) sind wegen ihrer bioziden und einzigartigen elektrischen und optischen Eigenschaften in der Umwelttechnologie von großem Interesse, insbesondere in der Abwasserentsorgung, der Überwachung der Wasserqualität, der Wasser- und Luftreinigung und der CO₂-Reduktion. AgNPs werden konventionell durch physikalische und chemische Verfahren hergestellt. Biotechnologische Methoden erweisen sich nach aktuellem wissenschaftlichem Stand als umweltfreundliche und kosteneffiziente nachhaltige Alternative.

Im Rahmen der hier präsentierten Untersuchungen, wurden zellfreie Extrakte (ZFE) der Bierhefe *S. cerevisiae* als biologisches System für die Synthese von AgNPs verwendet. Nach erfolgreichen Versuchen unter dunklen Synthesebedingungen versus eine Bestrahlung mit weißem Licht wurde der Einfluss der Wellenlänge auf die Partikelbildung detailliert untersucht. Die Biosynthese wurde in einem dreistufigen Prozess durchgeführt: (i) Kultivierung der Hefe, (ii) Herstellung des ZFE und (iii) Synthesephase unter Bestrahlung mit blauem (471 nm), grünem (521 nm) und rotem (635 nm) Licht parallel zum Standardverfahren unter dunklen Bedingungen. Die Charakterisierung der resultierenden Nanokomponenten erfolgte mittels UV/VIS-Spektroskopie, dynamische Lichtstreuung (DLS), Zeta-Potential Messungen, Rasterelektronenmikroskopie (REM) und Energiedispersions-Röntgenspektroskopie (EDX). Es wurden erfolgreich sphärische AgNPs hergestellt, die eine bimodale Größenverteilung mit einer mittleren Partikelgröße von 15 nm und 80 nm aufwiesen. Die Bestrahlung mit blauem Licht führte zu kleineren AgNPs und einer gesteigerten Ausbeute um mehr als 90 % im Vergleich zur Synthese unter dunklen Bedingungen. *S. cerevisiae* erwies sich als geeignetes biologisches Modell für die Biosynthese von sphärischen AgNPs und Licht als vielversprechendes Werkzeug für die Feinabstimmung der resultierenden Nanomaterialien. Die hier vorgestellten Ergebnisse untermauern das große Potenzial von Bierhefe-Abfällen aus der Brauindustrie zur innovativen Schließung von Stoffkreisläufen.

[1] R., Hubert, R., Domenig, M., Thaler, P. und Lampert, C., "Rückstände aus der Nahrungs- und Genussmittelproduktion: Materialien zur Abfallwirtschaft", Umweltbundesamt GmbH, Wien, Österreich, REP-0403, 403. ISBN 978-3-99004-207-6, 2012.

[2] "Brauwelt 5/2025", in *Brauwelt*, Mär. 2025. [online]. Verfügbar: <https://epub.brauwelt.com/de/profiles/36e9a489cc09/editions>.

Environmental Presentations

Day 2

Activated Carbon from Gasified Waste Wood: Potential and Challenges

D. Gurtner^{1,2,*}, A. Hofmann^{1,3}, C. Pfeifer²

1: Josef Ressel Centre for production of activated carbon from municipal residues, Department for Environmental-, Energy and Process Engineering, Management Center Innsbruck – MCI, Maximilianstraße 2, 6020, Innsbruck, Austria

2: Institute of Chemical and Energy Engineering, University of Natural Resources and Life Science – BOKU, Muthgasse 107, 1190, Vienna, Austria

3: Department of Environmental, Process and Energy Engineering, Management Center Innsbruck – MCI, Maximilianstraße 2, 6020, Innsbruck, Austria

* Correspondent author: david.gurtner@mci.edu

Keywords: Activated carbon, Gasification char, Physical activation, Waste wood, Adsorption

Abstract

This study evaluates the feasibility of producing renewable activated carbon (AC) from gasification char (GC) derived from waste wood. Sequential activation with H₂O and CO₂ achieved a maximum porosity of 763 m²/g and adsorption capacity of 209 mg/g, which is slightly below values for AC from gasified forestry residue biomass and commercial AC. Despite challenges such as high ash content and variability in GC and AC properties, activating gasified waste wood can be economically beneficial due to a lower mass loss during activation, in addition to being a low-cost, abundant feedstock. However, CO₂ activation can result in a too high micropore fraction, drastically reducing adsorption capacity due to pore blocking. Given the growing demand for AC driven by regulatory requirements and resource constraints, this research contributes to the substitution of fossil-based AC with organic waste materials.

Introduction

Global warming, resource depletion, and pollution necessitate advanced remediation methods. Activated carbon (AC) is widely used due to its porous structure, stability, and high adsorption capacity, enabling applications in purification, storage, and catalysis. AC is mainly derived from fossil coal and its demand is set to increase in response to the new EU regulations that require the elimination of pharmaceuticals in large wastewater treatment plants by 2045. Switzerland has previously demonstrated the viability of implementing AC on a large scale in wastewater treatment plants since 2016. Therefore, the use of renewable precursors such as biomass gasification by-products, namely gasification char (GC), is of paramount importance. GC represents approximately 10 wt% of the initial biomass feedstock, is a carbonaceous material with limited porosity and has no specific application areas [1]. However, physical activation of GC offers a potential pathway to produce high-quality AC, creating new opportunities for value-added valorisation. In this process, at high temperatures oxidising gases, such as H₂O and/or CO₂, increase porosity by partial gasification of the carbon skeleton, leading to the formation micropores (MIC (< 20 Å)), mesopores (20 – 500 Å) and macropores (> 500 Å). The activation of GC offers substantial economic potential and is frequently endorsed in literature [1, 2], but still represents a considerable research gap, possibly due to the inherent challenges associated with GC, including a soft skeleton, reduced porosity, high ash content and degree of graphitisation. To date, only a few studies [3–7] have been published on the activation of GC. In the studies [6, 7], the activation of forestry residue biomass (FRB), gasified in a floating-fixed-bed process [8] was comprehensively examined, with promising results being achieved. The FRB consists of wood chips and low-energy components such as bark, branches, tops and needles, which are a by-product from harvesting [8]. Nevertheless, the sustainability of energy from forest biomass is a subject of debate. However, a consensus emerges when wood was initially employed for material applications and subsequently for energy generation. The EU-wide requirement of cascading use, the rapid

escalation of FRB/biomass prices, the rising energy prices, and the recent scarcity of natural gas are driving gasification concepts that utilise inexpensive and abundant waste materials, such as waste wood (WW) from construction, demolition, pallets, furniture or chipboards. Consequently, in the future, large quantities of GC from WW, with no specific use cases, but with the potential for physical activation, will be available.

However, it is important to note that WW is inherently different to the fresh wood precursors typically used for activation [3–7], due to changes in microstructure and degradation of main components (cellulose, hemicellulose and lignin), which lead to a reduction in mechanical strength [9, 10]. Both chemical properties and physical composition vary owing to distinct pre-treatments, various biological factors (e.g. fungus), and natural or artificial ageing effects induced by heat, UV light, or mechanical stress [9, 10]. Accordingly, the objective of this study is to evaluate the potential of activating GC from gasified WW, in comparison to activated GC from FRB, as conducted in [6, 7].

Materials and methods

Three types of GC, sampled on different occasions from a novel two-staged bubbling fluidised-bed gasification process (described in [11]), were utilised as activation precursors. The gasification process utilised WW, which, according to [12], can be classified into AI, AII, and AIII: construction wood, demolition wood, and non-polluted wood emballages. As reference, activated GC from FRB gasified in a floating fixed-bed process [8], produced in previous studies [6, 7], was used. The biomass composition and gasification parameters for FRB (average value) and for the WW are listed in Table 1. WW2 and WW3 are the same biomass but sampled on different occasions.

Table 1: Biomass composition and gasification parameter

	Avg. FRB	WW1	WW2	WW3	
Biomass	C in wt%	45.0	43.2	50	
	H in wt%	5.8	5.6	6.3	
	N in wt%	0.7	0.7	0.6	
	FC ¹ in wt%	17.1	17.1	16.2	
	Ash in wt%	1.7	1.6	0.5	
Gasification	$T_{pyro.}$ in °C	460	316	334	313
	$T_{gasifi.}$ in °C	825	878	870	845
	CO in vol%	20.6	15.5	14.9	14.7
	H ₂ in vol%	20.1	11.4	11.2	12
	CH ₄ in vol%	3.8	1.9	1.3	2.1

¹ Fixed carbon

Moreover, for comparison, commercial activated carbon (COM) and GC from a co-current fixed-bed pellet gasification plant were used. However, no data concerning the biomass or gasification/activation parameters employed for these samples were available.

Production of activated carbon

In accordance with the findings of FRB GC activation, as outlined in [6, 7], a series of selected activation experiments were reproduced with the GC from WW. The GCs from WW were activated in a range of 750 – 850 °C for 12.5 – 20 min as batch-process in a fluidised-bed reactor (Figure 1), which was placed in a muffle furnace. Two permeable metal frits confined the reaction zone, which was filled with GC to approximately one-third of its volume. During heating and cooling, the reactor was flushed with nitrogen, and upon reaching the desired temperature, CO₂ and/or H₂O were introduced at 2 bar. For the activation with CO₂, a flow rate of 2 L/min was selected, while for H₂O, a mixture of 2 L/min H₂O and 0.5 L/min nitrogen was chosen. For a detailed methodological description, refer to [7].

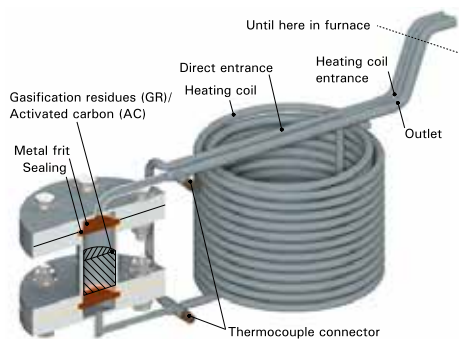


Figure 1: Fluidised-bed reactor for physical activation

Characterisation of activated carbon

Nitrogen adsorption isotherms were recorded at 77 K using a 3Flex system (3Flex, Micromeritics). The specific BET surface area was determined for GC ($S_{BET,GC}$) and AC ($S_{BET,AC}$) in accordance with the Rouquerol criteria. The pore size distribution (micro-, meso-, and macropores) was estimated via non-local density functional theory (NLDFT), employing the 'Het N2 Carbon Slit' (Non-negative Regularisation: 0.1, Version 2 deconvolution enabled) model. The proximate composition (moisture, fixed carbon (FC), volatile matter and ash) was assessed using thermogravimetric analysis (Mettler Toledo; TGA/DSC 3+), following DIN 51720:2001-03.

Adsorption of pharmaceuticals

Six OMPs were selected from the twelve guide substances outlined in the 2016 Swiss legislative guidelines and the European Parliament regulations [13]: DCF: Diclofenac (CAS-No. 15307-86-5, $\geq 97.5\%$, Thermo Fischer GmbH); BTZ: 1,2,3-Benzotriazole (CAS-No. 95-14-7, $\geq 99\%$, Carl Roth GmbH); MTP: Metoprolol (CAS-No. 37350-58-6, $\geq 98\%$, Thermo Fischer GmbH); CBM: Carbamazepine (CAS-No. 298-46-4, $\geq 98\%$, Sigma Aldrich GmbH); SMX: Sulfamethoxazole (CAS-No. 723-46-6, $\geq 98\%$, Sigma Aldrich GmbH); VST: Valsartan (CAS-No. 137862-53-4, $> 98\%$, Tokyo Chemical Industry).

OMP analysis was carried out using a UHPLC system (UltiMate 3000, Thermo Fisher Scientific) equipped with a C18 column (Acclaim TM 244 Polar Advantage II, 4.6×100 mm, $3 \mu\text{m}$ particle size). Method development was conducted by [14]. A stock solution containing six OMPs (10 mg/L each) in tap water (pH: 7.92 ± 0.02 , EC: $67.2 \pm 0.4 \mu\text{S/cm}$) was used in the adsorption experiments. A total of 25 mg AC was added to 500 mL of this solution (i.e. 50 mg/L) and mixed in an overhead shaker at 12 rpm for 24 h. The equilibrium loading (q_e) was determined based on the concentration difference normalised to the charcoal concentration in the stock solution.

Results and discussion

The present paper is divided into two sections, which share the same objective: namely, to evaluate the potential of activating gasified waste wood. This study is a concise supplement to [6, 7], where more details are available.

Activation of various feedstocks under uniform conditions

In the initial section (Table 2 – largest value underlined and bold), GC derived from a wide range of biomass feedstocks (pellets, FRB or WW) were activated under uniform conditions (CO₂, 850 °C, 20 min). This conditions were chosen based on the anticipated enhanced activation stage, as observed in [7]. Consequently, differences in the effectiveness of the activation experiments arising from variations in GC properties should be more apparent.

The mass loss during activation (W_{loss} – in Table 2), which determines the economic viability of the activation process, ranges from 25.9 – 39.9 wt%. The porosity, expressed as $S_{BET,GC}$, ranges between 206 – 539 m²/g, with 539 m²/g (ID 1.1) being exceptionally high. This is likely attributable to the precursor (pellets), which provided a dense and robust framework, as evidenced by a high true density of 1553 kg/m³, that is conducive to high porosities. In contrast, GC from low-quality WW has a maximum true density of only 1362 kg/m³ (ID 1.13), whereas GC from FRB reached only 1422 kg/m³ (ID 1.9). Accordingly, the $S_{BET,GC}$ of WW (240 – 363 m²/g) is significantly lower, followed by the $S_{BET,GC}$ of FRB (206 – 317 m²/g). Furthermore, the share of MIC is higher in the GC from WW (45.6 – 59.2 %), than in the GC from FRB (26.2 – 36.1 %). The reason for the elevated $S_{BET,GC}$ and MIC fraction in WW GC relative to FRB GC is difficult to comprehend, as it is contingent on a multitude of parameters (temperature and residence time in gasification and pyrolysis as well as their technology, feedstock characteristics, etc.) and is therefore not discussed further.

The correlation between $S_{BET,GC}$ or $S_{BET,AC}$ and the true density of GC is strong ($R^2 = 0.89$ and 0.87 , respectively). A similar strong correlation ($R^2 = 0.93$) is observable between $S_{BET,GC}$ and $S_{BET,AC}$. Apart from these correlations, no significant correlations were identified in relation to the micropores (MIC in Table 2) or the true density of the AC.

The $S_{BET,AC}$ ranges between 410 – 919 m²/g. The exceptionally high value of 919 m²/g (ID 1.2) is once again attributable to the use of pellets as a precursor. The maximum $S_{BET,AC}$ from WW is 629 m²/g (ID 1.14), which is slightly lower than the maximum $S_{BET,AC}$ from FRB (672 m²/g – ID 1.4). Overall, the correlation between $S_{BET,GC}$ or $S_{BET,AC}$ is found to be highly significant ($R^2 = 0.93$), suggesting that, regardless of the precursor, porosity can be developed to a comparable extent. This renders gasified WW a potentially viable option for activation.

However, based on the calculated relative increases between $S_{BET,GC}$ and $S_{BET,AC}$ ($\Delta_{BET,rel}$ in Table 2), WW exhibits greater variability (52–130 %) compared to FRB (87–133 %). This high variability complicates the development of a standardised activation approach for GC derived from WW [2]. In addition, GC from WW exhibits an elevated ash content, which constrains porosity development. Furthermore, the ash content in WW GC – particularly with regard to heavy metal concentrations – might exceed quality threshold values (e.g. those specified by the World Biochar Certificate).

Activation of selected feedstock under various conditions

As demonstrated in Table 2 and the extant literature [2, 15], there can be substantial variation in the properties of GC. In the second section of this study, two GCs – one derived from FRB and the other from WW – with an intermediate $S_{BET,GC}$ (WW1 and FRB1), were selected for further activation experiments under various conditions (Table 3). In accordance with the conditions specified in [7], WW1 was activated under identical conditions and compared to FRB1.

Table 2: GCs derived from various gasified biomass feedstocks, activated under uniform conditions (CO₂, 850 °C, 20 min)

ID	Gasified biomass	Sample	w_{loss} in wt%	S_{BET} in m ² /g	$\Delta_{BET,rel}$ in %	MIC in vol%	$\Delta_{MIC,rel}$ in %	FC in wt%	Ash in wt%	True density in kg/m ³
1.1	Pellets	GC	-	539 ± 9	71	30.1 ± 0.3	1	88 ± 0	8 ± 0	1553 ± 28
1.2		AC	39	<u>919 ± 9</u>		30.3 ± 0.8		79 ± 0	12 ± 0	1601 ± 19
1.3	FRB1	GC	-	287 ± 4	133	36.1 ± 0.5	27	81 ± 1	10 ± 0	1399 ± 22 [7]
1.4		AC	39.9	672 ± 8		49.5 ± 0.5		79 ± 0	14 ± 1	1589 ± 59 [7]
1.5	FRB2	GC	-	206 ± 0	99	26.2 ± 0.0	37	87 ± 0	7 ± 0	1307 ± 3 [6]
1.6		AC	27.5	410 ± 2		41.4 ± 1.7		85 ± 0	9 ± 0	1504 ± 17 [6]
1.7	FRB3	GC	-	230 ± 4	92	27.2 ± 0.8	27	77 ± 0	13 ± 0	1258 ± 11 [6]
1.8		AC	28.7	441 ± 5		37.2 ± 1.3		75 ± 1	17 ± 0	1436 ± 9 [6]
1.9	FRB4	GC	-	317 ± 2	87	36.1 ± 0.5	25	82 ± 0	10 ± 0	1422 ± 8 [6]
1.10		AC	39.9	593 ± 8		48.5 ± 1.6		77 ± 0	14 ± 1	1567 ± 14 [6]
1.11	FRB5	GC	-	281 ± 3	73	36.1 ± 0.3	6	80 ± 0	11 ± 0	1410 ± 41 [6]
1.12		AC	25.9	485 ± 1		38.2 ± 1.1		78 ± 0	15 ± 0	1539 ± 48 [6]
1.13	WW1	GC	-	308 ± 1	104	45.6 ± 1.5	32	78 ± 0	12 ± 0	1362 ± 33
1.14		AC	26.1	629 ± 9		66.9 ± 0.2		78 ± 0	16 ± 0	1734 ± 80
1.15	WW2	GC	-	240 ± 2	130	59.2 ± 1.5	13	70 ± 0	18 ± 0	1329 ± 7
1.16		AC	29.1	553 ± 9		68.2 ± 1.4		69 ± 0	25 ± 0	1832 ± 60
1.17	WW3	GC	-	363 ± 6	52	49.4 ± 0.4	34	79 ± 2	13 ± 2	1352 ± 6
1.18		AC	28.4	551 ± 1		<u>74.7 ± 0.9</u>		70 ± 3	25 ± 3	1642 ± 5

To facilitate a more intuitive presentation, samples that have been activated under identical conditions are arranged one below the other in Table 3. For the activated samples, the largest value of each response is underlined and marked bold. Additionally, for each parameter set, the deviation between FRB1 and WW1 has been calculated and compared with the overall deviation between FRB and WW of the respective parameter. The following mathematical symbols represent the scale of deviation:

- \gg or \ll Above-average deviation
- $>$ or $<$ Below-average deviation
- \approx The deviation is lower than $\pm 5\%$

The S_{BET} of AC is consistently higher for activated FRB than for WW, reaching maximum values of 812 m²/g (ID 2.7) and 795 m²/g (ID 2.8), respectively. However, since the AC obtained from FRB was produced under optimised conditions (elaborated in [7]), the selected parameters are more suitable for FRB than for WW. In particular, when activation was conducted with H₂O, the difference in $S_{BET,AC}$ is significant. This can perhaps be explained by the fact that H₂O activation is more challenging to adjust, thereby rendering the appropriate parameter selection more crucial for a successful activation [7]. Furthermore, the AC from WW contains a greater amount of non-porous ash.

The MIC values are generally higher for gasified and activated WW, particularly when CO₂ was used as the activation agent. CO₂ is known to promote superior MIC formation [7], a phenomenon that seems to appear more pronounced when WW is employed as the precursor. Micropores are recognised for yielding high adsorption capacities; however, if the molecules are too large, an excessive MIC fraction may exert a negative effect, as meso- and macropores are essential for mass transfer and for preventing pore blocking. This effect is observable in certain CO₂-activated WW samples, notably in ID 2.4, where, despite a high S_{BET} of 629 m²/g, the q_e is only 111 mg/g_{GC} due to a too high MIC fraction of 66.9%. In contrast, in ID 2.10, although $S_{BET,AC}$ is only 513 m²/g, the q_e reached 113 mg/g_{GC} because the MIC fraction is lower (60.3%).

The adsorption capacity q_e is smaller for GC from FRB, than from WW (27.9 mg/g_{GC} vs. 35.6 mg/g_{GC}), which could perhaps be attributed to the higher proportion of MIC in WW (36.1% vs.

45.6%). However, for activated FRB q_e is consistently higher than for activated WW, likely due to the previously noted excessive proportion of MIC in WW. Overall, sequential activation (H₂O+CO₂) of FRB yields the highest q_e , being only 17% lower than that of commercial AC (COM). By sequential activation also the highest q_e for activated WW was achieved, at only 23% below the q_e for COM.

In order to assess the trade-off between AC yield and porosity, the ‘absolute’ surface area ($Abs.S_{BET}$) was calculated by multiplying S_{BET} by $(1 - w_{loss})$. Analogously, the ‘absolute’ adsorption capacity ($Abs.q_e$) was calculated. These parameters enable the quantification of yield-oriented porosity/adsorption per gram of GC used, thereby facilitating a more economical evaluation of the activation process. Since w_{loss} is mostly lower for WW activation, $Abs.S_{BET}$ and $Abs.q_e$ are for activated WW partly higher, as in ID 2.4 and 2.8, despite the lower S_{BET} . Thus, from an economic perspective, using WW may be preferable in terms of ‘absolute’ surface/adsorption capacity, particularly since WW is the less expensive biomass.

Conclusion

This study demonstrates the potential of valorising waste wood (WW) gasification by-products by transforming the low-value gasification char (GC) into high-value, renewable activated carbon (AC). The highest porosity (763 m²/g) and adsorption capacity (209 mg/g) with gasified WW as precursor was achieved by sequential H₂O+CO₂ activation. However, those values are slightly below the values from activated forestry residue biomass (812 m²/g, 225 mg/g) and commercial activated carbon (991 m²/g, 271 mg/g). Furthermore, the high ash content and a considerable variability in AC derived from WW may pose challenges for its application. However, activating GC from WW can be economically beneficial, not only due to the lower cost of WW but also due to reduced mass loss during activation. Consequently, higher yield-oriented porosity and adsorption capacity per gram of GC can be obtained, despite lower porosity and adsorption capacity per gram of AC. Both GC and AC from WW exhibited an increased proportion of MIC, which, when excessively high, led to a rapid decline in adsorption capacity due to pore blocking caused by large pharmaceutical molecules.

Table 3: GC from gasified waste wood and forest residue biomass activated under various conditions

ID	Gasified biomass	Sample	AA	T in °C	t in min	w _{loss} in wt%	S _{BET} in m ² /g _{GC}	Abs.S _{BET} in m ² /g _{AC}	MIC in vol%	q _e in mg/g _{GC}	Abs.q _e in mg/g _{AC}	Ash in wt%
2.1	FRB1	GC	-	-	-	-	287	287	36.1	28	-	10
2.2	WW1		-	-	-	-	308	308	45.6	38	-	12
2.3	FRB1	AC	CO ₂	850	20	39.9	672	404	49.5	183	110	15
2.4	WW1					>>	>	<<	>>	>	66.9	111
2.5	FRB1	AC	H ₂ O	850	12.5	51.4	795	386	45	192	94	18
2.6	WW1					=	>>	>	=	<<	44	177
2.7	FRB1	AC	H ₂ O +CO ₂	850	10+10	60.8	812	318	49.3	225	88	19
2.8	WW1					>>	>	<<	>>	>	415	55
2.9	FRB1	AC	CO ₂	817	16	24	552	420	44.9	153	116	13
2.10	WW1					>	>	<<	=	>	411	60.3
2.11	FRB1	AC	H ₂ O	750	20	24.9	677	508	45.5	181	136	11
2.12	WW1					<	>>	>>	<	>>	414	54
2.13	-	COM	-	-	-	-	991	-	55.6	271	-	16

Despite several challenges, there is promising potential for activating gasified WW, especially from an economic perspective. Future research should prioritise ensuring more consistent GC properties (benchmark GC) in WW gasification, facilitating the development of widely applicable optimal activation parameters to enhance the competitiveness of AC from gasified WW.

Acknowledgments

The financial support by the Austrian Federal Ministry of Labour and Economy, the National Foundation for Research, Technology and Development and the Christian Doppler Research Association is gratefully acknowledged.

References

- [1] A. A. Ahmad, M. A. Ahmad, U. F. Md Ali, and K. Ken, "Gasification char residues management: Assessing the characteristics for adsorption application," *Arabian Journal of Chemistry*, vol. 16, no. 9, p. 104993, 2023, doi: 10.1016/j.arabjc.2023.104993.
- [2] A. Abdelaal, V. Benedetti, A. Villot, F. Patuzzi, C. Gerente, and M. Baratieri, "Innovative Pathways for the Valorization of Biomass Gasification Char: A Systematic Review," *Energies*, vol. 16, no. 10, p. 4175, 2023, doi: 10.3390/en16104175.
- [3] T. Maneerung, J. Liew, Y. Dai, S. Kawi, C. Chong, and C.-H. Wang, "Activated carbon derived from carbon residue from biomass gasification and its application for dye adsorption: Kinetics, isotherms and thermodynamic studies," *Bioresource technology*, vol. 200, pp. 350–359, 2016, doi: 10.1016/j.biortech.2015.10.047.
- [4] M.-H. To *et al.*, "Waste biomass gasification char derived activated carbon for pharmaceutical carbamazepine removal from water," *Resources Environment and Information Engineering*, vol. 1, no. 1, pp. 36–44, 2019, doi: 10.25082/REIE.2019.01.005.
- [5] S. Kilpimaa, H. Runtti, T. Kangas, U. Lassi, and T. Kuokkanen, "Physical activation of carbon residue from biomass gasification: Novel sorbent for the removal of phosphates and nitrates from aqueous solution," *Journal of Industrial and Engineering Chemistry*, vol. 21, pp. 1354–1364, 2015, doi: 10.1016/j.jiec.2014.06.006.
- [6] D. Gurtner, M. Kresta, M. Maurer, A. Hofmann, and C. Pfeifer, "Self-sustained physical activation at pilot-scale integrated in commercial wood gasification plant: A path to renewable activated carbon, PAH removal and electrical efficiency improvement," 2025, doi: 10.2139/ssrn.4942992.
- [7] D. Gurtner, J. O. Back, D. Bosch, A. Hofmann, and C. Pfeifer, "Renewable Activated Carbon from Wood-Based Gasification Char: A Comprehensive Study on Physical Activation," *Carbon Resources Conversion*, p. 100310, 2025, doi: 10.1016/j.crcn.2025.100310.
- [8] M. Huber, M. Huemer, A. Hofmann, and S. Dumfort, "Floating-fixed-bed-gasification: From Vision to Reality," *Energy Procedia*, vol. 93, pp. 120–124, 2016, doi: 10.1016/j.egypro.2016.07.159.
- [9] K. Kránitz, W. Sonderegger, C.-T. Bues, and P. Niemz, "Effects of aging on wood: a literature review," *Wood Science and Technology*, vol. 50, no. 1, pp. 7–22, 2016, doi: 10.1007/s00226-015-0766-0.
- [10] D. Gurtner *et al.*, "Mechanical strength characterisation of pyrolysis biochar from woody biomass," *Energy*, vol. 285, p. 129366, 2023, doi: 10.1016/j.energy.2023.129366.
- [11] M. Kresta, D. Gurtner, L. Nohel, A. Hofmann, and C. Pfeifer, "Experimental study and characterisation of a novel two stage bubbling fluidised bed gasification process utilising municipal waste wood," *Fuel Processing Technology*, vol. 266, p. 108156, 2024, doi: 10.1016/j.fuproc.2024.108156.
- [12] Bundesministerium der Justiz, *Altholz - Verordnung über Anforderungen an die Verwertung und Beseitigung von Altholz*. Accessed: Jan. 17 2022. [Online]. Available: <https://www.gesetze-im-internet.de/altholz/BJNR330210002.html>
- [13] European Parliament, *Legislative Observatory: 2022/0345(COD): Urban wastewater treatment. Recast*. [Online]. Available: [https://oeil/popups/ficheprocedure.do?reference=2022/0345\(COD\)](https://oeil.secure.europarl.europa.eu/oeil/popups/ficheprocedure.do?reference=2022/0345(COD))
- [14] J. Marx, J. Back, L. Hoiss, M. Hofer, T. Pham, and M. Spruck, "Chemical Regeneration of Mixed-Matrix Membranes for Micropollutant Removal from Wastewater," *Chemie Ingenieur Technik*, vol. 95, no. 9, pp. 1416–1427, 2023, doi: 10.1002/cite.202300075.
- [15] A. Pollex, T. Zeng, S. Bandemer, A. Ulbricht, K. Herrmann, and D. Brätkow, "Characteristics of gasification chars - Results from a screening campaign," *Biomass and Bioenergy*, vol. 179, p. 106962, 2023, doi: 10.1016/j.biombioe.2023.106962.

Adsorptive Removal of PFAS Using a Fluorinated Ion Exchange Polymer

A. J. Schobel^{1,†}, J. Back¹, J. Freilinger², M. Larch¹, J. Marx¹, M. Spruck¹, H. Schottenberger², M. Rupprich³, C. Huck², R. Bakry^{2,†}

1: Dept. of Environmental, Process and Energy Engineering, MCI-The Entrepreneurial School, Austria

2: Dept. of Analytical Chemistry and Radiochemistry, Leopold-Franzens-University Innsbruck (LFU), Austria

3: Dept. of Ecopreneurship, University of Applied Sciences and Arts Northwestern Switzerland (FHNW), Switzerland

†: Author passed away before the completion of this work

* Correspondent author: j.schobel@mci4me.at

Keywords: PFAS, Polymer, Activated Carbon, Adsorption

1 Introduction

Per- and polyfluoroalkyl Substances (PFAS) are defined as substances containing at least one fully fluorinated methyl or methylene carbon atom.^[1] The carbon-fluorine bonds of PFAS result in a high thermal and chemical stability, lipophobic and hydrophobic properties. Due to those properties they are widely used in industry for example in paints, varnishes, anti-stain coatings, waterproof coatings and fire-fighting foams.^[2] The exposure to PFAS is correlated with several adverse health effects such as carcinogenicity, endocrine disruption, immunotoxicity, reproductive disorders and neurotoxicity.^[3] They are primarily released into the environment through the discharge of fluoropolymer factories, wastewater treatment plants and from locations, where firefighting foam has been applied.^[4] The high thermal and chemical stability and the lipophobic and hydrophobic properties of PFAS makes them highly persistent and bioaccumulative.^[5] They have already been detected in human blood across the population of developed countries, drinking water, surface water and soils.^[6,7] The main source of PFAS exposure for human beings is drinking water.^[6] In 2026 the new limit of PFAS concentration in drinking water is set to not exceed $0.5 \mu\text{g L}^{-1}$ in the European Union.^[8]

Various technologies have been examined regarding their applicability in PFAS removal from the environment including ultraviolet irradiation, reverse osmosis and nanofiltration. The major drawback of those technologies are the high costs associated with their application.^[9] More cost efficient technologies for the removal of PFAS currently used for effective water remediation are adsorption-based technologies using activated carbon (AC) both in powdered (PAC) and granulated (GAC) form and ion exchange resins (IX).^[10] Long-chain PFAS (>7C) are effectively removed by AC. However, AC does not effectively remove short-chain PFAS. Other adsorbents, such as ion exchange resins, present a drawback concerning their limited efficiency in complex water matrices containing varied concentration of PFAS and electrolytes. Moreover, their regenerability is often limited.^[11] In recent research, the application of fluorinated materials has showed promising results for the removal of PFAS.^[12] This research examines the synthesis and characterization of a highly selective fluorinated ion exchange polymer for the removal of PFAS from ground water. As representatives for the group of short chain PFAS perfluorobutanoic acid (PFBA) and hexafluoropropylene oxide dimer acid (HFPO-DA), also known as GenX are chosen. The long-chain PFAS are represented within this work through perfluorooctanoic acid (PFOA). The chemical structures of the used PFAS are shown in figure 1.

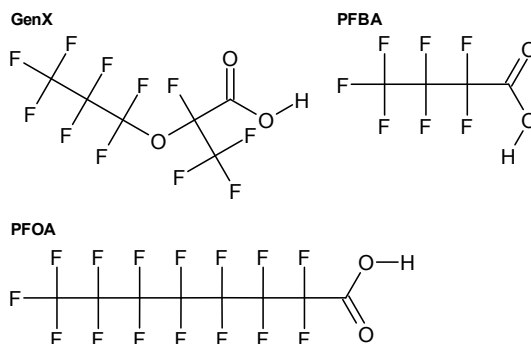


Fig. 1: Chemical Structure of GenX, PFBA and PFOA

2 Methods

2.1 Adsorbent Preparations

The experiments were conducted for the fluorinated ion exchange polymer and as a comparison for the commercially available activated carbon “Carbopal AP Supra” from Donau Carbon. The adsorbents were milled with the ultra centrifugal mill ZM300 from Retsch with 2300 rpm and for approximately 10 s using a 12 mm sieve. The particle size distribution was analyzed with the “Mastersizer 2000” from Malvern Panalytical using the wet dispersion unit “Hydro 2000G” from Malvern Panalytical. The FP was dispersed in ethanol and the activated carbon was dispersed in a mixture of 50 % ethanol and 50 % water. The resulting d_{10} , d_{50} and d_{90} are listed in table 1.

Tab. 1: d_{10} , d_{50} and d_{90} of FP and PAC after milling

Adsorbent	$d_{10} / \mu\text{m}$	$d_{50} / \mu\text{m}$	$d_{90} / \mu\text{m}$
FP	1.53	5.01	43.2
PAC	4.84	15.3	41.8

2.2 Adsorption Kinetics

The adsorption kinetics were conducted with a ratio of mg adsorptive to g adsorbent of 100. The single-component kinetics were conducted with a concentration of 1 mg L^{-1} PFAS and an adsorbent concentration of 10 mg L^{-1} . The kinetics were conducted over a time period of 48 h with the sampling times 5, 10, 15, 20, 30, 45, 90, 120, 180 and 240 min. The samples were taken with a 2 mL syringe and a $0.45 \mu\text{m}$ regenerated cellulose syringe filter.

2.3 Adsorption Isotherms

The single-component adsorption isotherms were conducted with an initial concentration of the adsorptive of 0.1 mg L^{-1} and 1 mg L^{-1} and an adsorbent concentration varied in a range from 0.25 to 200 mg L^{-1} . The contact time between the adsorbent and adsorptive was 24 h. The samples were taken with a 2 mL syringe combined with a $0.45 \mu\text{m}$ regenerated cellulose syringe filter.

2.4 PFAS Analytics

The PFAS samples were analyzed with the HPLC system “Waters Acquity Premier” coupled with the mass spectrometer triple quadrupole “Waters Xevo TQD”. The HPLC column used was the “Waters Acquity UPLC® BEH C18 column” with a particle size of 1.7 μm , a diameter of 2.1 mm and a length of 100 mm, in combination with the pre-column “Acquity UPLC® BEH C18 VanGuard™” with a particle size of 1.7 μm . To remove PFAS contaminations from the system, an additional “Waters Atlantis™ Premier BEH C18 AX5” column with a particle size of 5 μm , a diameter of 2.1 mm and a length of 50 mm was used.

The system was operated in reversed-phase mode using a gradient method with reversed osmosis water containing 2 mmol L⁻¹ ammonium acetate and a 95/5 (v/v) mixture of methanol and reversed osmosis water containing 2 mmol L⁻¹ ammonium acetate as solvents.

3 Results and Discussion

3.1 Polymer Synthesis

The fluorinated ion exchange polymer is synthesized through ultraviolet irradiation initialized free radical polymerization using a newly developed monomer including imidazolium as well as a fluorinated carbon chain. A scanning electron microscopy picture of the surface of the polymer is shown in figure 1.

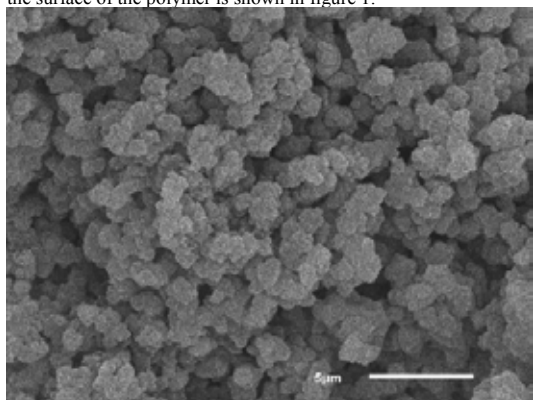


Fig. 1: Scanning electron microscopic graphic of porous structure of the developed fluorinated ion exchange polymer

The fluorinated ion exchange polymer adsorbs PFAS through a dual binding mechanism. The first mechanism is the ion exchange with the imidazolium moiety and the second mechanism is the fluorine-fluorine interaction which selectively binds fluorinated substances to the carbon-fluorine backbone. A schematic figure of the two mechanisms is depicted in figure 2.

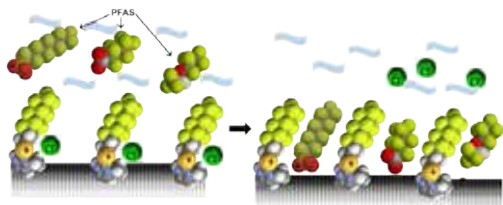


Fig. 2: Interaction mechanism of the fluorinated ion exchange polymer

3.2 Adsorption Kinetics

The resulting graphs of the single-component kinetic studies are shown in figures 3 and 4. The FP reaches the equilibrium within 24 h. For the PAC desorption mechanisms are shown after 24 h for PFOA and GenX.

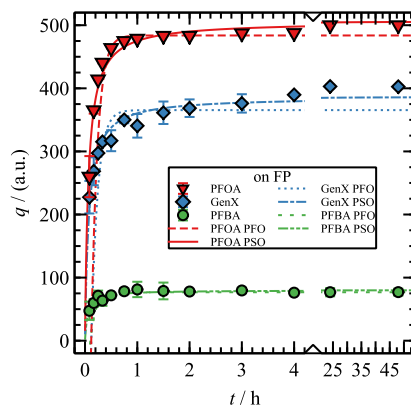


Fig. 3: Single-component kinetic study of PFOA, GenX and PFBA on FP

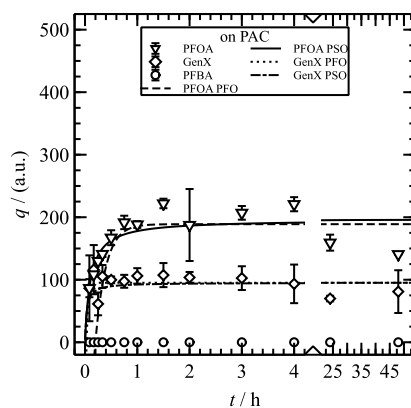


Fig. 4: Single-component kinetic study of PFOA, GenX and PFBA on PAC

3.3 Adsorption Isotherms

The newly developed FP achieves 12.2 times the maximum adsorption capacity according to the Langmuir isotherm model for PFOA, 5.1 times for GenX and 6.2 times for PFBA. Thus the FP outperforms the AC strongly for all three chosen PFAS. The adsorption isotherms are shown in figures 5, 6 and 7.

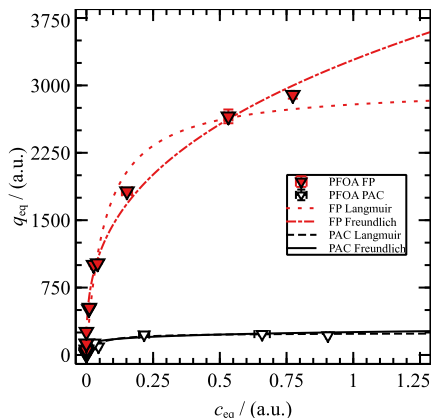


Fig. 5: Single-component-adsorption isotherm of PFOA onto FP and PAC with Langmuir and Freundlich Isotherms

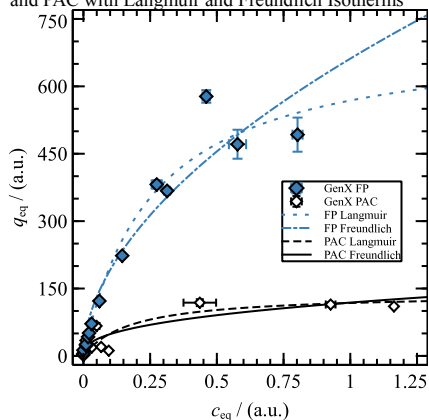


Fig. 6: Single-component adsorption isotherms of PFBA on FP and PAC with Langmuir and Freundlich fittings

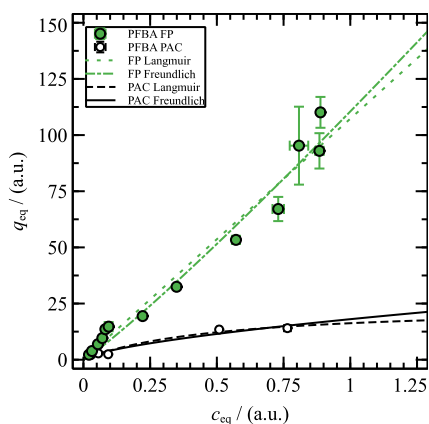


Fig. 7: Single-component adsorption isotherms of PFBA on FP and PAC with Langmuir and Freundlich Fittings

4 Conclusion

In conclusion, the synthesized fluorinated polymer (FP) reaches PFAS adsorption equilibrium within 24 h, whereas for the activated carbon desorption phenomena are shown after 24 h. The FP outperforms the commercially available PAC for all three chosen PFAS within the adsorption isotherms. Thus the FP shows promising results regarding the adsorption of PFBA, GenX and PFOA. Possible further developments are the integration of this FP into a membrane to enable easy scale-up and operability of the adsorbent.

References

- [1] OECD, Reconciling Terminology of the Universe Per- and Polyfluoroalkyl Substances, OECD Series on Risk Management, no. 61, 2021. url: https://www.oecd.org/en/publications/reconciling-terminology-of-the-universe-of-per-and-poly-uroalkyl-substances_e458e796-en.html
- [2] A. R. Carnero, A. Lestido-Cardama, P. V. Loureiro, L. Barbosa-Pereira, A. R. B. de Quirós, and R. Sendón, "Presence of perfluoroalkyl and polyfluoroalkyl substances (pfas) in food contact materials (fcm) and its migration to food," *Foods*, vol. 10, no. 7, p. 1443, 2021. doi: 10.3390/foods10071443
- [3] A. Chaudhary, W. Bashir, A. Majid, M. Qasim, E. Bughio, M. Fatima, and S. U. Din, "Pfas insights: A review of historical data, environmental applications, health effects, and pollution challenges in Pakistan," *Environmental Science & Policy*, vol. 167, p. 104056, 2025. doi: 10.1016/j.envsci.2025.104056
- [4] C. R. Ohoro, J. F. Amaku, J. Conradie, C. Olisah, K. G. Akpomie, A. Malloum, S. O. Akpotu, K. A. Adegoke, E. S. Okeke, and E. O. Omotola, "Effect of physicochemical parameters on the occurrence of per- and polyfluoroalkyl substances (PFAS) in aquatic environment," *Marine Pollution Bulletin*, vol. 28, p. 117040, 2024. doi: 10.1016/j.marpolbul.2024.117040
- [5] Z. Abunada, M. Y. D. Alazaiza, and M. J. K. Bashir, "An overview of per- and polyfluoroalkyl substances (pfas) in the environment: Source, fate, risk and regulations," *Water*, vol. 12, no. 12, p. 3590, 2020. doi: 10.3390/w12123590
- [6] B. C. Crone, T. F. Speth, D. G. Wahman, S. J. Smith, G. Abulikemu, E. J. Kleiner and J. G. Pressman, "Occurrence of per- and polyfluoroalkyl substances (pfas) in source water and their treatment in drinking water," *Critical Reviews in Environmental Science and Technology*, vol. 49, no. 24, pp. 2359–2396, 2019. doi: 10.1080/10643389.2019.1614848
- [7] S. E. Fenton, A. Ducatman, A. Boobis, J. C. DeWitt, C. Lau, C. Ng, J. S. SMith, and S. M. Roberts, "Per- and Polyfluoroalkyl Substance Toxicity and Human Health Review: Current State of Knowledge and Strategies for Informing Future Research," *Environmental Toxicology and Chemistry*, vol. 40, no. 3, pp. 606–630, 2021. doi: 10.1002/etc.4890
- [8] H. Briellmann, G. Döberl, S. Weiß and J. Grath, "PFAS in Österreichs Grundwasser: Verbreitung, Bewertung und Rolle von Altstandorten als potenzielle Quellen," *Österreichische Wasser- und Abfallwirtschaft*, vol. 75, no. 9, pp. 491–502, 2023. doi: 10.1007/s00506-023-00976-8.
- [9] D. Q. Zhang, W.L. Zhang, Y. N. Liang, "Adsorption of perfluoroalkyl and polyfluoroalkyl substances (PFASs) from aqueous solution - A review," *Science of The Total Environment*, vol. 694, 133606, 2019. doi: 10.1016/j.scitotenv.2019.133606
- [10] S. Garg, J. Wang, P. Kumar, V. Mishra, H. Arafat, R. S. Sharma, L. F. Dumée, "Remediation of water from per-/poly-fluoroalkyl substances (PFAS) – Challenges and perspectives," *Journal of Environmental Chemical Engineering*, vol. 9, no. 4, 105784, 2021. doi: 10.1016/j.jece.2021.105784
- [11] T. H. Boyer, A. Ellis, Y. Fang, C. E. Schaefer, C. P. Higgins, T. J. Strathmann "Life cycle environmental impacts of regeneration options for anion exchange resin remediation of PFAS impacted water," *Water Research*, vol. 207, 117798, 2021. doi: 10.1016/j.watres.2021.117798
- [12] A. Singh, R. Lynch, J. Solomon, J. D. Weaver, A. R. May, "Development of novel fluor mop materials for remediation of perfluoroalkyl substances (PFAS) from groundwater," *Journal of Hazardous Materials*, vol. 448, 130853, 2023. doi: 10.1016/j.jhazmat.2023.130853



Individuelle Lösungen für die Membranfiltration.

Vom ersten Gespräch bis
zur Realisierung.

- ① Individuelle
Konzeptentwicklung
- ② Wirtschaftliche und
technische Beratung
- ③ Technische
Serviceleistungen

Unsere Basis

30 Jahre Membranfiltration, praxisnahe
Konzepte und ein motiviertes, junges
Team.

Unsere Mission

Der Einsatz der Membrantechnologie
zur Ressourcenschonung durch
Kreislaufwirtschaft und Nachhaltigkeit.

Was uns auszeichnet

Wir nehmen uns Zeit für persönliche
Beratung, präzise Planung und
maßgeschneiderte Filtrationslösungen.
Produktunabhängig, ganzheitlich und
lösungsorientiert.



On the formation of a galvanic element in blast furnaces and its use for process diagnostics

S. Moll^{1,*}, J. Felser², G. Lengauer³, N. Schlemmer⁴, J. Eisbacher-Lubensky⁵, C. Weiß¹

1: Chair of Process Technology and Environmental Protection, Technical University of Leoben, Austria

2: Voestalpine Metal Engineering GmbH, Austria

3: Voestalpine Stahl GmbH, Austria

4: K1-MET GmbH, Austria

5: Chair of Ferrous Metallurgy, Technical University of Leoben, Austria

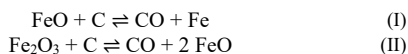
* Correspondent author: simon.moll@unileoben.ac.at

Keywords: blast furnace, galvanic cell, electromotive force, timeseries, tapping cycles

Thermo- and electrochemical processes acting as a source of electromotive forces (EMF) in the lower part of the blast furnace (BF) have been recognized for a long time. Based on voltage acquisition at the outer furnace shell, prior research proposed the use of the EMF-transient to indirectly monitor the liquid phase content in the furnace hearth. In our investigation the amplitude and shape of the EMF signal during the tapping cycle turns out to be strongly dependent on furnace operation. Oxide melt experiments and electric potential measurements are performed in lab-scale crucibles and used together with the furnace derived EMF transients to clarify the source of the EMF signal. A model for the charge separation is developed, based on the electronic and ionic conductors involved in the redox reactions near the interfaces between hot metal, slag, solid carbon and gas phase. For model verification, the resulting resistivity network model is compared to the measured voltage response of a high temperature model cell. EMF signals at the BF are monitored at several circumferential positions on the outer steel shell and the signal-based model prediction is implemented in the process control as a melt level indicator. During tapping the drop of the melt level typically declines with increasing distance from the tap hole. The fine-structure of the EMF signal during the tapping cycle provides detailed insight into the drainage behavior and dead man dynamics.

Introduction

Observations on the existence of electric currents in the BF system date back to the early 20th century. Ruff reported that a compass needle is being deflected in the vicinity of a BF. The accountable magnetic field arises from a direct current according to Biot-Savart law. Already in this early stage, scientists attributed the current source to a galvanic element inside the BF with the governing equations (I) and (II) [1].



Coke acts as the anode, iron as the cathode and the slag with varying amounts of iron oxides (ferric as well as ferrous) as the electrolyte. Other hypotheses were that the current is caused by triboelectric or thermoelectric effects. However, these were at least partially dismissed. In addition to these theoretical considerations, Ruff reported experimental evidence regarding the validity of a galvanic cell acting as a current source. To prove this concept, metallic iron containing ferrous meta silicate was melted and sparged with oxygen [1]. The melt was contacted with a carbon rod and an iron wire, which resulted in a potential difference between the electrodes. The same experiment without sparging did not exhibit a measurable voltage [1]. This was probably the case due to the shielding of the iron cathode by the dispersed iron particles between the electrodes, which formed distributed local elements.

At-site, the signal pick-up for observing the effect is conveniently performed at the outside of the BF steel shell. The signal is

significantly influenced by the internal resistance network, which partially short-circuits the galvanic element. This resistance network reflects the operating state of the BF [1].

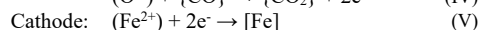
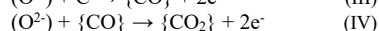
Reaction mechanism of the galvanic cell inside blast furnaces

As the exact mechanism of the reactions that give rise to the observed current is of great importance for the interpretation of transients in the voltage drops over the furnace shell, the present work aimed to revisit the experimental examination of the galvanic cell inside the BF.

Dorofeev et. al. distinguish between different contributions to the overall electromotive force [2]:

- Oxidation reactions of pre-reduced iron oxide and carbon in the raceway
- Direct reduction of iron oxide in the heterogeneous slag/coke layer below the tuyeres
- Oxidation of dissolved iron in the hot metal by iron oxides at the hot metal/slag interface
- Thermoelectric voltages caused by the furnace lining and steel shell

Neglecting thermoelectric effects, the net reaction from equation (I) can be split into the anodic and cathodic partial reactions (III), (IV) and (V). At this point it should be noted that the Boudouard equilibrium, which is important for the indirect (gas) reduction with CO, also represents an electron transfer reaction at the coke surface. The according electrochemical cell diagram is given in equation (VI). It is assumed that this reaction system (VI) gives rise to the majority of the net electromotive force that leads to the observed electric effects.



To test the validity of this working hypothesis, an experiment was carried out in which the cell was simulated. For this purpose, a graphite crucible was filled with pig iron and iron oxide-enriched blast furnace slag (BFS) and heated to 1450 °C in a radiation furnace in an inert atmosphere. In the molten state, a graphite electrode and a pure iron electrode were lowered into the melt. Care was taken to ensure that the graphite electrode contacted the slag and the pure iron electrode contacted the pig iron. In order to prevent electrical contact between iron wire and slag, the wire was guided through the slag in a corundum tube. This cell configuration is illustrated in Figure 1. Measurements of the cell voltage range between approximately 100 – 300 mV (see result image on right side of Figure 2). To investigate the effect of an increased reduction potential in the gas phase, CO was fed into the furnace chamber.

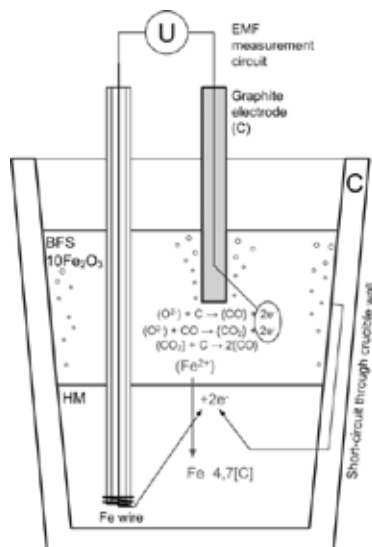


Figure 1: Schematic representation of the experimental setup to confirm the existence of a measurable EMF due to the reduction reaction of iron from an iron enriched BFS into hot metal (HM).

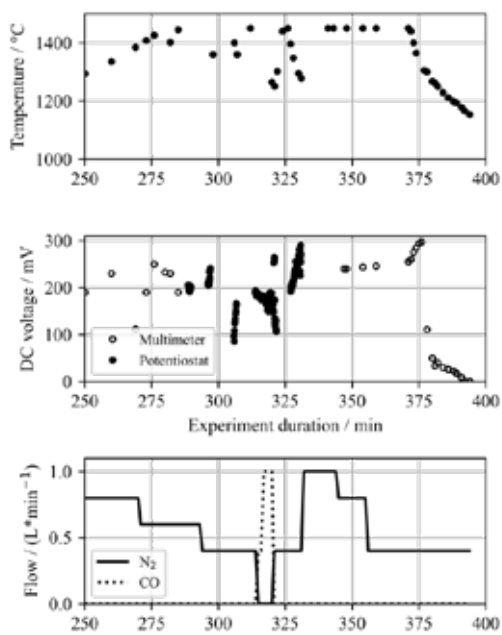


Figure 2: Measurement results from the illustrated cell configuration; the cell is heated in a MoSi₂ type, vacuum ready furnace with a free volume of approximately 30 L.

Considering the anodic reaction (III) and the cathodic reaction (V), which results in the sum reaction (I), the Gibbs reaction enthalpy is $\Delta_r G^\circ = -112.2 \text{ kJ} \cdot \text{mol}^{-1}$. For reversible reactions this free enthalpy gives rise to a cell voltage of E° , according to equation (VII), involving the transfer of $n = 2$ electrons (F is the Faraday constant).

$$E^\circ = - \frac{\Delta_r G^\circ}{n \cdot F} = \frac{112.2 \cdot 10^3 \frac{\text{J}}{\text{mol}}}{2 \cdot 96485 \frac{\text{C}}{\text{mol}}} = 0.58 \text{ V} \quad (\text{VII})$$

The measured voltage, however, does not reflect the true EMF because of partial short-circuiting of the cell due to parasitic currents through the crucible wall, as illustrated in Figure 1. A similar case applies this EMF measurement at the BF, where the short circuit is additionally enhanced by the coke layer (which forms a sponge-like network in the slag as well as in the pig iron across the furnace cross-section) and by the multi-layered wall of refractory lining plus steel shell.

Measurements of the potential differences on the BF shell have a history as a predictive tool for the hearth's liquid level [3, 4]. Taking into account the resistivities of the characteristic zone of the furnace hearth (coke, slag, combustion space, refractory materials, and hot metal), Gomes et. al. [4] derived a lumped circuit element model for the electric network (Figure 3a). However, it shall be noted that the EMF source as a simplification is localized explicitly at the hot metal / slag interface in the idealized layered illustration by Gomes et. al. (see definition of the half-cells). Contrary, in the BF a distributed EMF source may be assumed more realistically, as the coke bed penetrates the melt pool at least partially. In a different approach, Ito et.al. [3] describe a method for the hearth level prediction by application of an external electric field onto the furnace shell and measurement of potential difference (which is influenced by the inner constitution of the BF) in the sense of a 4-point (Kelvin) probing as illustrated in Figure 3b. The Ito-approach comes with the advantage that the signal is less affected by the thermal influence of the furnace.

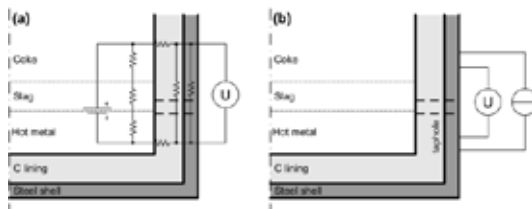


Figure 3: Schematics of the two alternative approaches for the model circuit by Gomes et. al. (a) and Ito et. al. (b) for the evaluation of the internal electrical network.

Diagnostic application of the EMF signal for blast furnace operation

Observation of the EMF signal time series allows correlation with specific events during the operation of a BF, which will be described in this section. The measurement of the vertical potential difference is realized by pick-up wires made of low carbon steel that are welded onto the furnace shell. Vertically, the welds are located below the tuyeres and at the height of the hearth floor. Laterally, four positions have been chosen in angles 9°, 63°, 171° and 297° to the tap hole (clockwise; ϕ_1 , ϕ_2 , ϕ_3 and ϕ_4 ; see inset in Figure 4a). The signals are digitized using voltage transmitters with a measurement range of $\pm 1.25 \text{ mV}$ and a resolution of 16 bit. These values are recorded in the process control system, making it possible to correlate them with all other measured variables recorded there, thus enabling anomalies to be interpreted. Figure 4 illustrates the EMF time series for four operation states. The subfigures show the standard condition (a) as a baseline to compare with the cases of high FeO content in the slag (b), redrilling (c) and a blow-in procedure during BF-startup (d, e). Savitzky-Golay smoothing was applied to the raw data (polynomial order = 3, window size $ws = 201$ for cases a, b, c, e; $ws = 2501$ for case d).

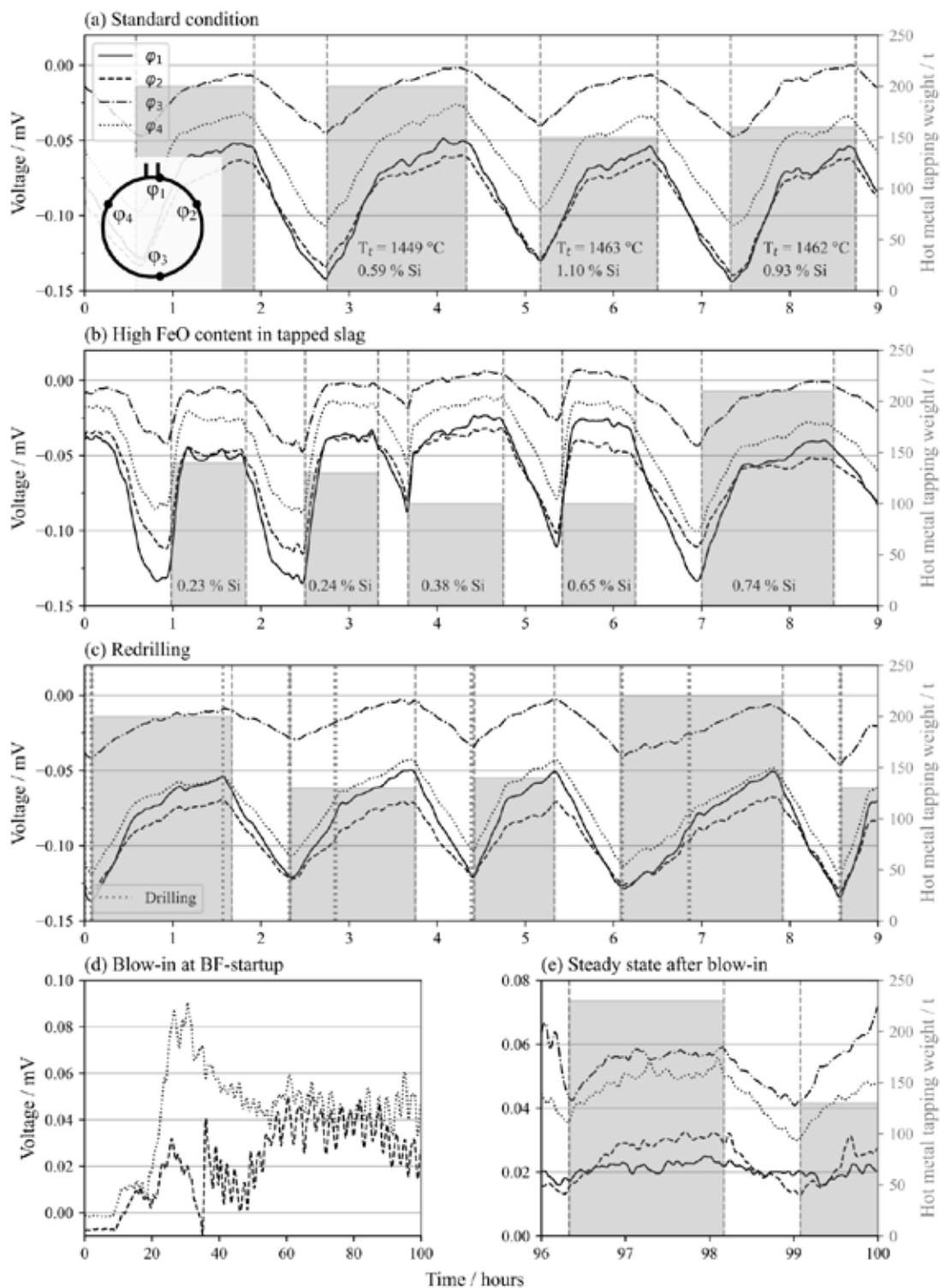


Figure 4: Smoothed EMF signal measurements on the blast furnace shell for four exemplary operating conditions at four sensors located at $\varphi_1 = 9^\circ$, $\varphi_2 = 63^\circ$, $\varphi_3 = 171^\circ$, and $\varphi_4 = 297^\circ$ circumferentially from the tap hole. The grey fields mark the tapping periods and their heights indicate hot metal tapping weights. Trough temperatures T_t ; hot metal silicon content in wt.-%.

A phenomenological as well as – in a first attempt – a mechanistic description of the four operation states shall be given in the following.

a) Standard condition:

During the hearth filling phase, a continuous increase in the signal's absolute value is observed. During tapping (grey fields) a two-phase outflow is indicated by the time-gradient of the signal. These phases are attributed to the outflow of hot metal and subsequently slag, respectively. However, the transition between these phases can be faded.

b) High FeO content in tapped slag:

A decrease in silicon content in the hot metal suggests that the reduction potential in the furnace is lowered. This results in an increased iron oxide content of the slag and therefore reduced yield. The considerably lower viscosity of the FeO-containing slag strongly affects drainage behavior. The EMF signal reflects this condition by steeper gradients during tapping followed by a saturation both during hearth filling and tapping.

c) Redrilling:

Due to tap-hole blockages (for example by coke pieces), a redrilling can be necessary after the initial tapping start. The decision-making in this regard is currently based on the experience of a trained employee. However, a comparison of the EMF signal from a redrilled tap (at 2.8 h and 6.8 h in Figure 4c) with a standard case shows that signal gradient during hot metal tapping is lower than during an unobstructed tapping. Including the signal in the decision-making process can therefore increase productivity.

d) Blow-in after relining:

After the heating of the hearth, iron production is started by feeding of ore. The discontinuity at 35 h is repeatedly observed during the blow-in of the BF and marks the establishment of the electrochemical redox system during the time-instant of first slag formation. The system settles into the standard condition after multiple tapping cycles.

Conclusion

It can be stated that electrical measurement techniques can be beneficially applied in the blast furnace process for process control. Our studies suggest further research in the direction of impedance tomography application and fundamental research on the electrochemistry of the relevant metal/slag-reactions, as they might provide a physico-chemical basis for future smelter and electric arc furnace design.

References

- [1] W. Ruff, *Elektrizität an Hochöfen*. Stahl und Eisen 47 (1927), 37, pp. 1543–1545.
- [2] V.N. Dorofeev and A.M. Novokhatskii, Origin of difference in electric potentials on blast furnace shell. *Steel in the USSR* (1984), 14, pp. 10–12.
- [3] T. Ito, J. Yotsuji and A. Nagamune, Development of Pig Iron and Molten Slag Level Measurement Technique for Blast Furnace. *ISIJ Int.* 54 (2014), 11, pp. 2618–2622. doi:10.2355/isijinternational.54.2618
- [4] F.S.V. Gomes, J.L.F. Salles and L.A. Wasem, A new prediction model for liquid level in blast furnaces based on time series analysis. 2011 9th IEEE International Conference on Control and Automation (ICCA), pp. 772–777, Santiago, Chile (12/19/2011 - 12/21/2011), IEEE.

Carbonation behavior of Ca-rich steel slags: Influence of process parameters and mineralogical composition

S. Reiter^{1,*}, M. Lehner¹

¹: Chair of Process Technology and Environmental Protection, Technical University of Leoben, Austria

* Correspondent author: sarah.reiter@unileoben.ac.at

Keywords: Aqueous carbonation, mineralization, mineralogy, CO₂ sequestration, secondary materials

Introduction and Objectives

Carbonation describes the exothermic reaction of metal oxides (MeO) with CO₂, leading to the formation of their respective carbonates (MeCO₃), as described in equation (1). In nature, this reaction is particularly prevalent for Ca- or Mg-bearing minerals such as Olivine, Serpentinite and Wollastonite within ultramafic rocks, referred to as silicate weathering [1].



From a thermodynamic perspective, carbonates represent the most stable derivatives of CO₂, making the reaction particularly relevant for CO₂ sequestration, offering a potential pathway for secure and long term CO₂-storage [2, 3].

In addition to ultramafic rocks, many industrial solid residues are rich in Ca- and Mg- bearing minerals, deeming them suitable feedstocks for carbonation. Due to the generally enhanced reactivity because of the higher chemical instability of these materials compared to ultramafic rocks, recent research has increasingly focused on the carbonation of industrial byproducts. These include residues from the cement, refractory, and paper industries, combustion slags and ashes, construction and demolition waste, as well as slags from iron and steel production [1].

Although these secondary materials are not as geologically abundant as ultramafic rocks, they are produced in substantial amounts. For instance, in Austria alone, approximately 0.6 million tons of slags from iron and steel production were generated as waste in 2021, in addition to 1.9 million tons of slag classified as a byproduct [4, 5]

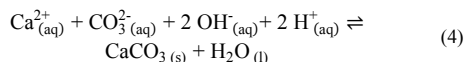
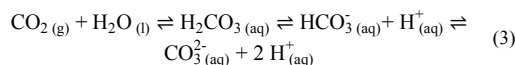
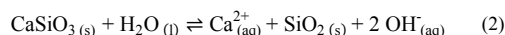
In addition to generating large volumes of residues, the iron and steel industry is a major source of “hard-to-abate” emissions, referring to emissions that persist even after all mitigation measures have been applied [6]. Therefore, carbonation of steel slags offers an attractive opportunity to mitigate these emissions by repurposing own waste streams.

Although carbonation is thermodynamically favorable at ambient conditions, the reaction is characterized by its inherently slow kinetics, especially when applied to solid materials itself. To address this limitation, direct aqueous carbonation presents a promising process route, where an aqueous phase acts as a solvent for Ca- or Mg-ions and the gaseous CO₂ [1, 3]

When Ca- or Mg-rich materials dissolve in water, they typically create highly alkaline environments due to the formation of OH⁻, as exemplified by CaSiO₃ in equation (2) [7]. CO₂ dissolves into the liquid phase, forming carbonic acid, which, under alkaline conditions, further dissociates into bicarbonate and carbonate ions (eq. (3)). The optimal pH range for the carbonation reaction is typically between 8 and 9, where most carbonate species exist as bicarbonates, enabling both effective CO₂ dissolution and dissociation into carbonate ions [3, 8]. The leached Ca- or Mg-ions then react with the formed carbonate ions, precipitating as solid carbonates (eq.(4)) [9].

To enhance mineral dissolution, the process is usually performed at elevated temperatures. However, since CO₂ solubility decreases with higher temperatures, it is necessary to increase the CO₂-

pressure to counteract this effect. Consequently, the overall CO₂-uptake is therefore influenced by the interaction of mineral dissolution, carbonate ion availability within the aqueous phase, and carbonate precipitation [1, 9].



Within this work, two steel slag types –blast furnace (BF) slag and basic oxygen furnace slag (Linz-Donawitz (LD) slag) – are investigated for their CO₂-uptake during direct, aqueous carbonation at four distinct reaction conditions. Initial experiments conducted at relatively mild pressure and ambient temperature aim to assess the CO₂-uptake under low-energy conditions, while subsequent experiments at elevated pressure and temperature are designed to explore the potential for process intensification.

In addition, experiments are performed by introducing NaHCO₃ and NaCl into the liquid phase. Sodium bicarbonate, which acts as a buffering agent, maintains the pH within the optimal range of 8 to 9, thereby potentially enhancing carbonation efficiency [8, 10]. This approach, typically applied for Mg-rich ultramafic rocks [8], addresses the research gap regarding the use of such additives in the carbonation of Ca-rich secondary feedstock.

Materials and Methods

In their natural state, both slag samples exhibit a coarse morphology. Consequently, they are crushed and grinded using a ball mill, followed by separation of the 90-125 μm particle size fraction for experimental investigation. The chemical composition of this fraction is analyzed using X-ray fluorescence (XRF) analysis and is presented in Table 1. Prior to experiments, the samples are dried at 105 °C for a minimum of 2 hours.

Table 1: Chemical composition of the BF and LD-slag sample

Species in wt.%	BF-slag	LD-slag
SiO ₂	14.73	14.55
Al ₂ O ₃	12.79	0.78
Fe ₂ O ₃	37.49	29.78
MgO	5.73	7.82
CaO	21.69	40.66
SO ₃	0.24	0.08
LOI	-0.79	-1.00

For carbonation experiments, a stirred 300-mL batch reactor (Parr Instruments) is used. The experimental conditions are summarized in Table 2. In each experiment, nine grams of sample are suspended in 100 mL of deionized water, resulting in a solid-to-liquid ratio of 90 g L⁻¹. The suspension is loaded into the batch reactor, which is subsequently sealed. The stirrer speed is set to 600 rpm. For

experiments conducted at 100 °C (Exp. No. 3 and 4) the reactor is heated using an electrical heating jacket. Once the desired temperature is reached, CO₂ is injected into the reactor from a connected supply tank to achieve a total pressure of 5 (Exp. No. 1) or 20 bar (Exp. No. 2 to 4). A forward-pressure control valve located between the supply tank and the reactor maintains a constant pressure ± 0.5 bar throughout the reaction time of 2 hours. In Exp. No. 4, instead of pure deionized water, a solution of deionized water containing 0.64 M NaHCO₃ and 1 M NaCl is used.

Table 2: Process parameters of carbonation experiments

Exp. No.	Pressure, bar	Temperature, °C	Additives, -
1	5	20	no
2	20		
3	20	100	yes
4		100	

For experiments conducted at 100°C, the reactor is cooled to 80 °C after the reaction time before releasing the CO₂-pressure by opening the gas outlet valve. The reactor is unsealed, and the product suspension is filtered using a pleated filter with retention range of 5 to 32 µm. The remaining solid residue is then dried at 105 °C for a minimum of 2 hours and subsequently prepared for further analysis.

To assess the CO₂-sequestration potential of the slag samples, the theoretical maximum CO₂-uptake (U_{th}) in kilograms CO₂ per ton of feed material is calculated using a modification of the Steinour/Huntzinger equation (5). The equation evaluates the maximum amount of CO₂ that can be sequestered within a material if all available CaO and MgO phases are converted into their respective carbonates [11].

In this work, a modification is used, as both the original Steinour formula and its later adaptation by Huntzinger [12] also account for the formation of sodium and potassium carbonates. However, since K₂CO₃ and Na₂CO₃ are known to be water-soluble [13] and thus are not suitable for long-term CO₂ storage, they are excluded from the calculation of the theoretical CO₂-uptake. Furthermore, while the Huntzinger modification accounts for the reduction of theoretical CO₂-uptake due to the presence of pre-existing calcium carbonates, it does not consider existing magnesium carbonates. To address this, the MgCO₃ content is subtracted from the total MgO-content. All components within the calculation are expressed in weight percent.

$$U_{th} = \frac{0.785 \times (\%CaO - 0.56 \times \%CaCO_3 - 0.7 \times \%SO_3)}{1.091 \times (\%MgO - 0.48 \times \%MgCO_3)} \times 10 \quad (5)$$

The experimental CO₂-uptake, expressed in kg CO₂ per ton of feed material as well, is determined by Total Carbon Analysis (TCA) and calculated according to equation (6), where CO_{2raw} and CO_{2carbonated} represent the CO₂ contents in weight percent of the raw and carbonated sample, respectively.

$$CO_2\text{-uptake} = \frac{CO_{2carbonated} - CO_{2raw}}{100 - CO_{2carbonated}} \times 10 \quad (6)$$

To identify the carbonate minerals formed during carbonation, Thermogravimetric Analysis (TGA) is performed by heating the samples to 1100°C in an air atmosphere at a heating rate of 20 °C min⁻¹. In addition, gas analysis is applied, using a Fourier Transform Infrared Spectroscopy (FTIR), enabling the detection of gaseous decomposition products such as CO₂ and H₂O.

Carbonation efficiency (CE) in percent is calculated as the ratio of percentual, experimental CO₂-uptake to the theoretical uptake U_{th}, as given in equation (7).

$$CE = \frac{CO_2\text{-uptake}}{U_{th}} \times 100 \quad (7)$$

Semi-quantitative X-ray diffraction (XRD) analysis is performed to determine the relative abundances of crystalline phases in both the raw and carbonated sample exhibiting the highest CO₂-uptake for each slag type. Reported values are normalized to the crystalline fraction, as amorphous phases cannot be detected via this method.

Results and Discussion

For the raw BF-slag sample an initial CaCO₃ content of 3.42 wt.-% is determined, whereas the LD-slag exhibits no initial carbonate content. Accordingly, theoretical CO₂-uptakes U_{th} of 216.3 kg t⁻¹ and 387.8 kg t⁻¹ are calculated for the BF- and LD-slag sample, respectively.

Figure 1 illustrates the CO₂-uptake and carbonation efficiency of (a) the BF-slag and (b) LD-slag samples across the four experimental conditions.

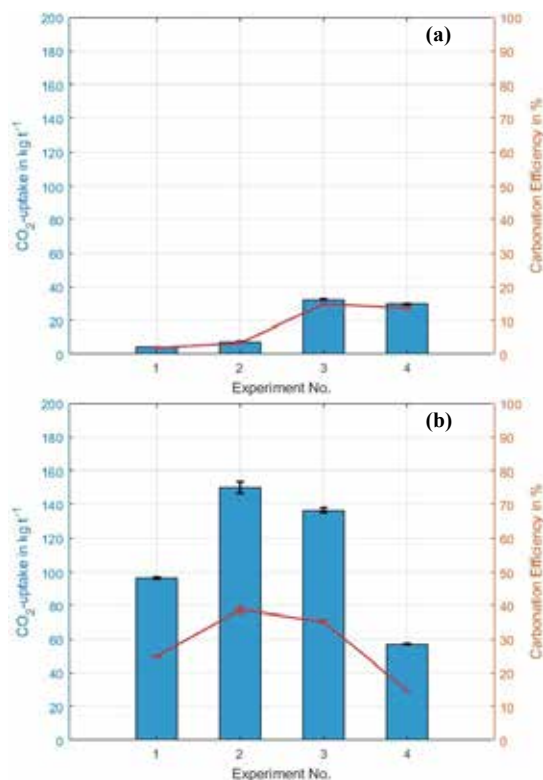


Figure 1: CO₂-uptake in kilograms per ton of feed material (blue beams) and carbonation efficiency in percent (orange line) for the BF-Slag (a) and LD-Slag (b) sample across Exp. No. 1 to 4

For the BF-Slag sample, CO₂-uptakes of 4.1 and 7.3 kg t⁻¹ are determined in experiments 1 and 2, respectively. Increasing the temperature to 100 °C in experiment 3 significantly enhances the CO₂-sequestration to 32.6 kg t⁻¹, obtaining the highest carbonation efficiency of 7.8 % for this slag type. The addition of salt additives in experiment 4 does not result in a further increase, yielding a slightly lower CO₂-uptake of 29.9 kg t⁻¹.

The LD-slag sample demonstrates a significantly higher CO₂ sequestration capacity across all experimental conditions. In experiment 1, an uptake of 94.6 kg t⁻¹ is recorded. Increasing the pressure to 20 bar in experiment 2 further enhances the uptake to 150.4 kg t⁻¹, corresponding to a maximum carbonation efficiency of 38.8 %. Unlike the BF-Slag sample, increasing the temperature to

100 °C does not yield further improvement, with a slightly reduced uptake of 136.4 kg t⁻¹ observed in experiment 3. The addition of salts in experiment 4 results in a significantly lower CO₂-sequestration of 57.1 kg t⁻¹.

XRD results are presented in Figure 2 for (a) the raw BF-slag and the carbonated sample resulting from experiment 3, and (b) the uncarbonated LD-slag and carbonated sample resulting from experiment 2, as these experimental conditions promote the highest CO₂ uptake for the materials, respectively.

The most prominent mineral phases within the raw BF-slag sample are Gehlenite (Ca₂Al₂SiO₇), β-Belite (also Larnite, a polymorph of Ca₂SiO₄), Fe/Mn-Oxides, Magnetite (Fe₃O₄), Kirschsteinite (CaFeSiO₂), Tricalcium aluminate (also C₃A or Ca₃Al₂O₆). 3 wt.-% of Calcite (CaCO₃) is detected within the crystalline phase, being consistent with TCA/TGA results.

XRD of the carbonated BF-slag reveals minor changes in the mineralogical composition, with the most prominent being the formation of Calcite. Regarding the reactive mineral phases, β-Belite appears to be the most reactive, while gehlenite and C₃A participate to a lesser extent. The carbonation of Ca-silicates leads to the formation of amorphous silica phases [14], and therefore, a shift in the ratio of amorphous to crystalline minerals is likely. Consequently, a reduction in the overall amount of crystalline compounds can be expected, however this cannot be quantified within XRDs without the application of Rietveld refinement.

The crystalline phases of the LD-slag sample consist of approximately 70 wt.-% Belite in total, with β-Belite being the most prominent polymorph at 54 wt.-%, followed by the α- and γ-Belite polymorphs. The remaining contributing crystalline phases include Brownmillerite (Ca₂(Al,Fe)₂O₅), Wuestite (FeO) and Hedenbergite (CaFeSi₂O₆). No initial carbonate content is determined via XRD, which is consistent with TCA/ TGA results.

After carbonation, a significant increase in calcite formation is observed. The main reactive mineral phase is again β-Belite, followed by α- and γ-Belite. Partial carbonation of Brownmillerite is also evident, while the remaining crystalline phases remain largely unaffected.

To assess why one slag sample exhibits higher reactivity under varying experimental conditions, it is essential to recognize that various factors influence carbonation behaviour. These include the morphological properties of the material, such as particle size, surface area and porosity. Additionally, the solubility of each mineral, which is influenced by the properties of the aqueous phase, (e.g. pH and ionic strength), has a significant impact on overall reaction kinetics. Process parameters, such as temperature and CO₂ partial pressure affect the solubility of CO₂ in water, thereby influencing carbonation as well. Importantly, these parameters are not independent; they influence each other to some extent, which in turn affects overall reactivity. As a result, attributing differences in performance to a single factor is challenging without further detailed investigations. Nevertheless, based on the available results, several preliminary interpretations can be identified.

Generally, depending on whether mineral dissolution or the availability of carbonate ions in the aqueous phase are the limiting factor, the CO₂-uptake can be positively influenced by either increasing the temperature or CO₂ pressure [9, 15]. Focusing on the key mineral phases – Gehlenite in BF-slag and β-Belite in LD-slag – both minerals exhibit limited dissolution rates at ambient temperatures. In theory, both minerals benefit from increased temperature [15], as seen for the BF-slag, where carbonation efficiency improves at 100 °C. However, this behaviour cannot be observed for the LD-slag sample, suggesting that the solubility of β-Belite is sufficient at ambient temperatures and that carbonate ion availability is the limiting factor.

However, another potential reason for the decreased reactivity of the LD-slag at 100 °C could be a pH effect [9]. The introduction of CO₂ into the suspension ultimately lowers its pH, which generally enhances mineral solubility [15].

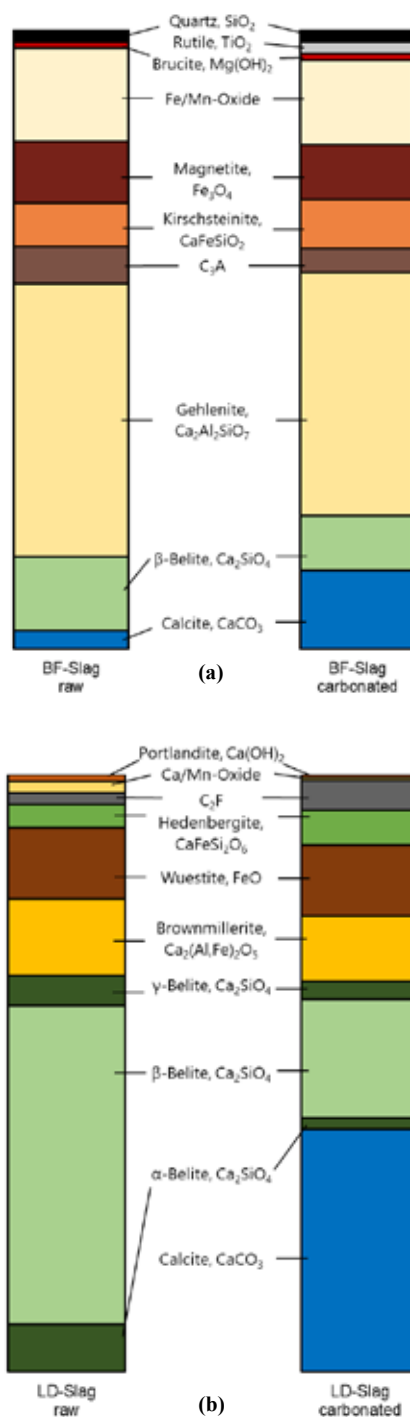


Figure 2: Semi-quantitative XRD-results representing the relative abundance of crystalline phases for (a) the raw BF-slag and the carbonated sample from Exp. No. 3 and (b) the raw LD-slag and the carbonated sample from Exp. No. 2

At higher temperatures, the pH reduction is less pronounced due to the decreased CO₂ solubility. For the LD-slag, this limited pH decrease might shift the solubility dynamics, reducing carbonation effectiveness despite the elevated temperature. In contrast, at ambient temperature, the more significant pH reduction likely enhances carbonation, which, along with the increased availability of dissolved CO₂, leads to the higher CO₂-uptake.

However, it needs to be addressed that the results presented in this work are contrary to other studies (e.g. [16]), where an increase in temperature clearly enhanced carbonation efficiency.

The addition of salts to the aqueous phase has no positive effect on carbonation efficiency for BF-slag and clearly negatively impacts the LD-slag. This contradicts the findings of Ren et al. [17], who observe an increase in carbonation efficiency for BF-slag using NaCl solution, attributing it to a reduced water activity and accelerated calcium ion dissolution. These results, along with the temperature effects on LD-slag, require further investigation.

Nevertheless, a significant fraction of Ca-bearing minerals remains unreacted under the given process conditions. Na et al. [18] highlight particle size as a key factor in enhancing carbonation activity, suggesting that optimizing particle size is a promising strategy to improve carbonation efficiency. Extending the reaction time might increase CO₂-uptake as well, but carbonation kinetics generally slow down with reaction time, due to the formation of passivation layers, such as Ca-depleted silica from Ca-silicates. Additionally, the precipitation of carbonates can create an inert layer that prevents further reaction [3, 12, 16]. This phenomena is well documented for steel slags, with Na et al. [18] noting the formation of passivation layers from calcium carbonate, and Lekakh et al. [19] reporting similar effects in electric arc and ladle furnace slag carbonation, where the product layer hinders carbonate conversion and leaching behavior.

Conclusion and Outlook

The carbonation results indicate that the LD-slag sample is well-suited for the aqueous carbonation process, with a substantial CO₂-uptake of 150.4 kg t⁻¹ at ambient temperatures. In contrast, the BF-slag demonstrates limited CO₂ sequestration across all conditions, although an increase in temperature improves its carbonation yield 32.6 kg t⁻¹. Salt additives do not enhance carbonation efficiency for either slag type.

Despite the presence of several Ca-rich mineral phases and a high theoretical CO₂-uptake for both materials, carbonation efficiency is likely limited by metal ion solubility. Of the present minerals, β-Belite exhibits the highest reactivity, therefore showing highest carbonation potential. Gehlenite on the other hand, is not carbonated to the same extent. However, further studies are needed to understand the influence of process parameters on specific minerals.

Additionally, the formation of an inert product layer around particles might inhibit further reaction. To achieve complete carbonation, reducing particle size and removing inert layers, for instance through grinding, is inevitable.

References

- [1] F. Schinnerl, T. Sattler, G. Noori-Khadjavi, and M. Lehner, "Direct aqueous mineral carbonation of secondary materials for carbon dioxide storage," *Journal of CO₂ Utilization*, vol. 88, p. 102942, 2024, doi: 10.1016/j.jcou.2024.102942.
- [2] J. G. Driver, E. Bernard, P. Patrizio, P. S. Fennell, K. Scrivener, and R. J. Myers, "Global decarbonization potential of CO₂ mineralization in concrete materials," *Proceedings of the National Academy of Sciences of the United States of America*, vol. 121, no. 29, e2313475121, 2024, doi: 10.1073/pnas.2313475121.
- [3] W. J. J. Huijgen, G.-J. Witkamp, and R. N. J. Comans, "Mineral CO₂ sequestration by steel slag carbonation," *Environmental science & technology*, vol. 39, no. 24, pp. 9676–9682, 2005, doi: 10.1021/es050795f.
- [4] Federal Ministry for Climate Action, Environment, Energy, Mobility, and Innovation and Technology, "Federal Waste Management Plan (BAWP) 2023 - Part 1,"
- [5] B. M. BMF, 79/21 MRV: *Carbon Management – Eine Säule der österreichischen Klimapolitik*, 2023.
- [6] BMK, "Österreichische Carbon Management Strategie (CMS)," Wien, 2024.
- [7] N. L. Ukwattage, P. G. Ranjith, and X. Li, "Steel-making slag for mineral sequestration of carbon dioxide by accelerated carbonation," *Measurement*, vol. 97, pp. 15–22, 2017, doi: 10.1016/j.measurement.2016.10.057.
- [8] William Oconnor, D.C. Dahlin, G.E. Rush, S.J. Gerdemann, L.R. Penner, and D.N. Nilsen, "Aqueous Mineral Carbonation: Mineral Availability, Pretreatment, Reaction Parametrics, and Process Studies," 2005.
- [9] A. A. Olajire, "A review of mineral carbonation technology in sequestration of CO₂," *Journal of Petroleum Science and Engineering*, vol. 109, pp. 364–392, 2013, doi: 10.1016/j.petrol.2013.03.013.
- [10] W. O'Connor, D.C. Dahlin, G.E. Rush, S.J. Gerdemann, L.R. Penner, and D.N. Nilsen, "Aqueous Mineral Carbonation: Mineral Availability, Pretreatment, Reaction Parametrics, and Process Studies," 2005, doi: 10.13140/RG.2.2.23658.31684.
- [11] F. Abdul, A. Iizuka, H.-J. Ho, K. Adachi, and E. Shibata, "Potential of major by-products from non-ferrous metal industries for CO₂ emission reduction by mineral carbonation: a review," *Environmental science and pollution research international*, vol. 30, no. 32, pp. 78041–78074, 2023, doi: 10.1007/s11356-023-27898-y.
- [12] D. N. Huntzinger, J. S. Gierke, S. K. Kawatra, T. C. Eisele, and L. L. Sutter, "Carbon dioxide sequestration in cement kiln dust through mineral carbonation," *Environmental science & technology*, vol. 43, no. 6, pp. 1986–1992, 2009, doi: 10.1021/es802910z.
- [13] RB Temple and CJ Lockyer, "Solubility Data for Na₂CO₃ and K₂CO₃ Dissolved in Molten NaNO₃/KNO₃ Eutectic,"
- [14] N. K. Bui, R. Kurihara, M. Kanematsu, H. Hyodo, T. Noguchi, and I. Maruyama, "Effect of temperature on binding process of calcium carbonate concrete through aragonite crystals precipitation," *Composites Part B: Engineering*, vol. 283, p. 111625, 2024, doi: 10.1016/j.compositesb.2024.111625.
- [15] M. A. Saleh, M. P. Ryan, J. M. Trusler, and S. Krevor, "The interfacial processes controlling carbon dioxide mineralisation in magnesium and calcium silicates," *Fuel*, vol. 380, p. 132969, 2025, doi: 10.1016/j.fuel.2024.132969.
- [16] A. Poletini, R. Pomi, and A. Stramazzo, "CO₂ sequestration through aqueous accelerated carbonation of BOF slag: A factorial study of parameters effects," *Journal of environmental management*, vol. 167, pp. 185–195, 2016, doi: 10.1016/j.jenvman.2015.11.042.
- [17] E. Ren, S. Tang, C. Liu, H. Yue, C. Li, and B. Liang, "Carbon dioxide mineralization for the disposition of blast-furnace slag: reaction intensification using NaCl solutions," *Greenhouse Gases*, vol. 10, no. 2, pp. 436–448, 2020, doi: 10.1002/ghg.1837.
- [18] H. Na, Y. Wang, X. Zhang, J. Li, Y. Zeng, and P. Liu, "Hydration Activity and Carbonation Characteristics of Dicalcium Silicate in Steel Slag: A Review," *Metals*, vol. 11, no. 10, p. 1580, 2021, doi: 10.3390/met11101580.
- [19] S. N. Lekakh, C. H. Rawlins, D. Robertson, V. L. Richards, and K. D. Peaslee, "Kinetics of Aqueous Leaching and Carbonization of Steelmaking Slag," *Metall Mater Trans B*, vol. 39, no. 1, pp. 125–134, 2008, doi: 10.1007/s11663-007-9112-8.

Mechanistical approach for the electrical conductivity calculation of oxidic melts with focus on steelmaking slags

N. Schlemmer^{1,*}, I. Marschall¹, S. Moll², C. Weiß²

1: K1-MET GmbH, Austria

2: Chair of Process Technology and Environmental Protection, Technical University of Leoben, Austria

* Correspondent author: nina.schlemmer@k1-met.com

Keywords: Metallurgical slags, electrical conductivity, electric steelmaking, oxidic melts, viscosity, correlation

Redox reactions – chemical processes involving electron transfer – form the basis of most fundamental pyrometallurgical processes. To develop a comprehensive understanding of these reactions and to explore opportunities for process optimization or redesign, it is crucial to investigate both ionic and electronic conduction phenomena in metallurgical slag melts, as electrical conductivity not only serves as a valuable indicator of slag composition but also offers key insights into the underlying reaction mechanisms.

In our investigation, the electrical conductivity of molten calcium silicate slags is determined using a four-electrode setup, commonly referred to as the extended Van der Pauw configuration. This method involves measuring the complex impedance of the melt across a frequency range of 0.1 to 100.0 kHz at various electrode immersion depths. Slags of different compositions are examined and temperature-dependent electrical conductivity data are correlated with viscosity using both the Arrhenius equation and the Vogel-Fulcher-Tammann (VFT) approach. In addition to these semi-empirical correlations, a mechanistic model is applied, inspired by the analogy between diffusive transport of momentum and mass. Within this framework, ionic conduction in the molten slag is linked to viscosity data. The model treats ionic conductivity as the cumulative result of ion-specific mobility, charge, and concentration, offering a fundamental perspective on ionic transport mechanisms in molten slags. Finally, a comparison is made between the model predictions and the experimentally measured conductivity values.

Introduction

In molten slags, the overall electrical conductivity (σ) results from the combined contributions of ionic conductivity (σ_i) and electronic conductivity (σ_e), as expressed in equation (1) [1].

$$\sigma = \sigma_i + \sigma_e \quad (1)$$

Ionic conduction occurs through the migration of anions and cations under the influence of an external electric field. This mechanism becomes more pronounced at higher temperatures, as the reduced viscosity of the melt allows for a greater mobility of the ions [2]. Electronic conduction, on the other hand, is based on the movement of electrons, which becomes progressively hindered by lattice vibrations as temperature rises (positive temperature coefficient behavior in solids) [3]. In systems containing multivalent cations (e.g. Fe^{2+} and Fe^{3+}), electronic conductivity can also result from the transfer of electrons between these cations – a process known as electron hopping. This mechanism requires thermal activation and is therefore enhanced at elevated temperatures [4].

To describe this temperature-dependent behavior of electrical conductivity in molten slags, both the Arrhenius and Vogel-Fulcher-Tammann (VFT) equations are commonly employed. These approaches are not only applicable to electrical conductivity but are also widely used to characterize the temperature-dependent viscosity of molten slags. However, in contrast to viscosity, electrical conductivity is generally observed to increase with increasing temperature. Within the framework of the Arrhenius approach, both

viscosity (η) and electrical conductivity (σ) are expressed in terms of their respective pre-exponential factors (η_0 and σ_0), an activation energy (E_a), the universal gas constant (R) and the absolute temperature (T), as shown in equations (2) and (3) [5].

$$\ln(\sigma) = \ln(\sigma_0) - \frac{E_a}{R \cdot T} \quad (2)$$

$$\ln(\eta) = \ln(\eta_0) + \frac{E_a}{R \cdot T} \quad (3)$$

In contrast, the Vogel-Fulcher-Tammann (VFT) equation (equations (4) and (5)) introduces a constant B , which has the dimension of temperature and a characteristic temperature T_0 , which differs from the glass transition temperature [6]. Due to the temperature dependence of the activation energy, many materials exhibit a deviation from Arrhenian behavior – particularly at lower temperatures – which can be more accurately described by the Vogel-Fulcher-Tammann equation [7].

$$\ln(\sigma) = \ln(\sigma_0) - \frac{B}{T - T_0} \quad (4)$$

$$\ln(\eta) = \ln(\eta_0) + \frac{B}{T - T_0} \quad (5)$$

By applying both the Arrhenius and Vogel-Fulcher-Tammann approaches, a correlation between the viscosity and the electrical conductivity of slag melts can be established. This correlation provides a basis for the prediction of the electrical conductivity of a given molten slag system as a function of its viscosity [5]. In addition to the semi-empirical correlation, a mechanistic model based on the ionic theory of slags can be employed to analyze the ionic conductivity as a function of the slag's viscosity.

The ionic model assumes that molten metallurgical slags primarily consist of dissociated ionic species [8]. In the context of steelmaking, the main chemical components of slags typically include CaO , SiO_2 , Fe_2O_3 , Al_2O_3 , MgO , MnO and FeO , with the actual composition varying depending on the raw materials, the process route and type of steel being produced [9]. These oxides – particularly silicates – are believed to form an extended ionic network already in the solid state, which remains at least partially intact upon melting [8]. Within this framework, the fundamental structural units of the slag can be categorized into network formers (e.g. $[\text{SiO}_4]^{4-}$, $[\text{AlO}_3]^{3-}$), network modifiers (e.g. Ca^{2+} , Fe^{2+} , Fe^{3+} , Mg^{2+}), anions (e.g. O^{2-} , S^{2-}), and amphoteric cations (e.g. Al^{3+}), each of which plays a distinct role in determining the melt's physico-chemical properties [10].

Even steelmaking slags can thus be described as three-dimensional networks based on $[\text{SiO}_4]^{4-}$ tetrahedra, in which each Si^{4+} is coordinated by four O^{2-} anions, forming covalent Si-O-Si bridges. The addition of alkali or alkaline earth metals (e.g. Mg^{2+} , Ca^{2+}) breaks these bridges, forming ionic non-bridging oxygens. Further

depolymerization may lead to the formation of free oxygen ions not bonded to silicon [11]. Al^{3+} ions can be incorporated into the silicate network as additional network formers when a sufficient amount of charge-balancing cations, such as Ca^{2+} and Mg^{2+} , is available. These cations then serve primarily to maintain charge neutrality and therefore no longer act as network modifiers. In this configuration, Al^{3+} substitutes for Si^{4+} in tetrahedral coordination, forming four covalent Al–O bonds and thereby contributing to the polymerization of the slag structure [12]. However, at high Al_2O_3 concentrations, Al^{3+} can also function as a network modifier, exhibiting five- or sixfold coordination and promoting depolymerization of the silicate network. This dual structural role reflects the amphoteric nature of Al_2O_3 in metallurgical slags [13]. Similarly, iron species can act either as network formers or network modifiers, depending on their oxidation state. Fe^{2+} typically functions as a network modifier, leading to depolymerization of the silicate network. Fe^{3+} , on the other hand, can – analogous to Al^{3+} – substitute for Si^{4+} in tetrahedral coordination and contribute to network polymerization, or exist in higher coordination states and thereby promote depolymerization [12].

Building on this structural understanding, the mechanistic model interprets ionic conductivity as the cumulative effect of the mobility, charge and concentration of the individual ionic species present in the melt. This approach incorporates the principle that a constant transport velocity of ions is achieved when the electrical force and the frictional force are in equilibrium. Thereby, the relationship depicted in equation (6) for the maximum transport velocity (\bar{v}_{max}) is established. In this formula, z denotes the number of elementary charges e_0 , E is the electric field strength, η the dynamic viscosity and r the ionic radius [2].

$$\bar{v}_{max} = \frac{z \cdot e_0 \cdot \bar{E}}{6 \cdot \pi \cdot \eta \cdot r} \quad (6)$$

The parameters defined in equation (6) can be summarized into the electrophoretic mobility μ , resulting in the form for the calculation of the maximum transport velocity given in equation (7) [14].

$$\bar{v}_{max} = \bar{E} \cdot \mu \quad (7)$$

Based on the electrophoretic mobility the ionic conductivity σ_i (with i denoting ionic) can be calculated according to equation (8), where n denotes the concentration of charge carriers [3, 15, 16]. Thus, the ionic conductivity is directly proportional to both the number and the mobility of the charge carriers [17].

$$\sigma_i = n \cdot z \cdot e_0 \cdot \mu \quad (8)$$

This framework leads to the expression presented in equation (9) for the ionic conductivity of a melt containing multiple ionic species – as is the case for molten metallurgical slags – where j indexes the individual ionic species. In this context, the conductivity is described as the cumulative contribution of the ion-specific mobility, charge and concentration [15, 16].

$$\sigma_i = \frac{1}{6 \cdot \pi \cdot \eta} \sum_{j=1}^n \frac{n_j \cdot z_j^2 \cdot e_0^2}{\Gamma_j} \quad (9)$$

Therefore, according to equation (9), the electrical conductivity is inversely proportional to the viscosity and the ionic radius and directly proportional to the ion concentration and the square of the ionic charge. Consequently, with increasing temperature, the viscosity of the melt decreases, which enhances the ionic mobility and leads to a corresponding increase in electrical conductivity [16], in agreement with the trends described earlier by the Arrhenius and Vogel-Fulcher-Tammann approaches.

Electrical Conductivity Measurement Method

Within this study, the specific electrical conductivity of molten slag systems was determined using the Van der Pauw technique, a four-electrode method designed for solid samples of arbitrary shape. In this method, the electrodes are placed along the edge of the sample at arbitrary distances around its perimeter (as illustrated in Figure 1) [17]. The specific resistance of the sample ρ , defined as the reciprocal of the specific electrical conductivity, is calculated based on the sample thickness (d) and the measured resistance values ($R_{AB,CD}$ and $R_{BC,DA}$). These resistance values are obtained through impedance spectroscopy by alternating the current and voltage paths (i.e. switching between configurations ‘1’ and ‘2’) and applying equivalent circuit approximation methods [18].

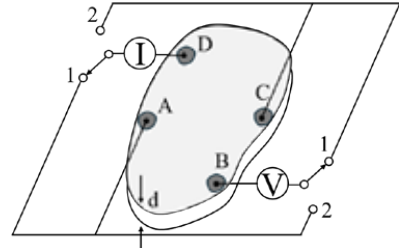


Figure 1: Schematic representation of a sample with thickness d , equipped with electrical contacts following the Van der Pauw method. The electrical resistances are determined by alternating the contact configuration between ‘1’ and ‘2’. Based on [18]

To account for uncertainties regarding the sample thickness, Aya and Saito [19] modified the Van der Pauw method by introducing measurements at two different electrode immersion depths (denoted as W_1 and W_2). This modification exploits the fact that the impedance difference between these two immersion depths can be attributed to a homogeneous component of the current density distribution, which can be modeled as a parallel circuit. Based on this approach, the specific resistance can be determined according to equation (10) and the electrical conductivity is obtained as its reciprocal (with j denoting the respective immersion depth).

$$\rho = \frac{2 \cdot \pi}{\ln(2)} \cdot \frac{R_{W1} \cdot R_{W2} \cdot (W_2 - W_1)}{R_{W1} - R_{W2}}; \quad \sigma = \rho^{-1} \quad (10)$$

$$R_{Wj} = \frac{R_{AB,CD(Wj)} + R_{BC,DA(Wj)}}{2}$$

To account for the complex impedance behavior of the measurement cell, impedance spectroscopy is employed over a broad frequency range. The extraction of the resistance values ($R_{AB,CD}$ and $R_{BC,DA}$), also referred to as the electrolyte resistance (R_E) is accomplished by applying an equivalent circuit approximation, as illustrated in Figure 2. In addition to the electrolyte resistance, the equivalent circuit includes the double-layer capacitance (C_{DL}), the charge transfer resistance (R_{CT}) and the line inductance (L_L), which arises from the long, unshielded electrode wires inside the furnace chamber. The electrolyte resistance is obtained through numerical optimization methods [2, 20].

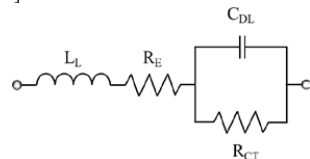


Figure 2: Extended Randles equivalent circuit model with electrolyte resistance R_E , charge transfer resistance R_{CT} , line inductance L_L , and double-layer capacitance C_{DL} . Based on [2]

Electrical Conductivity Experimental Setup

The electrical conductivity of two distinct molten slag systems was measured at various temperatures employing the extended Van der Pauw configuration. The chemical compositions of the slags are provided in Table 1.

Table 1: Chemical compositions of the investigated slag systems (in wt.-%).

Slag	CaO	SiO ₂	MgO	Al ₂ O ₃
	[wt.-%]			
Slag 1	43.7	40.3	7.4	8.5
Slag 2	47.8	44.1	8.2	0.0

The conductivity measurements were performed in a radiation-heated vacuum furnace equipped with MoSi₂ heating elements, operated under continuous argon purging. Electrochemical impedance spectroscopy was carried out using a Gamry Interface 1010E potentiostat over a frequency range of 0.1 to 100.0 kHz. The setup employed molybdenum electrodes ($d = 1.0$ mm) inserted into an alumina four-hole capillary and a graphite crucible containing the molten slag. The difference in electrode immersion depths ($W_2 - W_1$) was 4.0 mm. Proper immersion of the electrode wires into the melt was confirmed by resistance measurements. The evaluation of the electrical conductivity data, including the extraction of the electrolyte resistance, was performed using the previously described equivalent circuit approximation. The measurements were conducted in a temperature range of 1400 – 1600 °C, commencing from the highest temperature.

In addition to the conductivity measurements, the viscosity of Slag 1 was determined, at various temperatures, using a rheometer (Anton Paar, FRS 1800, equipped with a gas-tight option; rotating cylinder method) at a shear rate of 10 s^{-1} .

Results & Discussion

The temperature-dependence of the measured viscosity and electrical conductivity data was fitted using both the Arrhenius (equations (2) and (3)) and Vogel-Fulcher-Tammann models (equations (4) and (5)), as shown in Figure 3 Figure 4. For the viscosity data, both fitting approaches yielded a coefficient of determination (R^2) of close to 1.00. In contrast, for the electrical conductivity data, the Arrhenius model resulted in an R^2 of 0.83, whereas the VFT model achieved an R^2 of 0.97. This improvement clearly reflects the non-Arrhenian behavior observed at lower temperatures and highlights the VFT model's better suitability in representing the temperature-dependent electrical conductivity of molten slags.

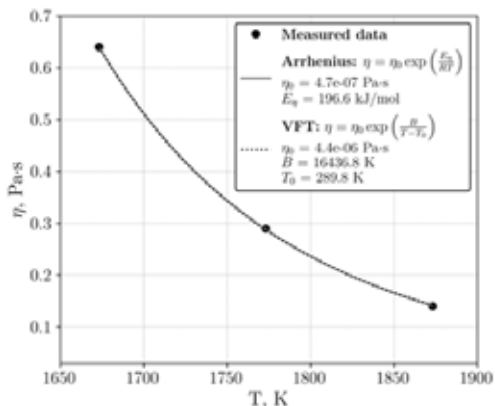


Figure 3: Measured viscosity of Slag 1 at a shear rate of 10 s^{-1} , as a function of temperature, fitted with Arrhenius and VFT models.

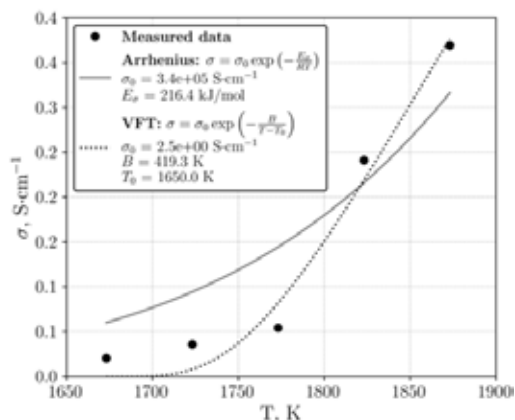


Figure 4: Measured electrical conductivity of Slag 1 as a function of temperature, fitted with Arrhenius and VFT models.

Since both viscosity and electrical conductivity exhibit a temperature dependence that can be described by either the Arrhenius or the Vogel-Fulcher-Tammann model, a direct semi-empirical correlation between $\ln(\eta)$ and $\ln(\sigma)$ can be established. This relationship is expressed in equation (11), where n reflects the ratio of the characteristic activation parameters, and m accounts for the effects of the respective pre-exponential factors, serving as an offset independent of temperature. This correlation provides a basis for predicting the electrical conductivity of a given slag system from its viscosity data and vice versa [5].

$$\ln(\eta) = n \cdot \ln(\sigma) + m \quad (11)$$

The applicability of the correlation described by equation (11) is demonstrated in Figure 5. A distinct linear relationship between $\ln(\eta)$ and $\ln(\sigma)$ for Slag 1 is observed across the investigated temperature range (1673 K, 1773 K and 1873 K). The derived fitting parameters for this system are $n = -0.50$ and $m = -2.53$.

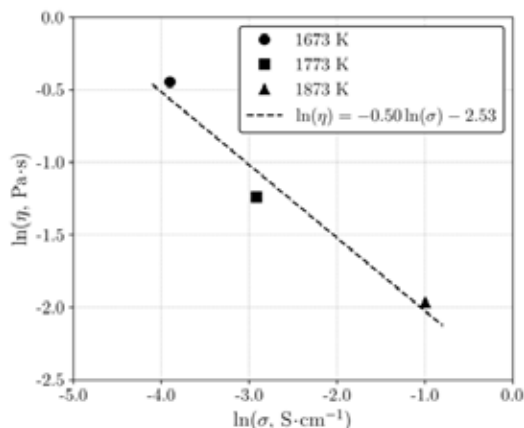


Figure 5: Correlation between the logarithm of viscosity and the logarithm of electrical conductivity for Slag 1 at different temperatures. The dashed line represents the linear fit according to equation (11)

In addition to the described semi-empirical correlation, a mechanistic model based on the ionic theory of slags was applied, as defined by equation (9). Within this approach, it is assumed that all ions are freely available to carry charge (e.g., Ca^{2+} , Mg^{2+} , Si^{4+} , O^{2-} for Slag 2), thereby neglecting the possible formation of neutral

species or ionic complexes, which could significantly reduce the effective number of mobile charge carriers in the melt. This simplification is due to the complexity of accurately describing the dynamic structural behavior of molten slags [21]. To evaluate the validity of this theoretical approach, model predictions were compared with experimental results. Figure 6 presents the measured and calculated electrical conductivity values for Slag 2 as a function of temperature.

The viscosity values used for the calculation were estimated based on the established Kalmanovitch-Frank and Riboud models [22]. Consistent with the assumptions previously outlined for the ionic conduction model, the concentration of charge carriers was derived from the chemical composition of Slag 2, assuming complete dissociation of all oxide species into freely mobile ions.

The measured electrical conductivity exhibits a steady increase with rising temperature, which is consistent with the enhanced mobility of ionic species at elevated temperatures. The calculated conductivity values follow a similar trend but systematically underestimate the experimental data across the entire temperature range. This discrepancy is likely attributable to the simplified assumptions of the model, particularly the neglect of detailed structural dynamics, such as changes in the degree of polymerization, variations in the effective charge carrier concentration and possible changes in the ionic radii within the molten state. The average relative deviation between measured and calculated conductivity values is approximately 16 %. Overall, the reasonable agreement between measured and calculated values confirms the applicability of the mechanistic model based on the ionic theory, for predicting ionic conductivity trends in molten slags, despite the simplifications involved.

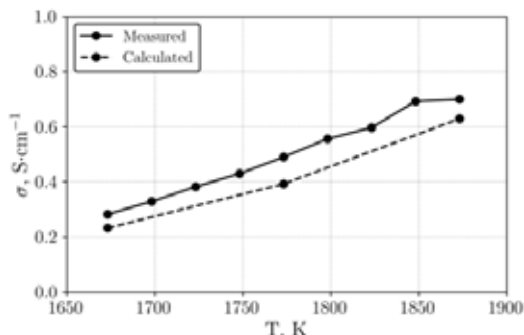


Figure 6: Comparison between measured and calculated electrical conductivity values for Slag 2 as a function of temperature.

References

- [1] M. Barati und K. S. Coley, "Electrical and electronic conductivity of CaO-SiO₂-FeOx slags at various oxygen potentials: Part II. Mechanism and a model of electronic conduction," *Metall Mater Trans B*, Jg. 37, Nr. 1, S. 51–60, 2006, doi: 10.1007/s11663-006-0085-9.
- [2] C. H. Hamann und W. Vielstich, *Elektrochemie*, 4. Aufl. Weinheim: Wiley-VCH-Verlag GmbH & Co. KGaA, 2005.
- [3] R. E. Hummel, *Electric properties of materials: An introduction for engineers*. Berlin, Heidelberg: Springer, 1985.
- [4] H.-J. Engell und P. Vygen, "Ionen- und Elektronenleitung in CaO-FeO-Fe₂O₃-SiO₂-Schmelzen," *Ber Bunsenges Phys Chem*, Jg. 72, Nr. 1, S. 5–12, 1968, doi: 10.1002/bbpc.19680720104.
- [5] G.-H. Zhang und K.-C. Chou, "Correlation Between Viscosity and Electrical Conductivity of Aluminosilicate Melts," *Metall Mater Trans B*, Jg. 43, Nr. 4, S. 849–855, 2012, doi: 10.1007/s11663-012-9674-y.
- [6] G. Tammann und W. Hesse, "Die Abhängigkeit der Viscosität von der Temperatur bei unterkühlten Flüssigkeiten," *Z. Anorg. Allg. Chem.*, Jg. 156, Nr. 1, S. 245–257, 1926, doi: 10.1002/zaac.19261560121.
- [7] D. B. Dingwell *et al.*, "The glass transition and the non-Arrhenian viscosity of carbonate melts," *American Mineralogist*, Jg. 107, Nr. 6, S. 1053–1064, 2022, doi: 10.2138/am-2021-7752.
- [8] W. A. Fischer und D. Janke, *Metallurgische Elektrochemie*. Berlin, Heidelberg: Springer Berlin Heidelberg, 1975.
- [9] L. Bing, T. Biao, M. Zhen, C. Hanchi und L. Hongbo, "Physical and Chemical Properties of Steel Slag and Utilization Technology of Steel Slag at Home and Abroad," *IOP Conf. Ser.: Earth Environ. Sci.*, Jg. 242, S. 32012, 2019, doi: 10.1088/1755-1315/242/3/032012.
- [10] H. W. Gudenau, "Materialsammlung zum Praktikum Metallurgie," Begleitliteratur zur Vorlesung "Stahlmetallurgie", Institut für Eisenhüttenkunde, RWTH Aachen, Aachen, 2002.
- [11] M. Sajid, C. Bai, M. Aamir, Z. You, Z. Yan und X. Lv, "Understanding the Structure and Structural Effects on the Properties of Blast Furnace Slag (BFS)," *ISIJ Int.*, Jg. 59, Nr. 7, S. 1153–1166, 2019, doi: 10.2355/isijinternational.ISIJINT-2018-453.
- [12] B. O. Mysen, *Silicate Glasses and Melts*, 2. Aufl. (Developments in Geochemistry v.10). Saint Louis: Elsevier Science & Technology, 2018. [Online]. Verfügbar unter: <https://ebookcentral.proquest.com/lib/kxp/detail.action?docID=5606602>
- [13] S. Seetharaman, *Treatise on Process Metallurgy, Volume 1: Process Fundamentals*. Oxford: Elsevier, 2014. [Online]. Verfügbar unter: <https://ebookcentral.proquest.com/lib/kxp/detail.action?docID=1573348>
- [14] R. W. O'Brien und L. R. White, "Electrophoretic mobility of a spherical colloidal particle," *J. Chem. Soc., Faraday Trans. 2*, Jg. 74, S. 1607, 1978, doi: 10.1039/F29787401607.
- [15] E. Drioli und L. Giorno, *Encyclopedia of Membranes*. Berlin, Heidelberg: Springer Berlin Heidelberg, 2016.
- [16] T. Yoshino, "Laboratory Electrical Conductivity Measurement of Mantle Minerals," *Surv Geophys*, Jg. 31, Nr. 2, S. 163–206, 2010, doi: 10.1007/s10712-009-9084-0.
- [17] L. J. van der Pauw, "A Method of Measuring Specific Resistivity and Hall Effect of Discs of Arbitrary Shape," *Philips Research Reports*, S. 1–9, 1958.
- [18] F. S. Oliveira, R. B. Cipriano, F. T. Da Silva, E. C. Romão und C. A. M. Dos Santos, "Simple analytical method for determining electrical resistivity and sheet resistance using the van der Pauw procedure," *Scientific reports*, Early Access. doi: 10.1038/s41598-020-72097-1, 2020.
- [19] F. K. Aya und N. Saito, "The joint research regarding the development of a measurement method to generate material data of metallurgical slag systems with special focus on the electrochemical properties, i.e., electrical conductivity," Kyushu University, 2021.
- [20] S. Moll, "Vergleich impedanzspektroskopischer Methoden zur Leitfähigkeitsmessung an Schlackeschmelzen", Masterarbeit, Montanuniversität Leoben, 2023.
- [21] E. Thibodeau und I.-H. Jung, "A Structural Electrical Conductivity Model for Oxide Melts," *Metall Mater Trans B*, Jg. 47, Nr. 1, S. 355–383, 2016, doi: 10.1007/s11663-015-0458-z.
- [22] S. Vargas, F. J. Frandsen und K. Dam-Johansen, "Rheological properties of high-temperature melts of coal ashes and other silicates," *Progress in Energy and Combustion Science*, Jg. 27, Nr. 3, S. 237–429, 2001, doi: 10.1016/S0360-1285(00)00023-X.

Environmental Posters

Day 2

Wer was kann, kann hier alles können.

*Wir geben dir das Vertrauen,
die Freiheit und den Raum,
um im Job glücklich zu werden
und Ideen nicht nur
vorzuschlagen sondern auch
umzusetzen. Lern uns kennen.*

Entdecke deine
Chancen auf
spiegltec.com/karriere



Towards Robust Fuel Cell Systems: Mitigating the Risks of Over-Humidification

M. Käfer^{1,*}, V. Hacker¹, M. Bodner¹

¹: Institute of Chemical Engineering and Environmental Technology, University of Technology Graz, Austria

* Correspondent author: maximilian.kaefer@tugraz.at

Keywords: PEFCs, Over-humidification, Water management, Sensor calibration, Condensation, Fuel cell diagnostics

Polymer electrolyte fuel cells (PEFCs) are central to the transition toward sustainable and emission-free mobility. However, their operational reliability is highly sensitive to water management. Imbalances in humidity, particularly over-humidification, can trigger condensation in the flow channels and diffusion layers, leading to flooding, catalyst degradation, fuel starvation, and long-term membrane deterioration. These effects are amplified during operation, such as start-up or load cycling, where thermal and flow conditions fluctuate rapidly [1,2].

This research investigates humidity-driven degradation mechanisms using a modular experimental platform that replicates automotive environments, including over-humidification and dew point mismatches. Condensation is forced at specific locations before and after the cell (anode and cathode sides) to study localized flooding and system response. A key innovation is the calibration of a copper interdigitated electrodes-based sensor with defined water droplet quantities (microliter range), applied at a 90° angle, enabling precise quantification of condensation effects. Preliminary results show that the sensor detects water droplet formation within a response and recovery time of less than 20 seconds, achieving an accuracy of ±4%.

By monitoring signal dynamics and residence times of droplets, the work supports the development of adaptive water management strategies. The strategic sensor placement and integration with the data acquisition system enables early-stage diagnostics, providing crucial feedback for real-time control system optimization. These insights are critical for enhancing the robustness and service life of PEFC systems, advancing FCEVs as a durable and scalable clean mobility solution.

Acknowledgement

This project is funded by the Climate and Energy Fund and is carried out within the framework of the program “Zero Emission Mobility”.

References

- [1] X.R. Wang, Y. Ma, J. Gao, T. Li, G.Z. Jiang, Z.Y. Sun, Review on water management methods for proton exchange membrane fuel cells, *International Journal of Hydrogen Energy* 46 (2021) 12206–12229. <https://doi.org/10.1016/j.ijhydene.2020.06.211>.
- [2] X. Xu, K. Li, Z. Liao, J. Cao, R. Wang, A Closed-Loop Water Management Methodology for PEM Fuel Cell System Based on Impedance Information Feedback, *Energies* 15 (2022) 7561. <https://doi.org/10.3390/en15207561>.

Calibration of a Concrete Pump for Automated Shotcrete Application in Tunneling

Igor Schweigg^{1,2}, Gabriel Neumann¹, Thomas Senfter², Christian Mayer², Martin Pillei³, Rainer Antretter¹

1: BeMo Tunnelling GmbH, Austria

2: Dept. of Environmental, Process & Energy Engineering, MCI Innsbruck, Austria

3: Dept. of Industrial Engineering and Management, MCI Innsbruck, Austria

* Correspondent author: igor.schweigg@bemo.net

Keywords: Concrete pumping process, Process control in shotcrete application, Material flow consistency, Flow rate calibration

Considering the growing demand for urban infrastructure, automation in the construction industry is gaining increasing importance. Given the ongoing shortage of skilled labor and the simultaneously high demands on occupational safety and execution quality in tunnel construction, fully automated shotcrete application offers significant potential. The present work is part of a research project aimed at fully automating the shotcrete application process using a retrofitted Meyco Logica 15 application machine. A key element of this process is ensuring a constant concrete delivery rate, as it directly influences the quality and uniformity of the applied shotcrete layers.

The aim of the experimental series presented here was therefore to empirically determine the actual (effective) concrete delivery rate of the pump at various preset target flow rates. For this purpose, shotcrete was pumped into a receiving silo marked at a predefined target height. The time required to reach this mark was recorded, allowing the actual delivery rate to be calculated from volume and time.

The results showed significant deviations between the preset target delivery rate and the actual amount delivered. While the displayed and measured flow rates matched closely at low delivery rates, increasing discrepancies were observed at higher rates. These deviations are likely due to changes in the concrete's consistency caused by repeated pumping and resulting mechanical stress. The first five data points (7.1–9.7 m³/h) were deemed reliable and are now used as a basis for calibrating the control system for automated application. These findings thus represent an important contribution to the further development of fully automated shotcrete application processes in tunnel construction.

List of References

- [1] G. Girmscheid and S. Moser, "Fully Automated Shotcrete Robot for Rock Support," *Computer aided Civil Eng.*, vol. 16, no. 3, pp. 200–215, 2001, doi: 10.1111/0885-9507.00226.
- [2] S. B. Moser, *Vollautomatisierung der Spritzbetonapplikation - Entwicklung der Applikations-Prozesssteuerung: Entwicklung der Applikations-Prozesssteuerung*. Zugl.: Zürich, Techn. Hochsch., Diss., 2004. [Zürich]: vdf Hochsch.-Verl. an der ETH, 2004.

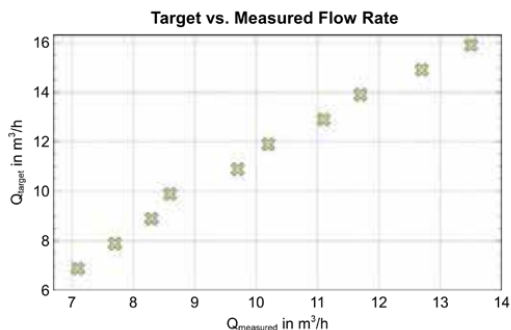


Figure 1: Comparison between target and measured flow rates. The figure shows that, at every data point, the target values consistently exceed the measured delivery rates.

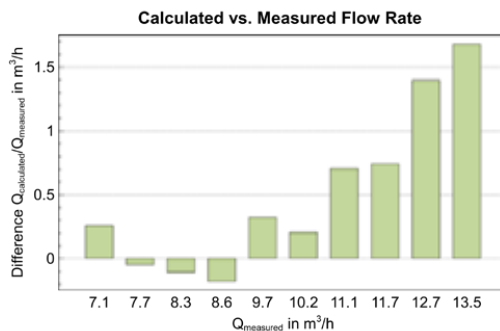


Figure 2: Comparison between the measured and the displayed calculated delivery rates. The results show good agreement between actual and calculated values up to 10.2 m³/h. Beyond this point, significant deviations occur, likely caused by changes in concrete consistency due to repeated recirculation and constant mechanical stress.

Decolourisation of Starch Hydrolysates Using Activated Carbon and Ultrafiltration

Alexander Trischack^{1,*}, Camila A. Cabeza¹, Amal El Gohary Ahmed¹, Christian Jordan¹, Michael Harasek¹

1: Institute of Chemical Environmental & Bioscience Engineering E166, Technische Universität Wien, 1060 Vienna, Austria

* Corresponding author: alexander.trischack@tuwien.ac.at

Keywords: Starch Hydrolysates, Decolourisation, Activated Carbon, Adsorption, Ultrafiltration

Starch hydrolysates can be produced using pH-driven or enzymatic methods. Enzymatic hydrolysis is the most widely used in the industry. This enzymatic process occurs in two stages: liquefaction by the action of amylases, followed by saccharification by glucoamylases. After the two-stage hydrolysis process, glucose syrup is produced with a determined initial sugar composition. The glucose, which is obtained from enzymatic hydrolysates, mostly has a brownish colour. This colouration can arise from several processes, including the Maillard reaction, pyrolysis, or caramelisation.

Nowadays, activated carbon and ion exchange resins are widely used to decolourise starch hydrolysates. Due to environmental regulations, ion exchange is prohibited in some cases. This shift has increased interest in membrane processes for colour removal; however, these methods have not yet been implemented in industrial applications.

In this research, the reduction of activated carbon dosage was examined by testing different ultrafiltration (UF) membranes. The experiments were conducted on a lab scale, using different activated

carbon (AC) dosages ranging from 1 to 8 kg per m³ to decolourise starch hydrolysate solutions. Untreated and ultrafiltration-treated starch hydrolysate solutions were tested to determine the optimal AC dosage and assess the performance of UF and AC treatments.

The optimal dosage for effectively decolourising untreated starch hydrolysates is determined to be 6 kg per m³ when working at a concentration of 30° Bx (1° Bx = 1 g sucrose / 100 g solution) and a temperature of 70°C. In contrast, for starch hydrolysates at a lower concentration of 20° Bx, the ideal dosage reduces to 4 kg per m³. Furthermore, it was observed that employing pre-treatment techniques, such as loose and tight UF membranes, does not significantly improve the decolourisation process compared to using syrup without pre-treatment.

This indicates that the pre-treatment methods may not enhance the decolourisation of starch hydrolysates. Further investigations should be conducted into utilising various types of membranes, such as nanofiltration and multistage setups, to explore potential enhancements to the process.

References:

- [1] H. Peter, *Glucose Syrups: Technology and Applications*, First edition. John Wiley & Sons, 2010.
- [2] M. W. Kearsley and S. Z. Dziedzic, *Handbook of Starch Hydrolysis Products and their Derivatives*, First edition. Dordrecht: Springer Science + Business Media, 1995. doi: 10.1001/918-1-4615-2159-4.

Upscaling of the Removal of Pharmaceuticals from Wastewater with Multi-channel Mixed-matrix membranes into pilot scale

Jana Marx^{1,2}, Santiago Nicolas Otaiza Gonzalez³, Sara Rodriguez Mozaz³, Lucas Leonel Alonso³, Judith Schobel¹, Werner Marktl⁴, Jan Back¹, Daniel Rattinger¹, Tung Pham², Martin Spruck¹

1: Department of Environmental, Process & Energy Engineering, MCI – The Entrepreneurial School, Maximilianstraße 2, Innsbruck, Austria

2: Research Institute of Textile Chemistry and Textile Physics, University of Innsbruck, Hoechststraße 73, Dornbirn, Austria

3: ICRA – Catalan water research institute, Scientific and Technological Park of the University of Girona, Emili Grahit 101, 17003 Girona, Spain

4: Josef Ressel Centre for production of activated carbon from municipal residues, Department for Environmental-, Energy and Process Engineering, Management Center Innsbruck_MCI, Maximilianstraße 2, Innsbruck, 6020, Tyrol, Austria

* Correspondent author: jana.marx@mci.edu

Keywords: environmental pollution, pharmaceutical elimination, wastewater analytics, membrane treatment

Mixed-matrix, multi-channel membranes (MCMMMs) with embedded powdered activated carbon have been successfully used to remove micropollutants from spiked tap water and wastewater [1, 2]. The main advantages of this combined filtration and adsorption process are reduced pressure requirements and protection of the powdered activated carbon from competitive adsorption with the dissolved organic material found in wastewater. Additionally, the system's chemical regeneration helps elongate its lifespan and ensure its reusability, even when the powdered activated carbon is fully loaded [1]. Removing micropollutants is especially important for pharmaceuticals found in conventional wastewater treatment plant effluent [3–7], as releasing pharmaceuticals into the environment through wastewater treatment plants is a significant issue with consequences for ecosystems and humans [8–11].

Previous studies on removing pharmaceuticals from spiked wastewater streams used MCMMM at concentrations of up to 15 mg/L. These high concentrations were necessary to better understand MCMMM's removal efficiency. However, applying MCMMM to the fourth stage of conventional wastewater treatment only makes sense if the system can remove realistic concentrations ranging from nano- to micrograms per liter over a long period. In this study, the concentrations of various pharmaceutical active compounds and their metabolites were quantified in the effluent of a wastewater treatment pilot plant using LC-MS/MS. The effluent is equal to the feed of the filtration plant. Additionally, the concentrations in the permeate after MCMMM filtration were analyzed.

Comparing the feed and permeate concentrations shows sufficient removal efficiencies for most of the analyzed pharmaceuticals. Fouling was not detected during a 144 hour filtration experiment with one regeneration after 72 hours.

Overall, the application of MCMMM on a pilot scale is a promising process for removing pharmaceuticals in the fourth stage of wastewater treatment.

References

- Marx J, Back J, Hoiss L et al. (2023) Chemical Regeneration of Mixed-Matrix Membranes for Micropollutant Removal from Wastewater. *Chemie Ingenieur Technik*. <https://doi.org/10.1002/cite.202300075>
- Marx J, Back J, Netzer F et al. (2024) Comprehensive characterisation of multi-channel mixed-matrix membranes and impact of water matrix variability on micropollutant removal. *Case Studies in Chemical and Environmental Engineering* 10:100930. <https://doi.org/10.1016/j.cscee.2024.100930>
- Almeida Â, Soares AMVM, Esteves VI et al. (2021) Occurrence of the antiepileptic carbamazepine in water and bivalves from marine environments: A review. *Environ Toxicol Pharmacol* 86:103661. <https://doi.org/10.1016/j.etap.2021.103661>
- Batucan NSP, Tremblay LA, Northcott GL et al. (2022) Medicating the environment? A critical review on the risks of carbamazepine, diclofenac and ibuprofen to aquatic organisms. *Environmental Advances* 7:100164. <https://doi.org/10.1016/j.envadv.2021.100164>
- Boxall AB, Wilkinson JL, Bouzas-Monroy A (2022) Medicating nature: Are human-use pharmaceuticals poisoning the environment? *One Earth* 5:1080–1084. <https://doi.org/10.1016/j.oneear.2022.09.009>
- Fernández M, Fernández M, Laca A et al. (2014) Seasonal occurrence and removal of pharmaceutical products in municipal wastewaters. *Journal of Environmental Chemical Engineering* 2:495–502. <https://doi.org/10.1016/j.jece.2014.01.023>
- Liu Y, Wang P, Gojenko B et al. (2021) A review of water pollution arising from agriculture and mining activities in Central Asia: Facts, causes and effects. *Environ Pollut* 291:118209. <https://doi.org/10.1016/j.envpol.2021.118209>
- Sanchez W, Sremski W, Piccini B et al. (2011) Adverse effects in wild fish living downstream from pharmaceutical manufacture discharges. *Environ Int* 37:1342–1348. <https://doi.org/10.1016/j.envint.2011.06.002>
- Schapira M, Manor O, Golan N et al. (2020) Involuntary human exposure to carbamazepine: A cross-sectional study of correlates across the lifespan and dietary spectrum. *Environ Int* 143:105951. <https://doi.org/10.1016/j.envint.2020.105951>
- Schriks M, Heringa MB, van der Kooij MME et al. (2010) Toxicological relevance of emerging contaminants for drinking water quality. *Water Res* 44:461–476. <https://doi.org/10.1016/j.watres.2009.08.023>
- Törnqvist R, Jarsjö J, Karimov B (2011) Health risks from large-scale water pollution: trends in Central Asia. *Environ Int* 37:435–442. <https://doi.org/10.1016/j.envint.2010.11.006>

Desorption of Micropollutants from Bio-based Gasification Chars in Wastewater Treatment

C. Margreiter^{1,2*}, F. Mittendrein³, A. Hofmann², A. O. Wagner¹

1: Dept. of Microbiology, The University of Innsbruck Austria

2: Josef Ressel Center for the Production of Activated Carbon from Municipal Residues, MCI Innsbruck, Austria

3: Dept. of Biotechnology & Food Engineering, MCI Innsbruck, Austria

* Correspondent author: Christian.Margreiter@mci.edu

Keywords: Micropollutants, Gasification Char, Wastewater Treatment

Environmental harmful micropollutants (eMPs) in wastewater are a growing concern for water quality and environmental health. In response, EU Directives now require wastewater treatment plants to implement a fourth stage of treatment. The use of bio-based gasification char (BGC) with high adsorption capacity for eMPs represents a promising approach to meet this requirement. After use as an adsorbent, BGC is typically transferred to anaerobic digesters with the wastewater treatment sludge line. High temperatures and acidic conditions can result in desorption of previously adsorbed eMPs. This study investigates the desorption behavior of eMP-loaded BGC under anaerobic conditions. BGC was loaded with selected eMPs (benzotriazole, metoprolol, sulfamethoxazole, valsartan, carbamazepine, diclofenac) from a floating fixed bed gasification plant. The desorption experiments were carried out both in water and in a mesophilic anaerobic digestion (AD) batch set up over a period of 47 days. Different desorption behaviors depending on the eMP were observed in the water-based tests. According to their low Freundlich isotherm K_f values, benzotriazole, sulfamethoxazole and metoprolol showed the highest desorption from BGC. These tests provide insight into desorption trends and inform future strategies for the safe application of BGC in sludge treatment processes. Further results from the AD trials will be reviewed in upcoming publications.

List of References

- [1] Margreiter, C., Probst, M., Prem, E.M., Hofmann, A., & Wagner, A.O. (2024). Gasification chars and activated carbon: Systematic physico-chemical characterization and effect on biogas production. *Heliyon*, 10 (10), e31264. <https://doi.org/10.1016/j.heliyon.2024.e31264>
- [2] Bosch, D., Back, J. O., Spruck, M., Nohel, L., Gurtner, D., Margreiter, C., Hofmann, A., & Bockreis, A. (2025). Addressing Europe's new hunger for sustainable activated carbon in wastewater treatment: Micropollutant removal with residual wood based adsorbents using different activation strategies. *Chemical Engineering Research and Design*, 217, 108–120. <https://doi.org/10.1016/j.cherd.2025.03.021>
- [3] Marx, J., Back, J., Hoiss, L., Hofer, M., Pham, T., & Spruck, M. (2023). Chemical regeneration of mixed-matrix membranes for micropollutant removal from wastewater. *Chemie Ingenieur Technik*, 95(9), 1416–1427. <https://doi.org/10.1002/cite.202300075>
- [4] Reif, D.; Saracevic, E.; Šabić Runjavec, M.; Haslinger, J.; Schaar, H.; Kreuzinger, N. (2020): Desorption of Organic Micropollutants from Loaded Granular Activated Carbon. *Water*, 12 (10), 2754. <https://doi.org/10.3390/w12102754>



Unsere **TIWAG**

Einfach stark

Mit Milliarden-
Investitionen in die
Energiezukunft.



Entdecken Sie den Mehrwert für Tirol! 



ISBN 978-3-200-10576-8